UNIVERSITY OF NOTTINGHAM

School of Mechanical, Materials, Manufacturing Engineering and Management

Predictive Finite Element Method for Axial Crush of Composite Tubes

Eng. Nuno F S Lourenço

Thesis submitted to the University of Nottingham
for the degree of Doctor of Philosophy
September 2002

Contents

Abstract

This thesis describes the development of a predictive Finite Element methodology for the crush behaviour and specific energy absorption of composite material tubes. Numerical studies were undertaken based on experimental data for the following composite materials:

- Continuous filament random mat (CoFRM) Glass/Polyester 6-ply laminate
- Braided Carbon/Vinylester
  - 2-ply, 3-ply, and 4-ply tubes
  - 0/+30°/-30°, 0/+45°/-45°, and 0/+60°/-60° fibre architectures

The modelling approach consists of treating intralaminar and interlaminar behaviour of the composite separately. An existing finite element material model is used to model intralaminar behaviour and a validation is undertaken against coupon tests. Interlaminar behaviour is modelled via a new delamination contact interface based on fracture toughness concepts. The development and application of the delamination algorithm in the commercial FE code PAM-CRASH is described and a validation against standard fracture toughness tests is included.

This work contains a detailed description of the procedure used to obtain the input parameters for the PAM-CRASH material model, which were collected from a range of standard coupon tests. A description of the modelling technique for the tubes is included, which comprises geometry, meshing details, boundary and loading conditions, and output readings. Results show good agreement with quasi-static experimental data for all the different tubes investigated.

The approach can be considered predictable as only coupon test data is used for the input parameters of the material model and the delamination contact interface.

Acknowledgements

The author would like to thank his supervisor Dr. NA Warrior for his guidance.

The work was funded jointly by the Automotive Composites Consortium, the EPSRC and the University of Nottingham.

The School of Mechanical, Materials Manufacturing Engineering and Management is thanked for the use of departmental facilities and the Faculty Workshop. The help of all technical staff is greatly appreciated, especially Roger Smith, Dave Smith, Paul Johns, and Geoff Tomlinson.

Special thanks to the other members of the Nottingham Crashworthiness Group, Chris Curtis, Dan Bailey, Martin Wilson, Mike Duckett, Edward Cooper, Richard Fernie, Mike Ribeaux, and Tom Turner.

Last but not least, to Dr. Anthony Pickett and all the staff at ESI GmbH for their contribution. A substantial part of this work was developed during a three-month placement at ESI GmbH, Frankfurt, Germany and their support is greatly appreciated.

This work is dedicated to my wife Sarah, my parents José Manuel and Joaquina, my brother José Luis and sister Heloísa, for all their love, support and encouragement.

Glossary

ACC	Automotive Composites Consortium
Anisotropic	Having properties which vary with direction within the material
CoFRM	Continuous Filament Random Mat
CPU	Central Processing Unit
CSM	Chopped Strand Mat
DCB	Double Cantilever Beam (Mode I fracture toughness test)
DOF	Degree of Freedom
ENF	End Notch Flexure (Mode II fracture toughness test)
FE	Finite Element
FEA	Finite Element Analysis
FEM	Finite Element Method/Model
HICAS	High velocity Impact of Composite Aircraft Structures
Interlaminar	Material properties which define mechanical behaviour between plies
Intralaminar	Material properties which define mechanical behaviour within plies
Isotropic	Having properties which do not vary with direction within the material
Lamina	A ply within a composite structure (laminate)
MMB	Mixed-Mode Bending (Mixed-mode fracture toughness test)
PC	Personal Computer
PEEK	Polyetheretherketone, a thermoplastic
Platen	Flat plate used to crush composite materials
Ply	Lamina
SEA	Specific Energy Absorption
Thermoplastic	Polymeric material, which is softened by the application of heat and hardened by cooling in a reversible process
Thermoset	Polymeric material, which is hardened by an irreversible chemical reaction
Tow	An assembly of fibre filaments
UD	Unidirectional
USCAR	United States Council for Automotive Research
[ ]	Numbers in square parenthesis refer to References in Chapter 10. The references are ordered alphabetically.

1.0 Introduction

Car crashes are complex events that result from the interaction of multiple factors. Among them the driver's behaviour, weather conditions, time of the day or the type of road have a relative influence which is independent of vehicle design. Most specialists agree that driver behaviour is the dominant factor that affects the probability of being involved in a car crash [39].

The ability to improve occupant safety in the event of a crash can however be controlled through optimising the energy absorption of the structural components of the vehicle [12]. It is in this context that research on the issue of crashworthiness has developed over the last three decades. Particularly in recent years it has been shown that, under impact, composite materials can absorb much more energy per unit mass than metals.

The advantage of metals lies in the existent computer modelling tools for simulation of crash events, which are an important factor to the reduction of costs associated with the development of a particular vehicle. Such computer codes have not yet provided predictive models of crush of composite materials due to the complex failure mechanisms that these show under impact. It is therefore of interest to develop numerical tools to model these phenomena.

1.1 Energy Absorbing Structures

In the event of a crash, the vehicle structure has to absorb as much of the kinetic energy as possible. This process should occur as smoothly as possible to minimise the accelerations to which the passengers are subjected. The ideal energy absorber has a force-displacement characteristic as shown in Figure 1-1 [9], where the total energy absorbed is equal to the area under the curve.

The purpose of using composite materials deals with optimising the energy absorption whilst keeping the response of the structure to impact as close to an ideal absorber as possible.

The most useful criterion to compare the relative performance of materials under impact is the Specific Energy Absorption (SEA), usually measured in kJ/kg (although some authors base their comparative studies on other criteria such as the mean crush load or specific mean crush Stress).

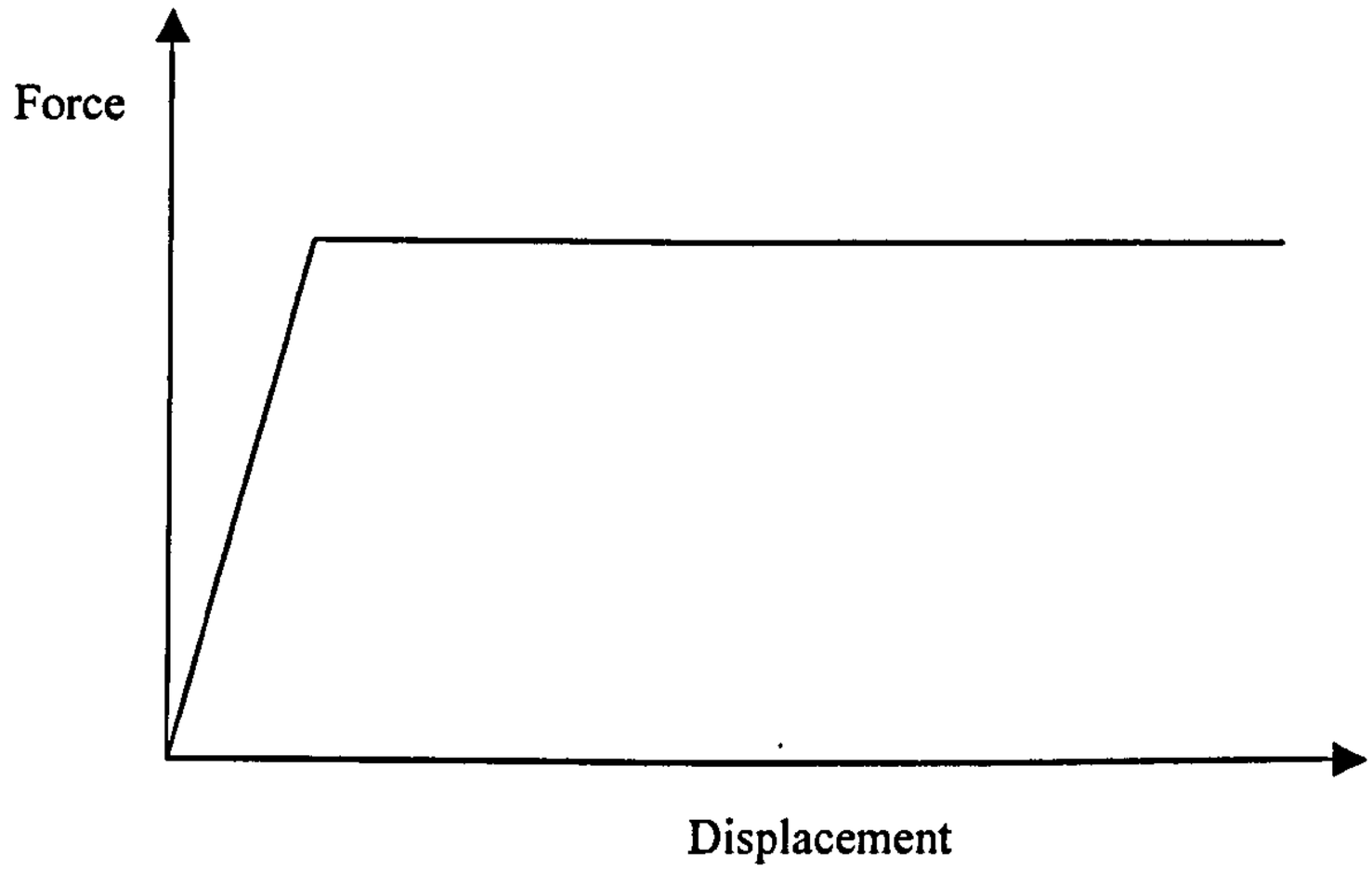

Figure 1-1 - Force v displacement characteristic of an ideal energy absorber

1.2 Composite Materials

Composites materials are made up of two or more non-miscible materials, with the purpose of obtaining improved physical and/or mechanical properties, which are function of the properties of each constituent material. For example two brittle materials like glass and polyester resin can be combined to produce a composite with mechanical properties, which are useful for the required application. Specifically for the automotive field, a more common concept of composite material is the combination of a *fibre* with a *matrix*. The fibre is usually a long and continuous material like the fibres used in textile industry. For structural applications the fibres should have high stiffness and strength. The matrix is, in a simplistic way, the "glue" that bonds the fibres to give the composite material its toughness.

Both fibres and matrix can be made of metallic, polymeric or ceramic material. However composites for automotive applications usually consist of glass or carbon fibres bonded by a resin matrix. Apart from more common thermoset polymers (e.g polyester, vinyl ester, epoxy), thermoplastic systems with short or long fibre reinforcements are now being used, allowing for faster and cheaper manufacturing as well as more recycling capabilities.

The techniques developed in the last two decades for the production of composite materials mean that today's production costs are no longer prohibitive. It is also possible to combine several components in one composite material part only, which can contribute to further cost reduction by decreasing the number of stamping, cutting and welding procedures.

1.3 Project Aims

The study of crush phenomena of composites is well documented (see Chapter 2) and the main failure mechanisms have been identified. The ability to simulate the behaviour of these structures under impact loading in a predictive way is crucial for the cost-effective application of these materials by the automotive industry. Much work has been published in the field of Finite Element modelling of composites and progress has been made regarding material models.

Several authors [2] [8] [9] [40] have addressed delamination modelling as one of the key areas for predictive modelling of composite crush. Applied research to date has not yet provided a model that will account for more complex loading situations typical of real structures subject to impact whilst using only experimental data as the input.

In the present investigation, a delamination approach based on fracture mechanics is developed and its implementation in the explicit Finite Element code PAM-CRASH™ is described. Validation of the model is performed against standard fracture toughness tests, based on experimental data collected at the University of Nottingham.

A multi-ply tube modelling approach, with accurate interlaminar behaviour, is developed and proved suitable to predict the quasi-static crush behaviour and energy absorption of circular composite laminate tubes. Although quasi-static tube crush is not a scenario representative of the failure mode of an entire vehicle, it still provides the correct overall trend that is experienced by a composite member during a crash [45]. Crush of a typical energy absorber consists of a pair of tubes attached between the bumper and the chassis of a vehicle. During the event, the tube crushes progressively and dissipates energy [4].

Other composite material structures have used the proposed delamination model, which are of relevance mainly to the aeronautical and aerospace industries. These are thin shell structures where the effects of impact damage are usually invisible to the naked eye but can have a severe effect in the mechanical behaviour of the material. One example of these studies is the work developed by Johnson and Pickett [33] in the HICAS research programme, which is of particular relevance to the work presented here as the delamination model described in Chapter 4 was the result of close collaboration with those authors and ESI GmbH [41].

2.0 Literature Review

2.1 Composites Tube Crush

Several authors have accepted the crushing of tubes as a suitable way to quantify the Specific Energy Absorption (SEA) of materials as well as to examine their crush behaviour [5] [17] [30].

Composite tube crush and the prediction of SEA has been the subject of numerous studies of which the ones mentioned in this work are but a few relevant examples. Research by authors such as Hull [31], Mamalis [36], Hamada [20], Ramakrishna [23], and Farley[15] are well known in the composites community.

2.2 Crush Modes of Composite Tubes

In this section a description of the crush mechanisms of composite tubes and types of failure associated with them is given. This description relies mainly on the work carried out by Hull [30].

Whereas metallic tubes fail by progressive folding (Figure 2-1), most composite material tubes tend to fail by progressive crushing (Figure 2-4). Some composite tubes also fail by progressive folding. This is the case with tubes reinforced with ductile fibre reinforcements such as Kevlar and Dyneema [23], and also with thin-walled tubes with carbon or glass reinforcements [29].

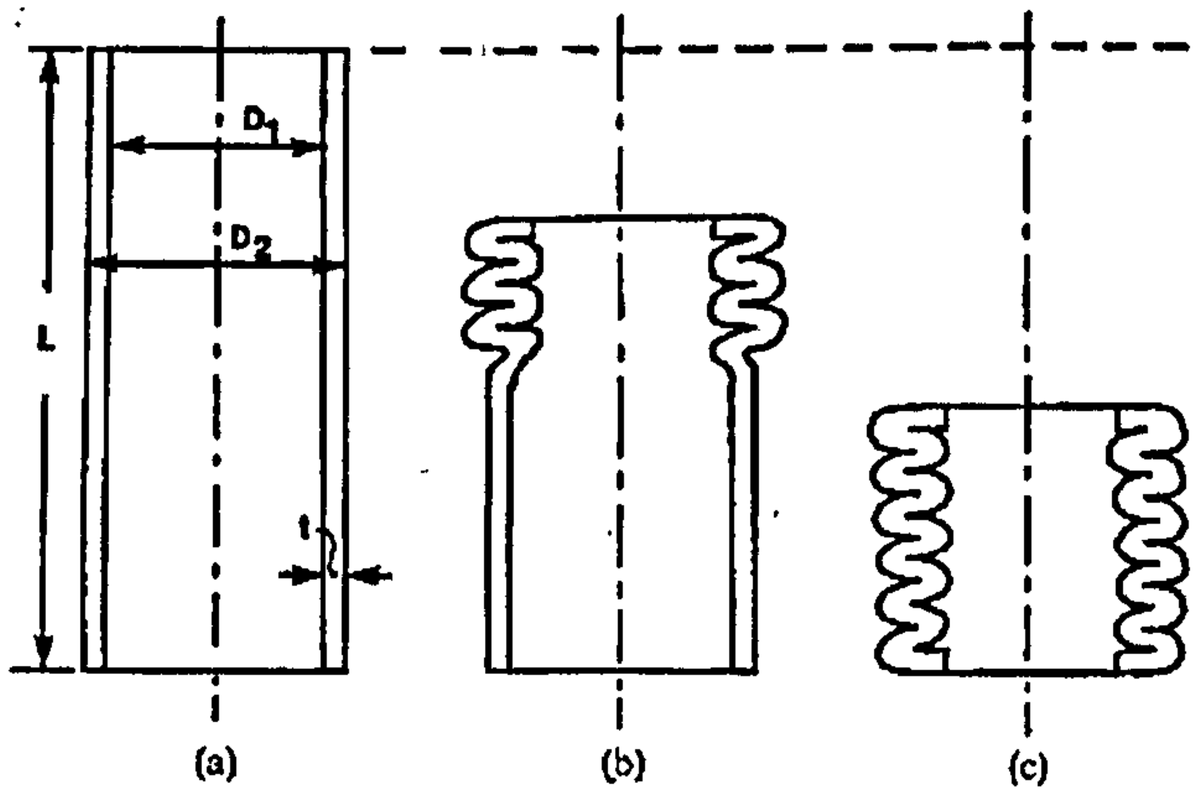

Figure 2-1 - Schematic representation of progressive folding: (a), undeformed tube; (b), progressive folding; (c), compacted tube [30].

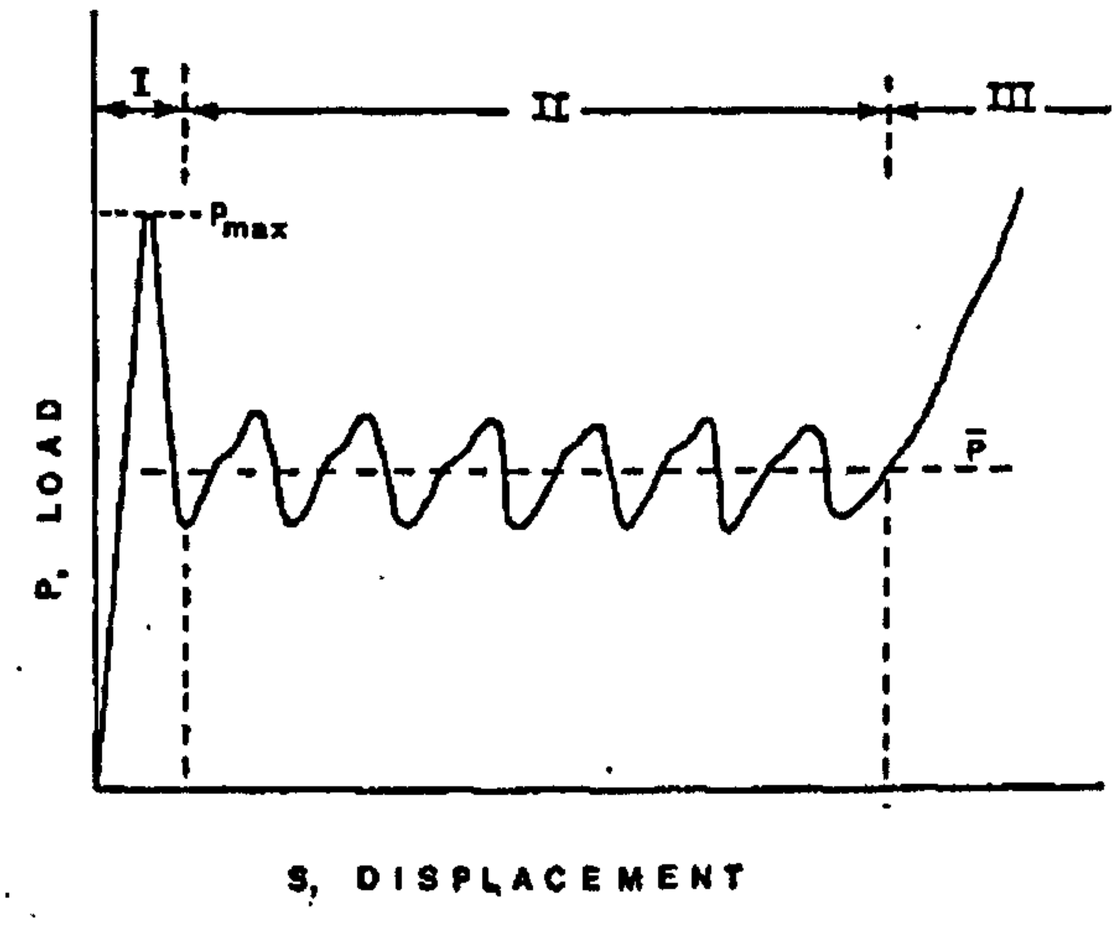

Figure 2-2 – Typical load-displacement curve for progressive folding: I, fold initiation; II, progressive folding; III, compaction [30].

If Euler buckling is avoided and failure is initiated, progressive crushing is exhibited by brittle (glass, carbon, etc.) reinforcement tubes and is caused by catastrophic brittle fracture of the composite material. Two types of crush modes can be observed – fragmentation mode and splaying mode, Figure 2-3.

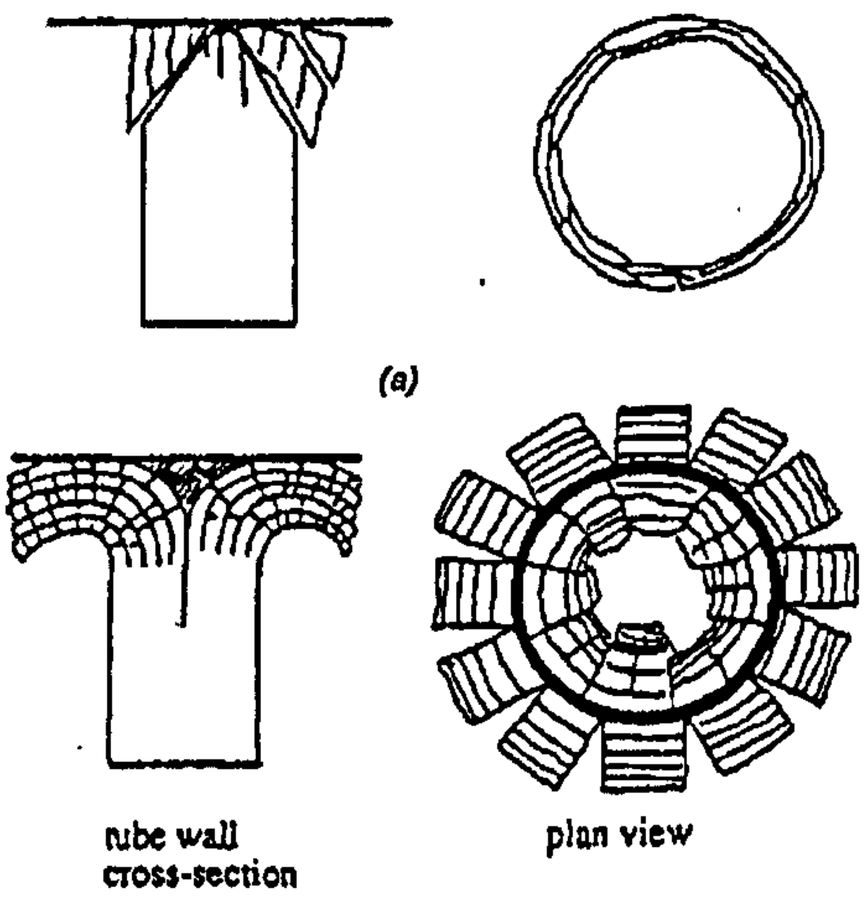

Figure 2-3 – Schematic diagram of brittle crushing modes of composite tubes: (a), fragmentation mode; (b), splaying mode [23].

A desirable crush mode is shown in Figure 2-3b) where there is a progressive damage of the tube and the controlled collapse exhibited is responsible for high energy absorption values. This failure can be induced by triggering fracture at one end of the tube, as illustrated in Figure 2-4a) where the upper end of the tube has been chamfered. A more detailed illustration of a chamfered composite laminate tube is shown in Figure 2-5.

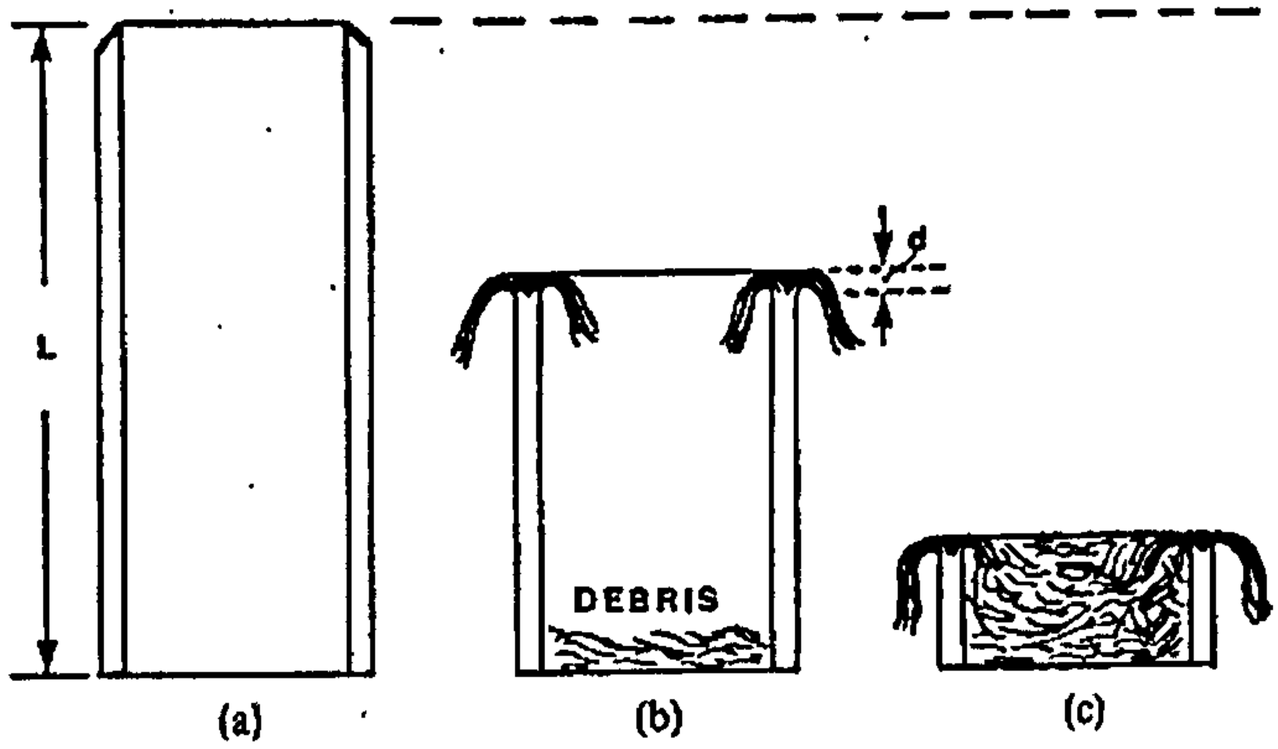

Figure 2-4 – Schematic representation of progressive crushing [30].

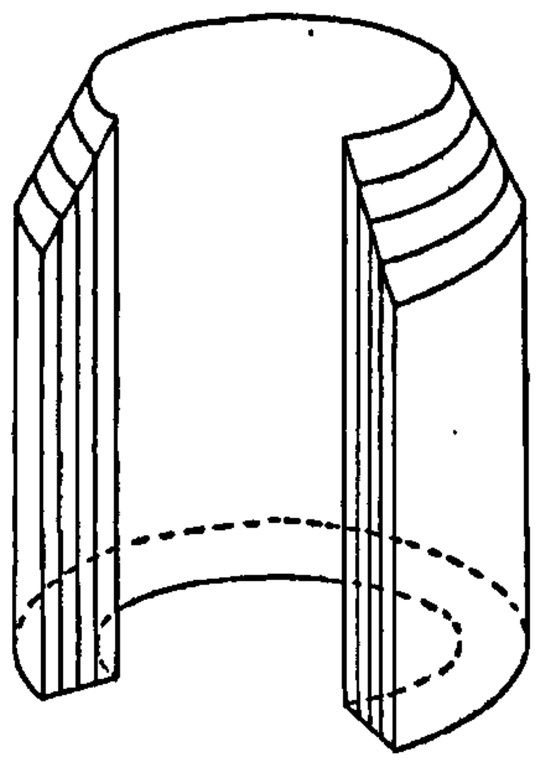

Figure 2-5 - Schematic of a chamfered composite laminate tube [30].

Before studying in more detail the crush zone, the behaviour and fracture modes of individual layers of a composite must be understood. A schematic representation of those modes is shown in Figure 2-6.

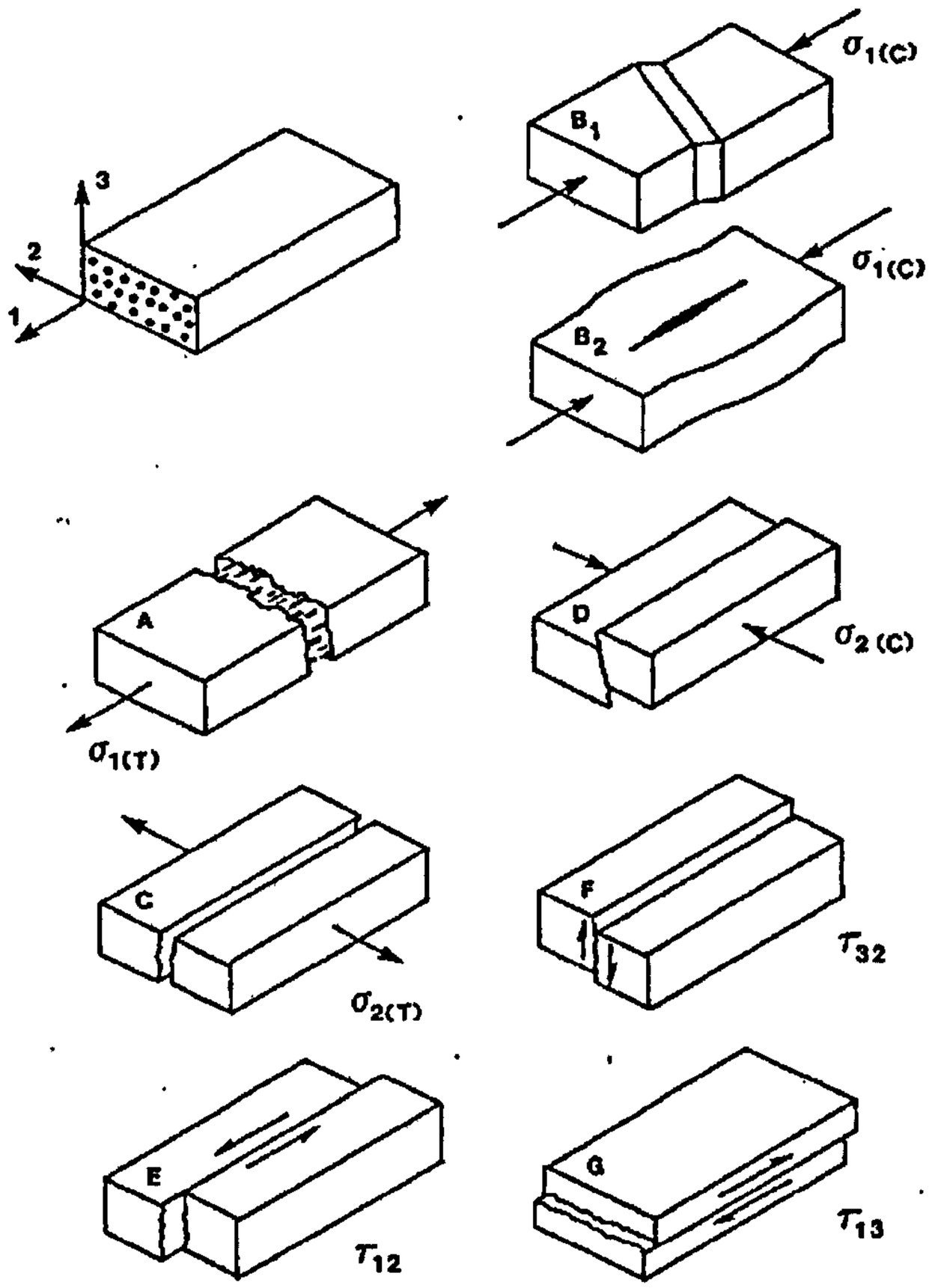

Figure 2-6 - Fracture modes of a unidirectional composite lamina [31].

The stiffness and strength properties of each layer are strongly dependent on the direction of applied load in relation to the fibre direction. Fracture occurs in tension, compression and shear parallel and normal to the fibre direction. Failure may also involve interlaminar fracture in tension and shear [31].

2.2.1 Splaying Crush Mode

Hull demonstrated the formation of a splaying mode crush zone in experimental work on $[0/90]_2$ glass fibre/polyester resin tubes [30], for which the cross-section is shown in Figure 2-7. The sequence of microfracture events leading to the formation of the stable crush zone is illustrated in Figure 2-8.

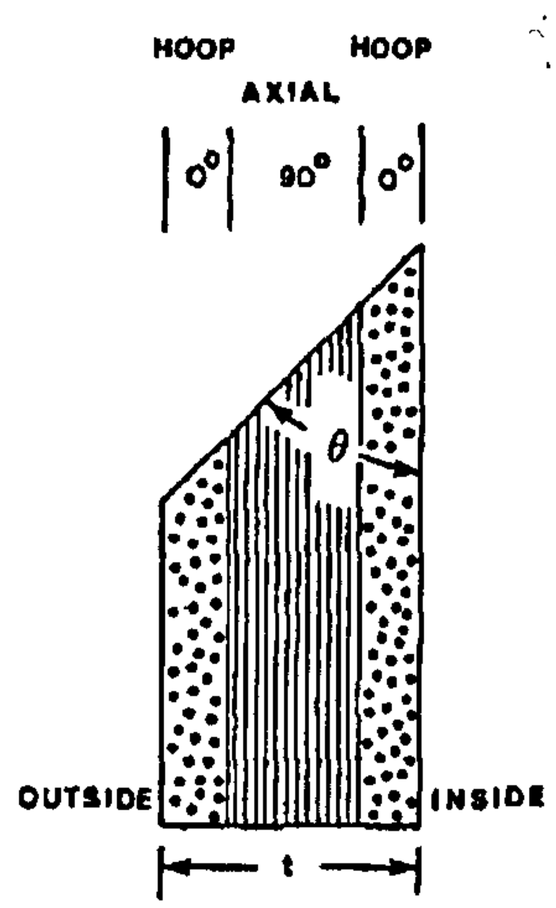

Figure 2-7 - Section through chamfered tube [30].

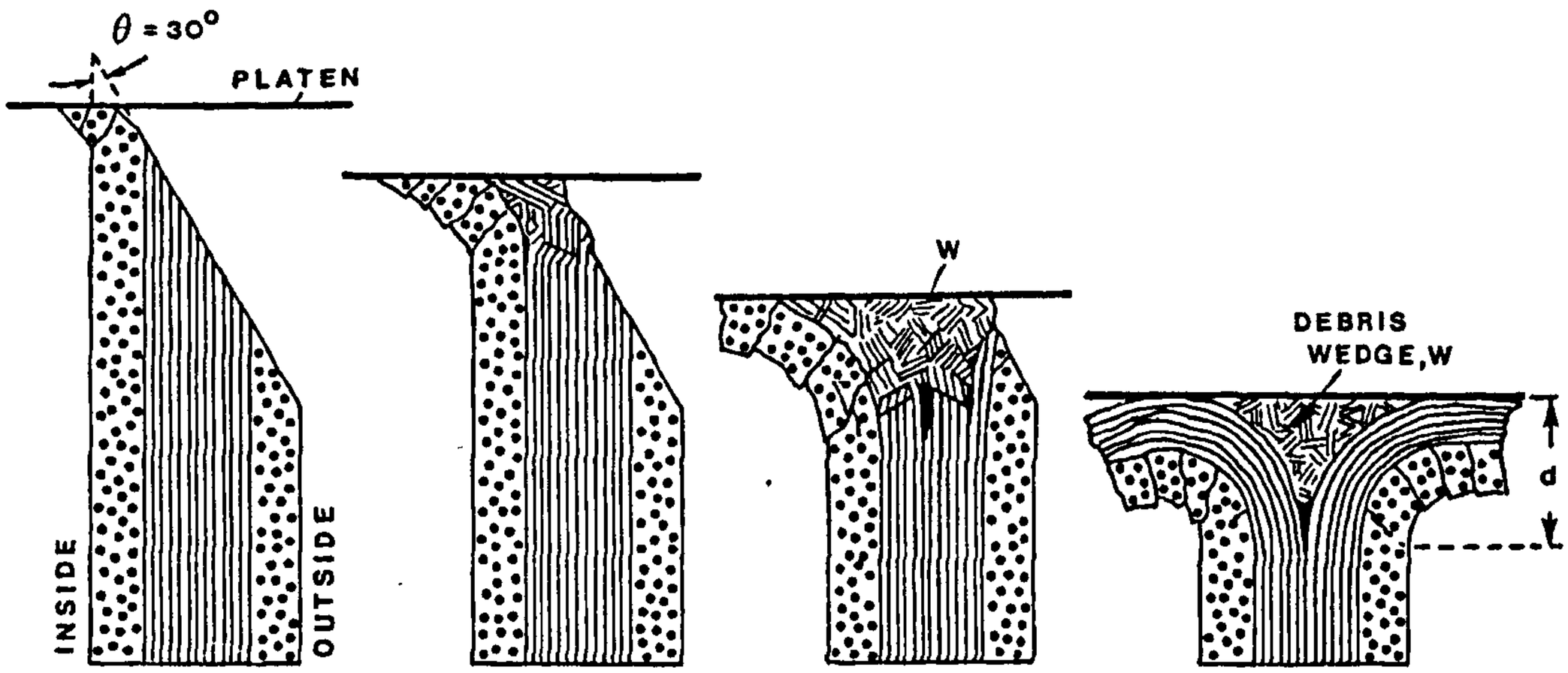

Figure 2-8 - Schematic representation of formation of splaying crush zone of $[0/90]_2$ tubes [30].

Duckett [11] carried out an investigation of the crush zone morphology of CoFRM glass/polyester tubes, Figure 2-9. The main modes of failure in the crush zone were identified and are illustrated in Figure 2-10.

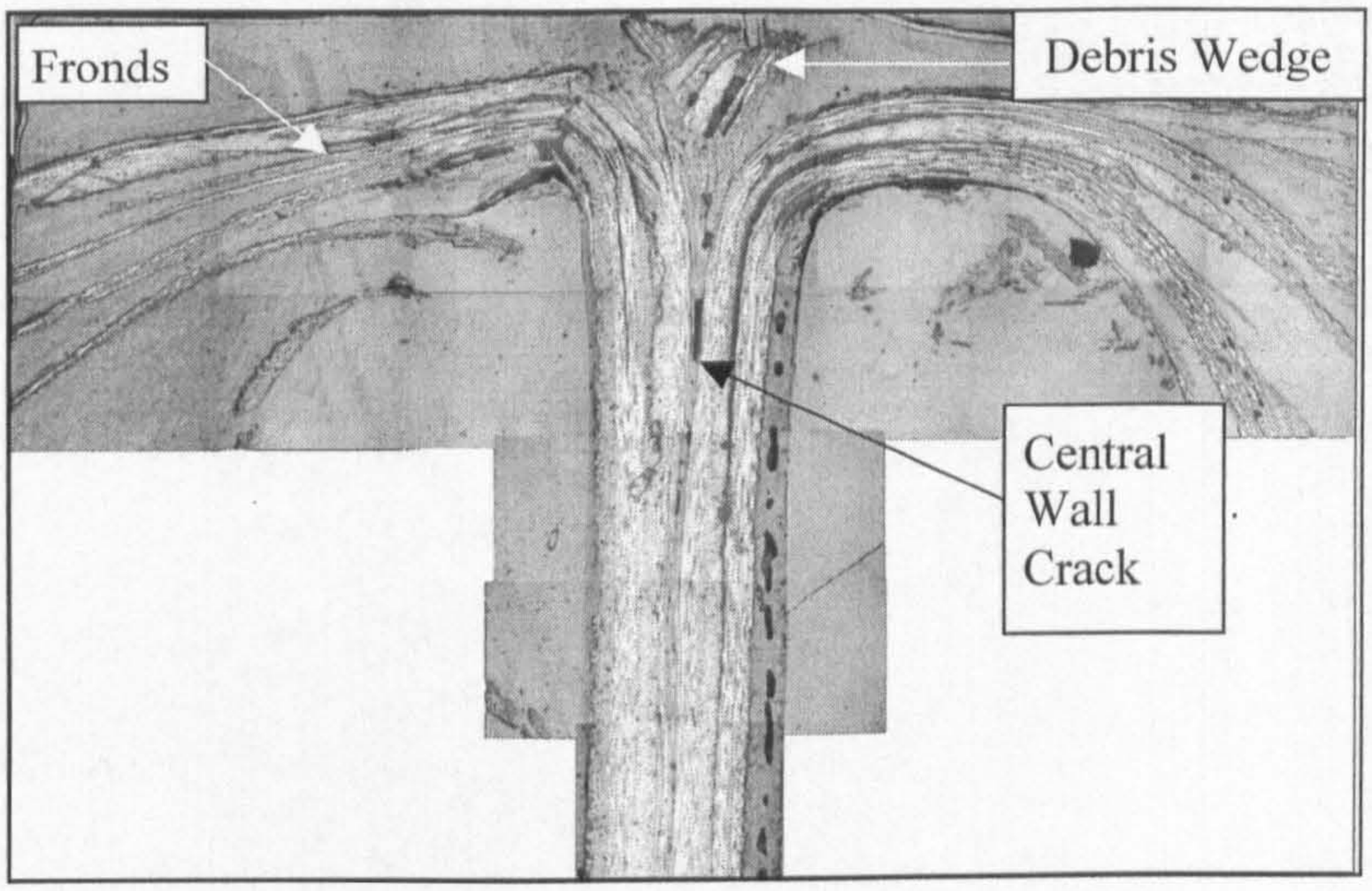

Figure 2-9 - Crush zone morphology of CoFRM glass/polyester tubes [11].

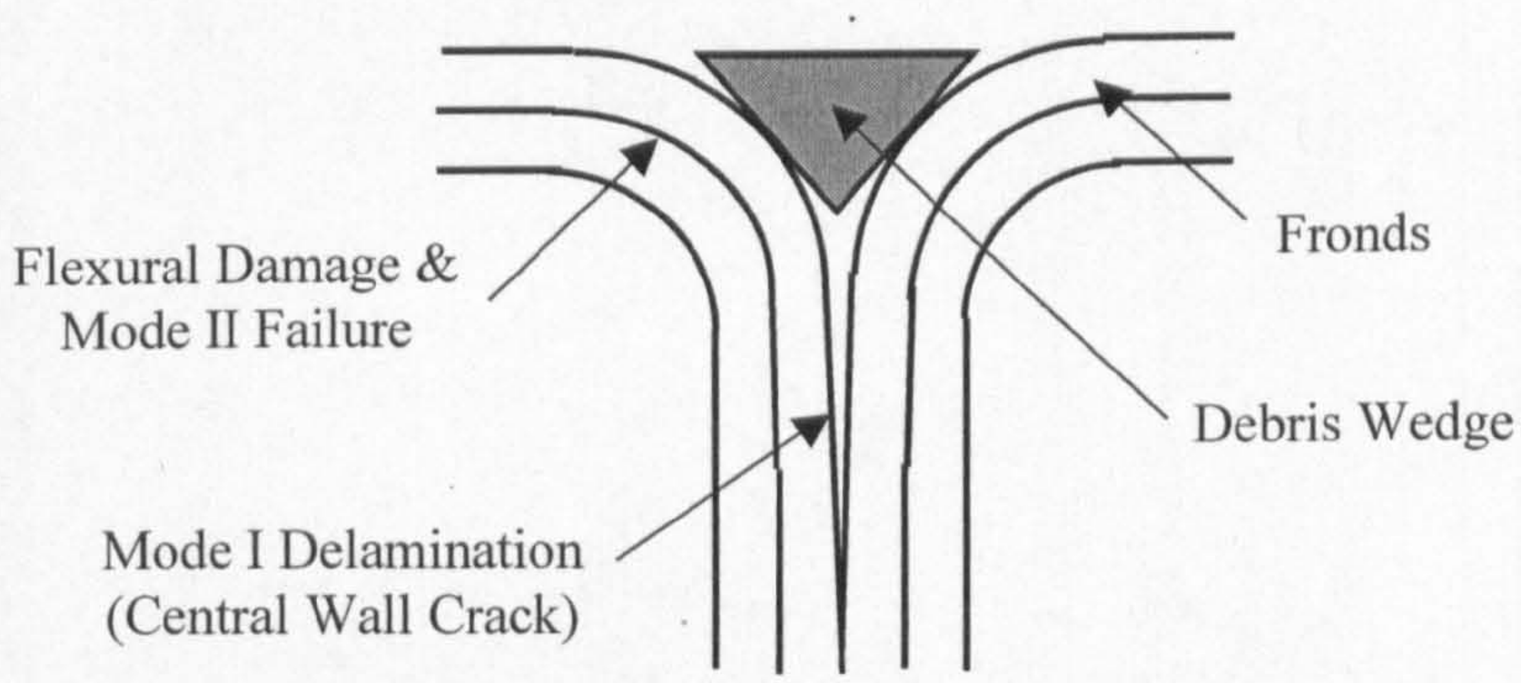

Figure 2-10 - Schematic of the crush zone of CoFRM Glass Polyester Tube

2.2.2 Specific Energy Absorption in Splaying Mode

The total energy absorbed for each of the tubes shown is given by the area under the load-displacement curves in Figure 2-2 and Figure 2-11. The specific energy absorbed (SEA) is the total energy divided by the mass of the portion of the tube that has been crushed.

The main parameters affecting SEA and crush modes are described by Hull [30] and are summarised below:

- Materials
- Fibre architecture and lay-up
- Geometric effects such as thickness to diameter ratio t/D (see Figure 2-1)

The initial slope of the load-displacement curve shown in Figure 2-11 depends on the type of trigger, and in the case of the chamfer trigger, the angle at which the tube is chamfered. Chamfer angle also influences the SEA as it varies the average load of zone II in Figure 2-11.

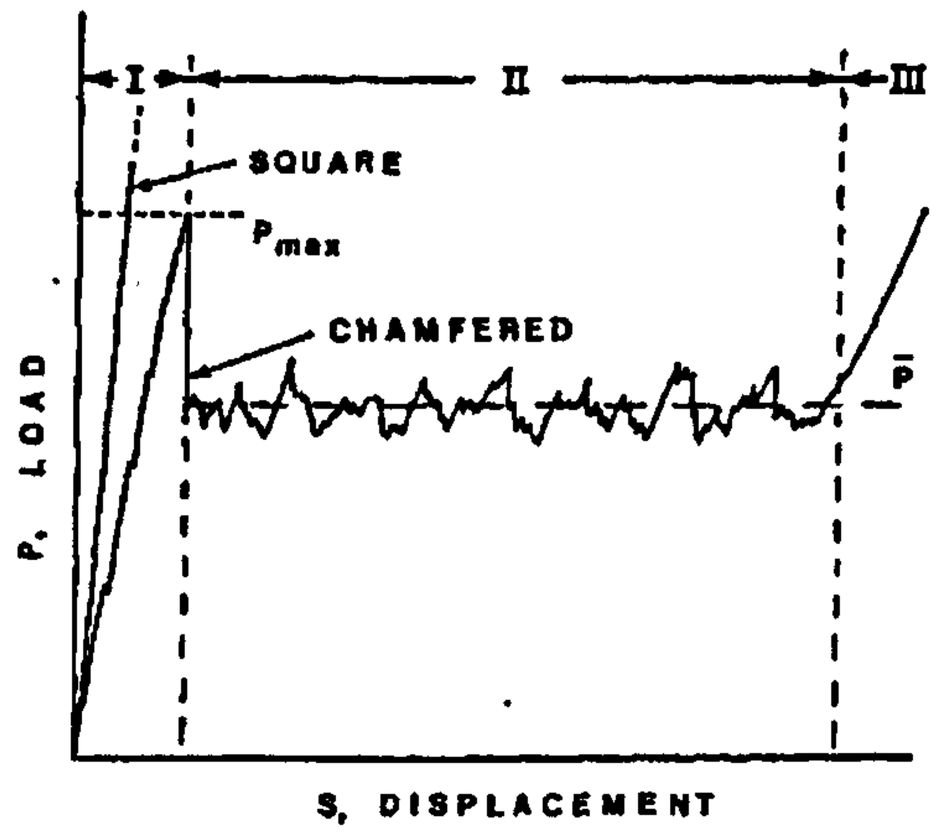

Figure 2-11 – Typical load-displacement curve of chamfered tube undergoing progressive crushing: I, formation of crush zone; II, progressive crushing; III, compaction of debris [30].

By varying the parameters above, it is possible to maximise the average crush load and therefore optimise the value of SEA, by having the tube behave like an ideal energy absorber as illustrated in Figure 1-1. An example of the load-displacement curve of a composite tube with optimised SEA is shown in Figure 2-12.

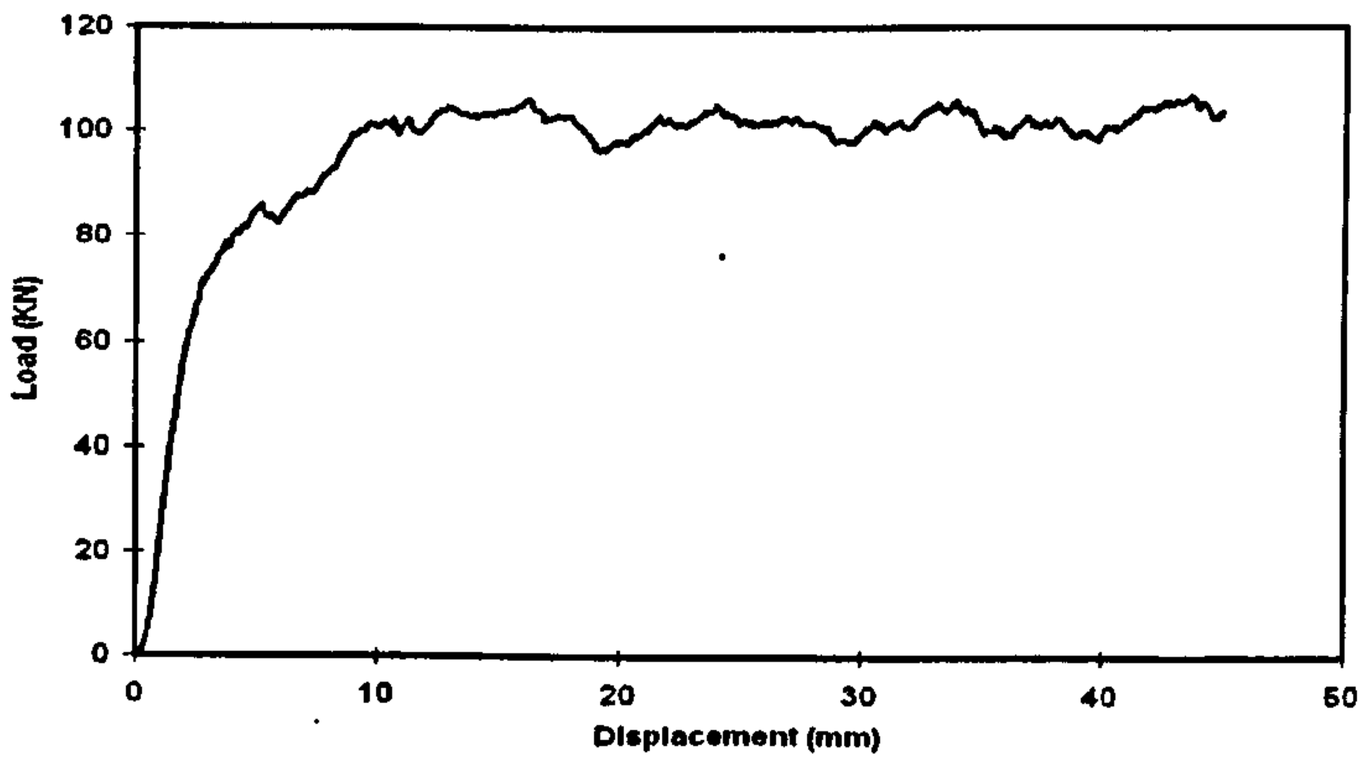

Figure 2-12 – Load-displacement curve of a tube optimised for crush energy absorption.

Implicit in Hull's description of parameters affecting the SEA are other material and geometric properties of the composite tubes. A detailed description of all the parameters affecting SEA is given by Hamada and Ramakrishna [23]. The authors divide the parameters into two categories - Intrinsic Variables and Extrinsic Variables. Details of those authors' approach are illustrated in Figure 2-13.

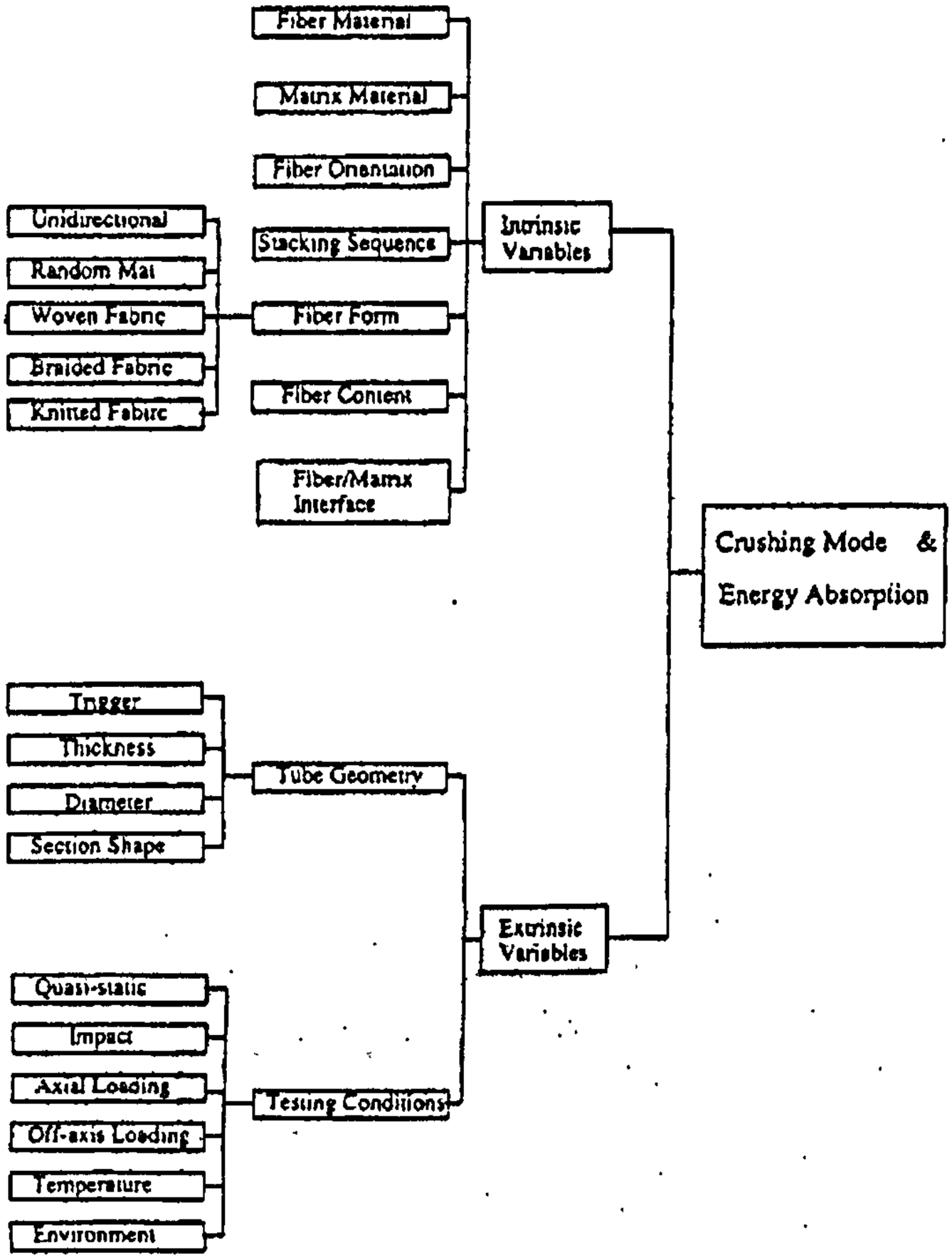

Figure 2-13 – Variables influencing the crushing mode and the energy absorption of composite tubes, Hamada and Ramakrishna [23]

The main energy absorbing processes in the splaying mode are [9]:

- Elastic-inelastic bending of the fronds
- Transverse shear of fibres
- Growth of centre-wall crack
- Splitting of fronds (interlaminar shear)
- Friction between fronds and crush platen
- Friction between fronds and debris wedge
- Friction between separated plies in the fronds
- Circumferential splitting of the outer fronds in tension
- Circumferential buckling of the inner fronds in compression

Farley [16] concluded that the two main energy-absorbing mechanisms in splaying are inter/intralaminar crack growth and friction. The formation of transverse shear of the fibres is a periodic event and the process is shown schematically in Figure 2-14. This process is partly the cause for the serrated nature of the load-displacement response (Figure 2-11). This serrated shape of the curve has also been attributed to stick-slip friction forces acting in the crush zone [19].

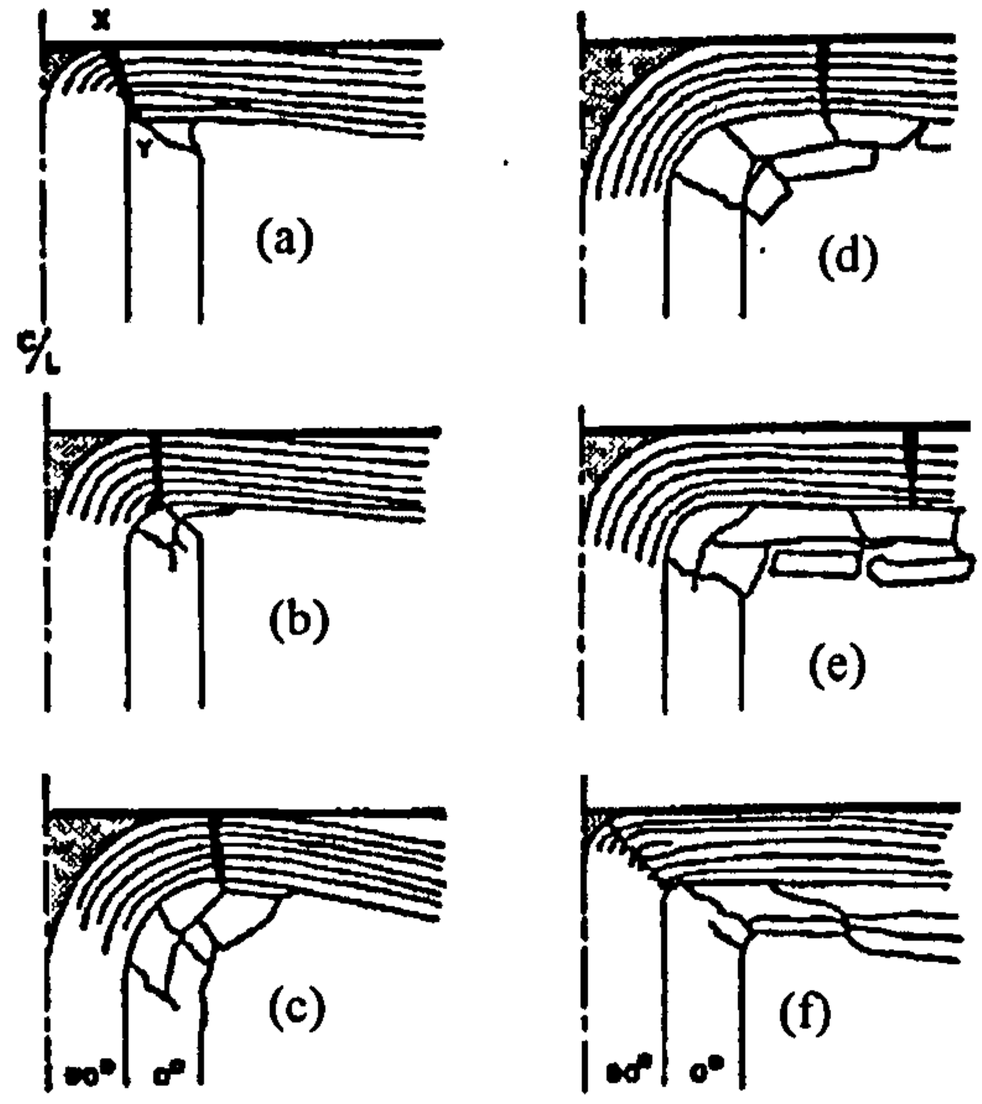

Figure 2-14 - Periodic shear of the fronds in splaying mode – axial displacement increasing from (a) to (f) [30].

2.3 Methods for Estimating Energy Absorption

In this section an overview of the main methods for estimating SEA of composite tubes is given.

2.3.1 Analytical Methods

Several authors have addressed the prediction of the energy absorption of composite tubes. A description of some of the relevant approaches is given hereon.

Mamalis et al. [35] studied the energy absorbed for tubes that crush in splaying mode, which is given by the following expression:

$$W_{total} = W_{friction} + W_{bend\_fronds} + W_{longit.\_crack} + W_{hoop\_splits}$$

$$W_{total} = \left[2\pi\overline{D}(\mu_1 P_1 + \mu_2 P_2)\right] + \left[2\pi\overline{D}\left(\int_0^{\theta} P_2 (l_s/2)d\theta + \int_{s_2}^{s} P_2 \theta ds\right)\right] + \left[R_{ad}\pi\overline{D}\{(s - s_1) + L_c\}\right] + \left[n(t/2)Gs\right] \quad (2\text{-}1)$$

Figure 2-15 shows the definition of each of the terms in equation (2-1), which is both a qualitative and quantitative description of the energy absorption process.

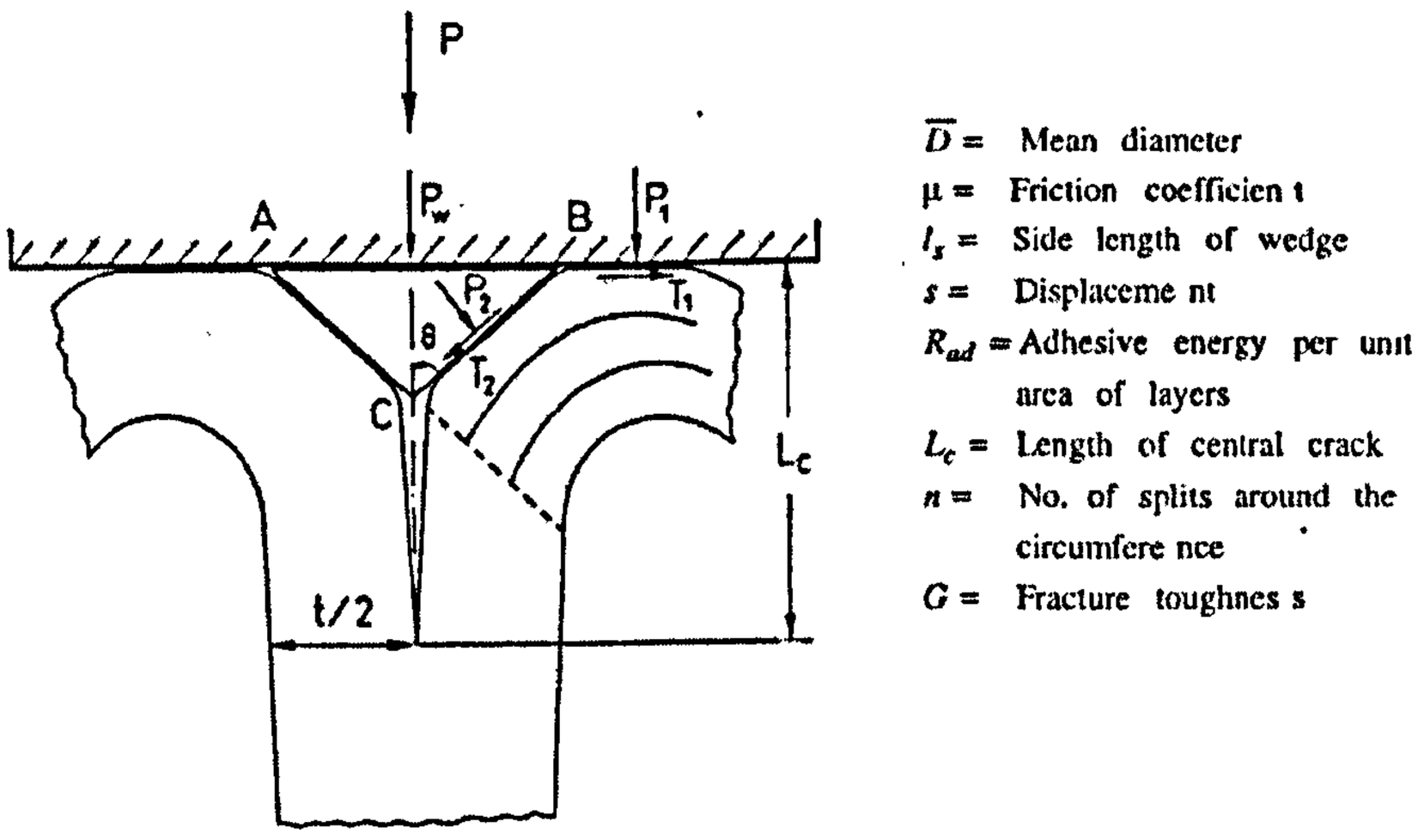

Figure 2-15 – Schematic for the Analytical Evaluation of the Crush Mode for Splaying [36]

Although excellent correlation was achieved with experimental results for tubes with two different architectures, some limitations to the model were found. These were:

- Crush zone is assumed to be symmetrical
- Fibre lay-up is not taken into account
- Wedge angle cannot be smaller than 90^0
- The equation relies on prior knowledge of crush zone geometry.

The last point above goes against the concept of a true prediction of SEA as the crush zone can only be examined after experimental crushing of the tube.

Quek et al [45] developed an analytical model to simulate the failure of braided and continuous strand mat (CSM) glass fibre tubes crushed quasi-statically with an initiator plug, Figure 2-16.

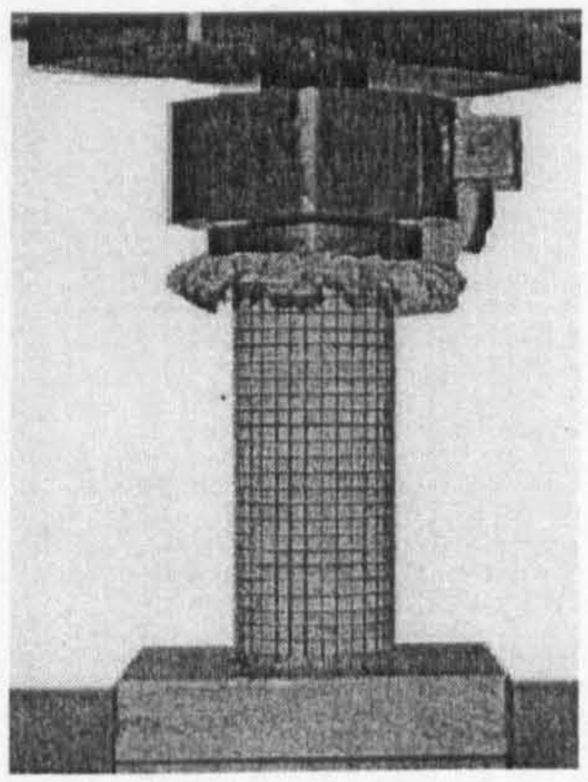

Figure 2-16 – Tube and initiator plug during experiment [45]

The analytical model was based on an axisymmetric formulation of the cylindrical shell equations in conjunction with ideas from classical fracture mechanics and continuum damage mechanics. The load displacement response of a crushed tube was considered to be divided in three stages, as shown in Figure 2-17.

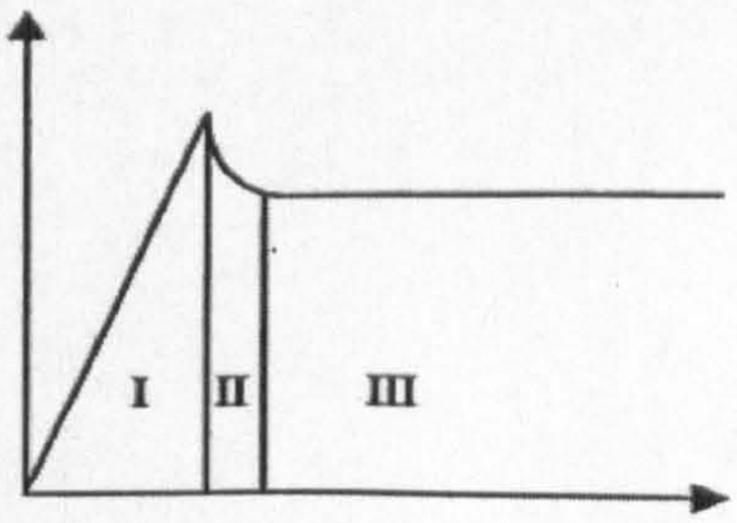

Figure 2-17 - Schematic of three crush stages [45]

The authors' work did not include a model for the transient stage II and considered that stages I (linear loading) and III (steady-state loading) were sufficient to calculate the tube's energy absorption, Figure 2-18.

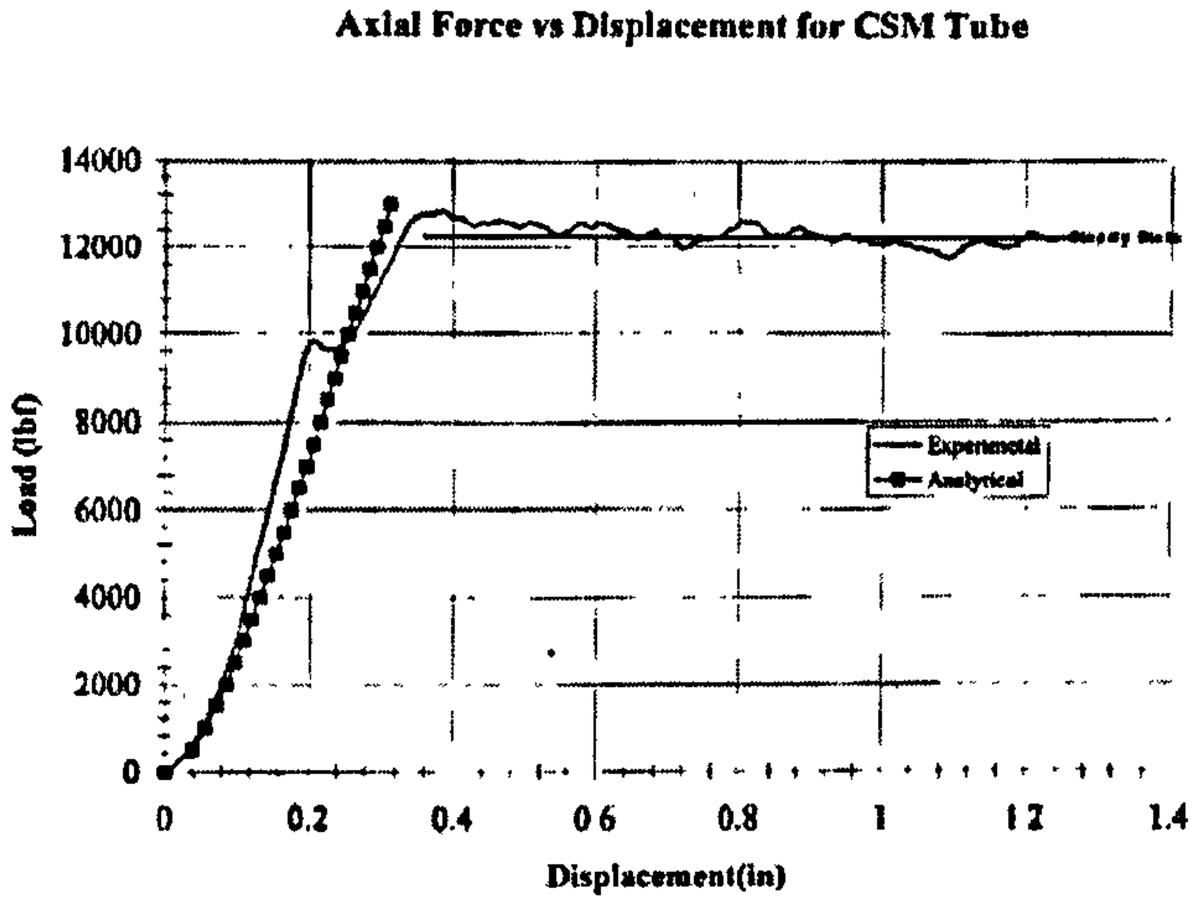

Figure 2-18 - Axial load-displacement of CSM tube [45]

For stage I, the governing equation is analogous to that of a beam on an elastic foundation, given by Equation (2-2) (refer to Figure 2-19).

$$Dw^{(4)}(x) + Pw''(x) + \frac{E_\theta h}{a^2} w(x) = \frac{P\nu_{x\theta}}{a} \tag{2-2}$$

where

$$D = \frac{E_x h^3}{12\left(1 - \nu_{x\theta}\nu_{\theta x}\right)} \tag{2-3}$$

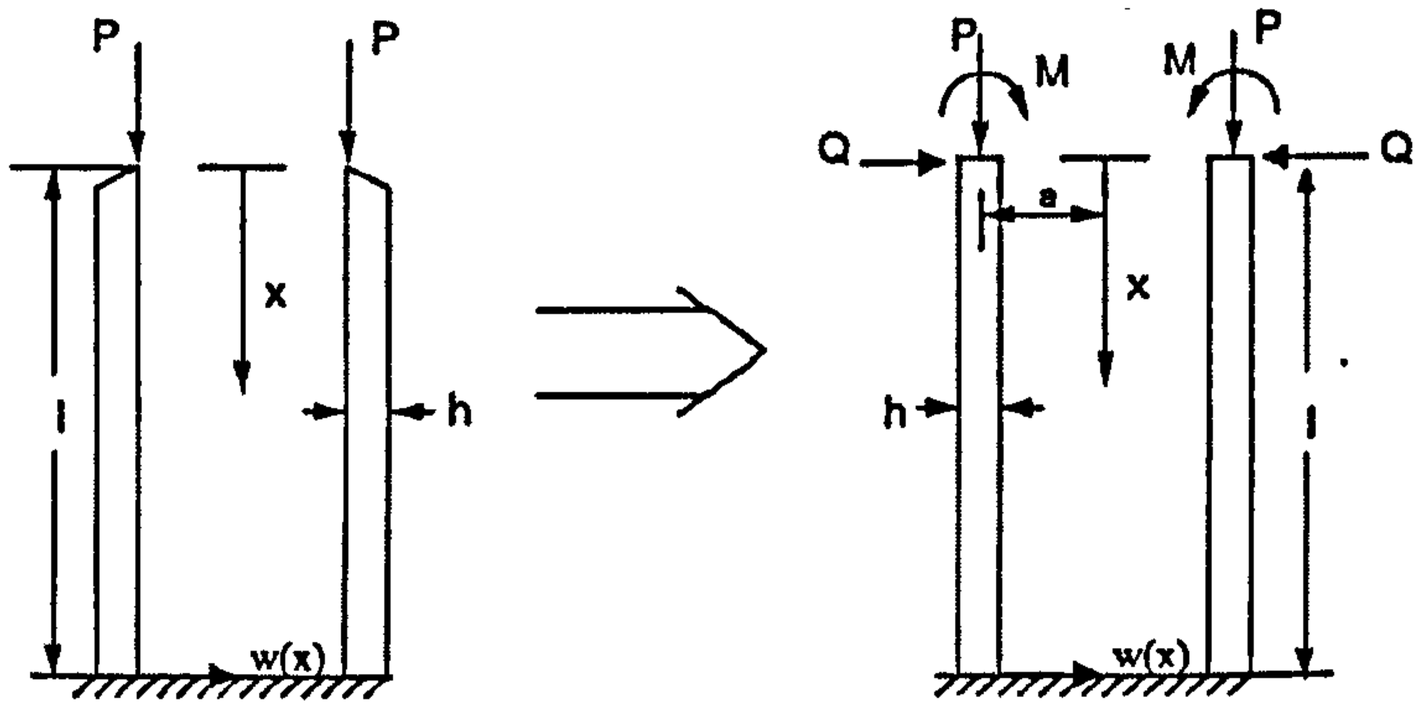

Figure 2-19 – External loads applied at initiator end [45]

P is the axial load divided by the cross sectional area of the tube, $w(x)$ the radial displacement of the shell, E_θ the hoop stiffness of the tube, E_x the modulus in the axial direction, a the tube radius, h the tube thickness and $v_{x\theta}$ is the axial Poisson's ratio. Values E_θ and E_x were obtained by performing tests on a ring cut-out from the tube.

For stage III, the steady-state axial load P_{ss} can be found using an energy balance approach, which is represented by Equation (2-4).

$$P_{ss}\left(\frac{d\Delta}{dl_d}-\mu\right)=\frac{dU}{dl_d}+nG_{axial}\frac{h}{\pi a}+G_d h+2NG_{lam} \tag{2-4}$$

The parameters above are described as follows:

P_{ss}	-	steady-state axial load per unit circumferential length
$d\Delta$	-	change in total load point displacement
dU	-	change in strain energy
dl_d	-	change in damage zone length corresponding to $dw(0)$ at steady-state
G_{axial}	-	energy released per unit area associated with axial cracking
G_d	-	energy released due to fibre debonding in the damage zone
G_{lam}	-	energy released per unit area associated with interlaminar matrix cracking
N	-	number of layers after delamination (due to interlaminar matrix cracking)
n	-	number of circumferential axial cracks
μ	-	Coulomb frictional coefficient

As can easily be deducted, some of the parameters above (such as N) required post-crush observation of a tube, Figure 2-20

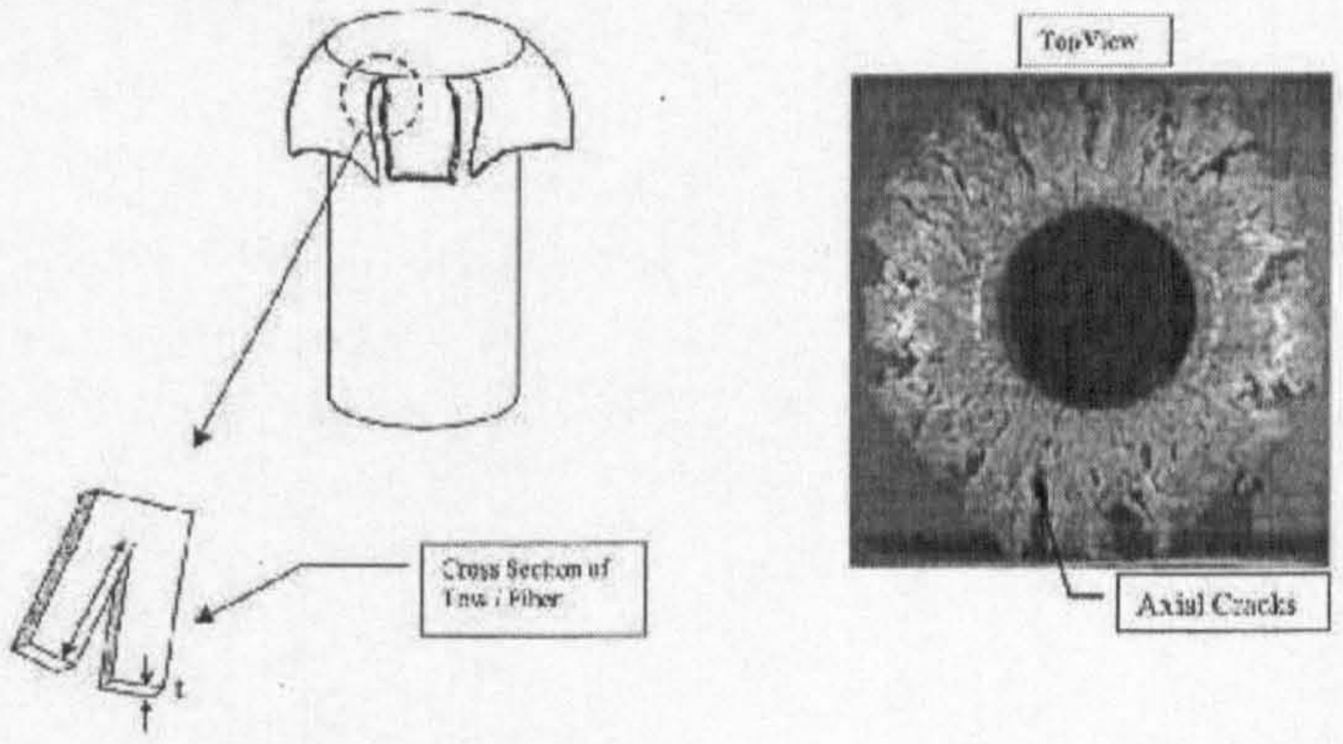

Figure 2-20 – Close up drawing of a crack region and top view of a damaged tube for a braided composite tube [45].

The model showed good accuracy of results for both materials tested but cannot be described as predictive since it requires post-experiment observation of the crushed tube to have all the parameters of equations (2-2) to (2-4).

2.3.2 Finite Element Methods

To date there has been a large number of publications involving the use of Finite Element Analysis (FEA) to model the behaviour of composite structures under impact loading conditions. One of the main advantages of FEA is that it is widely used in engineering and is generally accepted as the modelling tool for many applications. Therefore, there is a high number of software packages available which can be used for a wide variety of engineering problems. Another advantage is that geometric constraints that were discussed in some of the analytical methods discussed before are not present in FEA. It is not in the scope of this section to explain in detail the Finite Element method, as there is extensive literature on the subject.

2.3.2.1 Implicit and Explicit Integration

There are two fundamental types of finite element code, namely explicit and implicit. Implicit codes are better suited to model static and quasi-static problems, with mildly non-linear material behaviour and small displacements. An implicit time integration requires the assembly and inversion of a stiffness matrix to solve static systems. Convergence becomes difficult as the amount of non-linearity increases. This can be CPU intensive for large-scale problems.

Explicit codes generate approximate solutions to momentum based equations over small time-steps and are better suited to dynamic problems or problems involving a large amount of contact and material deformation [9]. The small time-step of an explicit analysis can be advantageous since high resolution in the time domain can be important in accurately capturing the non-linear behaviour of a system. This could be material non-linearity, geometric non-linearity (such as contact or friction) or material and geometric non-linearity in combination with large displacements. The small time-step size effectively allows the development of numerical techniques that linearise the non-linear behaviour allowing a non-iterative solution, i.e. an element by element solution of the system of equations. Consequently, there is negligible computational overhead for non-linear behaviour.

2.3.2.2 Typical Modelling Approaches for Composite Tube Crush

There are essentially four approaches typically followed to model tube crush using the finite element method. These are briefly described below.

Single Shell

This is the most widely used modelling approach, where the tube is represented by a single layer of shell elements, as shown in Figure 2-21. This modelling technique proves suitable for crushing of metallic tubes, which fold progressively, as seen previously. Many authors have used this approach together with a particular material and failure model. The failure criterion and post-yield behaviour are the main components in calculating the energy absorption.

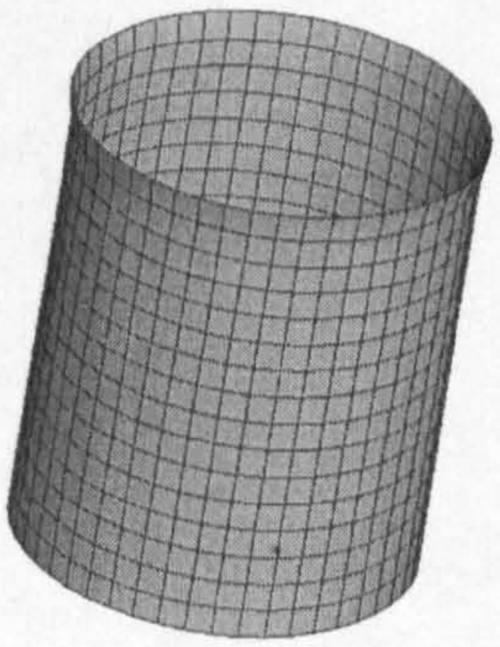

Figure 2-21 – Finite Element Model of a single shell composite tube

The FE model study shown in Figure 2-22 is of 1/8th of a CoFRM Glass/Polyester tube[9]. It shows one of the main pitfalls of a single-shell modelling approach – buckling of the structure.

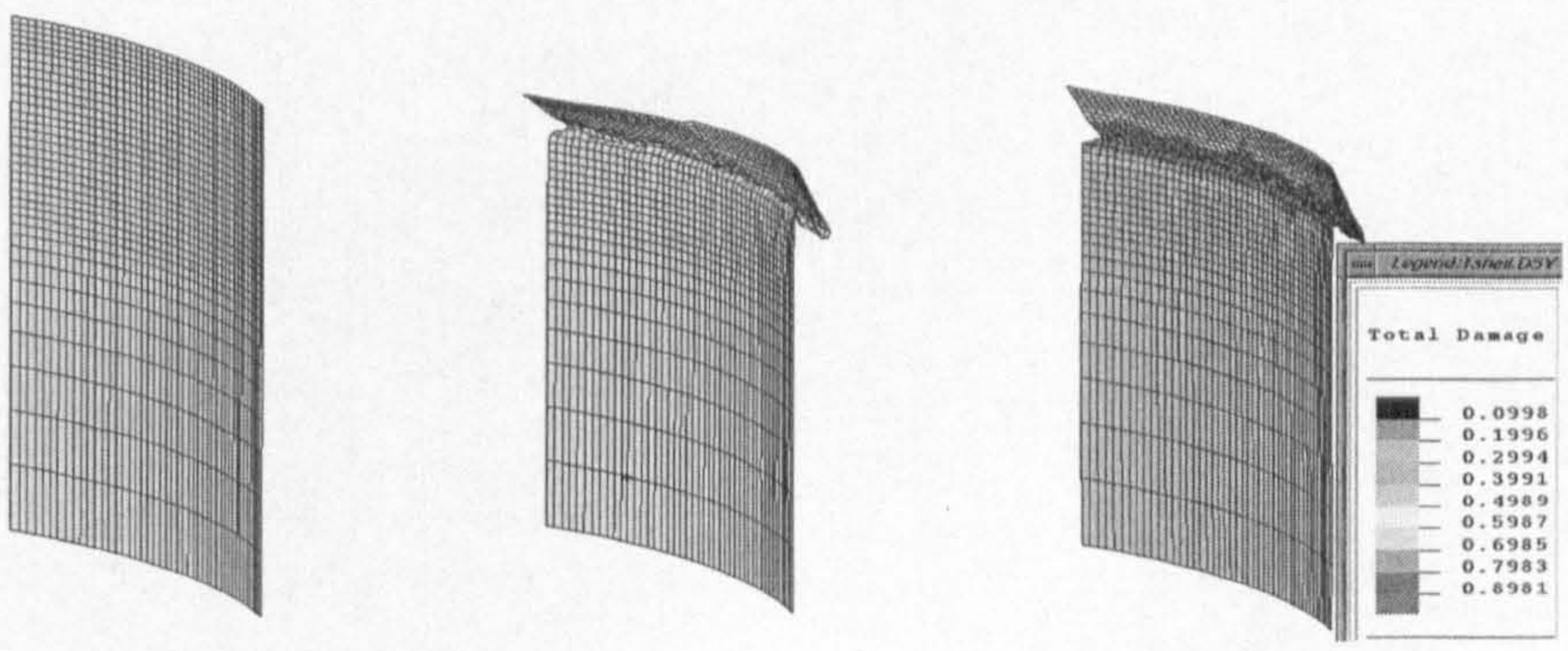

Figure 2-22 - Buckling observed for Single Shell Model [9]

It can be observed in the load-displacement response of this tube crush that the buckling of the shell severely affects the SEA prediction of the model. The structure loses its ability to withstand any load, Figure 2-23.

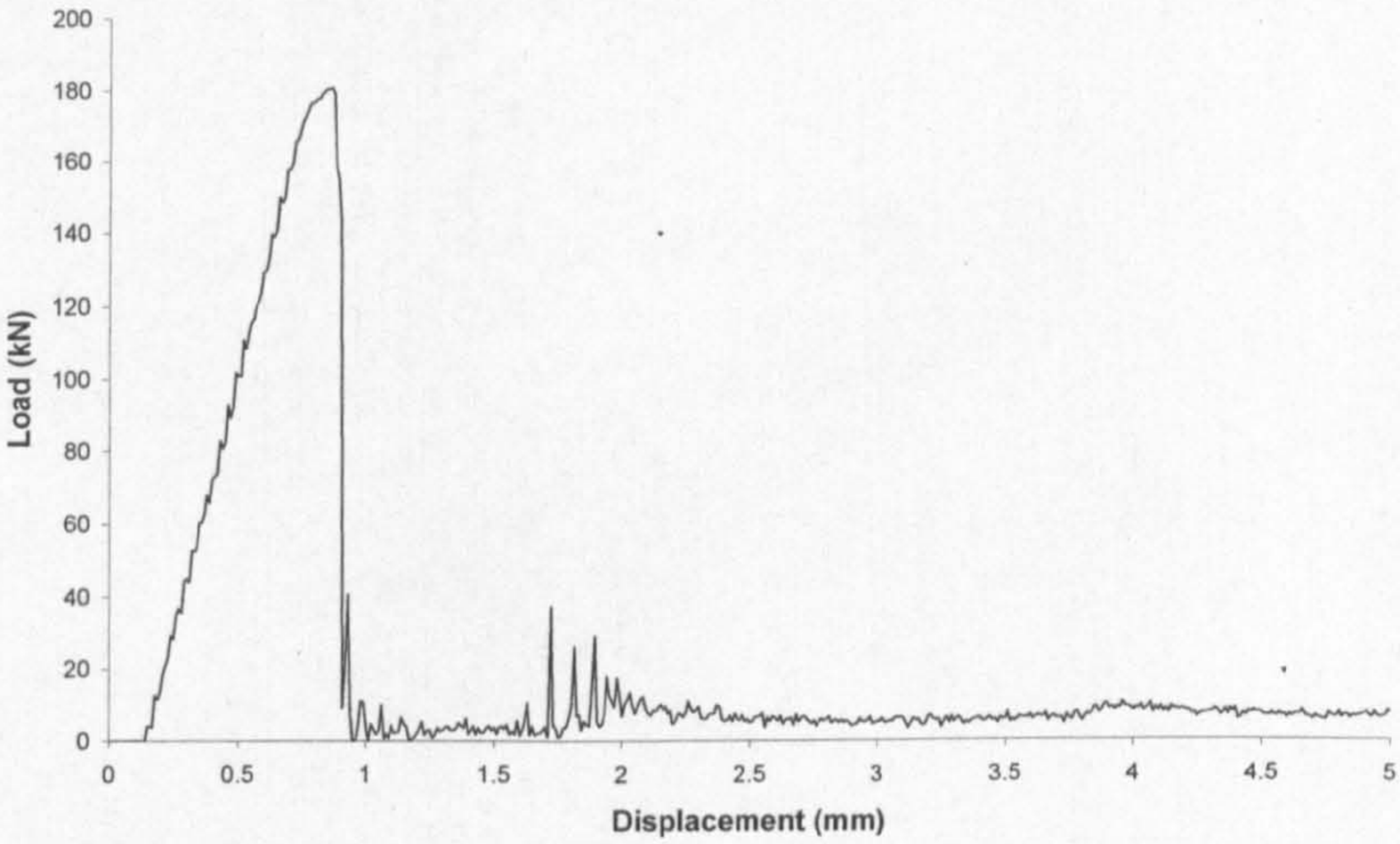

Figure 2-23 - Load-Displacement Response for CoFRM Single Shell Tube

Botkin et al [4] performed analyses on square tubes using the explicit commercial code LS-DYNA™. A composite damage model was implemented in LS-DYNA and good agreement between load-displacement curves of experimental and FE simulation was reached for several materials and geometries. However, it was difficult to determine a failure mode by observation of the deformed plot, Figure 2-24. Also, material data input was based on non-physical parameters, which required tuning to more closely represent the experimental results, and therefore a truly predictive capability was not demonstrated.

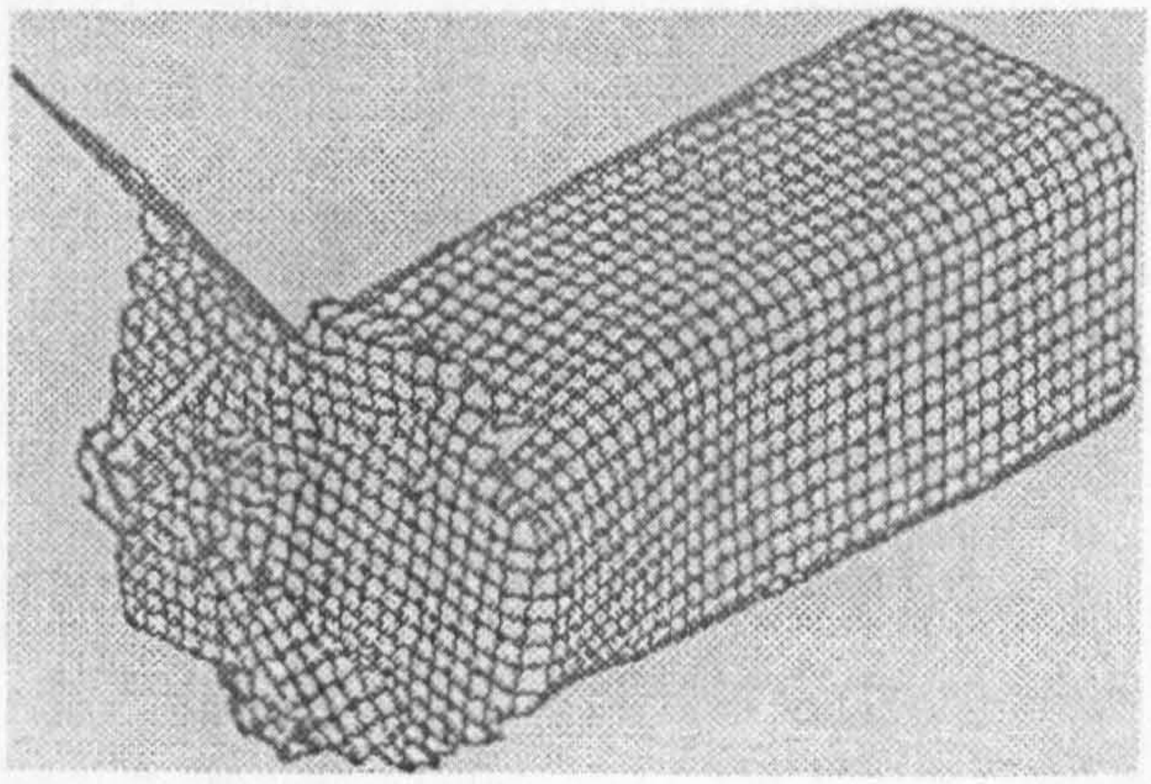

Figure 2-24 – Deformed shape of single shell tube model [4]

Philipps et al [42] modelled FRP crash cones in LS-DYNA using a layered material model, which allowed the definition of multilayered structures, Figure 2-25. The calculations for each layer were performed at the different integration points across the thickness of the shell elements. For each integration point a different orientation angle of the material properties was defined. No comparison with experimental results was made, which does not allow assessing the predictability of this method.

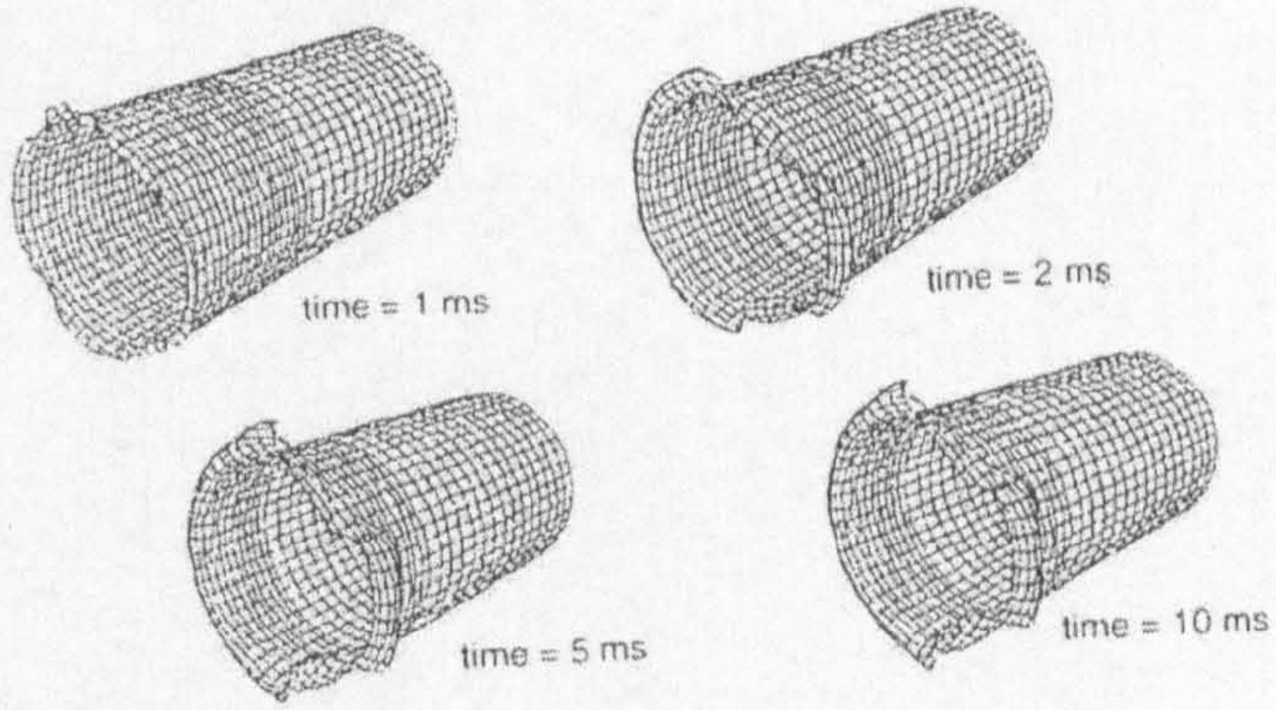

Figure 2-25 – FRP crash cones [42]

Haug et al [28] performed simulations of axially compressed box columns made of hybrid Carbon-Kevlar-Aramid sandwich walls, which corresponded to a subassembly of a TONEN prototype composite passenger car. The analyses were carried out in the explicit commercial code PAM-CRASH™. It was shown that this model can accurately model the progressive damage of the crush front but it was noticed that the initial brittle failure of the elements in that zone quickly propagated along the length of the tube. This resulted in a very irregular deformed mesh plot and a sudden drop in the resisting column force from an average plateau to about zero, which was not observed in experiments, Figure 2-26.

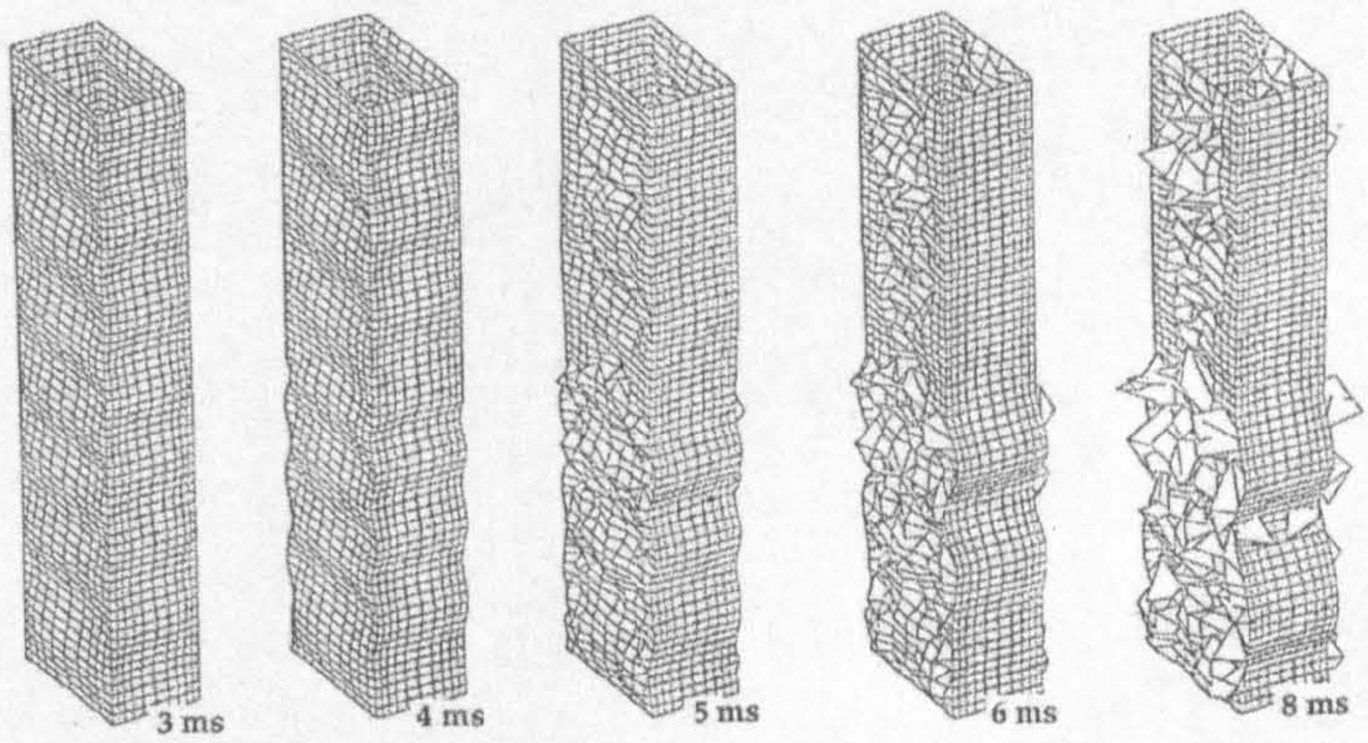

Figure 2-26 – Brittle material column impact [28]

Axisymmetric

Hamada and Ramakrishna [23] used axisymmetric elements for predicting the mean crush load. The authors concentrated on achieving an accurate representation of the splaying crush mode and centre wall crack propagation by modelling the formed debris wedge, Figure 2-27.

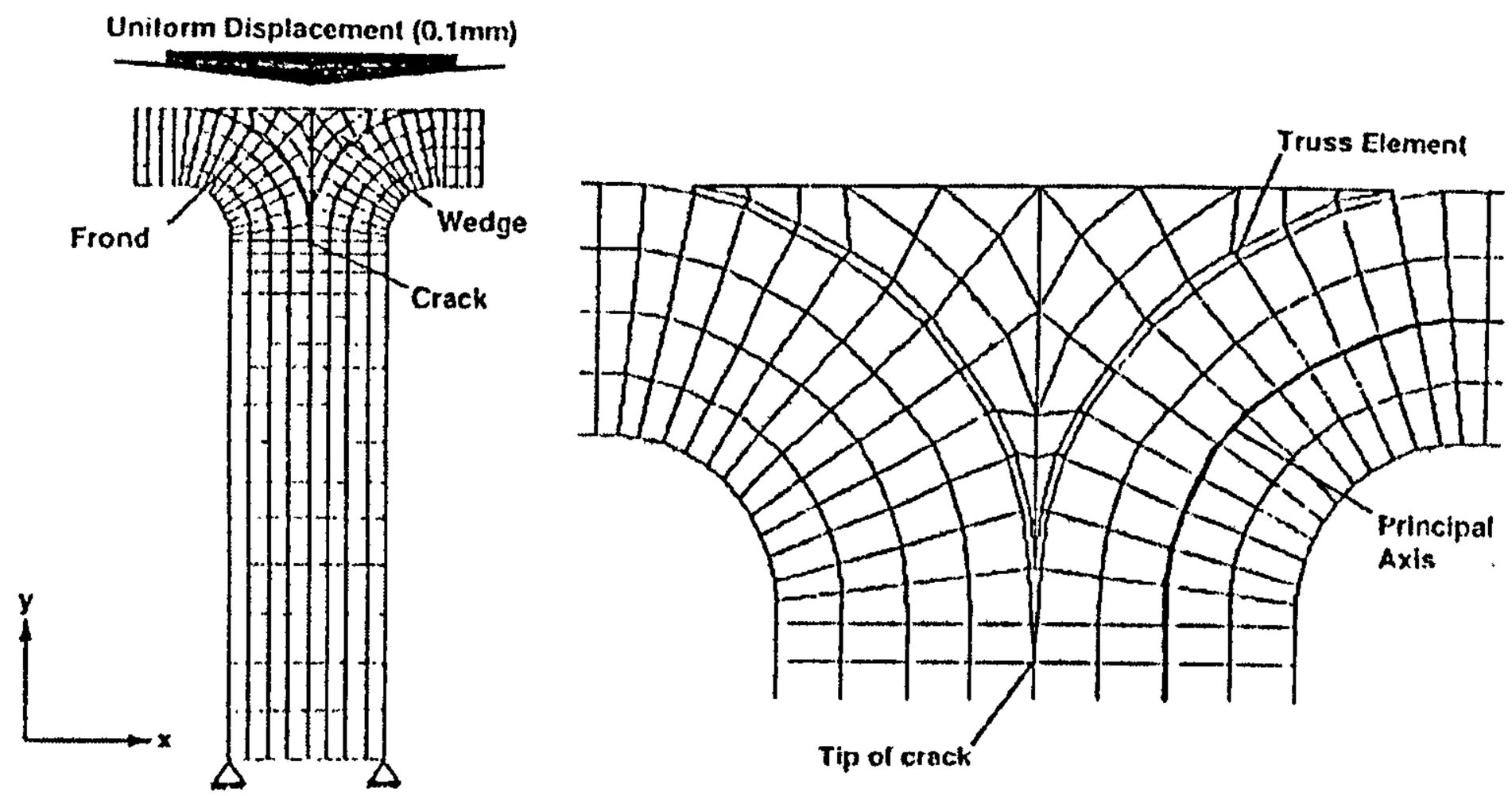

Figure 2-27 – Initial FEM mesh of a splaying mode crush zone [23]

Truss elements were used to represent the contact regions between the fronds and the debris wedge. Double nodes were made along the longitudinal crack and growth of the centre wall crack was related to fracture toughness of the material. The model did not take into account the hoop stresses. The effect of these was studied by the same authors [22] where tubes with different cross-sectional shapes were crushed: full circles, ¾ circle, ½ circle and ¼ circle. It was observed that all tubes crushed by splaying mode and that open tubes showed SEA values which were 10% to 20% lower than that of full circle ones.

The authors assumed that the centre wall crack propagation was the main energy absorption mechanism. The crack growth was determined by the fracture toughness of the composite material. The stress intensity factor at the crack tip is given by

$$K_{FEM} = \sigma_x \sqrt{\pi a} \tag{2-5}$$

where K_{FEM} is the calculated stress intensity factor, a is the crack length below the debris wedge and σ_x is the stress in the tube wall thickness direction.

When the calculated stress intensity factor is equal to the mode I fracture toughness of the composite material, the crack grows and the crushing progresses down the tube wall. The load required for the crack propagation is given by

$$P_{cal} = P_{FEM}(\pi D)\frac{K_{exp}}{K_{FEM}} \tag{2-6}$$

where P_{FEM} is the total applied load on the top surface of the crush zone in FEM analysis, D is the mean diameter of the tube, K_{exp} is the stress intensity factor of the composite material obtained from experiments.

In this linear calculation method, the applied load increases linearly with the displacement in the FEM analysis as shown in Figure 2-28. The deformation energy of the crush zone (U_{FEM}) is given by the triangular area under the load-displacement curve. In the crush experiment, the mean crush remains constant with increase of crush distance. The work done or the energy absorbed , U_{exp} during crushing process is given by the area under the curve. For a small displacement of δS, it is assumed that

$$U_{FEM} = U_{exp}$$

By comparing the areas under the load-displacement curves, the predicted mean crush load is given by

$$\overline{P}_{cal} = \frac{P_{cal}}{2} \tag{2-7}$$

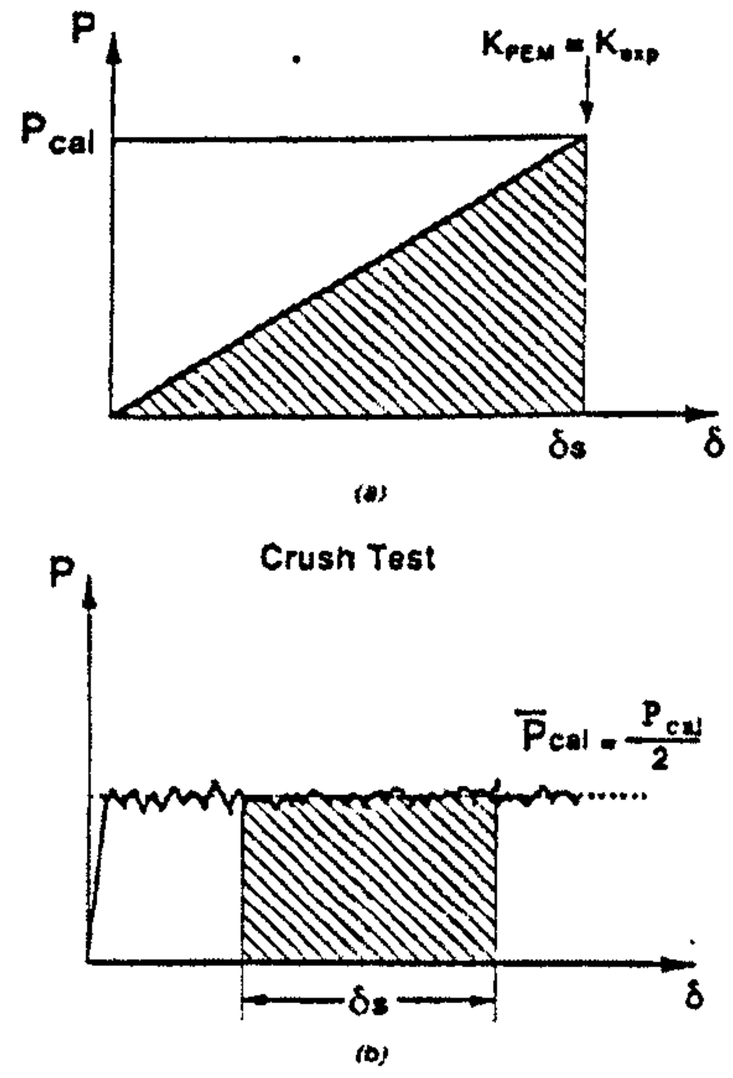

Figure 2-28 – Typical load-displacement curves obtained from (a) linear FEM analysis and (b) crush experiment [23].

By rearranging equations (2-6) and (2-7)

$$\overline{P}_{cal} = \frac{P_{FEM}}{2}(\pi D)\frac{K_{\exp}}{K_{FEM}} \tag{2-8}$$

The mean crush load and subsequently SEA are calculated from equation (2-8).

The authors reported predicted SEA values, which were between 8% and 16% lower than the experimental values. The closeness of results was attributed to the relative importance of longitudinal cracking compared to the other fracture mechanisms on the energy absorption capability of composite tubes.

The analysis method described above assumed a prior knowledge of the crush zone geometry and therefore this approach cannot be considered truly predictive. However, it emphasizes the relevance of interlaminar behaviour on SEA and progressive crushing through centre-wall crack propagation.

Multi-Shell

Farley and Jones [17] used an implicit FE code to model composite laminate tubes with layers of shell elements connected by zero-length springs, which represented the interlaminar region, Figure 2-29. Finite element nodes for each layer were coincident with adjacent layers.

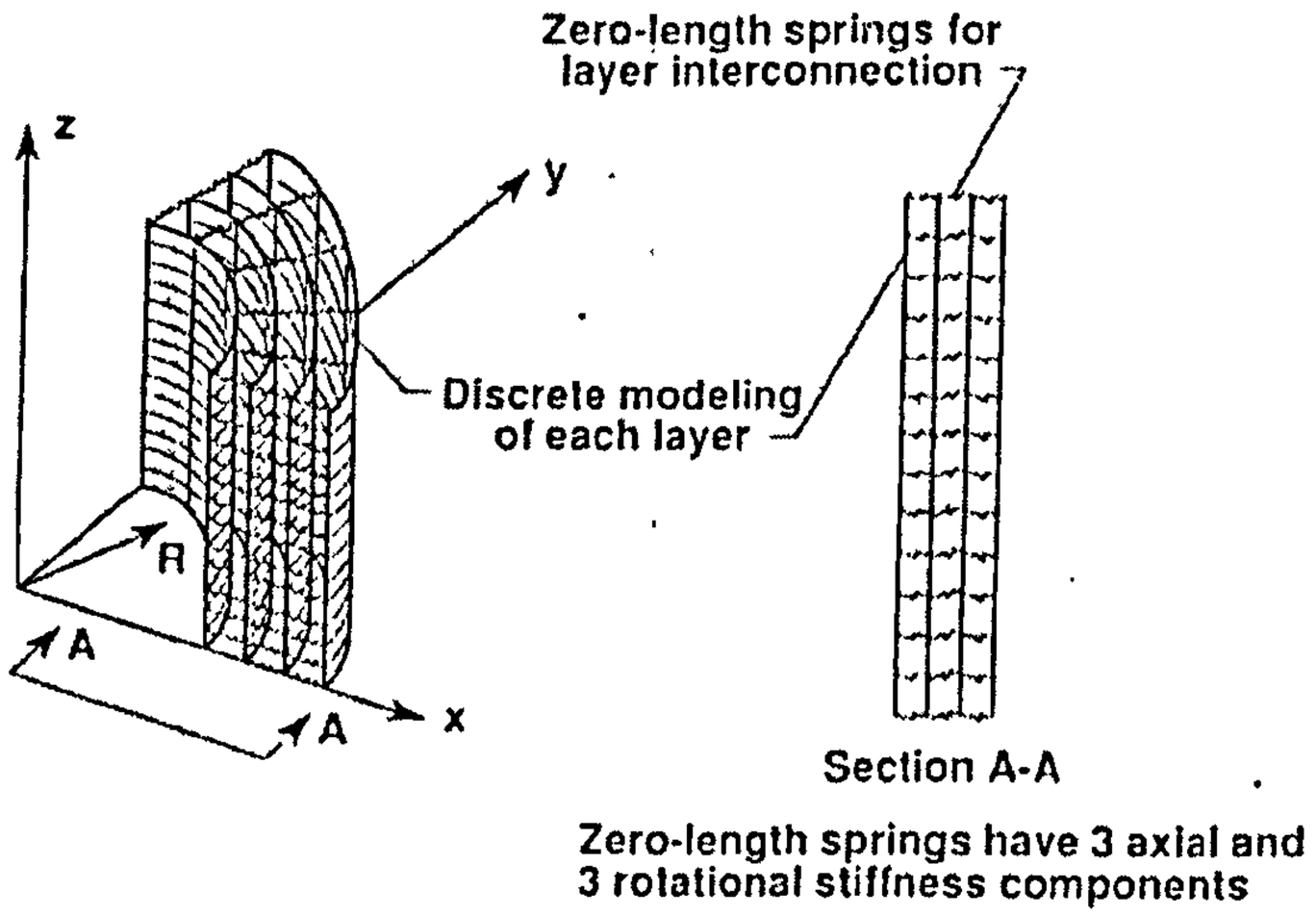

Figure 2-29 – Finite element model of composite tube [17]

Only a portion of the tube was modelled as the authors used boundary/symmetry conditions to reduce the number of degrees of freedom in the finite element model. This allowed for lower computational times. The authors based this on similar work done on crushing of metal tubes

where no significant differences were observed between the SEA values of tubes that crushed in both symmetrical and unsymmetrical modes. Therefore, assuming symmetry of the crush phenomenon was a good approximation.

Interlaminar crack growth was represented by the removal of the zero-length springs between layers as shown in Figure 2-30. The strain energy release rate, *G*, was used as the indicator in the model to determine when interlaminar crack growth occurred. Interlaminar crack growth was modelled by disconnecting coincident nodes of adjacent elements along an interface and calculating the strain energy associated with the resulting deformation state. Modes I and II of crack growth were assumed to be significant for the crushing of composite tubes.

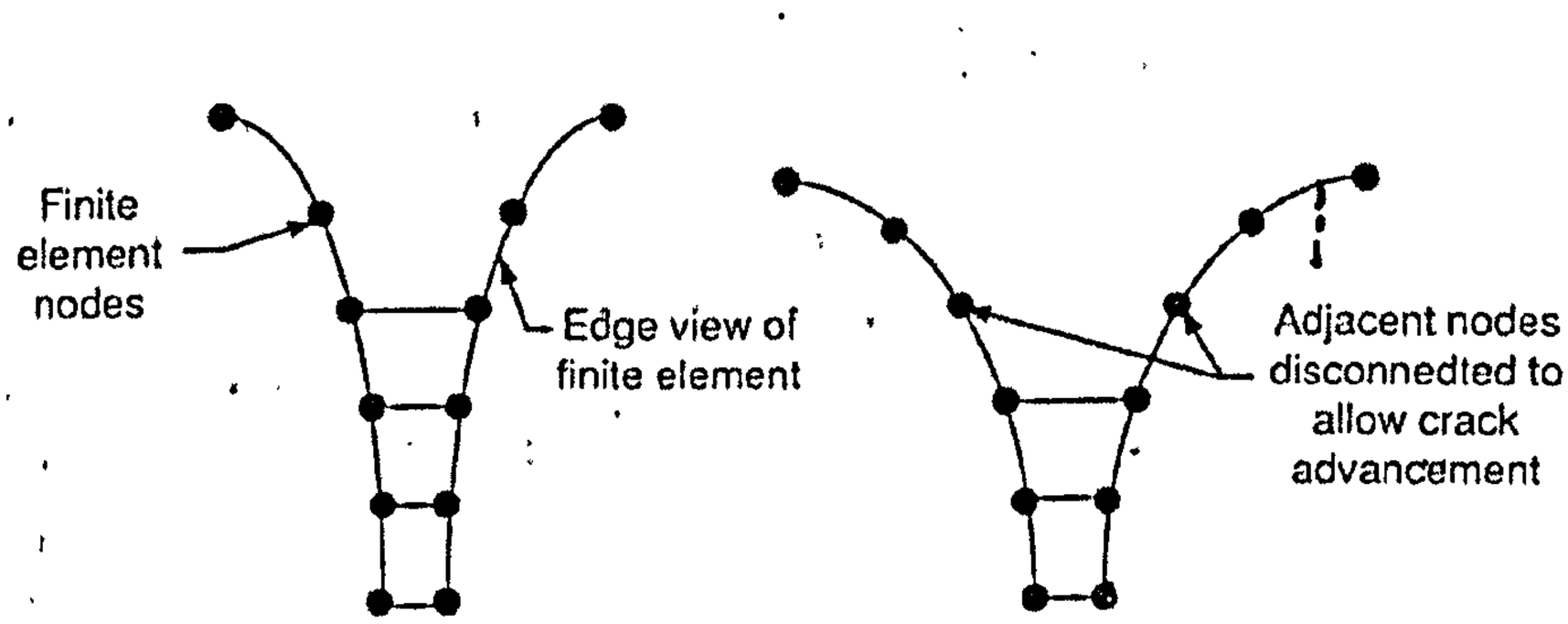

Figure 2-30 – Method of interlaminar crack growth in finite element model [17]

To deal with large deformations in FE crushing of composite tubes (geometric non-linearity), an incremental Newton-Raphson algorithm was used to ensure convergence of the solution. This is one of the drawbacks of an implicit solver, as when in the presence of geometric and/or material non-linearities, the solution process may become too computationally intensive or not converge at all. Another limitation of the implicit solver noted by the authors relates to the existence of bifurcation buckling loads, where the finite element stiffness matrix is singular. With an explicit solver there is no such limitation as the system of equations is solved element by element, with no need to iterate to convergence.

Reasonable agreement between analyses and experiments was obtained, for a range of materials, which suggests that the important phenomena of the crushing process were included in the model. However, apart from the bifurcation mentioned above, no reference was made as to how the initial stage of crushing was modelled, where buckling (singularity) starts the process.

Curtis [9] used a multi-shell element modelling approach applied to two different architectures of Glass/Polyester composite tubes. The work was performed using the explicit code PAM-CRASH™ and its Bi-phase material model. Reasonable agreement was achieved for CoFRM architecture but no significant prediction was achieved for uni-directional fibre composite tubes, where limitations of the Bi-phase material model were identified. These dealt with the fact that isotropic damage was applied to a highly anisotropic material. The concept of damage mechanics is explained later in this chapter.

The modelling procedure consisted of 6 layers of shell elements to model each of the single plies connected by a tied slideline contact interface (Type #32 in PAM-CRASH™) [41]. A full test program was devised to obtain the material properties required for the Bi-phase material input and a procedure to calculate the parameters of the material model was developed. Failure of the contact interface and subsequent crack propagation was defined in PAM-CRASH by the inclusion of normal and shear failure stresses shown below.

Tied Contact Criterion Type #32:

$$\left(\frac{\sigma_n}{AFailN}\right)^{A1} + \left(\frac{\sigma_s}{AFailS}\right)^{A2} \leq 1$$

where σ_n = stress normal to the interface

σ_n = stress normal to the interface

AFailN, *AFailS* are strength coefficients

A1, *A2* are constants

A relevant degree of calibration was required to obtain input parameters for the contact interface.

The principal reasons identified by Curtis for the poor quantitative correlation with experimental SEA values were: poor representation of the material behaviour under crush conditions, poor representation of the interlaminar bond, and difficulties arising from the use of discrete finite elements to represent a continuous process.

Curtis showed that the energy absorbed by propagation of the centre wall crack is negligible in terms of overall energy absorption of the tube. However, the presence of a centre wall crack has a clear governing effect on the crush mode. Therefore, one of the recommendations for future work was the need to develop a better representation of the delamination behaviour of composite materials.

Solid Element

Curtis [9] performed analyses of UD and CoFRM glass/polyester tubes using the commercial code PAM-CRASH. Solid elements were used to model each individual ply as well as each interface between plies, Figure 2-31.

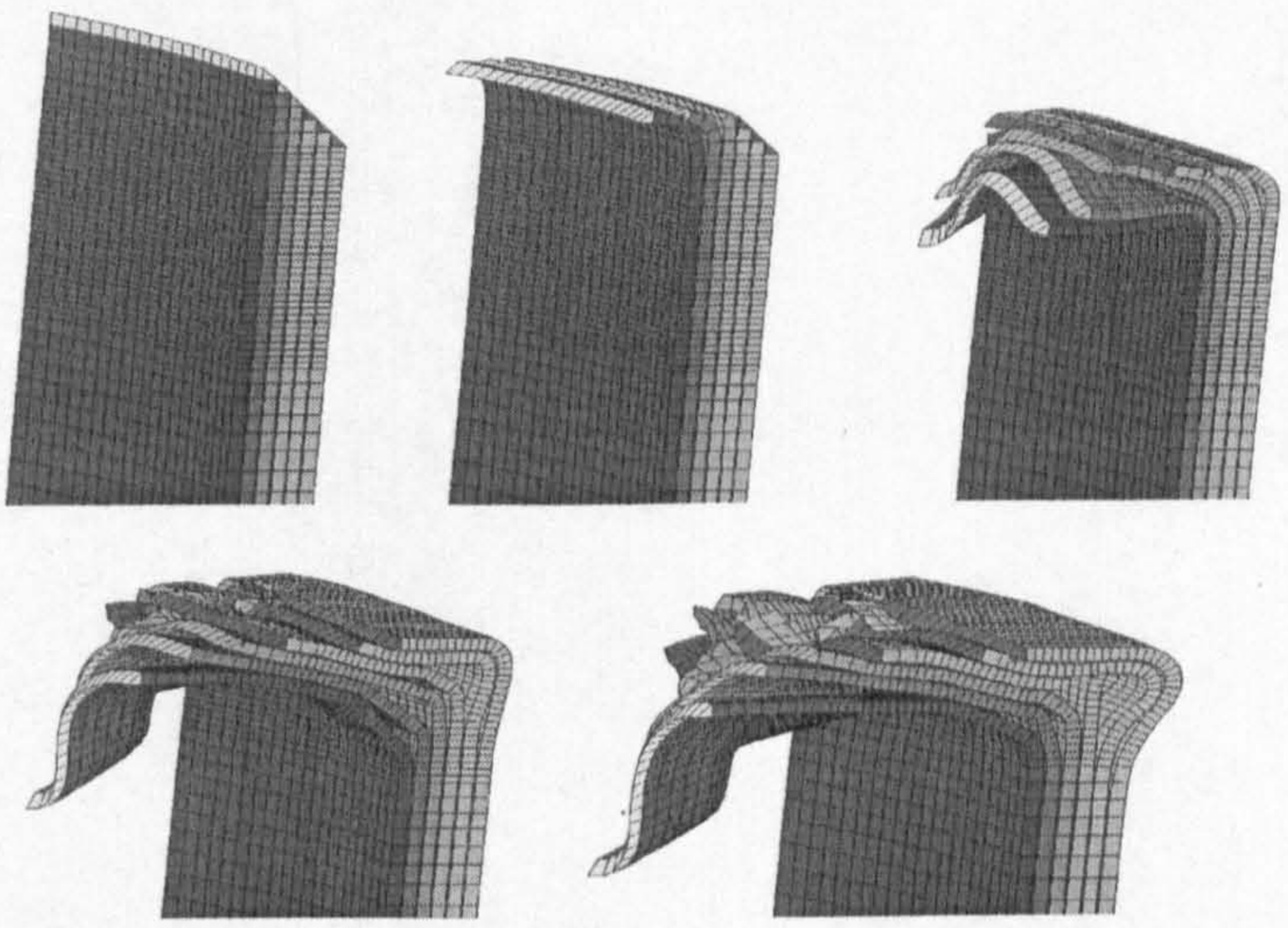

Figure 2-31 - Progressive Failure of the CoFRM Solid Element Model [9]

All elements were given similar material properties but the interface solids had a lower elimination strain. This lower value was intended to model crack propagation by "disconnecting" adjacent plies as interface elements were progressively eliminated.

In the analyses performed, no debris wedge was formed and all the plies tended to bend towards the inside of the tube, as shown in Figure 2-31. The average SEA amounted to just 14% of observed experimental values and clearly a large amount of energy was neglected. This relates to the observation by Fairfull et al [13] who estimated that the energy absorbed by frictional processes (platen-frond, wedge-frond) would be over 50% for glass cloth/epoxy composite tubes, even when crushed against a smooth platen.

Johnson and Pickett [33] modelled $1/16^{th}$ of a circular tube, as shown in Figure 2-32. A fine mesh of solid elements represented both the plies and inter-ply resin. The PAM-CRASH bi-phase orthotropic elastic damage model was used for the unidirectional plies and an elasto-plastic damage model for the resin rich interface layers.

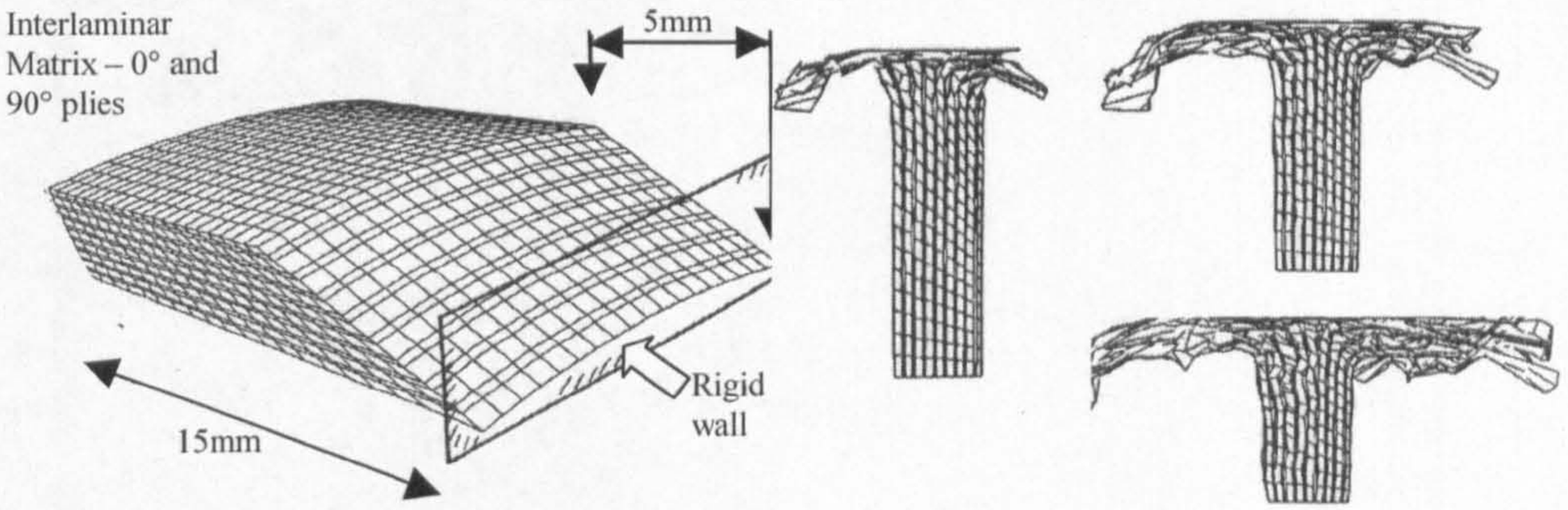

Figure 2-32 - Composite tube crushing: Simulation model and example results [33]

This approach was able to capture both ply and inter-ply failure but had the obvious disadvantage that a large number of elements were needed, limiting the method to small scale structures. Another limitation of this modelling approach was the poor aspect ratio of the solids representing the interlaminar region, as this can affect the accuracy of results. However, the model successfully replicated the splaying of the fronds although no clear debris wedge was visible.

2.3.2.3 Material Models for Finite Element Modelling of Composites

Common to all the approaches described above is the need to choose a material model and suitable failure criterion. The number of publications in these subjects is high and the ones described below are but a few of the most relevant ones.

Damage Mechanics

Elastic properties and failure criteria such as interactive criteria (e.g. Tsai-Wu [50] and Tsai-Hill [27]) and independent criteria (e.g. Hart-Smith [25][26], Hashin [27], and Hashin-Puck [44]) define the behaviour of a laminate up to first-ply failure but do not succeed in delivering an accurate characterisation of material behaviour past that point. It is therefore necessary to have a numerical representation of the level of damage in a volume of material, which relates to mechanical property degradation. This representation takes the form of a macroscopic variable, which evolves in a progressive manner and is dependent on the loading history [34].

The level of damage in a material relates to the extent of micro-cracks or defects which cause a degradation of material properties of that material. The concept of damage mechanics to model material behaviour can be explained by the following schematic.

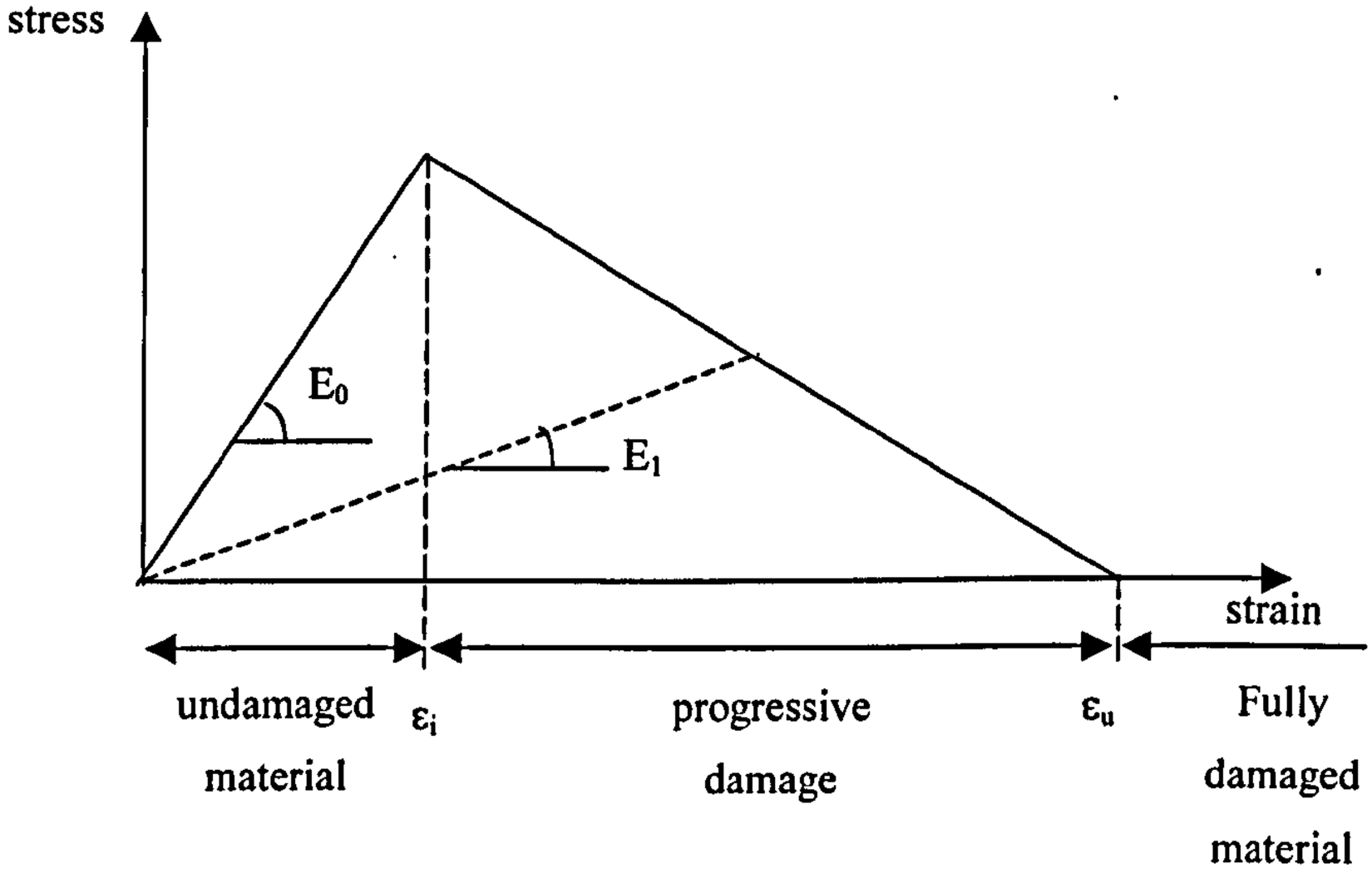

Figure 2-33 – Typical Elastic Damage Stress-strain relation

Figure 2-33 shows a typical damage law applied by numerous authors to characterise material property degradation in composite laminates. This approach is widely used in material models available in commercial FE codes and is particularly suited to explicit codes as it requires little computational effort, as opposed to non-linear models which can seriously hinder CPU times when analysing large scale structures [41].

The elastic-damage law affects the modulus of a material when a specified strain value ε_i is reached. At that point, the material is damaged progressively until fully damaged at strain ε_u. The governing equation for the elastic damage law is:

$$\sigma = E_0(1-d)\cdot\varepsilon \tag{2-9}$$

The damage parameter *d* varies between 0 (undamaged) and 1(fully damaged material). The values between those two limits applied to equation (2-9) define the strength of the material between ε_i strains and ε_u, which are predefined.

Damage models can be global (affecting the whole laminate) or specific for certain loading directions, or to the constituents of the laminate. An example of the latter one is the model used by Shahid and Chang [49] to model the progressive failure of composites under tensile and shear loadings. These authors used two damage parameters to model the accumulation of damage in the composite, one for fibre and another for the matrix behaviour.

Fracture Mechanics

The concept of fracture mechanics relates the progression of damage in a composite to the energy released during the damaging stage. It.has been used to predict the crack growth in composite laminates [3]. The main premise of any fracture mechanics based approach is that the energy released by relaxing of the material around a crack tip is greater than the energy required to progress crack growth.

The main drawback of fracture mechanics models is their general inability to predict nucleation and subsequent crack growth without pre-defining the geometry of the initial crack and path for it to propagate.

2.3.2.4 Delamination Modelling

Several authors have developed delamination models for application in Finite Element codes. Corigliano [7] and Reedy et al [48] identified damage mechanics modelling of the interlaminar region to be the simplest approach from a computational point of view. Common to most models is also the use of fracture toughness tests to characterise the behaviour of composites in delamination.

Delamination is the phenomenon of interlaminar material damage and subsequent degradation in material properties due to the type of loads represented in Figure 2-34 [51].

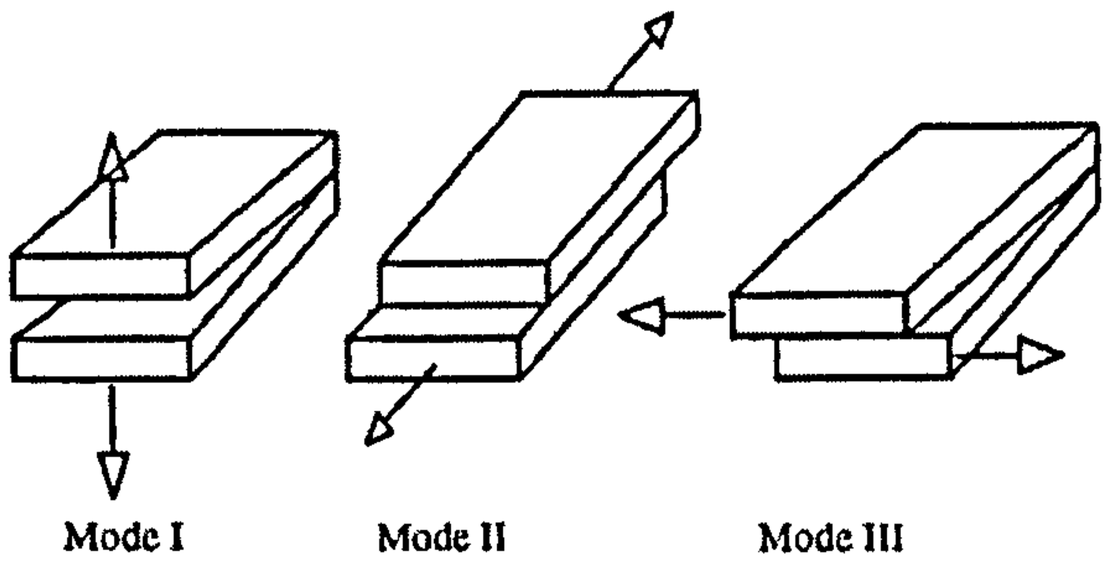

Figure 2-34 - Delamination Modes [51]

Typically there are three standard fracture toughness tests used to quantify the interlaminar behaviour of the composite laminate, namely the Double Cantilever Beam (DCB) for Mode I, the End Notched Flexure (ENF) test for Mode II, and the Mixed-Mode Bending (MMB) test for Mixed-Mode delamination.

Crisfield [8] proposed a model where fracture mechanics concepts are indirectly introduced by relating the energy absorbed in the damaging process to the material fracture energy *Gc*. For the interlaminar failure the interface energy is monitored and, if this is found to exceed the limiting value of fracture toughness G_C, then the crack is advanced. More correctly mixed mode loading exists and both mode I G_I and mode II G_{II} must be monitored with fracture depending on an interaction criteria of the form:

$$\left(\frac{G_I}{G_{IC}}\right)^m + \left(\frac{G_{II}}{G_{IIC}}\right)^n = e_D \qquad (2\text{-}10)$$

where G_I and G_{II} are the monitored interface strain energy in mode I and mode II respectively, G_{IC} and G_{IIC} are the corresponding critical fracture energies and constants m and n are chosen to fit the DCB, ENF and MMB test data. Delamination is assumed to extend if $e_D \geq 1$.

The softening traction/relative displacement relationship shown in Figure 2-35 is assumed. This curve is typical of damage mechanics methods, however fracture mechanics is indirectly introduced by relating the energy absorption (area under the stress-strain curve) to G_c. As in damage mechanics any unloading in the failure zone uses the partially damaged modulus and is therefore directed toward the origin.

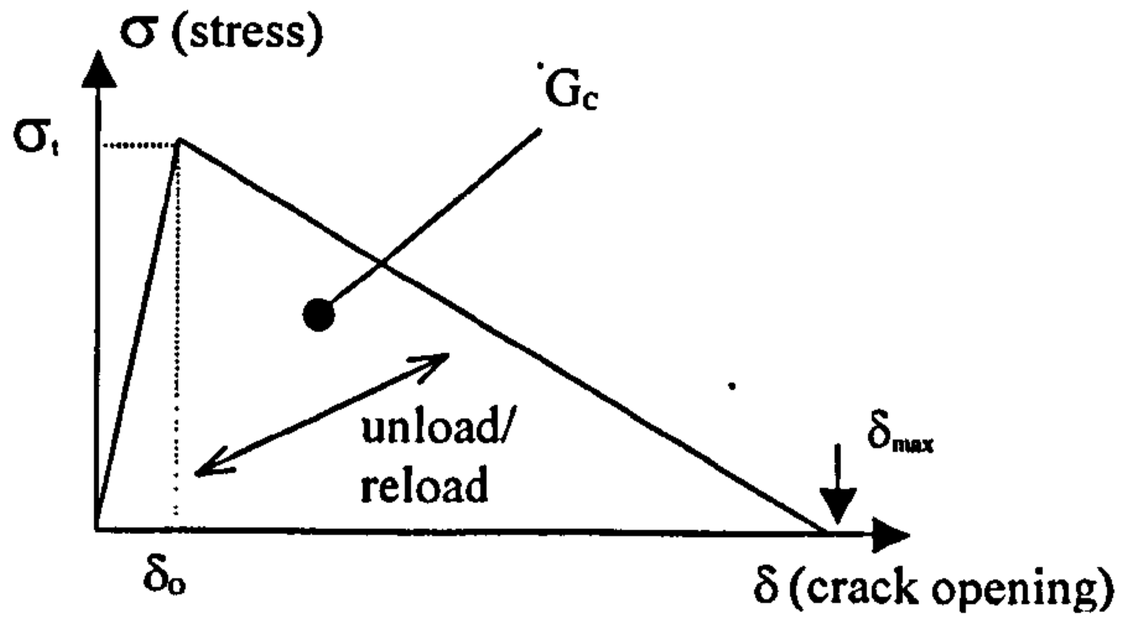

Figure 2-35 - Delamination Loading Curve [8]

For material with known delamination stress σ_t, and critical fracture energy G_c the required crack opening displacement δ_{max} may be computed. These arguments are applied to determine the required crack opening for $\delta_{I,max}$ (mode I) and $\delta_{II,max}$ (mode II). Summarising the expressions derived by Crisfield [8]:

$$\bar{\sigma} = \begin{Bmatrix} \bar{\sigma}_I \\ \bar{\sigma}_{II} \end{Bmatrix} = [I - D]E_O \begin{Bmatrix} \bar{\varepsilon}_I \\ \bar{\varepsilon}_{II} \end{Bmatrix} \tag{2-11}$$

$$= \left[I - \frac{\kappa}{1+\kappa} F \right] E_O \begin{Bmatrix} \bar{\varepsilon}_I \\ \bar{\varepsilon}_{II} \end{Bmatrix}$$

Where I is an identity matrix, E_O is the diagonal matrix of inter-ply mechanical properties. F and κ are terms defining the strain and interaction damage model given by:

$$F_{II} = \left[\frac{\bar{\varepsilon}_{\max}}{\bar{\varepsilon}_{\max} - \bar{\varepsilon}_O} \right]_{I,II} \tag{2-12}$$

$$\kappa = \sqrt{\left(\frac{\bar{\varepsilon}_I}{\bar{\varepsilon}_{OI}} \right)^{2m} + \left(\frac{\bar{\varepsilon}_{II}}{\bar{\varepsilon}_{OII}} \right)^{2n}} - 1 \tag{2-13}$$

where m and n are as defined in Equation (2-10). The analyses presented in [8] were performed with $m = n = 1$. Results showed good agreement with fracture toughness test results for a single delamination. However, the potential to handle multiple delaminations remained to be studied.

2.3.3 Summary of Finite Element Methods

Most numerical models of composite laminates have used finite element techniques to model the plies and ply interfaces. Generally failure criteria and damage mechanics have been used for modelling the propagation of multiple crack fronts, typical of applications involving the crushing of composite laminate structures. Fracture mechanics concepts have mostly been used to predict the propagation of a single crack emanating from an initial flaw.

Delamination modelling leading to accurate prediction of SEA and crush modes of composite tubes usually uses solid elements to represent both the plies and the inter-ply resin-rich areas, Figure 2-36 (as used in the *Solid Element* modelling approach described in Section 2.3.2.2). Due to the small thickness of these areas, the resulting mesh has solid elements with poor aspect ratio. A large number of small elements must be used which reduces time-step values[1], making the analysis CPU expensive and generally only feasible for small detailed studies only.

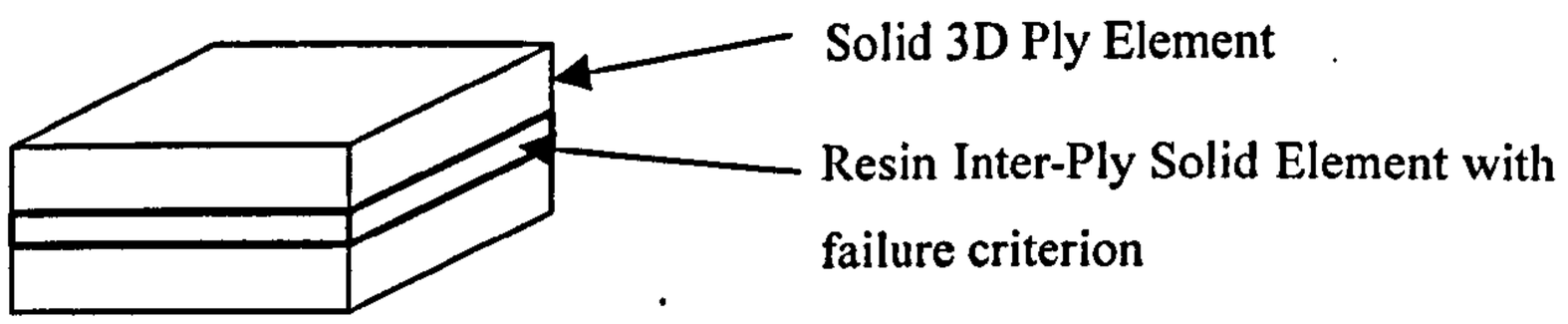

Figure 2-36 - Solid Element Approach

The application of fracture mechanics to predict the growth of multiple cracks in composite structures has so far been limited due to computational difficulties. However, these can be overcome using an explicit finite element formulation in which an element-by-element scheme and explicit integration solution is used to solve the structural dynamic equations.

In conclusion, many of the modelling approaches to date are either computationally expensive, not truly predictive, or do not deal with the geometry of a crushed tube, where the splayed fronds and delamination play such a relevant part in the crush mode. Indeed, even if the SEA due to delamination seems to account for only a small proportion of the total energy

[1] This statement assumes that these analyses are performed with explicit FE codes, since implicit algorithms are not computationally efficient for crash modelling.

absorbed by the tube, it is implicitly responsible for defining the crush mode, which in turn has a crucial effect in SEA value.

As a result, this work proposes the introduction of a delamination sub-routine in an explicit FE code, which combined with an appropriate formulation and modelling procedure, can provide the user with a predictive tool to simulate the crush of composite tubes.

3.0 Experimental Benchmarking Data

In this chapter, the materials, coupon and tube crush tests used to provide benchmarks for the validation of the predictive FE model are described.

3.1 Materials

Two composite materials were studied:

- Continuous filament random mat (CoFRM) manufactured from E-glass and polyester resin
- Braided Carbon with Vinylester resin.

These materials are briefly described below. Detailed testing programmes were developed by Curtis [9] – for CoFRM - and Duckett [11] - for Braided Carbon.

3.1.1 CoFRM Glass/Polyester

All coupon and tube specimens were manufactured using:

- Resin Transfer Moulding with vacuum assistance
- glass U750-450 Continuous Filament Random Mat (CFRM) containing 8% thermoplastic binder supplied by Vetrotex Ltd.
- Crystic 701 PA polyester resin supplied by Scott Bader Ltd.
- 1% methyl ethyl ketone peroxide (MEKP) M50 initiator supplied by Butanox

The curing regime used for all specimens was as follows:

- 24 hours cure at room temperature
- 3 hours post cure at 80◦C

Reinforcement volume fraction was 23.45%

A more detailed description of the manufacture of CoFRM specimens is given by Curtis [9].

3.1.2 Braided Carbon

Carbon/vinyl ester was studied as part of a programme funded by the Automotive Composites Consortium (ACC) of the USCAR. Flat plaques, 3mm and 13mm in thickness, were provided for coupon testing. Circular section tubes with three different wall thicknesses and square

section tubes were provided for the tubular crush tests. All tubes and plaques were provided by the ACC.

All the materials described in this section were manufactured using an epoxy vinyl ester matrix (Hetron 922) supplied by Ashland. Braided carbon was used as the reinforcement and three braid architectures (0°/±30°, 0°/±45° and 0°/±60) were investigated. Fortafil #556 fibres with a tow size of 80k were used for the axial tows and Grafil 34-700 fibres with a tow size of 12k were used for the braider tows. Figure 3-1 shows an example of the 0°/±30° braid architecture.

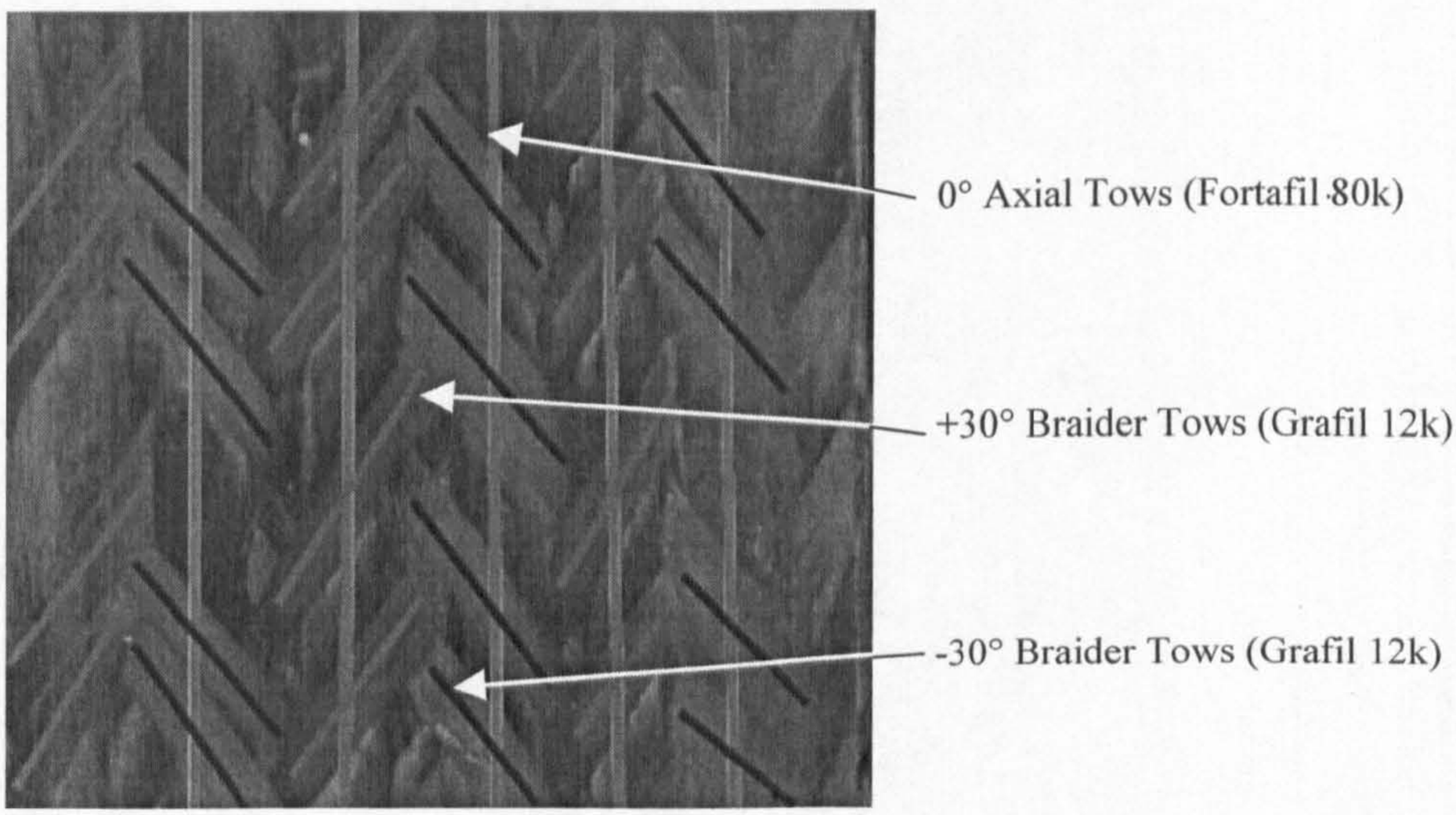

Figure 3-1 - 0°/±30° Braid Architecture

For all plaques and tubes, the resin and processing conditions were selected so that finished part properties would be representative of those obtainable from high speed, cost effective manufacturing processes.

3.2 Intralaminar Data

The set of intralaminar material properties and coupon tests to obtain them are presented in this section. The elastic properties obtained are shown in

Table 3-1.

Elastic Tensile Moduli	E_{1t}, E_{2t}, E_{3t}
Elastic Compressive Moduli	E_{1c}, E_{2c}, E_{3c}
Shear Moduli	G_{12}, G_{23}, G_{31}
Poisson's Ratios	ν_{12}, ν_{13}, ν_{23}, ν_{21}, ν_{31}, ν_{32}

Table 3-1 – Intralaminar Elastic Material Properties

The programme of tests devised to measure each of the required properties is summarised in Table 3-2 [9]. The post-first ply failure parameters must be calibrated using the stress-strain relations of each coupon test.

Required Properties	Evaluating Test
E_{1t}, ν_{12}, ν_{13}	In-plane 0° Tensile Test
E_{2t}, ν_{21}, ν_{23}	In-plane 90° Tensile Test
E_{3t}, ν_{31}, ν_{32}	Through-Thickness Tensile Test
E_{1c}	In-plane 0° Compressive Test
E_{2c}	In-plane 90° Compressive Test
E_{3c}	Through-Thickness Compressive Test
G_{12}	Iosipescu Shear Test
G_{23}	Iosipescu Shear Test
G_{31}	Iosipescu Shear Test

Table 3-2 - Material Properties and Test Methods for Calibration of Numerical Material Model

3.2.1 Coupon Testing

In this section the coupon tests for CoFRM and for the three architectures of Braided Carbon required to gather the in-plane material data are briefly described. A detailed description of the test procedures can be found in [9] and [11].

3.2.1.1 CoFRM Coupon Test Specimens

Figure 3-2 shows the Glass/Polyester CoFRM Specimens used to acquire the material properties shown in Table 3-2. Since the Glass/CoFRM material is quasi-isotropic in the laminate plane, there is need for only one tensile and one compressive test to define the in-plane tensile and compressive properties, therefore reducing the total number of tests required for the characterisation of material behaviour. Details of specimen dimensions can be found in Appendix 5.

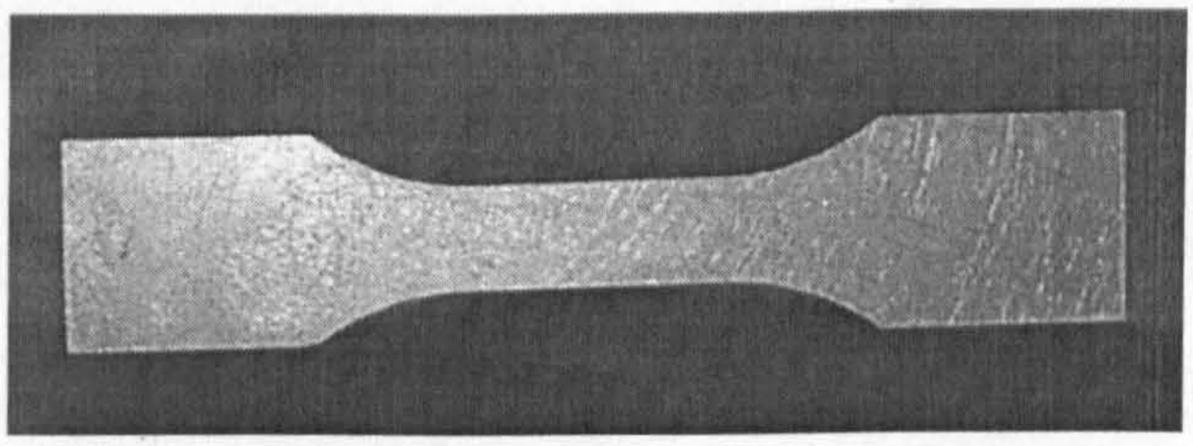

a)

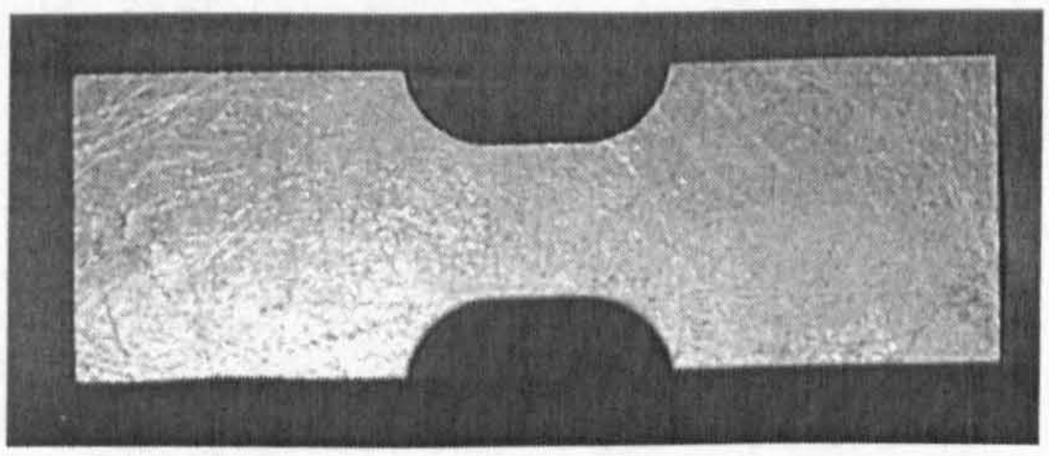

b)

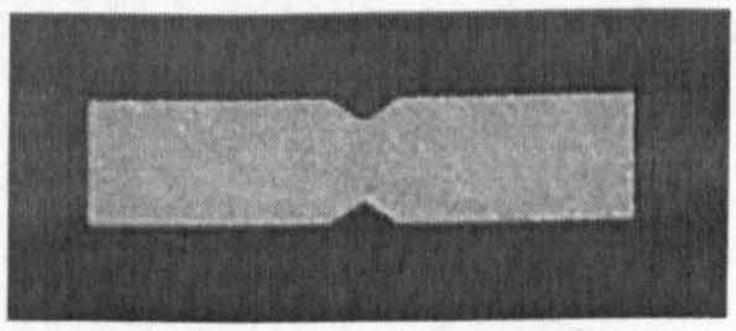

c)

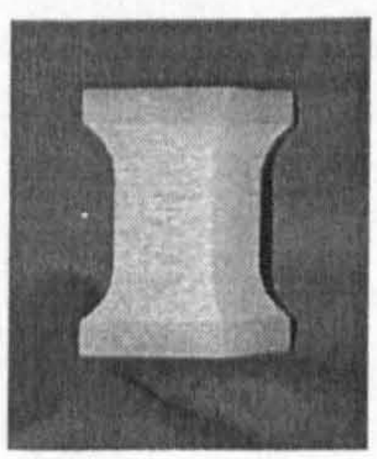

d)

Figure 3-2 - CoFRM Coupon Specimens **a)** Tensile **b)** Compressive **c)** Shear **d)**Through-Thickness

3.2.1.2 Braided Carbon Coupon Test Specimens

The braided carbon materials studied are anisotropic in the laminate plane. Therefore, unlike CoFRM, axial and transverse tests have to be performed. Figure 3-3 is a schematic of the fibre orientations defining axial and transverse directions for braided carbon coupon tests of the same fibre architecture (in this case, 0/+30/-30). Details of specimen dimensions can be found in Appendix 5.

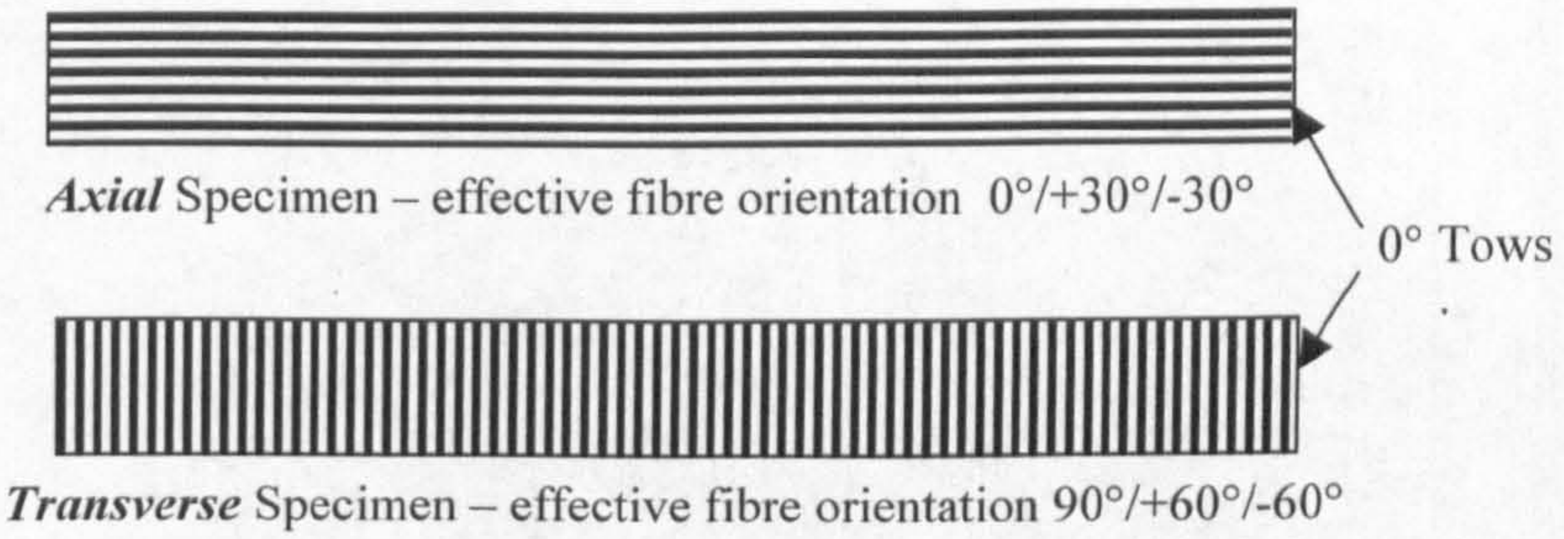

Figure 3-3 – Diagram showing definitions of Axial and Transverse specimens

Figure 3-4 shows the coupon specimens for Braided Carbon.

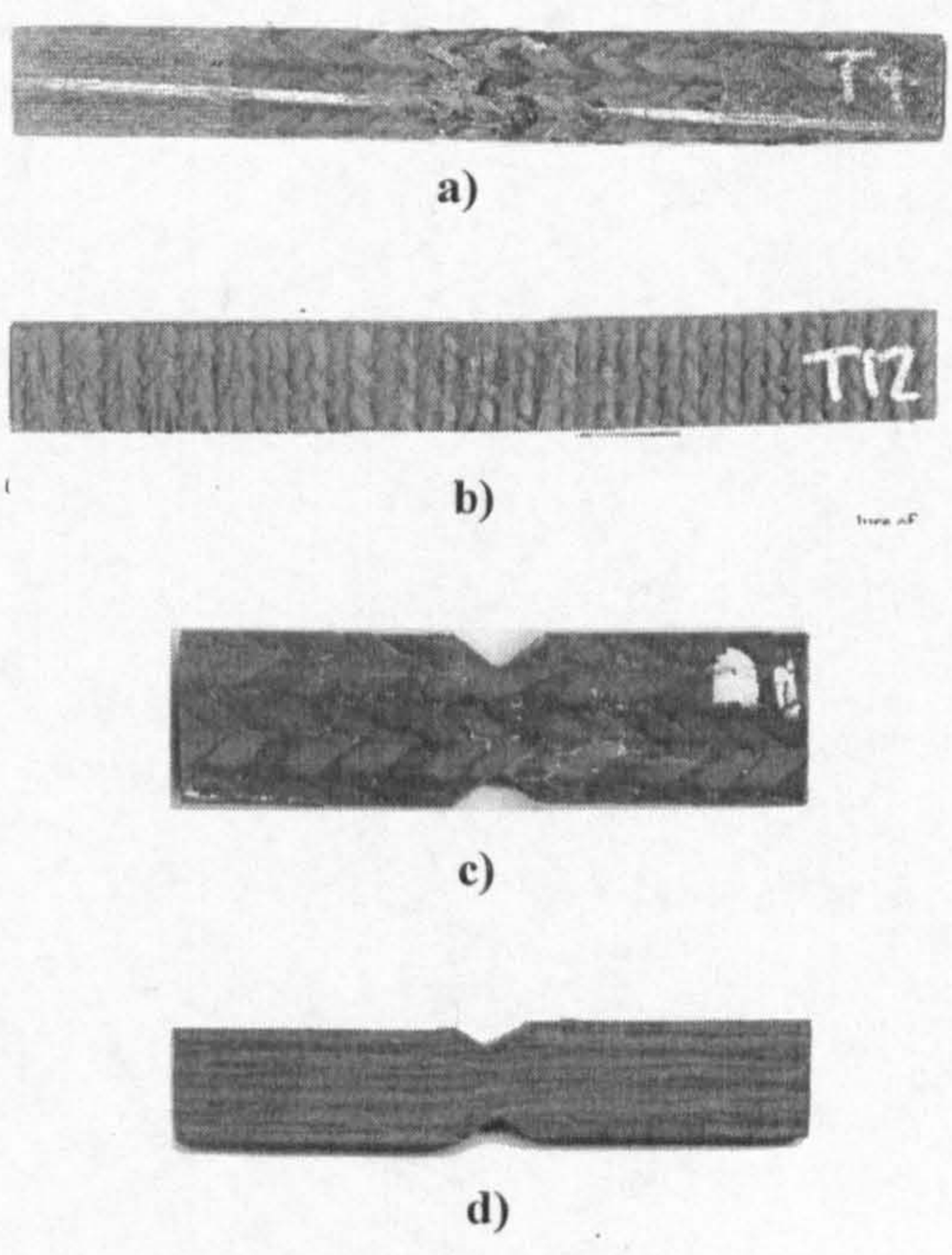

Figure 3-4 – Braided Carbon Coupon Specimens **a)** Axial **b)** Transverse **c)** In-plane Shear **d)** Through-Thickness Shear

3.3 Interlaminar Data

The following sections provide a description of the interlaminar fracture toughness tests. These tests were only carried out for CoFRM. The data for modes I and II for braided carbon was supplied by the ACC. No mixed-mode bending tests were performed on braided carbon.

3.3.1 Double Cantilever Beam Tests

The Double Cantilever Beam (DCB) test is used to quantify mode I fracture toughness of the composite laminate. The specimen is shown in Figure 3-5a) and a schematic of the test configuration can be seen in Figure 3-5b).

3.3.1.1 Test Conditions

All tests were conducted:

- in accordance with Double Cantilever Beam (DCB) Method ASTM D5528 – 94a [1]
- using an Instron 1195 test machine with a 50 kN load cell
- at a crosshead speed of 0.5 mm/min
- at room temperature (20°C)

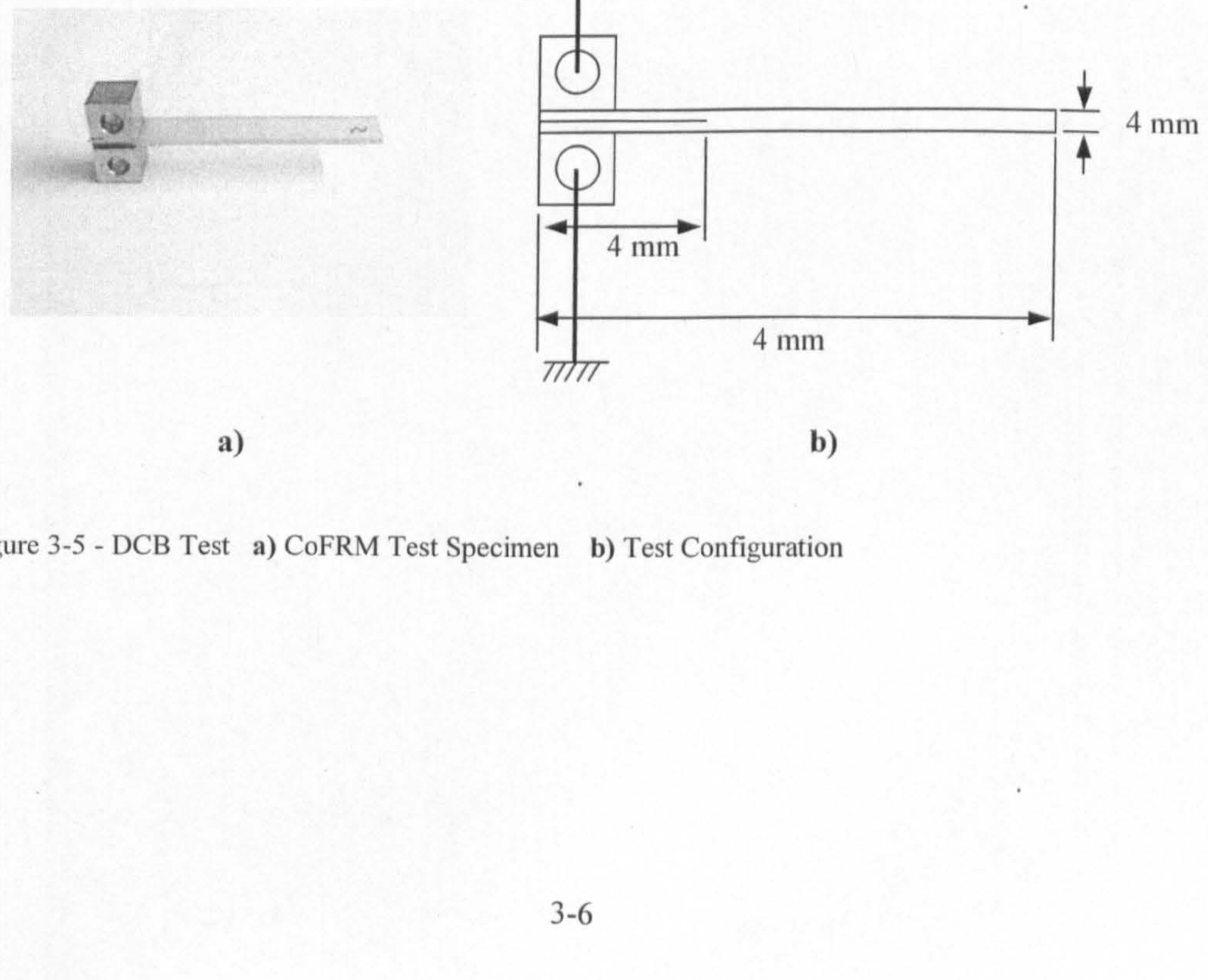

a) **b)**

Figure 3-5 - DCB Test **a)** CoFRM Test Specimen **b)** Test Configuration

3.3.2 End Notch Flexural Tests

The End Notch Flexural (ENF) test is used to quantify mode II fracture toughness of the composite laminate. The test in progress is shown in Figure 3-6a) and a schematic of the test configuration can be seen in Figure 3-6b).

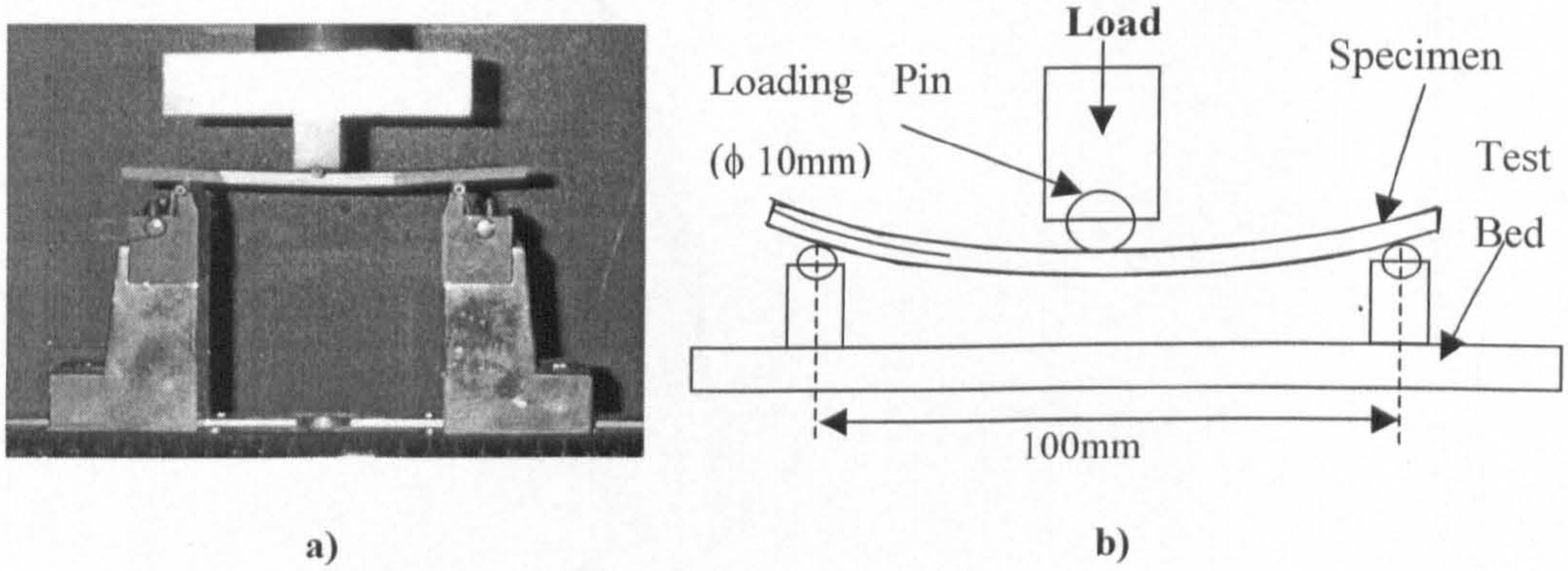

Figure 3-6 – ENF Test **a)** Testing in progress **b)** Test Configuration

3.3.2.1 Test Conditions

The test procedure is similar to a simple three point bending test. Five tests were conducted on an Instron 1195 testing machine, at a crosshead speed of 0.5mm/min. During testing, the progression of the crack tip was monitored using a travelling microscope. The Delsen method [10] was used to calculate G_{IIC} values from the load-displacement traces, using the following equation :

$$G_{IIC} = \frac{9a^2 Ps}{2B\left(2L^3 + 3a^3\right)}$$

GIIC = Mode II Fracture Toughness

a = Distance between the Crack Tip and Point of Loading at Maximum Load

P = Maximum Load

s = Load Point Displacement at Maximum Load

B = Specimen Width

L = Half the Load Span

More details about the test procedure can be found in [11].

3.3.3 Mixed-Mode Bending Tests

The purpose of this test is to quantify the mixed-mode behaviour of the laminate composite. The Mixed-Mode Bending test was first developed by Reeder and Crews [47] and further modified by Chen et al [6] in order to reduce the influence of the weight of the test machine on the resulting fracture toughness. A schematic of the MMB test configuration is shown in Figure 3-7.

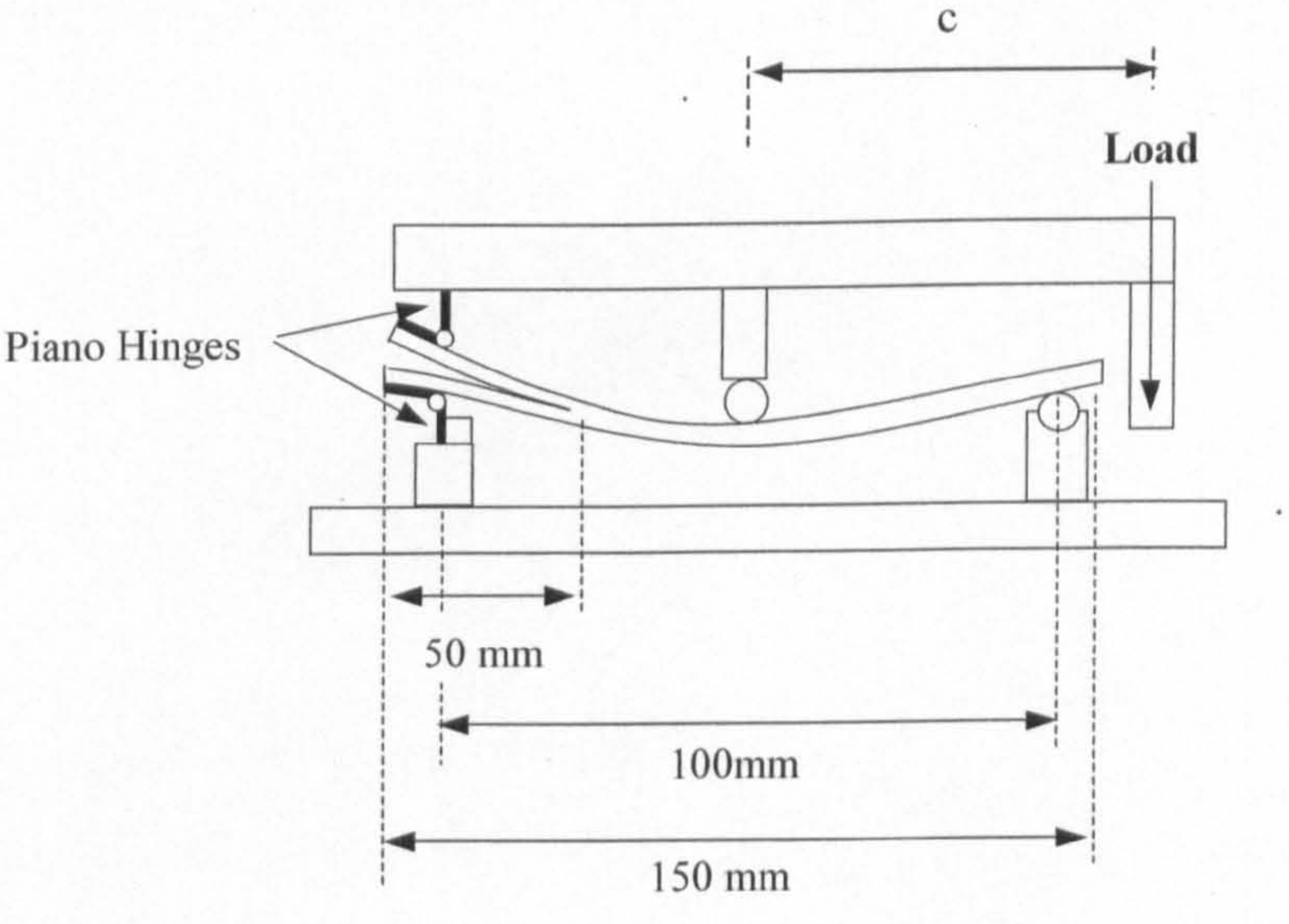

Figure 3-7 - MMB Test Configuration

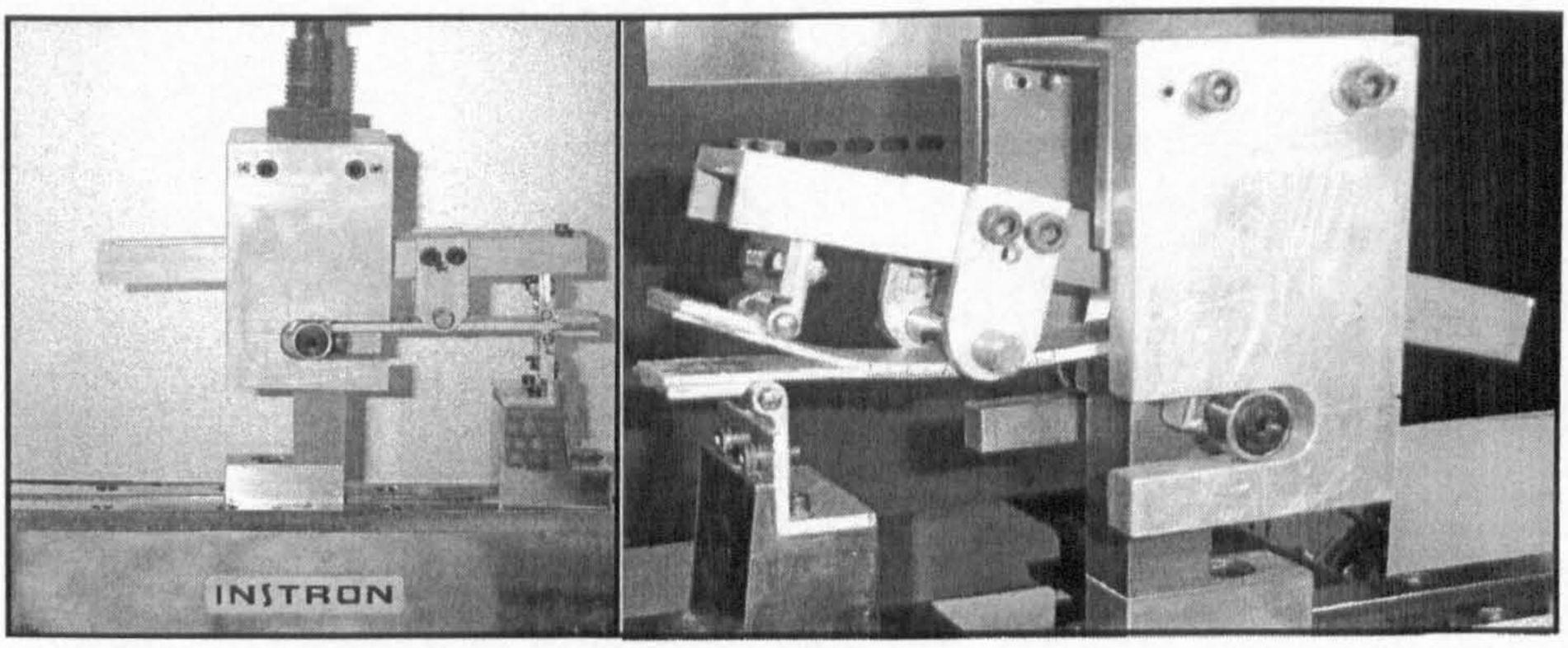

Figure 3-8 - MMB Testing in Progress

3.3.3.1 Test Conditions

Fracture toughness values G_c for Mixed-Mode are obtained from the load-displacement response curves, using the Delsen Method [10]. By varying the point of applied load (defined by c in Figure 3-7), different Mixed-Mode ratios can be tested. The Energy E_c required to propagate the crack by a certain amount a_i is given by the area under the load-displacement curve disregarding the elastic recovery energy, which is a measure of the compliance of the beams, Figure 3-9.

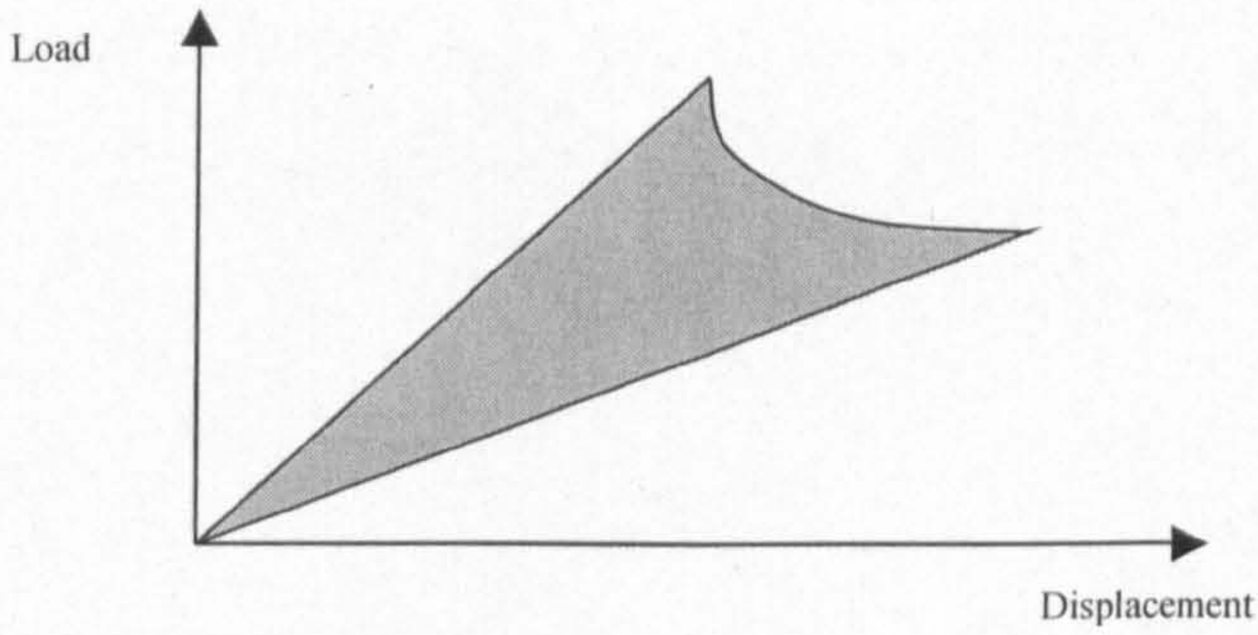

Figure 3-9 – Energy Required for Crack Propagation

The value of fracture toughness is obtained by,

$$G_c = \frac{E_c}{A}$$

where A is the Area of the propagated crack, calculated as the product between the measured crack length and the width of specimen (Figure 3-10)

$$A = a_c \cdot B$$

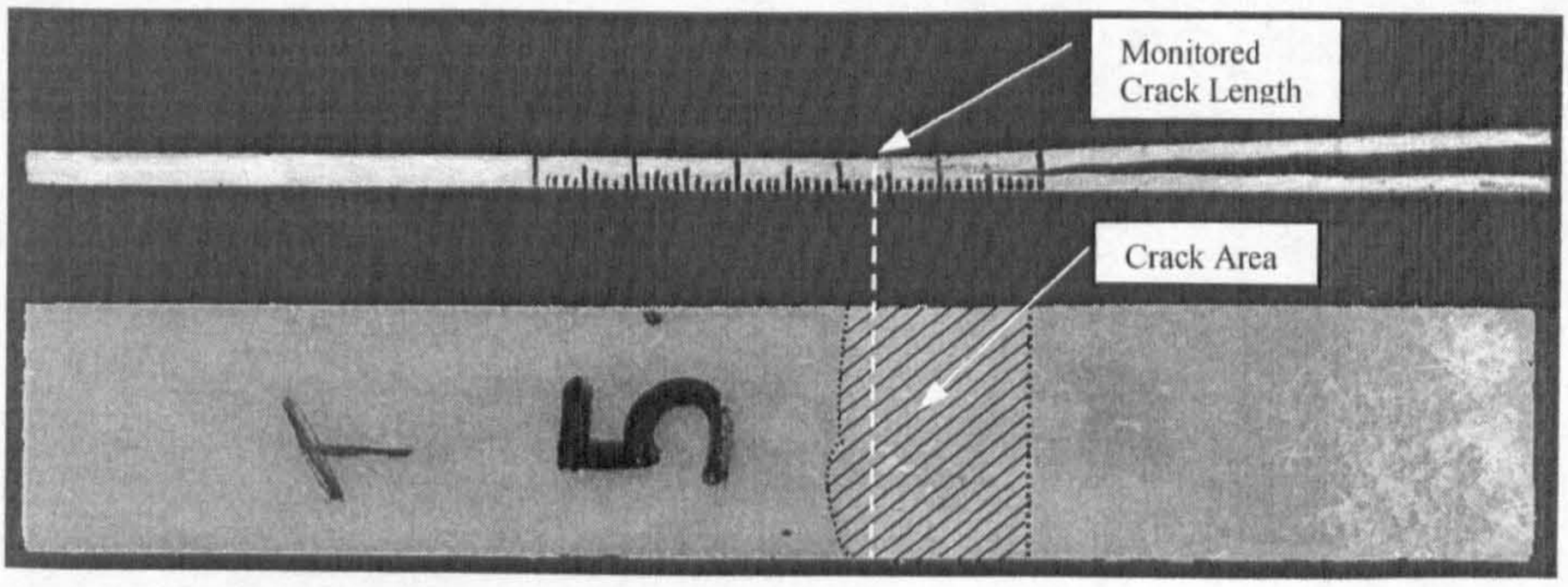

Figure 3-10 - Crack area and monitored crack length after MMB test

3.4 Tube Crush Data

In this section the experimental tube crush tests are briefly described. This work was performed at the University of Nottingham by Curtis [9] and Duckett [11]. A more detailed description of the tube specimens and test procedures can be found in the work by those authors.

3.4.1 Tube Geometry

The geometry of the different types of tubes tested is described in Figure 3-11.

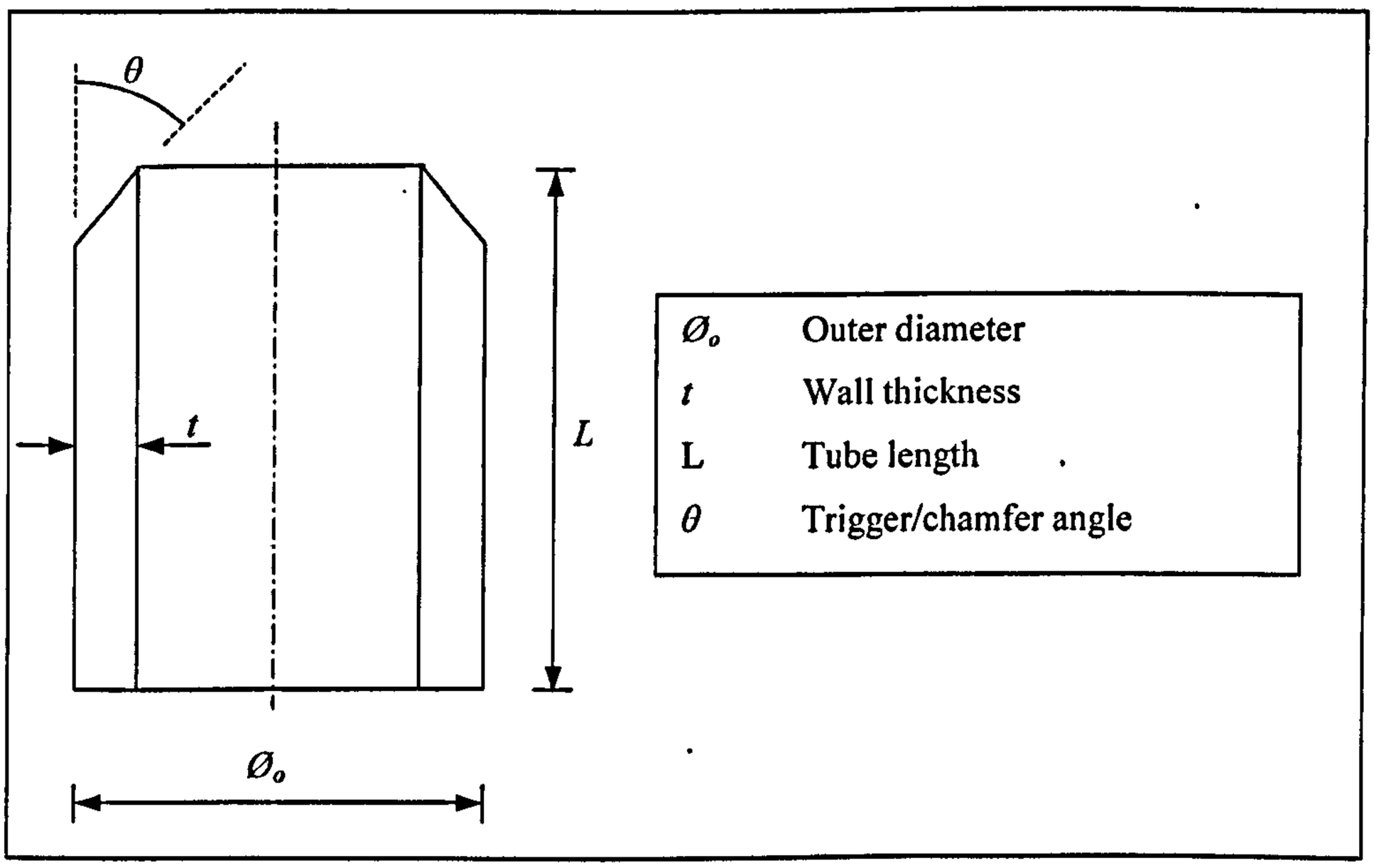

Figure 3-11 - Geometry of Circular Tubes (drawing not to scale)

The dimensions of all the tubes tested are shown in Table 3-3.

Geometry	CoFRM	Braided Carbon								
		0/+30/-30			0/+45/-45			0/+60/-60		
	6-ply	2-ply	3-ply	4-ply	2-ply	3-ply	4-ply	2-ply	3-ply	4-ply
$Ø_o$ [mm]	89	64	64	64	64	64	64	64	64	64
t [mm]	4	2	3	4	2	3	4	2	3	4
L [mm]	100	150	150	150	150	150	150	150	150	150
θ	45°	45°	45°	45°	45°	45°	45°	45°	45°	45°

Table 3-3 - Dimensions of Crush Tubes

3.4.2 Test Conditions

All tests were conducted:

- using an Instron 8500 servo hydraulic test machine with a 1000 kN load cell
- at a crosshead speed of 0.5 mm/min
- at room temperature (20°C)

The tubes were crushed between two flat, steel platens with a surface ground finish (Figure 3-12).

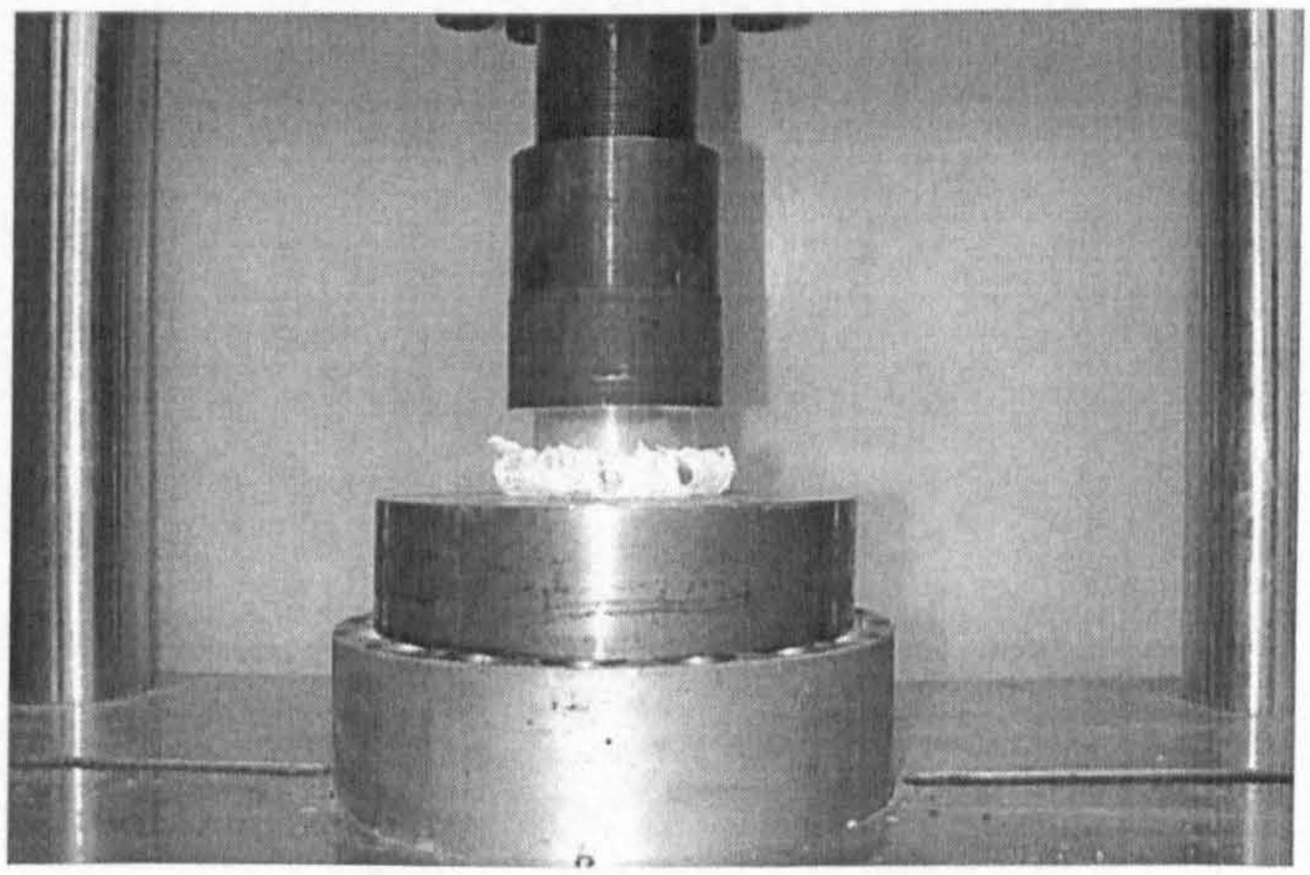

Figure 3-12 - Glass (CoFRM)/Polyester Tubular Crush Test

Load-displacement data was recorded directly from the Instron test machine onto a PC.

4.0 Material Models

In this chapter, the intralaminar and intralaminar material models in PAM-CRASH are described.

4.1 Intralaminar Model

4.1.1 PAM-CRASH Material Models

The general requirement for a Finite Element code to handle composite material modelling is that is has to be able to read anisotropic material properties, as composites are highly directional materials. Also, thermoset plastic composites can show various types of failure, ranging from brittle matrix cracking to controlled interlaminar crack growth. The most appropriate material model in the explicit FE code PAM-CRASH (version 2000) for modelling composite is the degenerate Bi-phase model, described in the sections below, although subsequent PAM-CRASH versions have included better models. An alternative material model, which showed promising results was also investigated initially – see Appendix 3.

4.1.2 Degenerate Bi-phase Material {Material Type 130/130, ITYP=0}

This material model is available for both shell and solid element formulations and is based on the Bi-phase model, where fibres and matrix are modelled as separate phases. The uniaxial properties of the fibres are superimposed on an orthotropic matrix, as shown in Figure 4-1, with each phase subject to a separate material behaviour and damage laws.

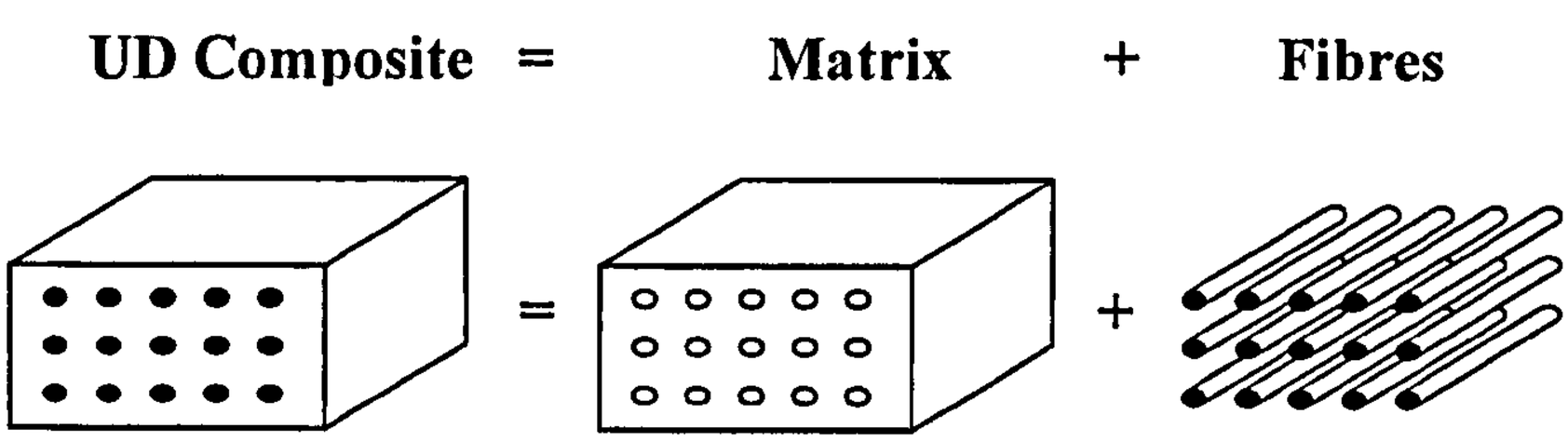

Figure 4-1 - Schematic of the Bi-phase Composite Model

In the degenerate Bi-phase model, the composite material is modelled as an orthotropic homogeneous matrix, which means there is no separate definition of fibre and matrix properties. Material behaviour is governed by an elastic damage law, described in Section 4.1.3. The degenerate version of the bi-phase model is generally recommended for bi-directional composite materials [41], which is the case for Glass/Polyester CoFRM (with quasi-isotropic in-plane behaviour) but not for Braided Carbon. However, the modelling approach proposed here separates in-plane from out-of-plane behaviour. This means that any material can have its in-plane properties modelled with the degenerate Bi-phase material, as in this plane, any material is bi-directional.

The material may be damaged as a result of either volumetric strain, deviatoric shear strain or a combination of the two. A mathematical description of the material damage law was previously presented by Curtis [9] and is repeated in Sections 4.1.3 and 4.1.4. Following Curtis's approach, only damage parameters based on deviatoric shear strain will be used, for simplicity of the calibration process.

The limitation of this material model lies in the fact that there is only one independent criterion to represent failure in all different loading directions. In practice, the actual values of strain at failure vary for the different orthotropy directions, yet they cannot be adjusted independently. It is therefore necessary to assess which strain direction should be used to base matrix damage on – a procedure for this is described in Chapter 5.

4.1.3 Material Damage Laws

This section shows a graphical description of the damage laws used in PAM-CRASH Degenerate Bi-phase material model.

(i) fracturing damage function :

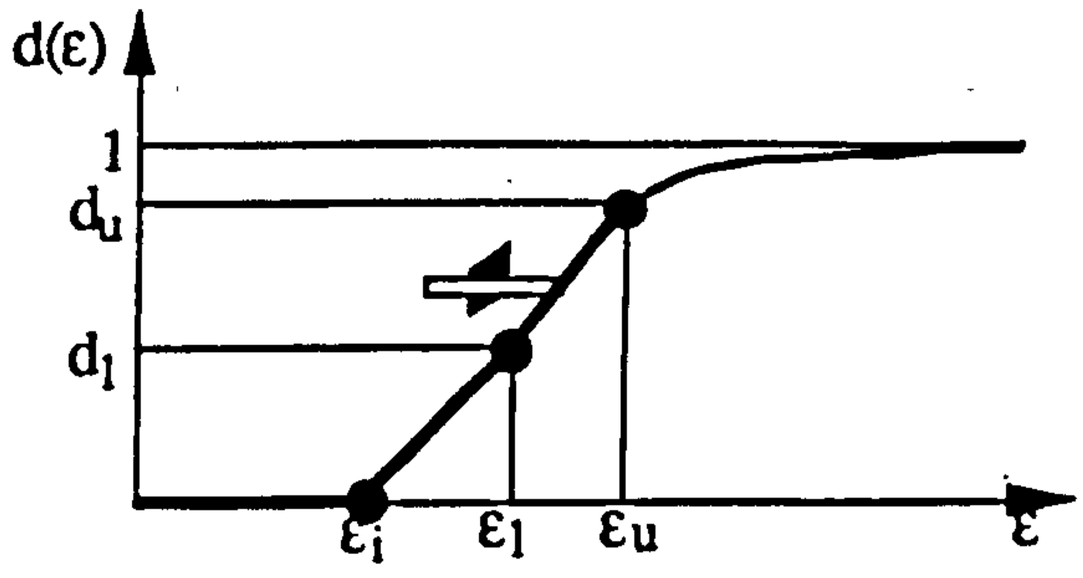

damage function d(ε)	range
$\frac{\varepsilon-\varepsilon_i}{\varepsilon_l-\varepsilon_i}d_l$	$\varepsilon_i < \varepsilon < \varepsilon_l$
$\frac{\varepsilon-\varepsilon_l}{\varepsilon_u-\varepsilon_l}(d_u-d_l)+d_l$	$\varepsilon_l < \varepsilon < \varepsilon_u$
$1-\frac{(1-d_u)\varepsilon_u}{\varepsilon}$	$\varepsilon_u < \varepsilon < \infty$

(ii) modulus damage :

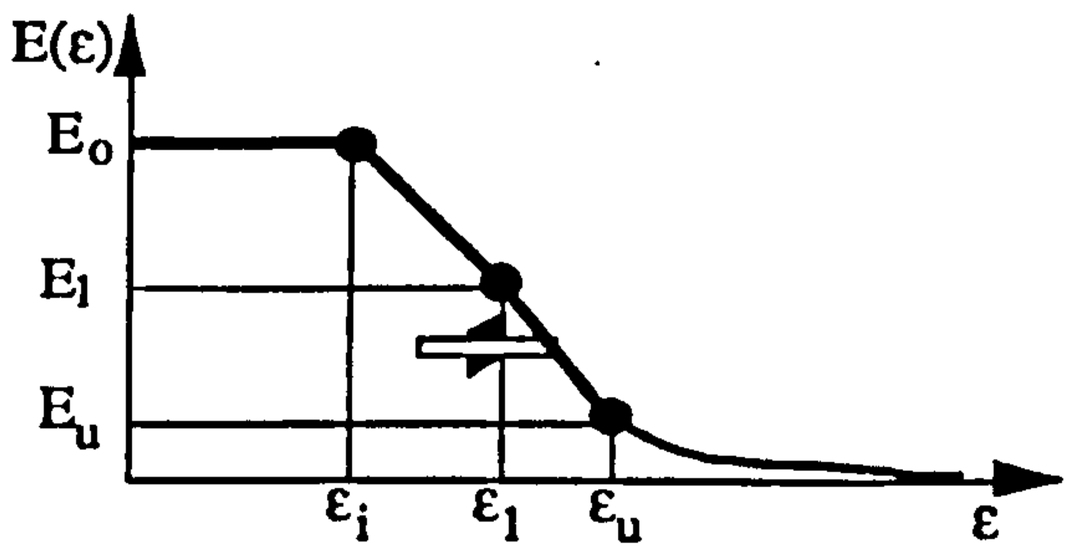

modulus damage
$E(\varepsilon) = [1-d(\varepsilon)]\, E_0$

(iii) stress-strain diagram :

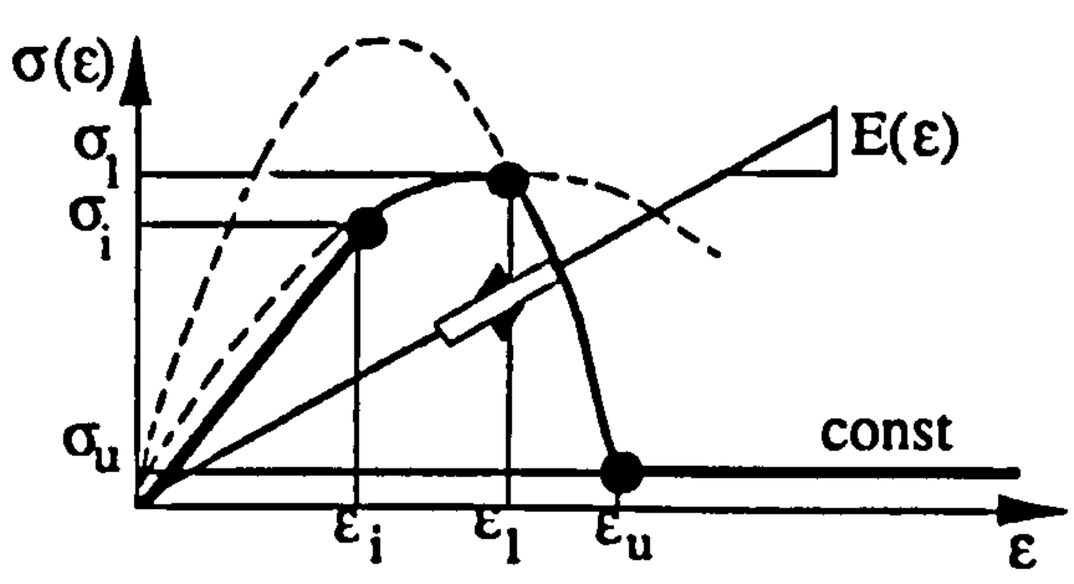

stress-strain relation d(ε)	range
$E_0\varepsilon\left(1-\frac{\varepsilon-\varepsilon_i}{\varepsilon_l-\varepsilon_i}d_l\right)$	$\varepsilon_i < \varepsilon < \varepsilon_l$
$E_0\varepsilon\left(1-d_l-\frac{\varepsilon-\varepsilon_l}{\varepsilon_u-\varepsilon_l}(d_u-d_l)\right)$	$\varepsilon_l < \varepsilon < \varepsilon_u$
$\sigma_u = E_0\varepsilon_u(1-d_u) = const$	$\varepsilon_u < \varepsilon < \infty$

Strain Definition

volume damage strain, d_v	$\varepsilon = \varepsilon_v = I_1 = \mathrm{tr}(\underset{\sim}{\varepsilon})$
shear damage strain, d_s	$\varepsilon = \varepsilon_s = \sqrt{J_2} = \sqrt{\frac{1}{2\mathrm{tr}\left(\underset{\sim}{\varepsilon} - \frac{\varepsilon_v \underset{\sim}{\delta}}{3}\right)^2}}$

TOTAL DAMAGE, $d = d_v + d_s$

but if $d > 1$ then $d = 1$

4.1.4 Evaluation of Damage due to the deviatoric shear Strain criterion

The deviatoric shear strain is defined as $\sqrt{J_2}$, where J_2 is the second deviatoric strain invariant. The second deviatoric stress invariant, J_2 may be expressed in terms of the stress invariants I_1, I_2, [36] [37] i.e.

$J_2 = I_2 + (1/3)\, I_1^2$ where

$$I_1 = \sigma_{11}^2 + \sigma_{22}^2 + \sigma_{33}^2$$
$$I_2 = \sigma_{12}^2 + \sigma_{13}^2 + \sigma_{23}^2 - (\sigma_{11}\sigma_{22} + \sigma_{22}\sigma_{33} + \sigma_{11}\sigma_{33})$$

where 1, 2, 3 represent orthotropy directions, NOT principal stress directions

The basic invariant equations for stress and strain have identical form provided that ε is used in place of σ and $\gamma/2$ in place of τ (when γ is defined as engineering shear strain, NOT tensor shear strain) [36] [37]. Hence the deviatoric strain invariant J_2 is:

$$J_2 = \frac{\varepsilon_{12}^2}{4} + \frac{\varepsilon_{13}^2}{.4} + \frac{\varepsilon_{23}^2}{4} + \frac{1}{3}\left(\varepsilon_{11}^2 + \varepsilon_{22}^2 + \varepsilon_{33}^2 + \varepsilon_{11}\varepsilon_{22} + \varepsilon_{22}\varepsilon_{33} + \varepsilon_{11}\varepsilon_{33}\right)$$

Thus, for the case when uniaxial stress σ_{11} is applied:

$(\varepsilon_{11} = \varepsilon_{11},\ \varepsilon_{22} = \nu_{12} \cdot \varepsilon_{11},\ \varepsilon_{33} = \nu_{13} \cdot \varepsilon_{11},\ \varepsilon_{12} = \varepsilon_{13} = \varepsilon_{23} = 0)$

$$\varepsilon_s^m = \sqrt{J_2} = \frac{\varepsilon_{11}}{\sqrt{3}}\sqrt{1+\nu_{12}+\nu_{13}-\nu_{12}\nu_{13}+\nu_{12}^2+\nu_{13}^2}$$

Similarly when uniaxial stress σ_{22} is applied it may be shown that

$$\varepsilon_s^m = \sqrt{J_2} = \frac{\varepsilon_{22}}{\sqrt{3}}\sqrt{1+\nu_{21}+\nu_{23}-\nu_{21}\nu_{23}+\nu_{21}^2+\nu_{23}^2}$$

And in the case where uniaxial stress σ_{33} is applied

$$\varepsilon_s^m = \sqrt{J_2} = \frac{\varepsilon_{33}}{\sqrt{3}}\sqrt{1+\nu_{31}+\nu_{32}-\nu_{31}\nu_{32}+\nu_{31}^2+\nu_{32}^2}$$

In the case of pure shear loading, τ_{12}

$(\varepsilon_{12} = \varepsilon_{12},\ \varepsilon_{11} = \varepsilon_{22} = \varepsilon_{33} = \varepsilon_{13} = \varepsilon_{23} = 0)$

$$\varepsilon_s^m = \sqrt{J_2} = \frac{\gamma_{12}}{2}$$

4.2 Interlaminar Model

In Chapter 2, the need to accurately model the interlaminar behaviour was identified as a crucial requirement for predictive modelling of composite material crush. In this section, a delamination model is described and its implementation into the PAM-CRASH code is discussed. This work was the result of a close collaboration between the author and Dr. AK Pickett at ESI GmbH, Germany.

4.2.1 PAM-CRASH Tied Slide Line – Contact Interface Type 32

The tied slide line contact algorithm in PAM-CRASH monitors, for each time step, the normal and shear displacements (δ_I and δ_{II}) of the slave node relative to its original (undeformed) position. It then applies forces to this node (F_I and F_{II}) to bring the node back to the undeformed position, as shown in Figure 4-2. These forces will take effect in the following time step.

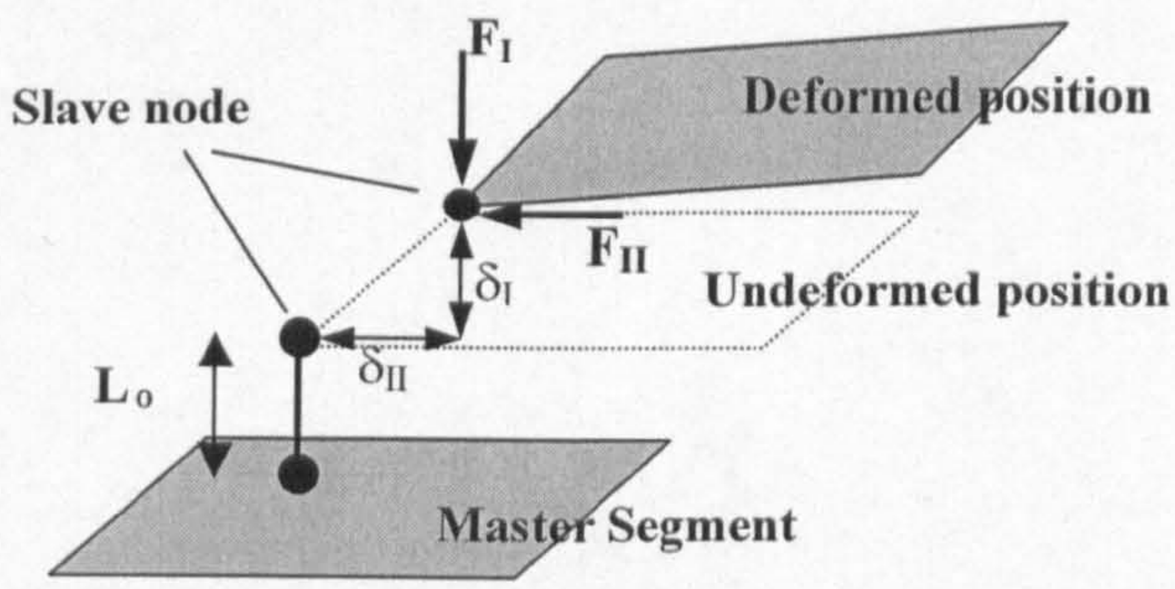

Figure 4-2 – Deformation Modes in Delamination on Finite Element Level

4.2.2 Delamination Model for PAM-CRASH

In the proposed delamination model, forces F_I and F_{II} will be related to Fracture Toughness parameters, as described below. The fracture energy absorption in each mode follows an elastic damage law, as described by Crisfield [8]. That model proposes the following stress-displacement curves for pure modes I and II delamination.

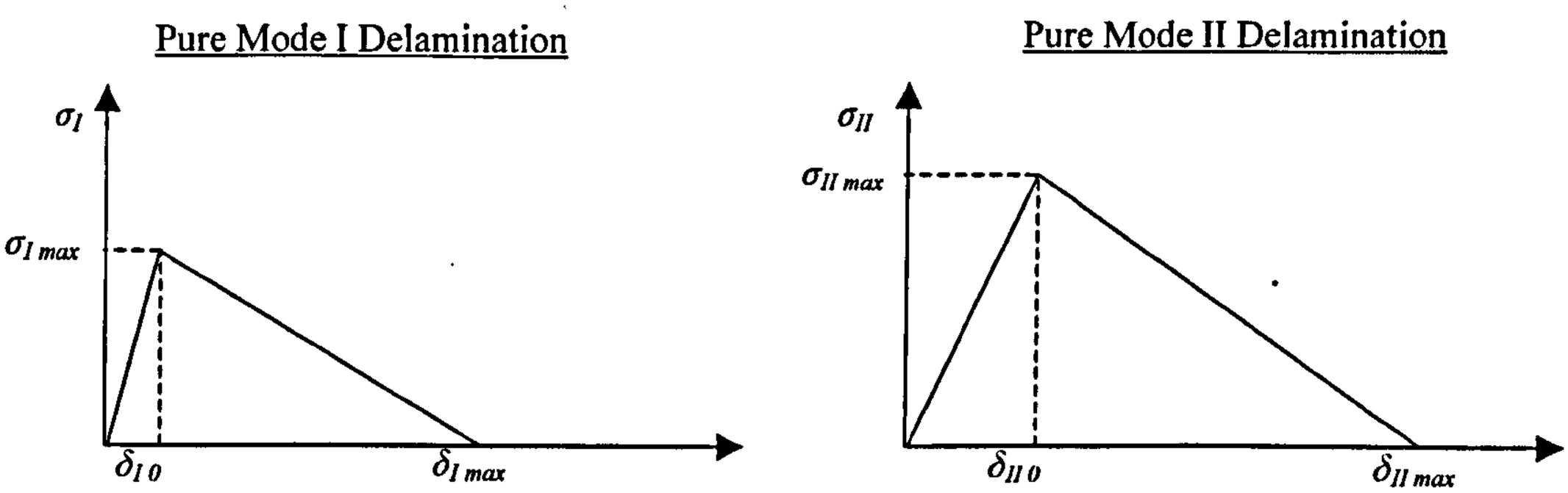

Figure 4-3 - Stress-displacement curves loading in for pure modes I and II

4.2.2.1 Input Values for the Delamination Model

The properties required to define the interlaminar behaviour of the composite material are:

E_0 through-thickness tensile modulus

G_0 through-thickness shear modulus

$\sigma_{I\,max}$ maximum interlaminar stress in mode I

$\sigma_{II\,max}$ maximum interlaminar stress in mode II

G_{Ic} mode I fracture toughness

G_{IIc} mode II fracture toughness

The values of $\sigma_{I\,max}$ and $\sigma_{II\,max}$ are usually related to through-thickness normal and shear yield stresses.

4.2.2.2 Relevant Parameters of the Model

For each of the curves shown in Figure 4-3, the area under the elastic range is the strain energy required to start damage of the interface, $G_{I\,0}$ (in case of pure mode I loading) or $G_{II\,0}$.

For mode I, in the elastic range we have:

$$\sigma_I = E_0 \cdot \varepsilon_I = \frac{E_0}{L_0} \cdot \delta_I \qquad (4\text{-}1)$$

Where L_0 is the distance between the ideal position of the slave node and the master element, as shown in Figure 4-2. Similarly, for mode II

$$\sigma_{II} = \frac{G_0}{L_0} \cdot \delta_{II} \tag{4-2}$$

Using equations (4-1) and (4-2), the normal and shear displacements, $\delta_{I\,0}$ and $\delta_{II\,0}$, are given by:

$$\delta_{I_0} = \frac{\sigma_{I_{max}}}{E_0} \cdot L_0 \qquad \text{and} \qquad \delta_{II_0} = \frac{\sigma_{II_{max}}}{G_0} \cdot L_0 \tag{4-3}$$

The values of maximum elastic strain energy for each mode can now be calculated.

$$G_{I_0} = \frac{1}{2}\sigma_{I_{max}}\delta_{I_0}$$

$$G_{I_0} = \frac{1}{2}\frac{\sigma_{I_{max}}^{\ 2}}{E_0}L_0 \tag{4-4}$$

For mode II

$$G_{II_0} = \frac{1}{2}\frac{\sigma_{II_{max}}^{\ 2}}{G_0}L_0 \tag{4-5}.$$

The areas under the load-displacement curves are the critical strain energies required for the failure of the interface (including the damaging range), i.e.

$$G_{Ic} = \frac{1}{2}\sigma_{I_{max}}\delta_{I_0} + \frac{1}{2}\sigma_{I_{max}}\left(\delta_{I_{max}} - \delta_{I_0}\right)$$

$$G_{Ic} = \frac{1}{2}\sigma_{I_{max}}\delta_{I_{max}} \tag{4-6}$$

For mode II

$$G_{IIc} = \frac{1}{2}\sigma_{II_{max}}\delta_{II_{max}} \tag{4-7}$$

From equations (4-6) and (4-7), the values of the maximum allowable displacements can be found

$$\delta_{I_{max}} = \frac{2 \cdot G_{I_c}}{\sigma_{I_{max}}} \qquad \text{and} \qquad \delta_{II_{max}} = \frac{2 \cdot G_{II_c}}{\sigma_{II_{max}}} \tag{4-8}$$

The values calculated in this section fully define the curves in Figure 4-3.

4.2.2.3 Linear Coupling Damage Model

In real structures, fracture energy absorption does not take place fully in one mode and the stress displacement curves are not the ones described in the previous section. This is due to the fact that there are normally both normal and shear displacements of the interface. The coupling between mode I and mode II fracture energy absorption depends on the material and can be measured via mixed-mode bending tests.

For the purpose of describing coupled delamination behaviour, it shall be assumed that the coupling between modes I and II fracture energies is linear for both the onset of damage (curve **(1)**) and failure (curve **(2)**). Indeed, Reeder [46] reports that for many materials, a linear coupling model can be used to simulate the mixed-mode failure process, even if experimental studies show that such an assumption may be too conservative [6] [47].

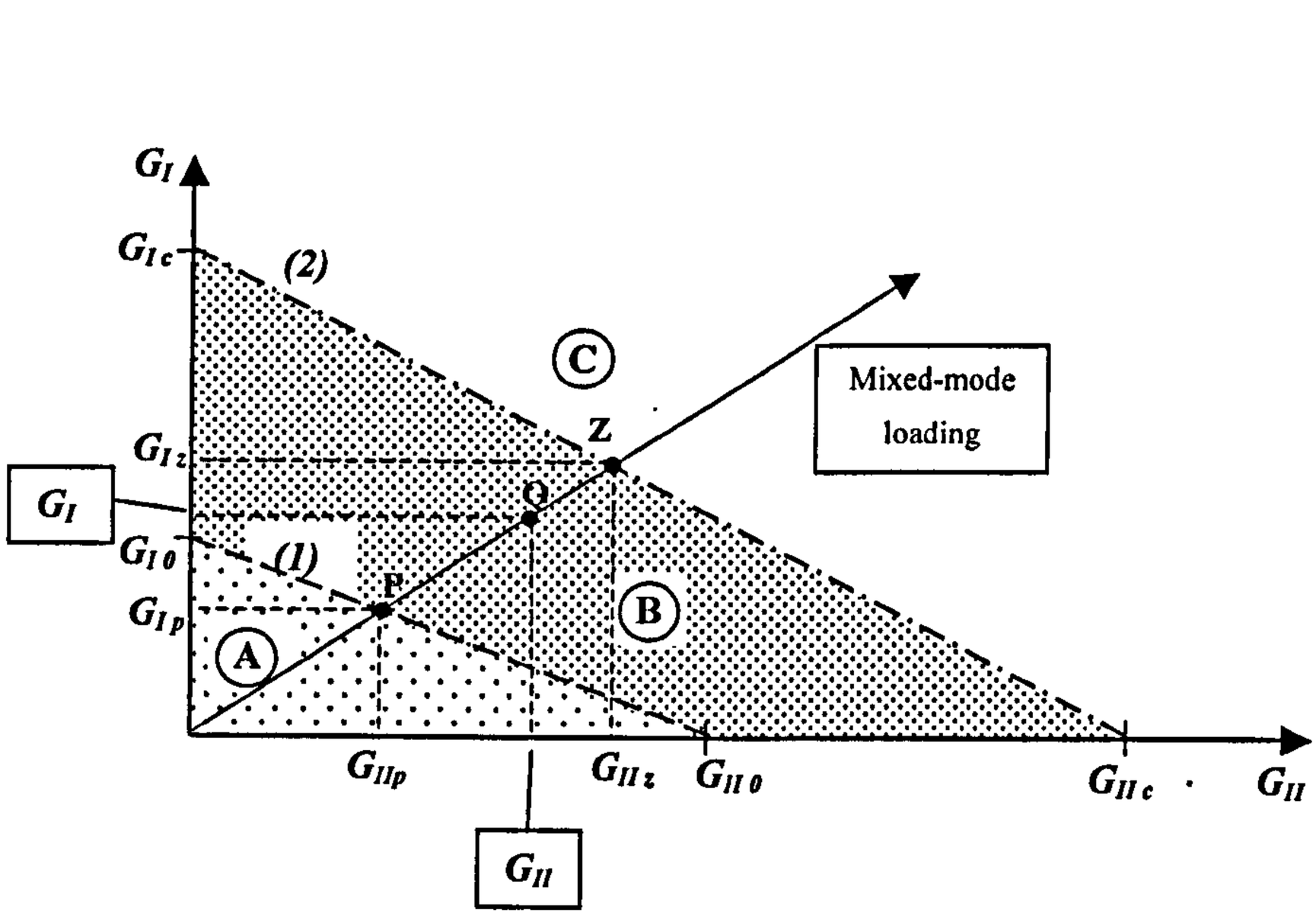

Figure 4-4 – Interlaminar Failure Regions

Figure 4-4 shows 3 regions into which the delamination process can be divided. These are:

- Region **A** – undamaged interface
- Region **B** – damaging interface
- Region **C** – Failed (fully damaged) interface.

The governing equations for curves **(1)** and **(2)** shown in Figure 4-4 are:

$$\frac{G_I}{G_{I_0}} + \frac{G_{II}}{G_{II_0}} = 1 \tag{4-9}$$

$$\frac{G_I}{G_{I_C}} + \frac{G_{II}}{G_{II_C}} = 1 \tag{4-10}$$

4.2.3 Delamination Algorithm

The following sections describe the basic steps of the delamination algorithm.

4.2.3.1 Reading Slave Node Displacements

Consider a typical mixed-mode loading path, as shown in Figure 4-4. For a certain time t in the analysis, the slave node has been displaced from its original/ideal position (Figure 4-2) and displacements δ_I and δ_{II} are read. Point **Q** represents the mixed-mode fracture energy absorbed due to those displacements at that instant in the analysis.

4.2.3.2 Onset of Damage

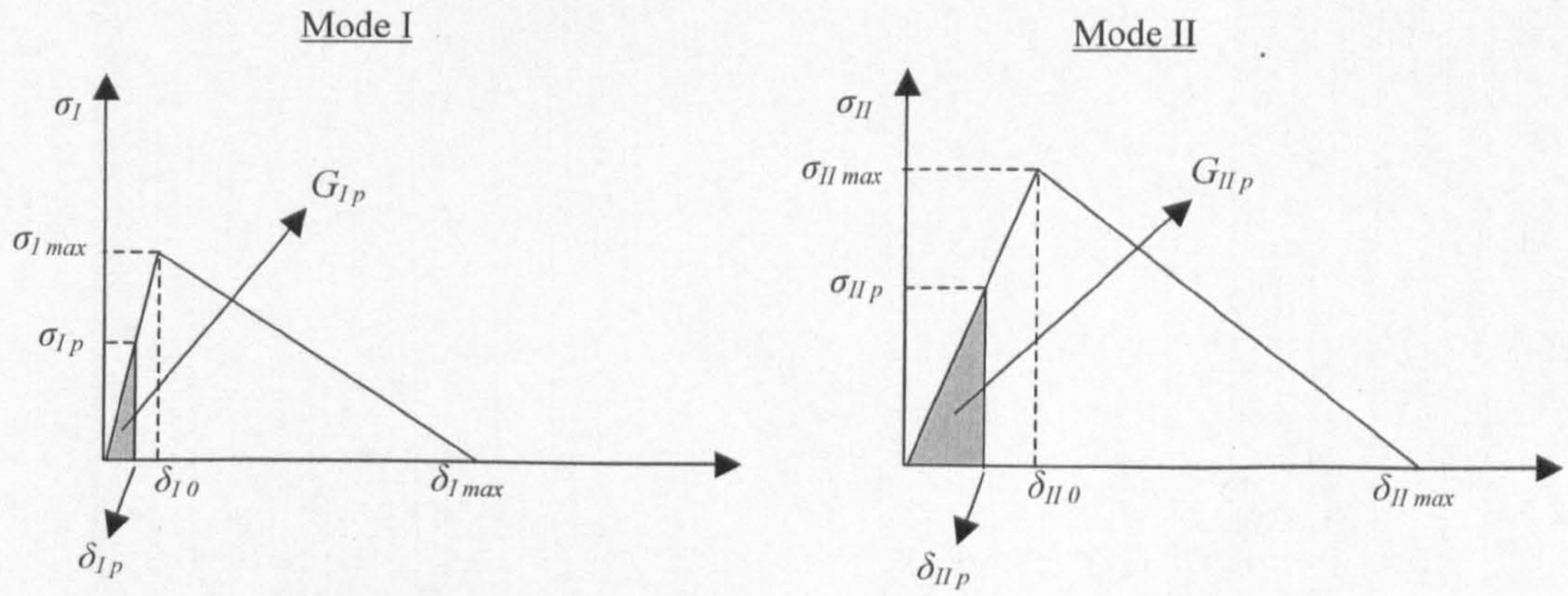

Figure 4-5 - Energy absorption at damage threshold

Figure 4-5 shows the energies absorbed up to point **P**, which represents the onset of damage. Those elastic energies absorbed are given by

$$G_{I_P} = \frac{1}{2}\sigma_{I_P}\delta_{I_P} \qquad \text{and} \qquad G_{II_P} = \frac{1}{2}\sigma_{II_P}\delta_{II_P} \tag{4-11}$$

Since we are still in the linear elastic domain

$$\sigma_{I_P} = \frac{E_0}{L_0}\delta_{I_P} \qquad \text{and} \qquad \sigma_{II_P} = \frac{G_0}{L_0}\delta_{II_P} \tag{4-12}$$

Thus yielding

$$G_{I_P} = \frac{1}{2}\frac{E_0}{L_0}\delta_{I_P}^{\,2} \qquad \text{and} \qquad G_{II_P} = \frac{1}{2}\frac{G_0}{L_0}\delta_{II_P}^{\,2} \tag{4-13}$$

Similarly, the elastic energy absorption in pure modes I and II delamination are:

$$G_{I_0} = \frac{1}{2}\frac{E_0}{L_0}\delta_{I_A}^{\,2} \qquad \text{and} \qquad G_{II_0} = \frac{1}{2}\frac{G_0}{L_0}\delta_{II_A}^{\,2} \tag{4-14}$$

The linear coupling between modes of fracture means that, at point **P**, equation (4-9) is used

$$\frac{G_{I_P}}{G_{I_0}} + \frac{G_{II_P}}{G_{II_0}} = 1$$

Simplifying using equations (4-13) and (4-14)

$$\left(\frac{\delta_{I_P}}{\delta_{I_0}}\right)^2 + \left(\frac{\delta_{II_P}}{\delta_{II_0}}\right)^2 = 1 \tag{4-15}$$

More generally, at any instant in the analysis

$$\left(\frac{\delta_I}{\delta_{I_0}}\right)^2 + \left(\frac{\delta_{II}}{\delta_{II_0}}\right)^2 = A \tag{4-16}$$

Where the value of A is checked at each time step

$$\begin{cases} A > 1 & \text{damage} \\ A \le 1 & \text{no damage} \end{cases} \tag{4-17}$$

Equations (4-16) and (4-17) define the condition for the onset of damage at any instant in the analysis.

4.2.3.3 Progressive Damage of the Interface

Once the onset of damage is reached, the energy absorption up to point Q is calculated as described below.

Stress Calculation

The first step is to calculate point **P**, i.e. the values of $G_{I\,p}$ and $G_{II\,p}$. For use in the following calculations, the ratio between normal and shear displacements is here defined as:

$$R = \left(\frac{\delta_I}{\delta_{II}}\right)^2 \tag{4-18}$$

This ratio applies to any pair of normal and shear displacements throughout the analysis, i.e. for point **P**

$$R = \left(\frac{\delta_{I_P}}{\delta_{II_P}}\right)^2 \tag{4-19}$$

Rearranging

$$\delta_{I_P}{}^2 = R \cdot \delta_{II_P}{}^2 \tag{4-20}$$

Substituting into equation (4-15)

$$R \cdot \left(\frac{\delta_{II_P}}{\delta_{I_0}}\right)^2 + \left(\frac{\delta_{II_P}}{\delta_{II_0}}\right)^2 = 1 \tag{4-21}$$

$$\delta_{II_P} \cdot \left(\frac{R}{\delta_{I_0}}\right)^2 + \left(\frac{1}{\delta_{II_0}}\right)^2 = 1 \tag{4-22}$$

$$\delta_{II_P} = \left(\frac{1}{\frac{R}{\delta_{I_0}^{\,2}} + \frac{1}{\delta_{II_0}^{\,2}}} \right)^{\frac{1}{4}} \tag{4-23}$$

Taking equation (4-20)

$$\delta_{I_P} = \sqrt{R \cdot \delta_{II_P}^{\,2}} \tag{4-24}$$

Once the displacements at point **P** are known - equations (4-23) and (4-24) – the respective stresses are calculated using equations (4-12), i.e.

$$\sigma_{I_P} = \frac{E_0}{L_0}\delta_{I_P} \qquad \text{and} \qquad \sigma_{II_P} = \frac{G_0}{L_0}\delta_{II_P}$$

Knowing the stresses and displacements at point **P** the energies can be calculated using equation (4-13)

$$G_{I_P} = \frac{1}{2}\frac{E_0}{L_0}\delta_{I_P}^{\,2} \qquad \text{and} \qquad G_{II_P} = \frac{1}{2}\frac{G_0}{L_0}\delta_{II_P}^{\,2}$$

The next calculation in the analysis is point **Z**, Figure 4-4. This point defines the energy absorbed at failure if the current displacement ration R was to be kept constant for the remaining of the analysis. Once the values of energies $G_{I\,p}$ and $G_{II\,p}$ are known, it is then possible to calculate the current stresses for each mode, σ_I and σ_{II}, Figure 4-6.

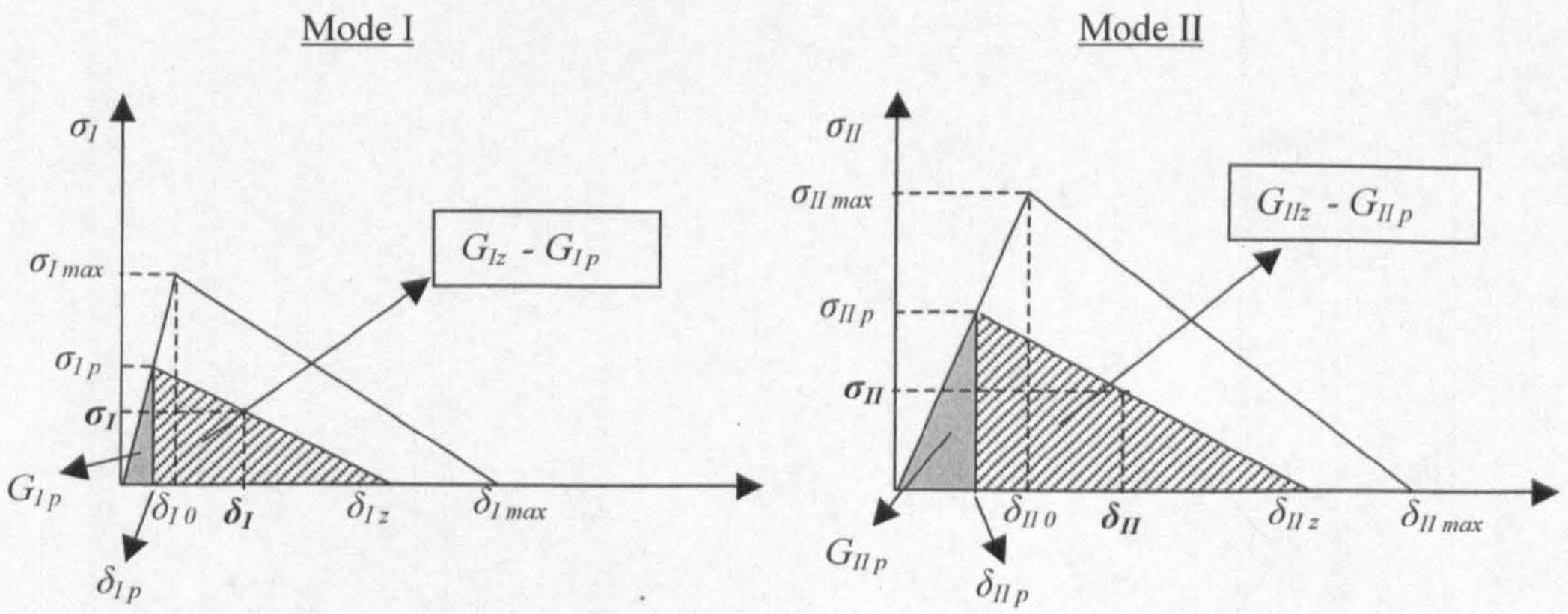

Figure 4-6 - Energy absorbed to Point **Z**

Applying Equation (4-10) to point **Z**

$$\frac{G_{I_z}}{G_{I_c}} + \frac{G_{II_z}}{G_{II_c}} = 1 \tag{4-25}$$

From Figure 4-5

$$\frac{G_{I_z}}{G_{II_z}} = \frac{G_{I_P}}{G_{II_P}}$$

Also, from Equation (4-13)

$$\frac{G_{I_P}}{G_{II_P}} = \frac{E_0}{G_0}\frac{\delta_{I_P}^{\ 2}}{\delta_{II_P}^{\ 2}} = \frac{E_0}{G_0} \cdot R$$

This yields

$$G_{I_z} = \frac{E_0}{G_0} \cdot R \cdot G_{II_z} \tag{4-26}$$

Substituting into Equation (4-25)

$$\frac{E_0}{G_0} \cdot R \cdot \frac{G_{II_z}}{G_{I_c}} + \frac{G_{II_z}}{G_{II_c}} = 1$$

$$G_{II_z} = \frac{1}{\frac{E_0}{G_0} \cdot \frac{R}{G_{I_c}} + \frac{1}{G_{II_c}}} \tag{4-27}$$

Equations (4-26) and (4-27) give the energy absorbed up to point Z. To calculate the respective displacements, we use the following relations (from Figure 4-6)

$$G_{I_z} = \frac{1}{2}\sigma_{I_P}\delta_{I_z} \tag{4-28}$$

$$G_{II_z} = \frac{1}{2}\sigma_{II_P}\delta_{II_z} \tag{4-29}$$

Displacements at point **Z** are then given by

$$\delta_{I_z} = \frac{2G_{I_z}}{\sigma_{I_P}} \tag{4-30}$$

$$\delta_{II_z} = \frac{2G_{II_z}}{\sigma_{II_P}} \tag{4-31}$$

It is now possible to calculate the stresses at the current time-step. They are given by

$$\sigma_I = \sigma_{I_P}\left(\frac{\delta_{I_z} - \delta_I}{\delta_{I_z} - \delta_{I_P}}\right) \tag{4-32}$$

$$\sigma_{II} = \sigma_{II_P}\left(\frac{\delta_{II_z} - \delta_{II}}{\delta_{II_z} - \delta_{II_P}}\right) \tag{4-33}$$

Damage Calculation

To calculate the damage values, we use the concept of an elastic damage law, shown in Figure 4-7 and Equation (4-34)

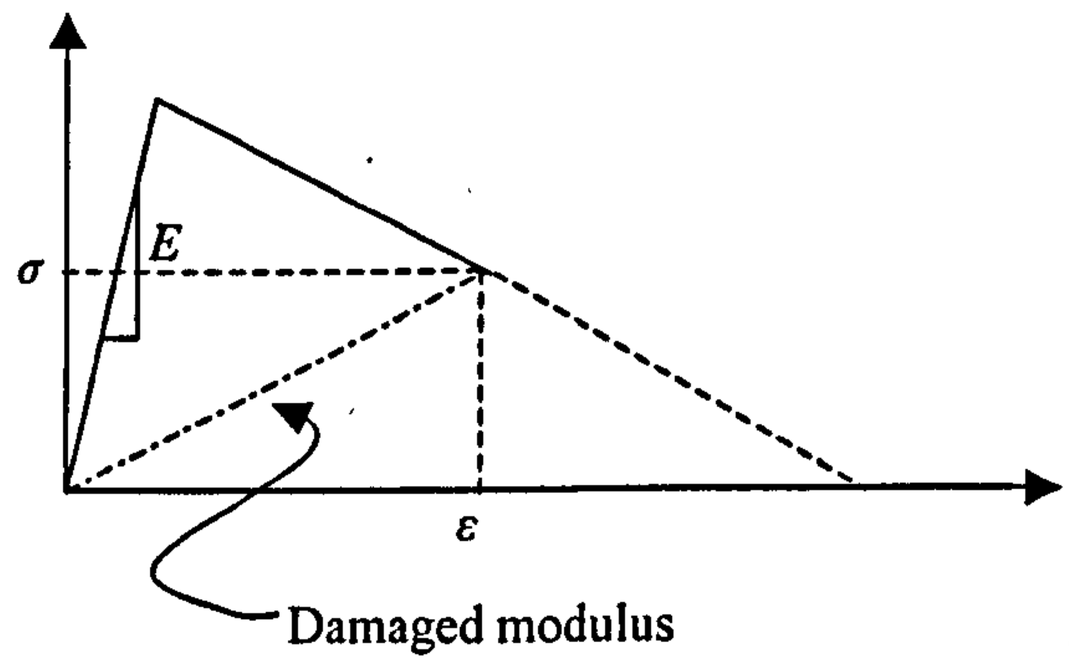

Figure 4-7 - Elastic Damage Modulus

$$\sigma = (1-d)\cdot E\cdot \varepsilon \tag{4-34}$$

Where d is the damage value and E is the elastic modulus.

Applying this concept to the stresses calculated in Equations (4-32) and (4-33), the damage incurred by the contact interface can be computed in the following way:

$$\sigma_I = (1 - d_I)\frac{E_0}{L_0}\delta_I$$

$$1 - d_I = \frac{\sigma_I L_0}{E_0 \delta_I}$$

$$d_I = 1 - \frac{\sigma_I L_0}{E_0 \delta_I} \tag{4-35}$$

$$d_{II} = 1 - \frac{\sigma_{II} L_0}{G_0 \delta_{II}} \tag{4-36}$$

4.2.3.4 Update Damage Onset

Once there is damage applied to the interface, the line defining the onset of damage is shifted as shown in Figure 4-8.

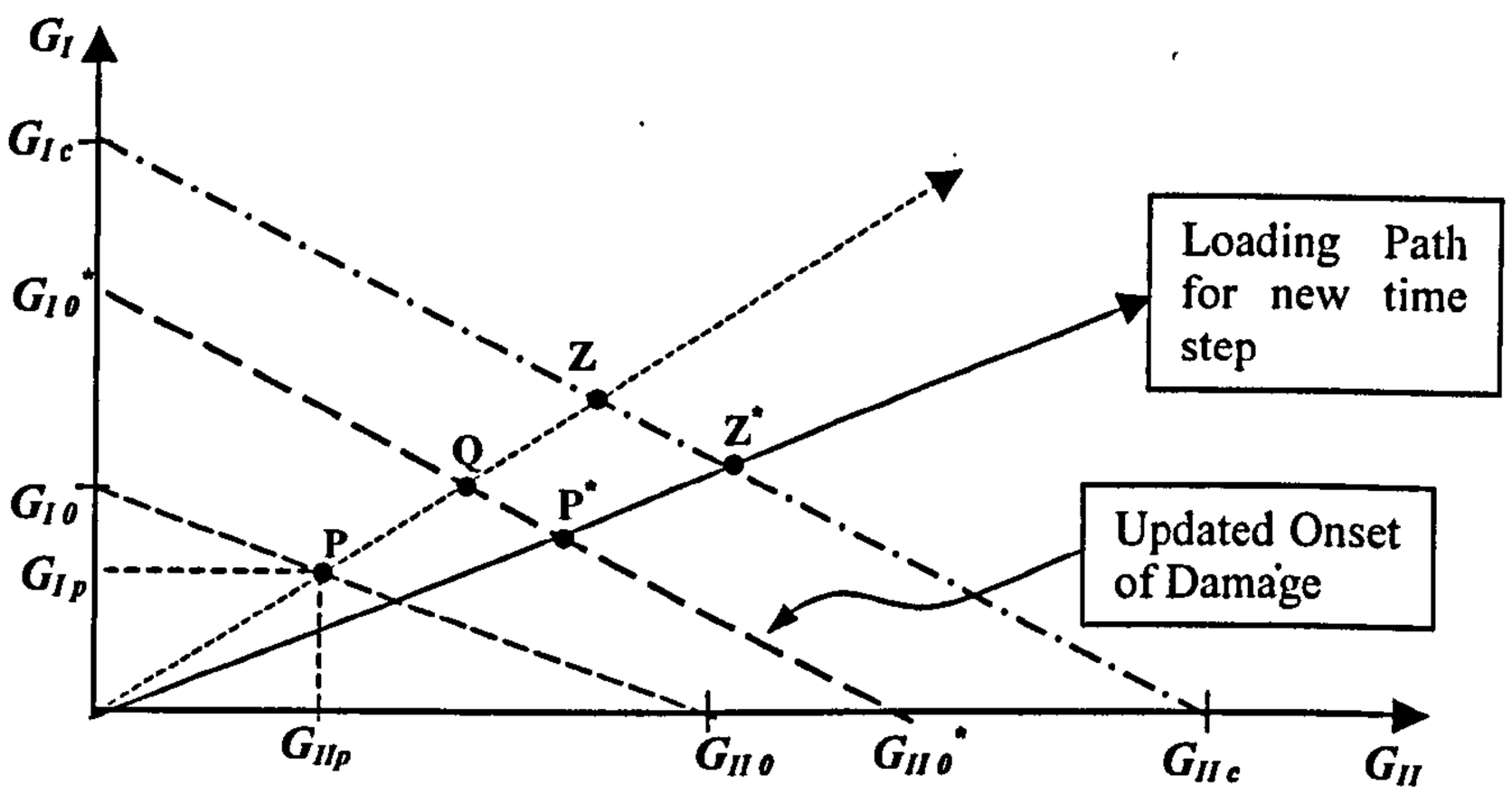

Figure 4-8 – Updated Onset of Damage and Mixed-Mode Loading Path for New Time Step

The values of G_{I0}^* and G_{II0}^* are the areas under the elastic portion of the damaged modulus, shown in Figure 4-9.Their values are given by Equations (4-37) and (4-38)

$$G_{I_0}^* = \frac{1}{2}(1 - d_I)\frac{E_0}{L_0}\delta_{I_0} \tag{4-37}$$

$$G_{II_0}^* = \frac{1}{2}(1 - d_{II})\frac{G_0}{L_0}\delta_{II_0} \tag{4-38}$$

After the update of these values, the analysis continues in another time step, for which the loading path may be the one shown in Figure 4-8. The process is then the same as described in the previous sections, with a new onset of damage $\mathbf{P}^*$ and failure $\mathbf{Z}^*$ being defined.

This process is repeated until the interface is fully damaged, i.e. $d_I = d_{II} = 1$, or in case of unloading, which is described in the section below.

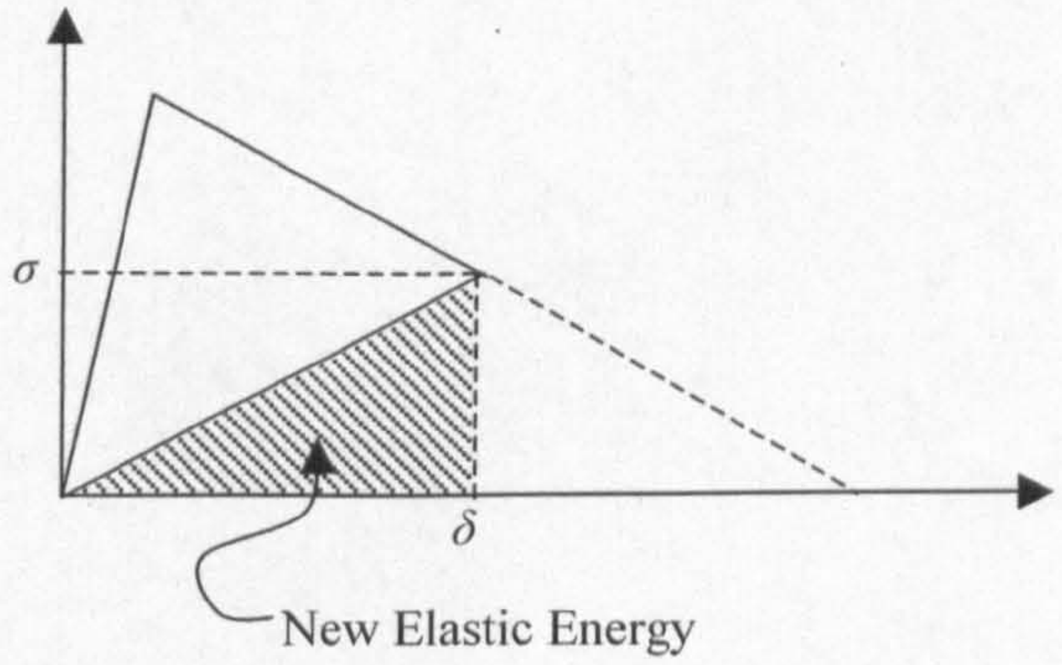

Figure 4-9 - Updated Elastic Energy

4.2.3.5 Unloading/Reloading Behaviour

If, at any instant in the analysis, the displacements are smaller than in the previous time step, then this is an unloading situation, where no energy is absorbed. This means that there is no shifting in the damage onset and that the stresses are given by Equations (4-37) and (4-38), with the damage value being the same as that of the previous time step. The stress-strain behaviour for unloading and reloading can be better described by observing Figure 4-10

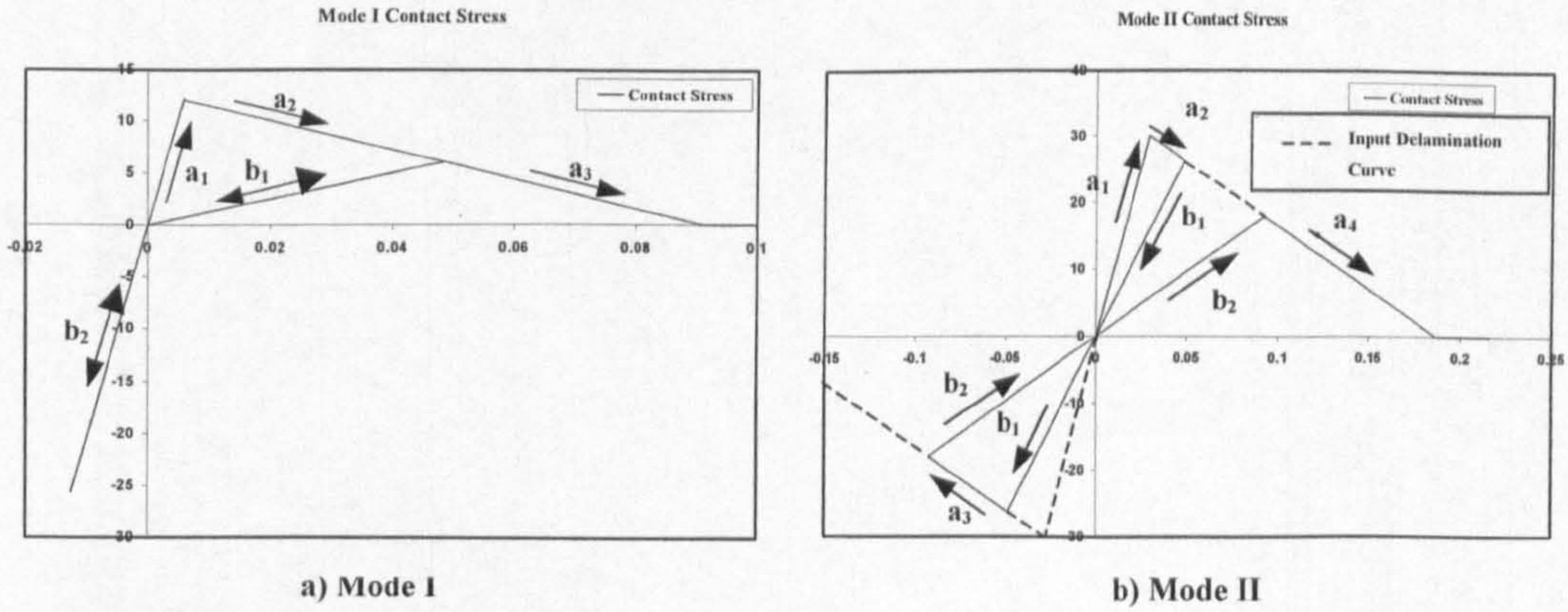

a) Mode I **b) Mode II**

Figure 4-10 – Unloading/Reloading Behaviour of Delamination Model. **a)** Mode I, **b)** Mode II.

Figure 4-10a) shows mode I loading of a simple single element test case. Path (a_1) shows the case of tensile loading. Damage initiates when σ_{Imax} (maximum stress for mode I) is reached – path (a_2). Path (b_1) represents the case of unloading in the partially damaged zone. Note that if unloading causes the gap to fully close (start of compressive behaviour) then the original undamaged modulus is used – path (b_2). Reloading follows paths (b_1) and (b_2) until the point where unloading started, after which path (a_3) is followed until failure occurs.

For mode II loading, the paths are similar except that damage is active for symmetric directions of loading, as shown in Figure 4-10b). Note further shear loading on path (a_3) causes accumulated mode II delamination damage. Reloading, on path (b_2), occurs with the accumulated damage modulus, until the original delamination curve is reached.

A graphical representation of the delamination algorithm is given in Figure 4-11.

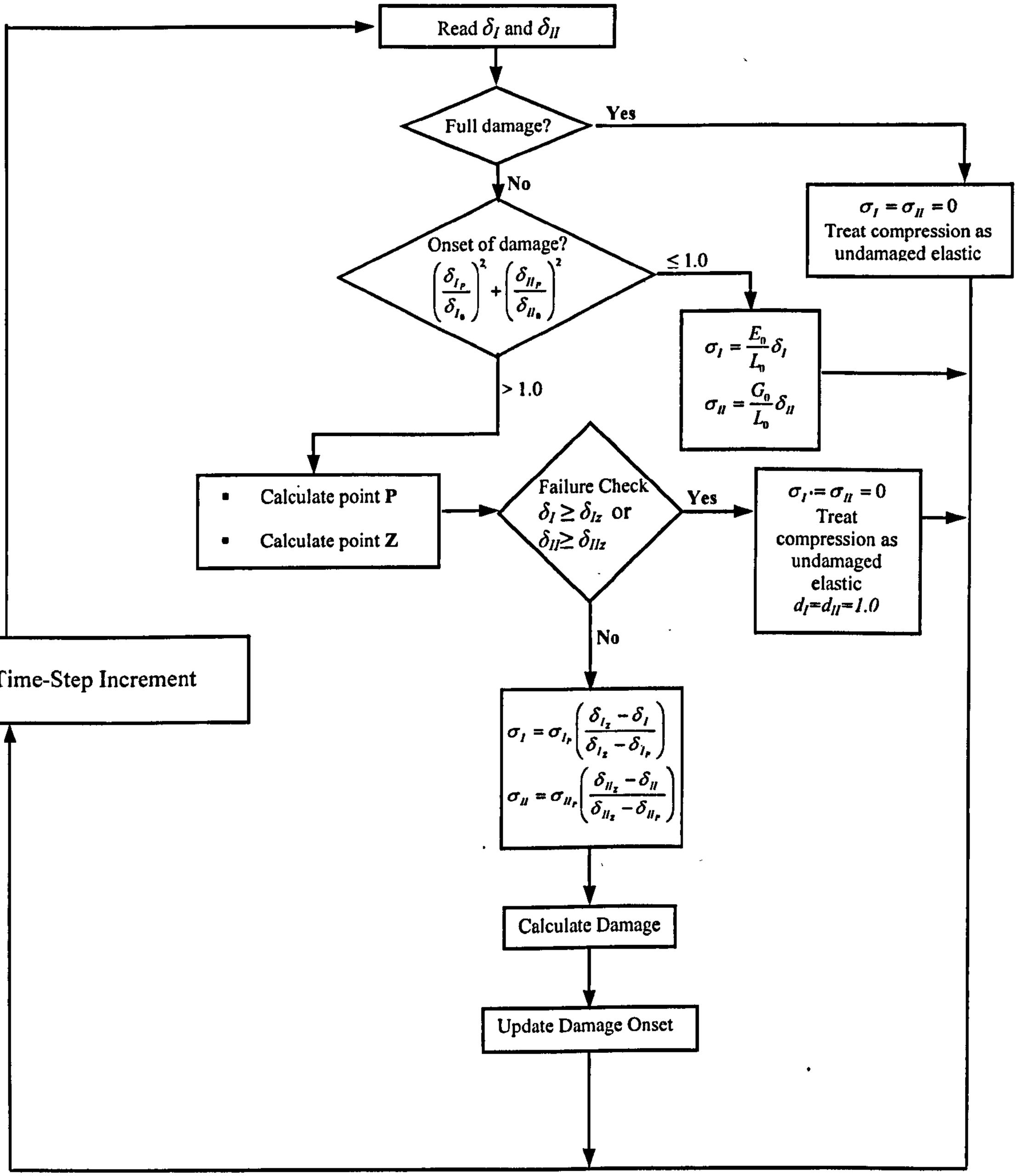

Figure 4-11 - Delamination Algorithm

5.0 Material Calibration

The procedure to build-up the PAM-CRASH material cards for both intralaminar and interlaminar data is described in this section. This process consists of achieving the best fit between the PAM-CRASH material model's curves and the coupon test results described in Chapter 3.

To compare the curves and produce the best fit in an automatic and time-effective manner, a Microsoft® Excel macro was programmed. The macro was initially programmed by Curtis [9] and was further developed by the author to include interlaminar behaviour described in Chapter 4.

The following description is based on CoFRM glass/polyester. Procedure for all three braided carbon architectures is the same.

5.1.1 Step One – Elastic Moduli and Poisson's Ratios

The locations of Elastic Moduli and Poisson's ratio values on the macro table are shown in Figure 5-1. There are two sets of values to input, for both tensile and compressive properties.

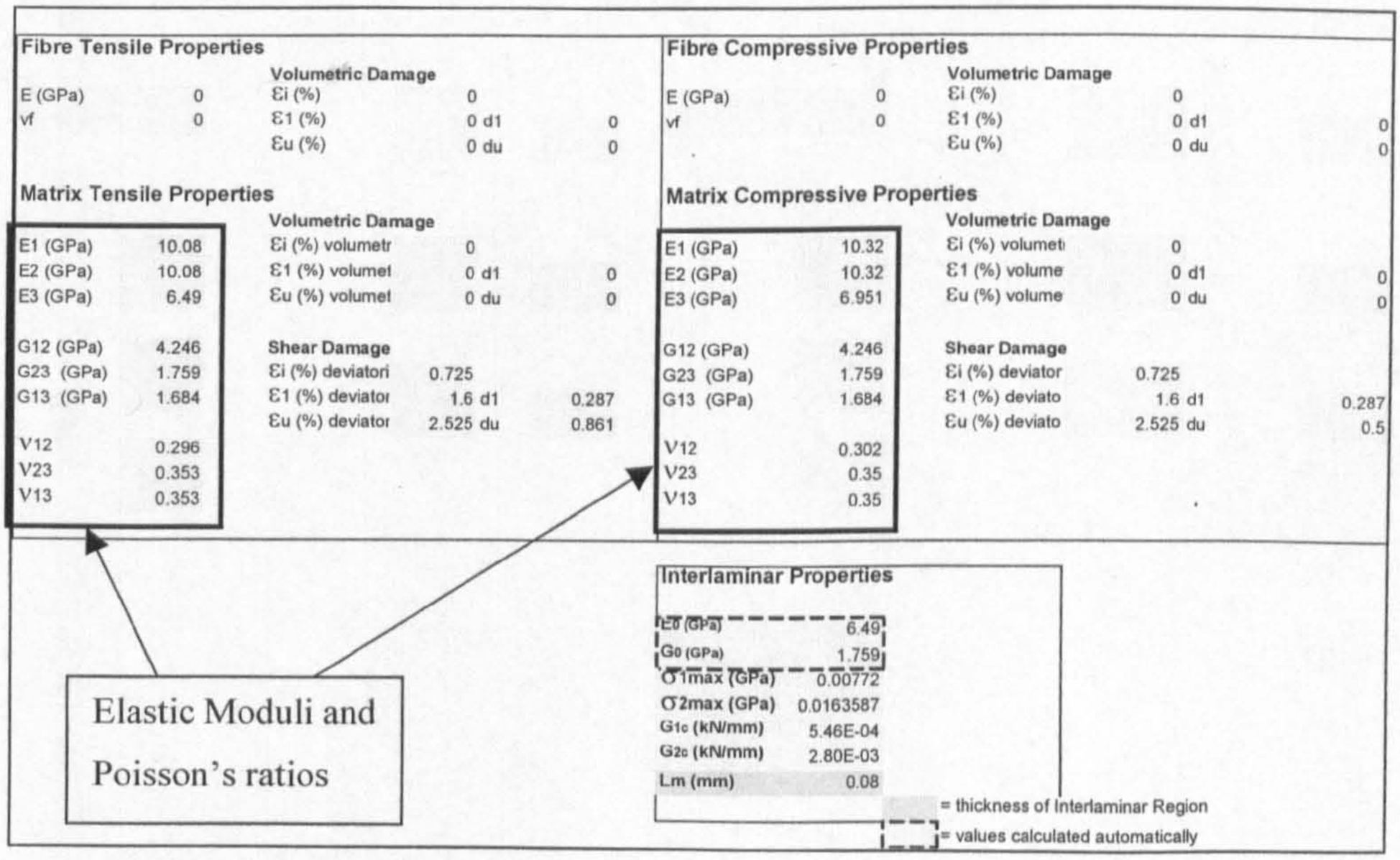

Figure 5-1 - Macro input showing location of Elastic Moduli and Poisson's ratios

The values of the tensile properties and which tests they were obtained from are shown in Figure 5-2.

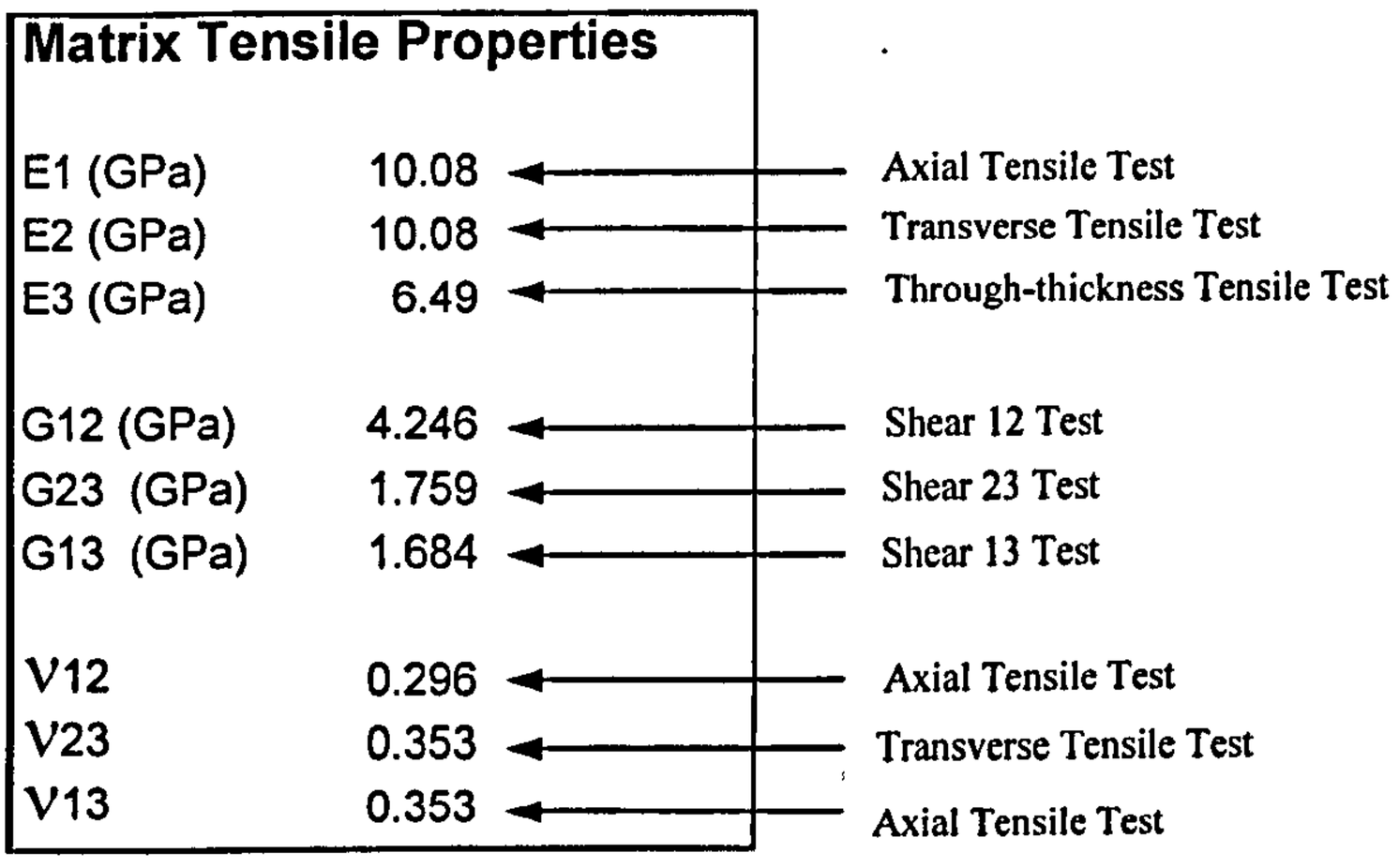

Figure 5-2 – Tensile values of CoFRM and coupon tests used to obtain them

Similarly, compressive properties and respective coupon tests are shown in Figure 5-3.

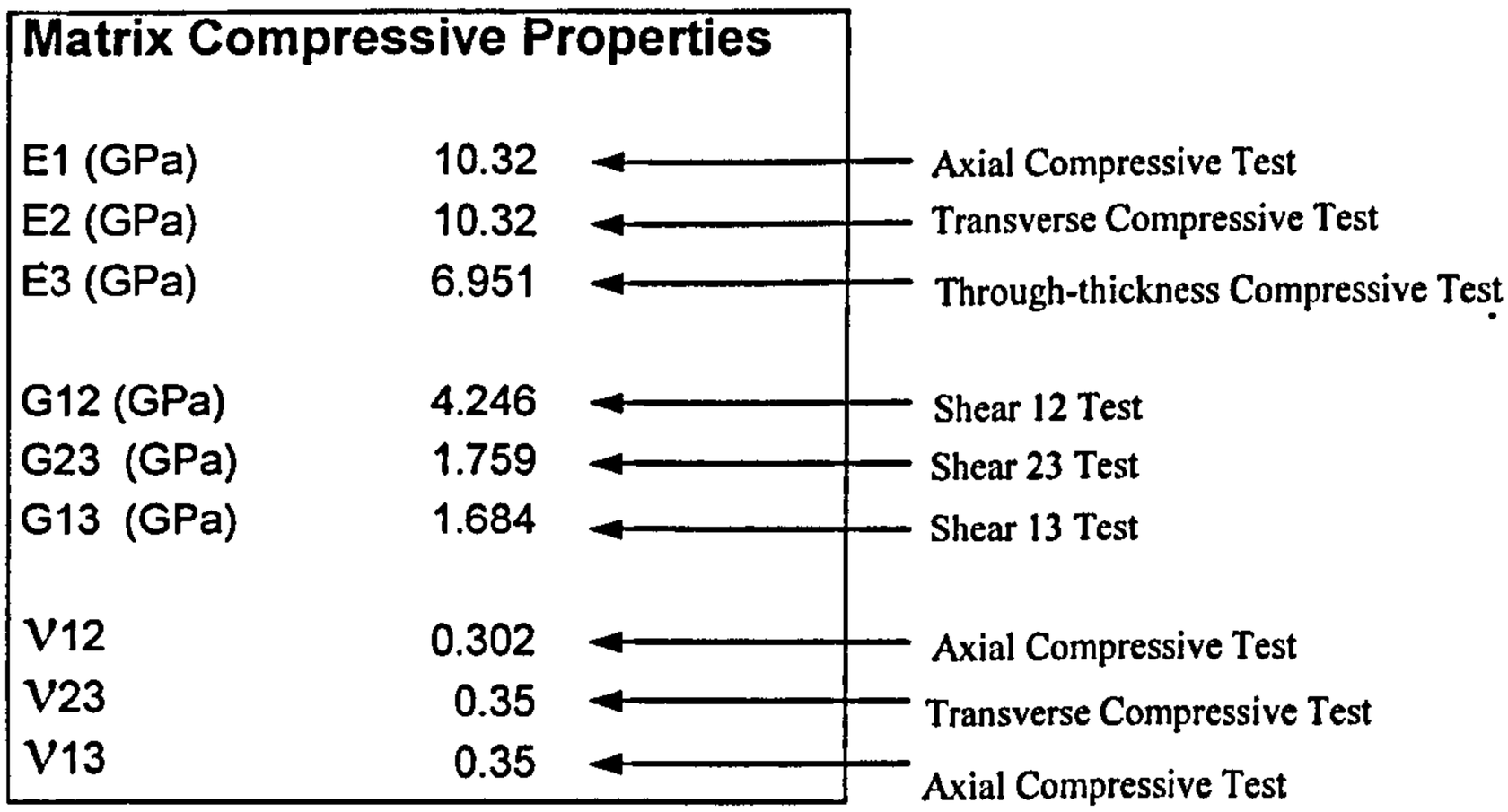

Figure 5-3 - Compressive values of CoFRM and coupon tests used to obtain them

There are no values of fibre properties to input in the Degenerate Bi-phase Material model, as the composite laminate is treated as a homogenous material, where the fibre properties are implicit in the matrix ones.

5.1.2 Step Two – Damage Parameters

The second step in obtaining the PAM-CRASH material card is to get the best possible fit between the stress-strain curves of the material model and the experimental coupon tests, using the material damage laws described in Section 4.1.3.

Since the whole composite laminate is treated as an orthotropic homogeneous matrix, there is only one independent damage criterion to represent failure of the ply in all the principal directions. This existence of an isotropic failure and damage criterion makes the calibration process subject to the engineering judgement of the analyst.

It can be observed in the coupon experimental data that for CoFRM the highest strain energy values absorbed during in-plane coupon tests occur in the Shear 12 test[1]. That test is therefore chosen to start the calibration of the damage parameters. The procedure is shown below.

The first step is to identify the three significant changes in stiffness of the material. The strains at which these changes of slope of the stress-strain curve occur are the engineering shear damage strains, shown in Figure 5-4.

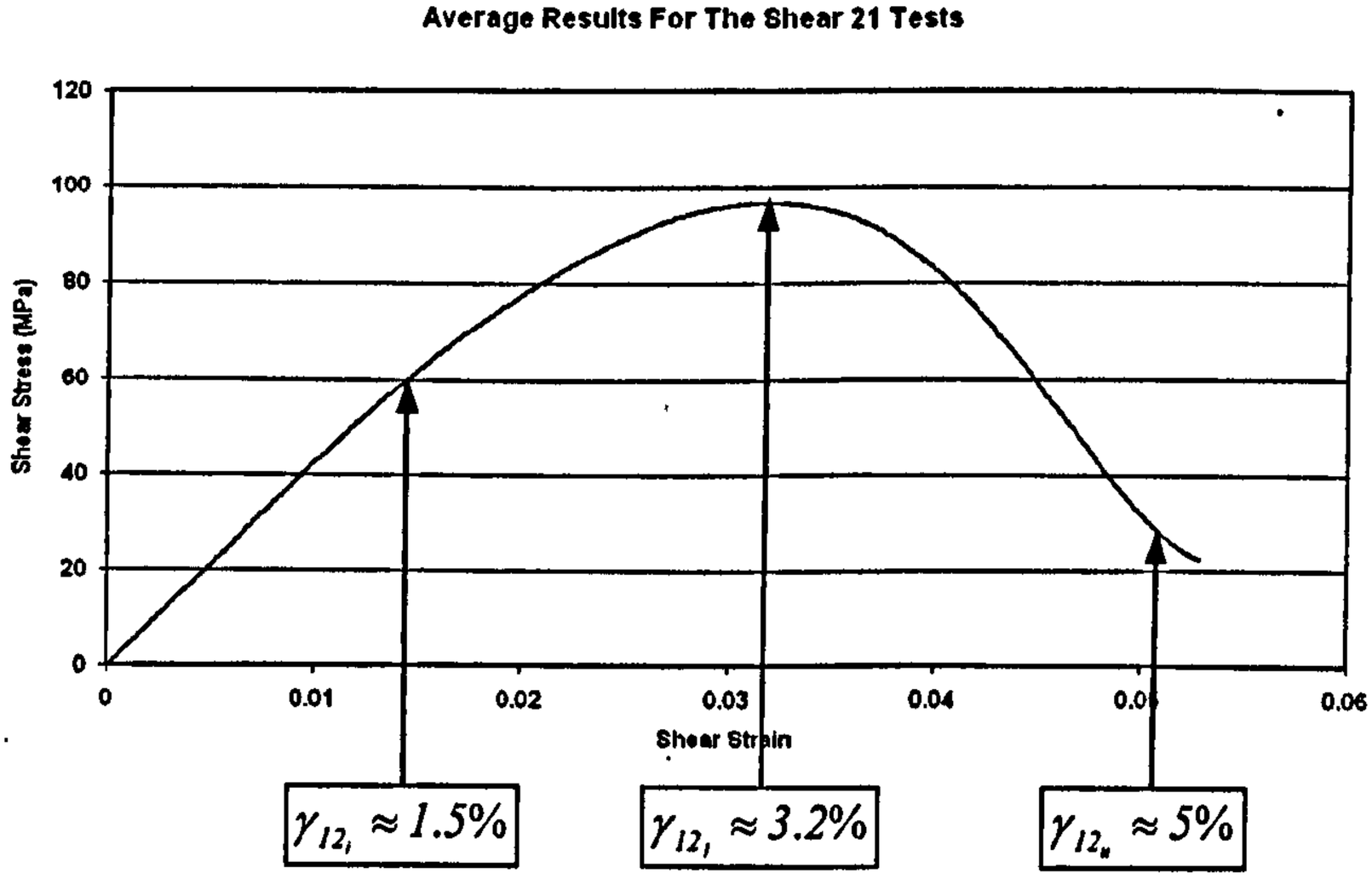

Figure 5-4 – Shear 12 Stress-strain plot showing engineering shear damage strains.

---

[1] It can be observed in the same data that strain values for the Shear 31 test are actually higher. However, this is an out-of-plane shear test and out-of-plane behaviour of the composite is dealt with through the delamination model.

The engineering shear strains above are related to the tensor shear strains (required by PAM-CRASH) by the equations in Section 4.1.4. The tensor shear strains are then defined as:

$$\varepsilon_{12_i} = \frac{\gamma_{12_i}}{2} \approx 0.75\%$$

$$\varepsilon_{12_I} = \frac{\gamma_{12_I}}{2} \approx 1.6\%$$

$$\varepsilon_{12_u} = \frac{\gamma_{12_u}}{2} \approx 2.5\%$$

The values above are then input in the macro table as shown below. For CoFRM, the same strain values are used for tension and compression but this may not be the case for all materials.

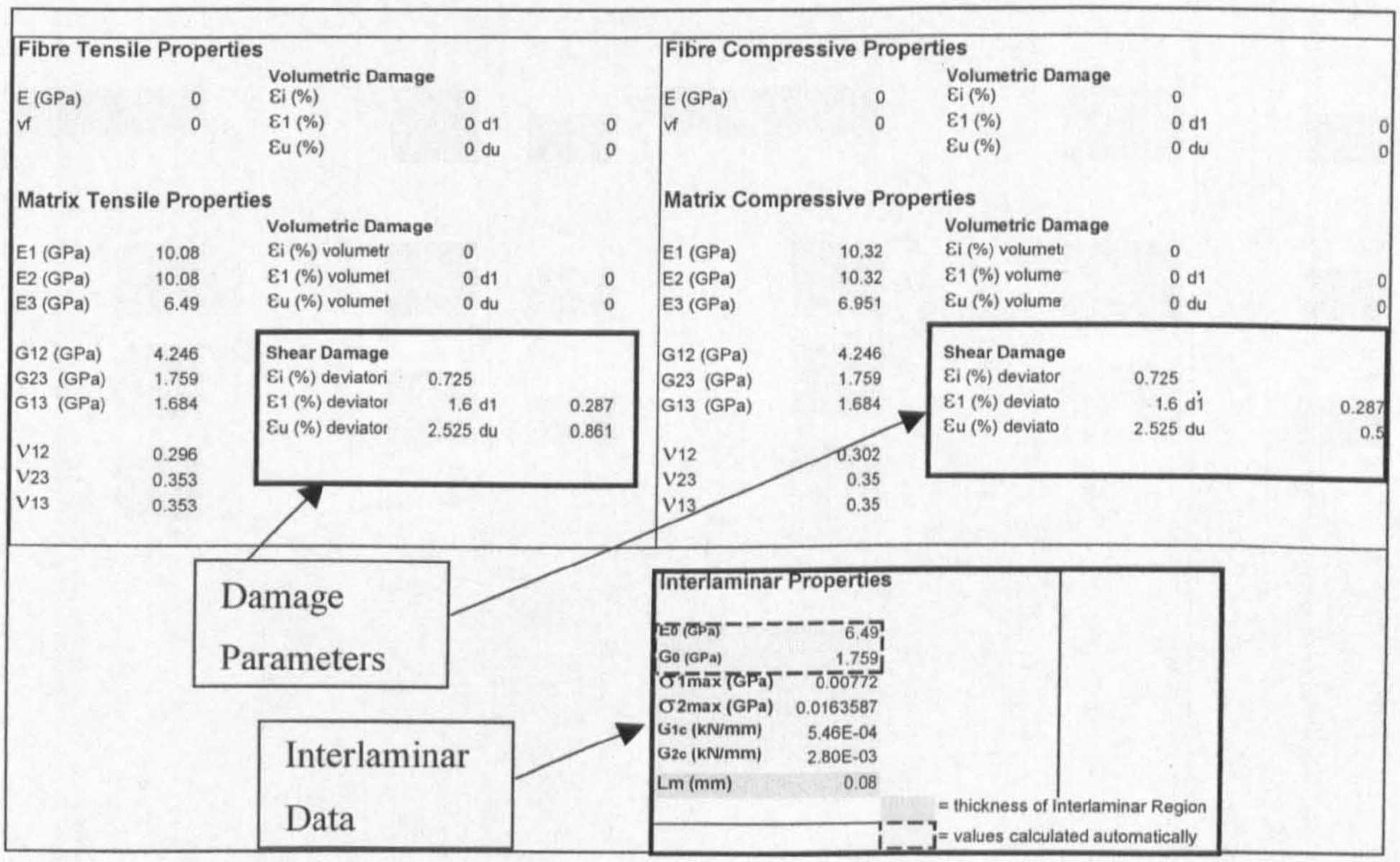

Figure 5-5 - Macro input showing location of Damage parameters and interlaminar data.

Parameters d_I and d_{II} are the damage values and range from 0.0 for an undamaged laminate to 1.0 for the fully damaged case. Their values are calibrated to get the best possible fit for the stress-strain curve. After calibration the agreement between experimental result and PAM-CRASH material law is shown below, for Shear 12.

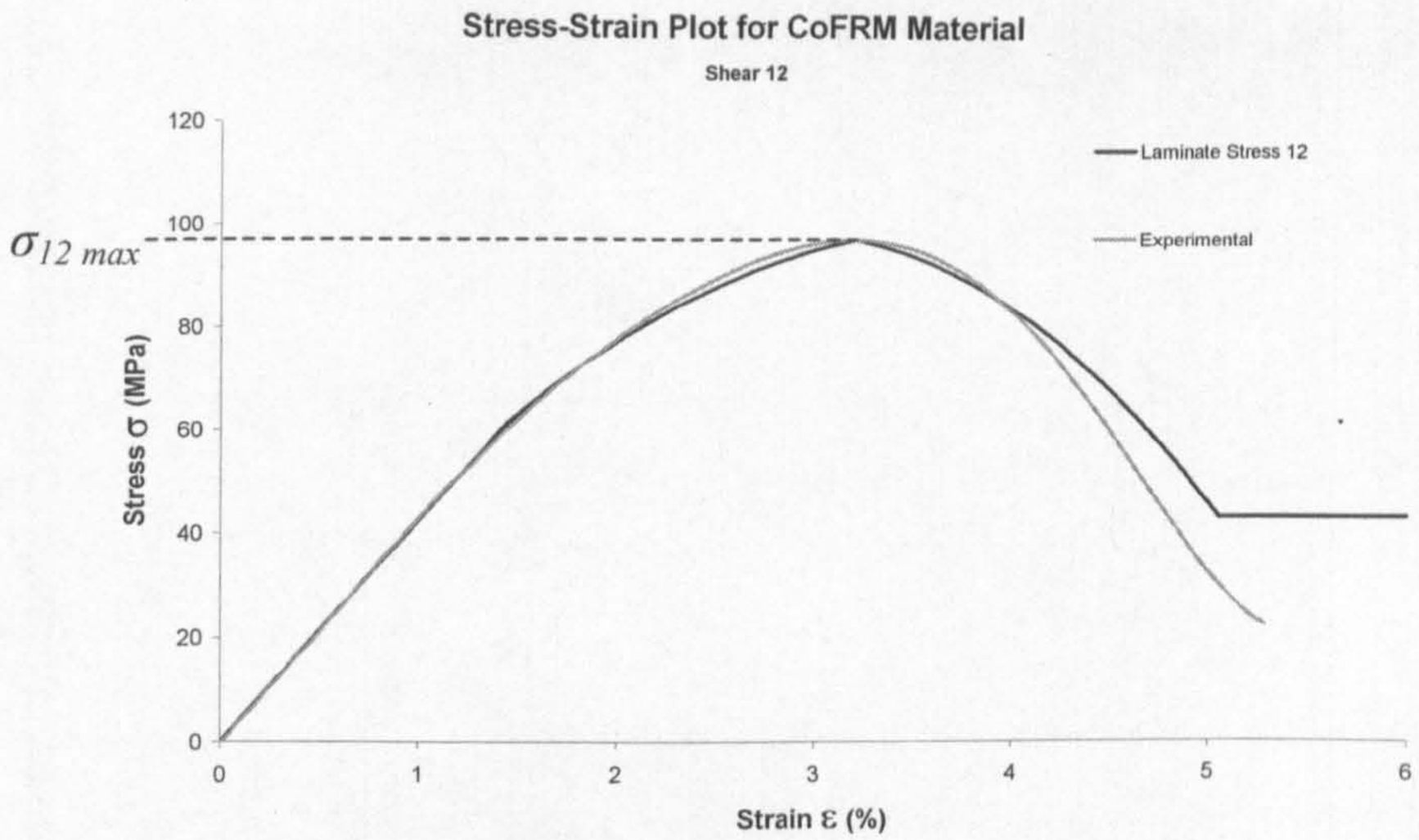

Figure 5-6 – Agreement between Shear 12 stress-strain curves – PAM-CRASH vs. experimental data

The residual strength shown after 5% strain is the result of imposing a maximum damage level lower than 1.0. This is done to avoid numerical instability. The values of damage parameters may be further calibrated to achieve the best possible agreement with all in-plane stress-strain curves.

In compression, in order to represent the incompressible nature of the failed and damaged material, the ultimate damage value is lower than in the tension case and is 0.5.

5.1.3 Step Three – Interlaminar data

As described previously in Section 5.1.2, the input values for the delamination model are related to through-thickness and interlaminar fracture toughness data. Figure 5-7 below shows in detail the interlaminar properties section of the macro table and the experimental tests used to obtain those values.

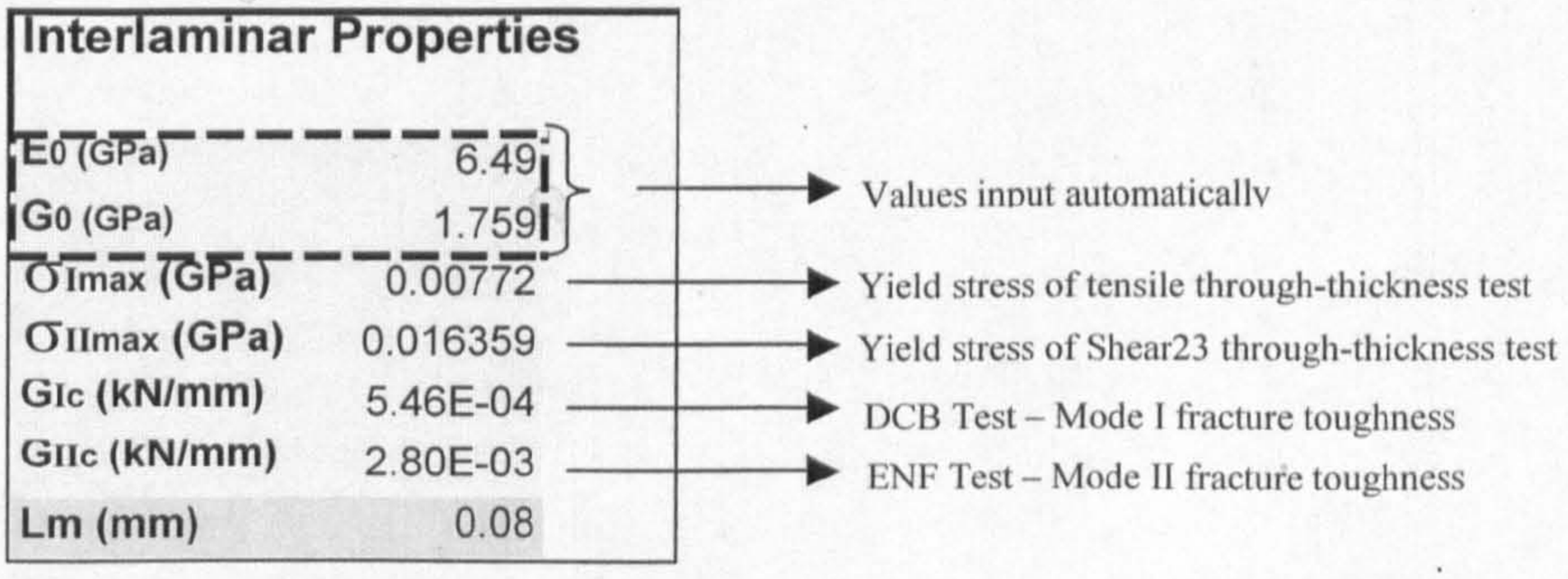

Figure 5-7 - Interlaminar values of CoFRM and details of how to obtain them

Values E_0 and G_0 are the through-thickness tensile and shear moduli, respectively i.e.

$E_0 = E_3$

$G_0 = G_{23}$

Parameter L_m is the thickness of the interlaminar layer. It was introduced in the delamination model for accuracy even though no measurements of such dimension were performed in the present work. A positive value must be chosen, as this is a requirement of the contact interface type #32. A value of 0.08mm was chosen for all tube models.

Once all the input parameters are defined, the Excel macro draws a comparison between the degenerate bi-phase stress-strain curves and results for each of the corresponding intralaminar coupon tests. The following sections include input parameters and respective comparisons between experimental results and plots obtained from the Excel macro for all the materials investigated.

5.2 Input Decks and Stress-Strain Behaviour

In the following sections, it can be observed that there is generally poor agreement in behaviour beyond failure, as a result of "smearing" properties. However, as stated previously, the crushing performance is not sensitive to damaged in-plane properties.

5.2.1 CoFRM

Fibre Tensile Properties				
		Volumetric Damage		
E (GPa)	0	Ei (%)	0	
vf	0	E1 (%)	0 d1	0
		Eu (%)	0 du	0
Matrix Tensile Properties				
		Volumetric Damage		
E1 (GPa)	10.08	Ei (%) volumetr	0	
E2 (GPa)	10.08	E1 (%) volume	0 d1	0
E3 (GPa)	6.49	Eu (%) volume	0 du	0
G12 (GPa)	4.246	Shear Damage		
G23 (GPa)	1.759	Ei (%) deviator	0.725	
G13 (GPa)	1.684	E1 (%) deviato	1.6 d1	0.287
		Eu (%) deviato	2.525 du	0.8
V12	0.296			
V23	0.353			
V13	0.353			

Fibre Compressive Properties				
		Volumetric Damage		
E (GPa)	0	Ei (%)	0	
vf	0	E1 (%)	0 d1	0
		Eu (%)	0 du	0
Matrix Compressive Properties				
		Volumetric Damage		
E1 (GPa)	10.32	Ei (%) volumet	0	
E2 (GPa)	10.32	E1 (%) volume	0 d1	0
E3 (GPa)	6.951	Eu (%) volume	0 du	0
G12 (GPa)	4.246	Shear Damage		
G23 (GPa)	1.759	Ei (%) deviator	0.725	
G13 (GPa)	1.684	E1 (%) deviato	1.6 d1	0.287
		Eu (%) deviato	2.525 du	0.5
V12	0.302			
V23	0.35			
V13	0.35			

Interlaminar Properties	
E0 (GPa)	6.49
G0 (GPa)	1.759
σ1max (GPa)	0.00772
σ2max (GPa)	0.016359
G1c (kN/mm)	5.46E-04
G2c (kN/mm)	2.80E-03
Lm (mm)	0.08

= thickness of Interlaminar Region

= values calculated automatically

Figure 5-8 - Input Parameters of CoFRM

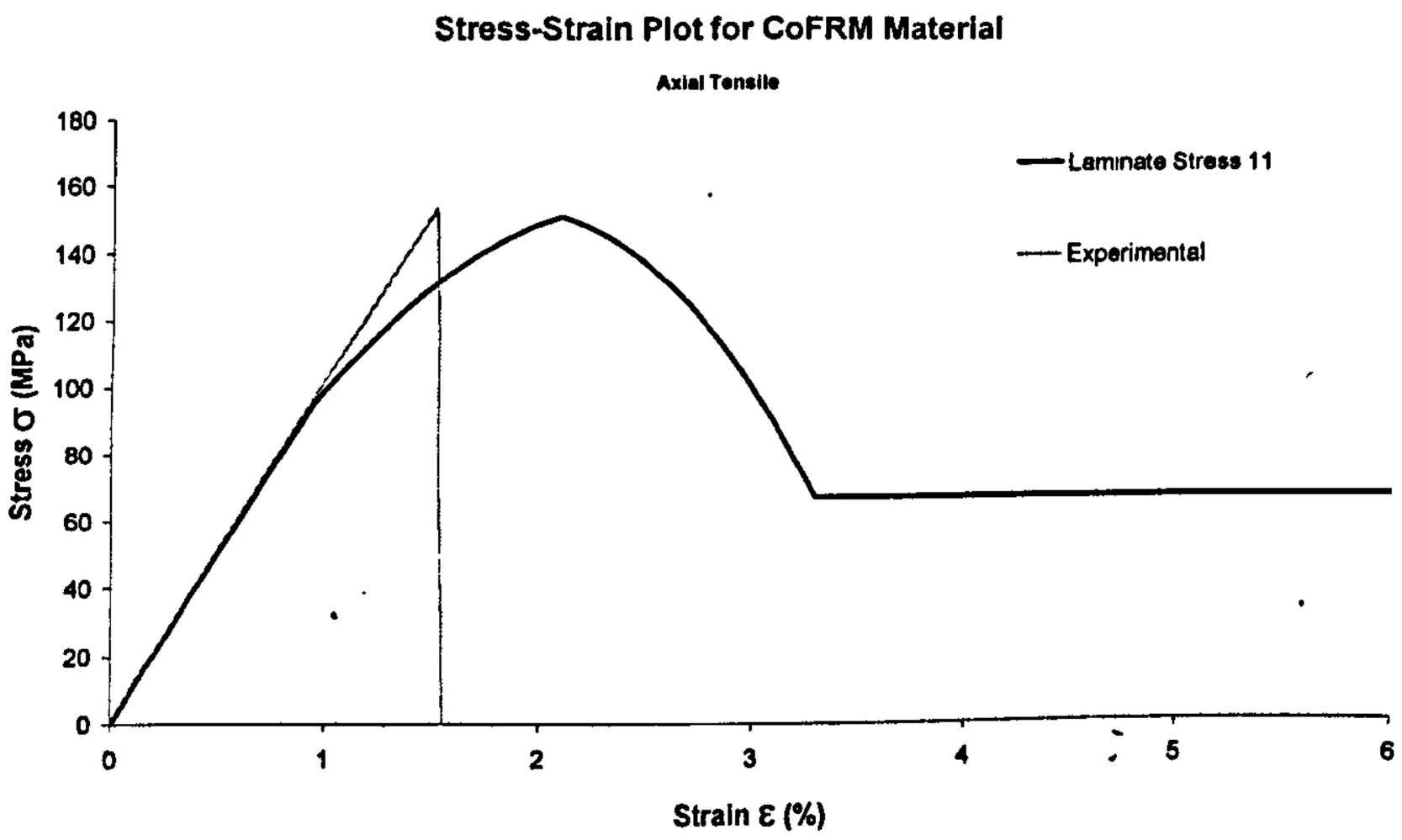
Stress-Strain Plot for CoFRM Material
Axial Tensile
Laminate Stress 11
Experimental
Stress σ (MPa)
Strain ε (%)
0
20
40
60
80
100
120
140
160
180
0
1
2
3
4
5
6

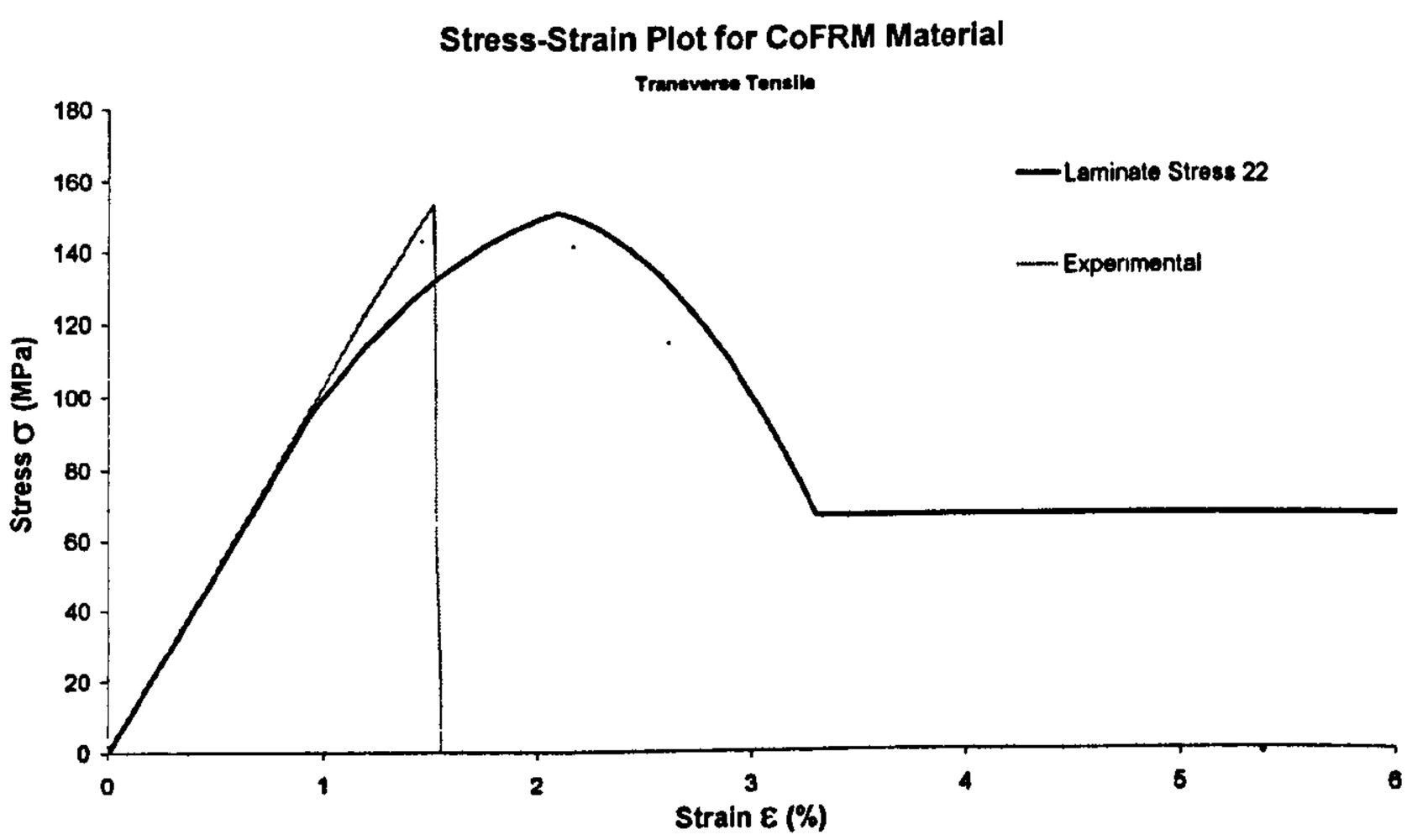
Stress-Strain Plot for CoFRM Material
Transverse Tensile
Laminate Stress 22
Experimental
Stress σ (MPa)
Strain ε (%)
0
20
40
60
80
100
120
140
160
180
0
1
2
3
4
5
6

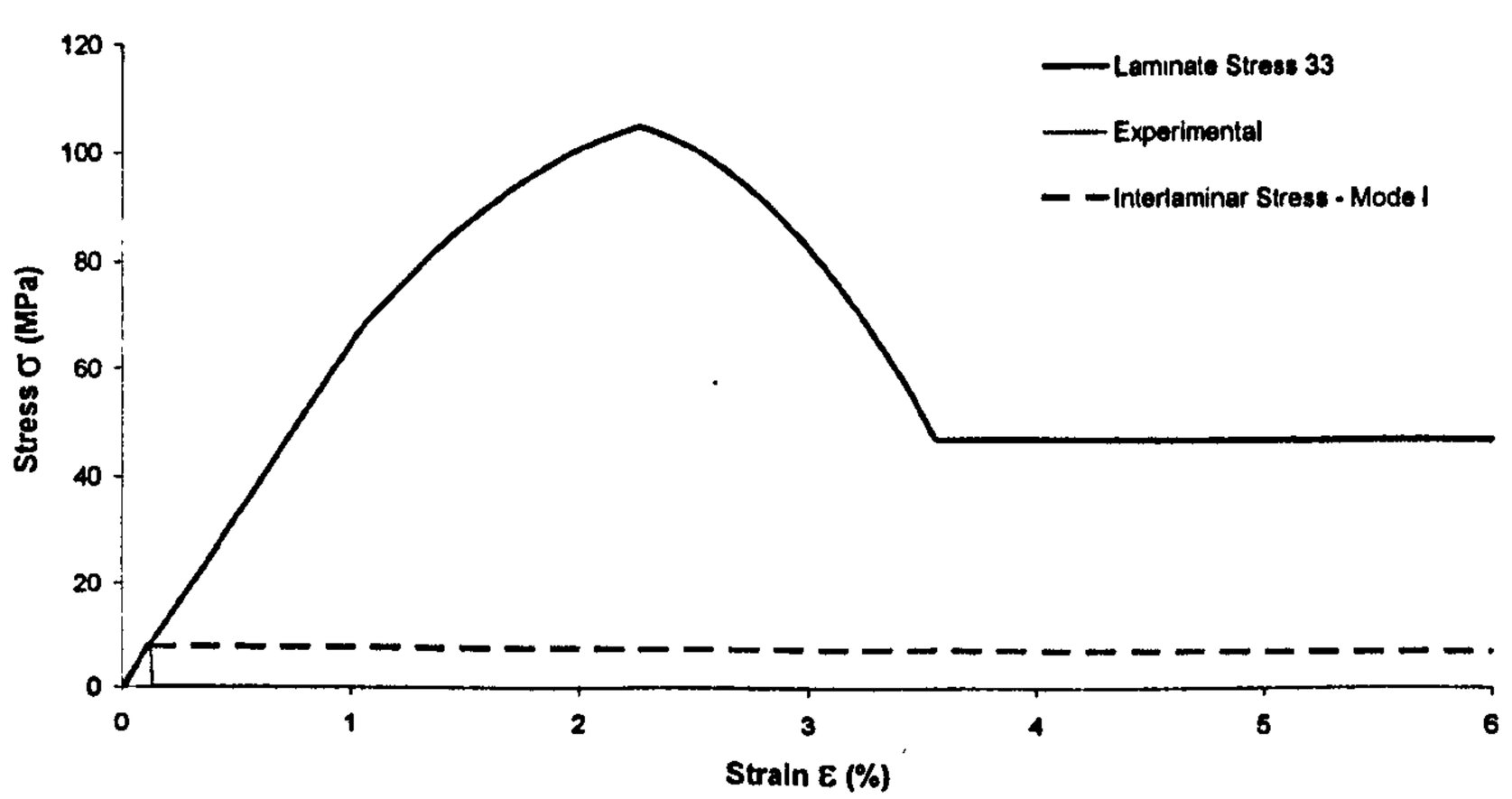
Stress-Strain Plot for CoFRM Material
Through-thickness Tensile
Laminate Stress 33
Experimental
Interlaminar Stress - Mode I
Stress σ (MPa)
Strain ε (%)
0
20
40
60
80
100
120
0
1
2
3
4
5
6

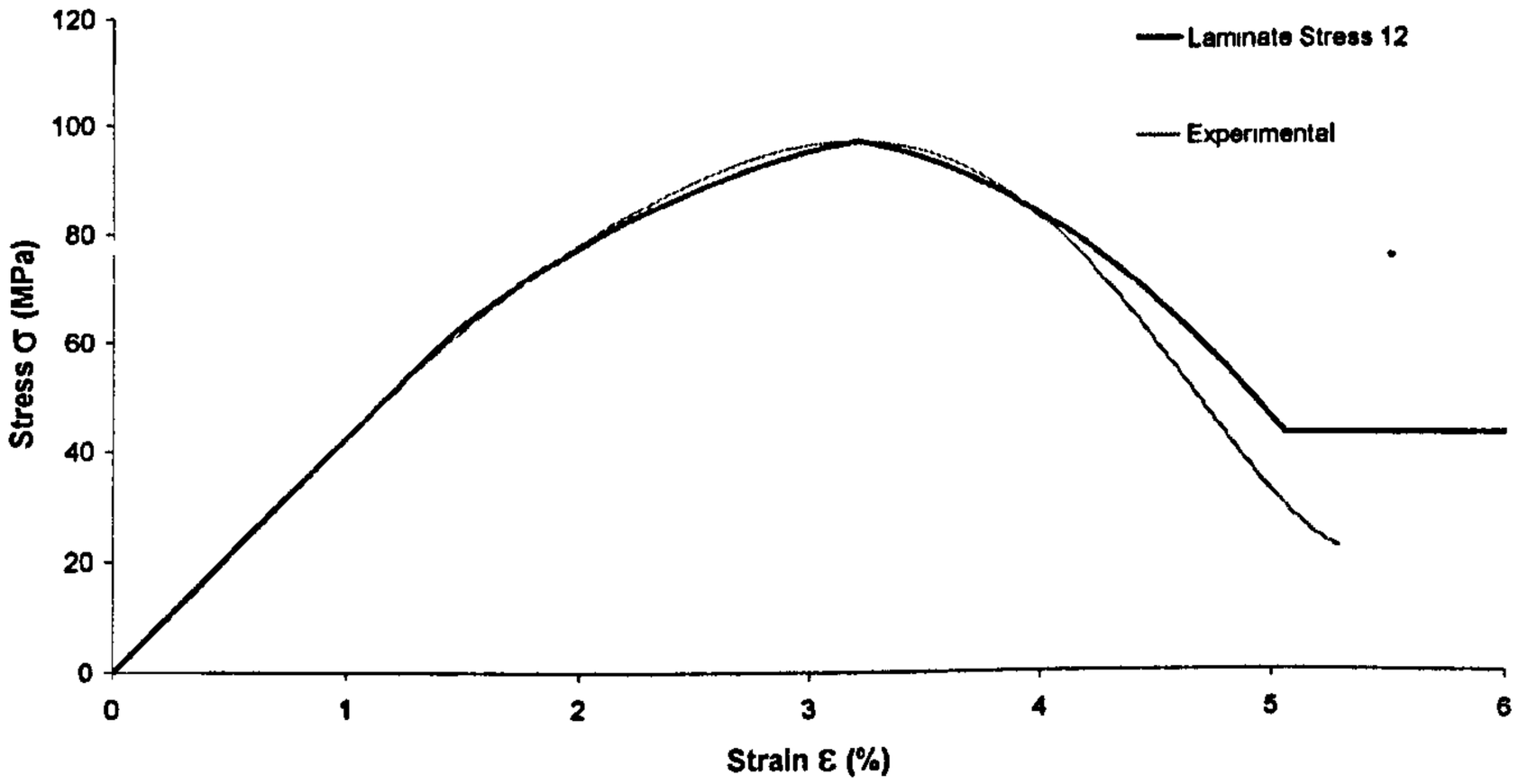
Stress-Strain Plot for CoFRM Material
Shear 12
Laminate Stress 12
Experimental
Stress σ (MPa)
Strain ε (%)
0
20
40
60
80
100
120
0
1
2
3
4
5
6

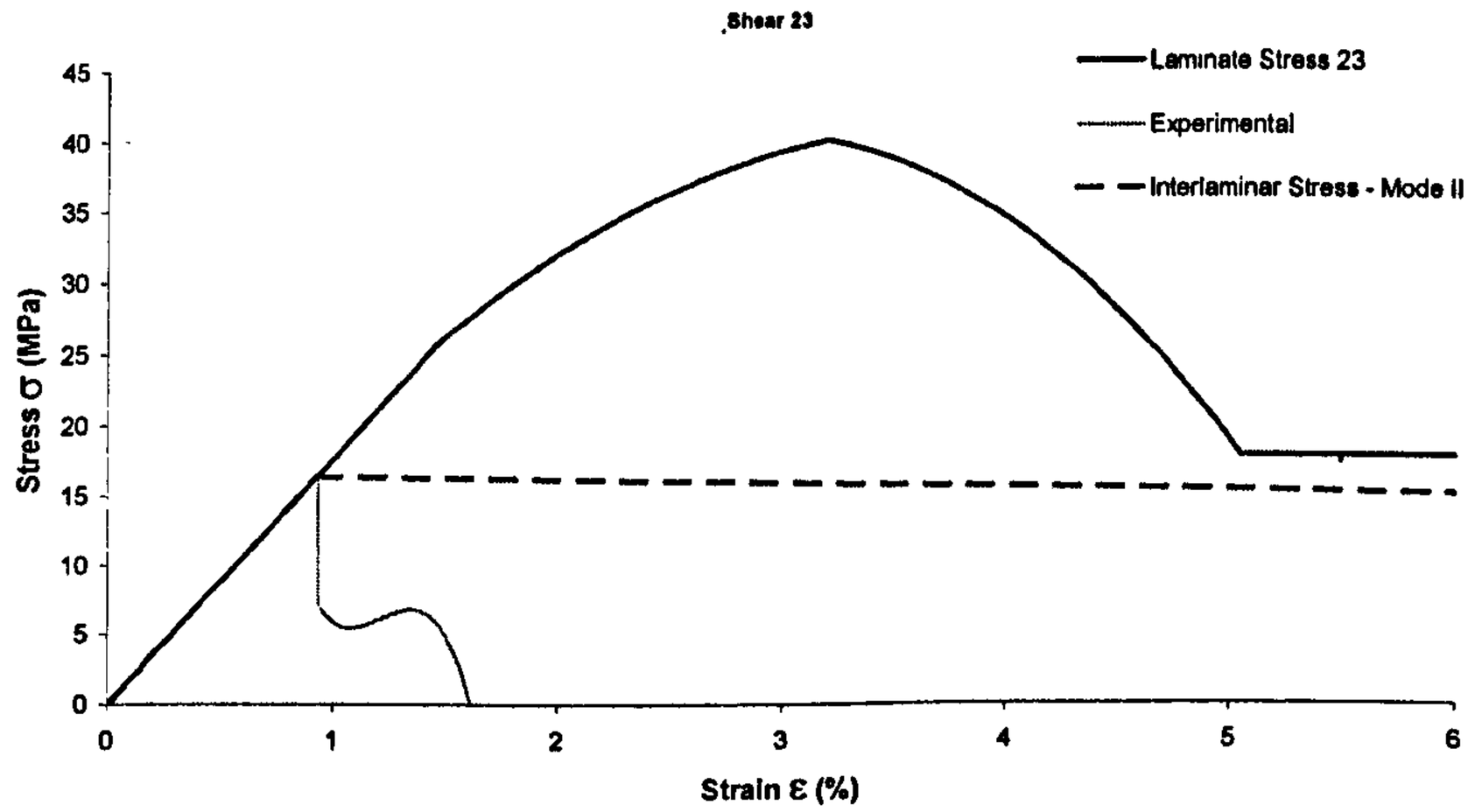
Stress-Strain Plot for CoFRM Material
Shear 23
Laminate Stress 23
Experimental
Interlaminar Stress - Mode II
Stress σ (MPa)
Strain ε (%)
0
5
10
15
20
25
30
35
40
45
0
1
2
3
4
5
6

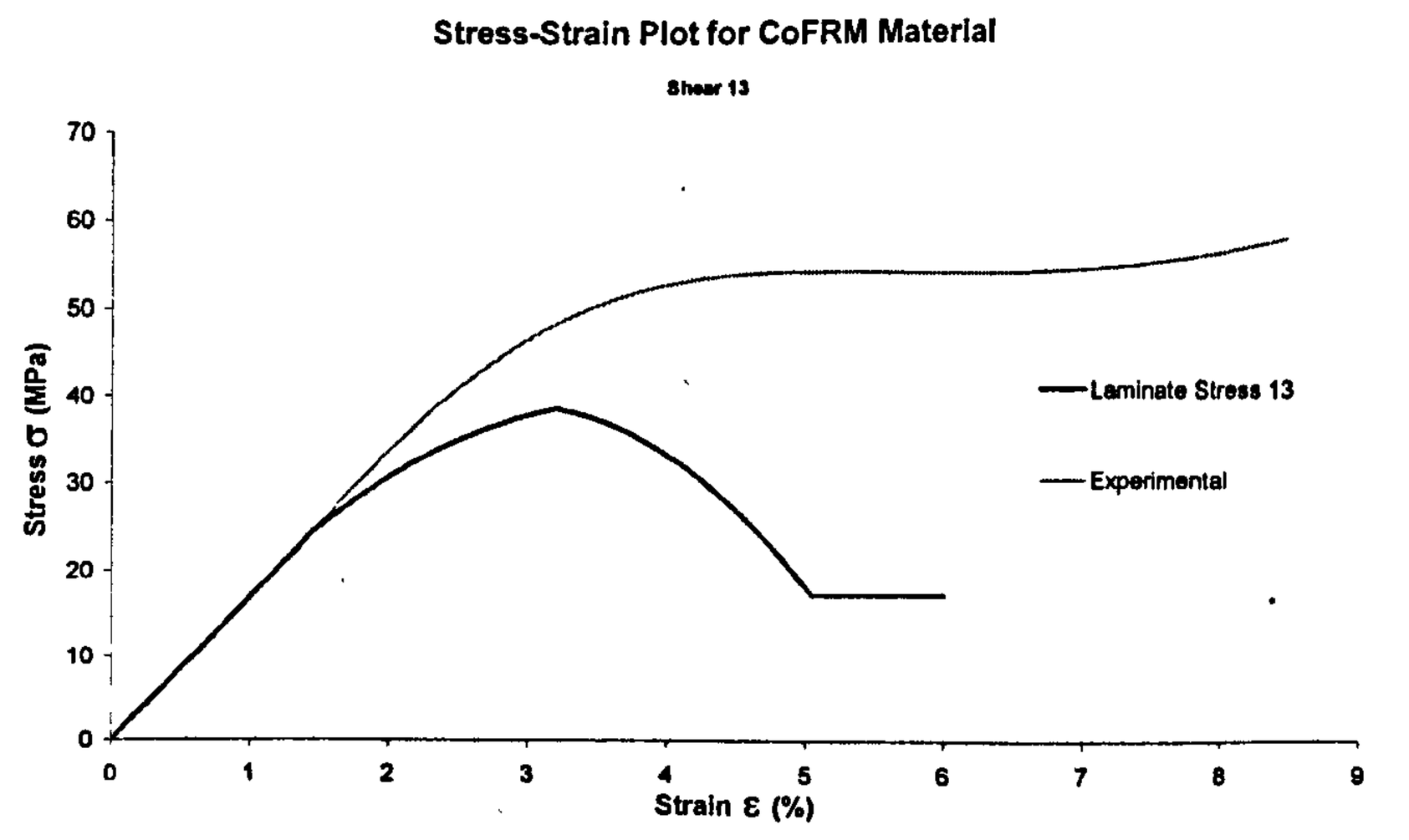
Stress-Strain Plot for CoFRM Material
Shear 13
Laminate Stress 13
Experimental
Stress σ (MPa)
Strain ε (%)
0
10
20
30
40
50
60
70
0
1
2
3
4
5
6
7
8
9

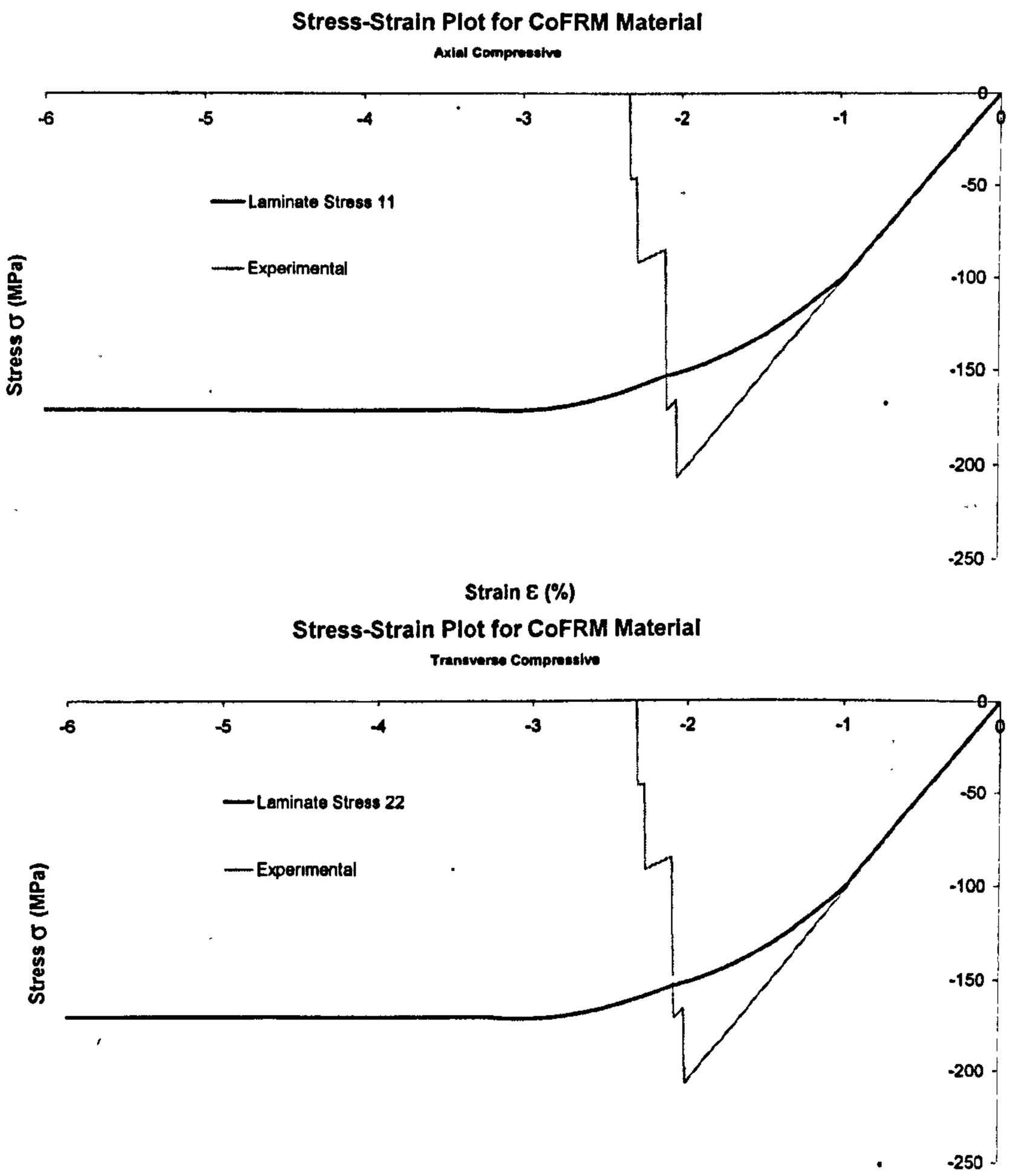
Stress-Strain Plot for CoFRM Material
Axial Compressive
Laminate Stress 11
Experimental
Stress σ (MPa)
Strain ε (%)
Stress-Strain Plot for CoFRM Material
Transverse Compressive
Laminate Stress 22
Experimental
Stress σ (MPa)
Strain ε (%)
Stress-Strain Plot for CoFRM Material
Through-thickness Compressive
Laminate Stress 33
Experimental
Stress σ (MPa)
Strain ε (%)

5.2.2 Braided Carbon 0/+30°/-30°

Fibre Tensile Properties				
		Volumetric Damage		
E (GPa)	0	εi (%)	0	
vf	0	ε1 (%)	0 d1	0
		εu (%)	0 du	0
Matrix Tensile Properties				
		Volumetric Damage		
E1 (GPa)	74.6	εi (%) volumet	0	
E2 (GPa)	1.22	ε1 (%) volumet	0 d1	0
E3 (GPa)	1.22	εu (%) volumet	0 du	0
G12 (GPa)	3.5	**Shear Damage**		
G23 (GPa)	3.5	εi (%) deviatori	0.5	
G13 (GPa)	3.5	ε1 (%) deviato	0.9 d1	0.2
		εu (%) deviato	1.6 du	0.7
ν12	0.5			
ν23	0.308			
ν13	0.263			

Fibre Compressive Properties				
		Volumetric Damage		
E (GPa)	0	εi (%)	0	
vf	0	ε1 (%)	0 d1	0
		εu (%)	0 du	0
Matrix Compressive Properties				
		Volumetric Damage		
E1 (GPa)	57.7	εi (%) volumet	0	
E2 (GPa)	3	ε1 (%) volume	0 d1	0
E3 (GPa)	3	εu (%) volume	0 du	0
G12 (GPa)	3.5	**Shear Damage**		
G23 (GPa)	3.5	εi (%) deviator	0.1	
G13 (GPa)	3.5	ε1 (%) deviato	1 d1	0.6
		εu (%) deviato	1.2 du	0.7
ν12	0.225			
ν23	0.482			
ν13	0.151			

Interlaminar Properties	
E0 (GPa)	1.22
G0 (GPa)	3.5
σ1max (GPa)	0.00772
σ2max (GPa)	0.0163587
G1c (kN/mm)	1.00E-03
G2c (kN/mm)	4.00E-03
Lm (mm)	0.08

= thickness of Interlaminar Region

= values calculated automatically

Figure 5-9 - Input Parameters of Braided Carbon 0/+30°/-30°

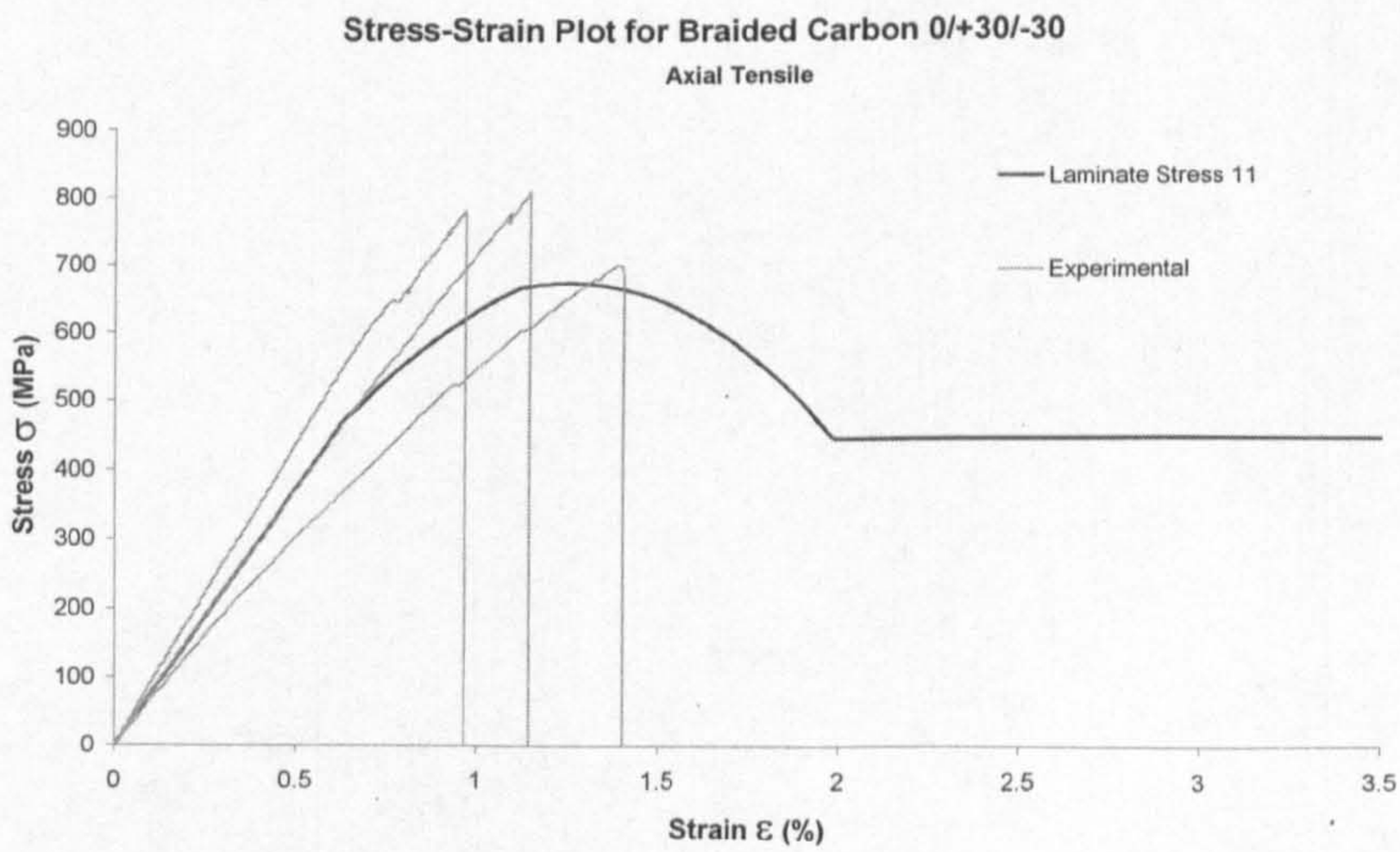

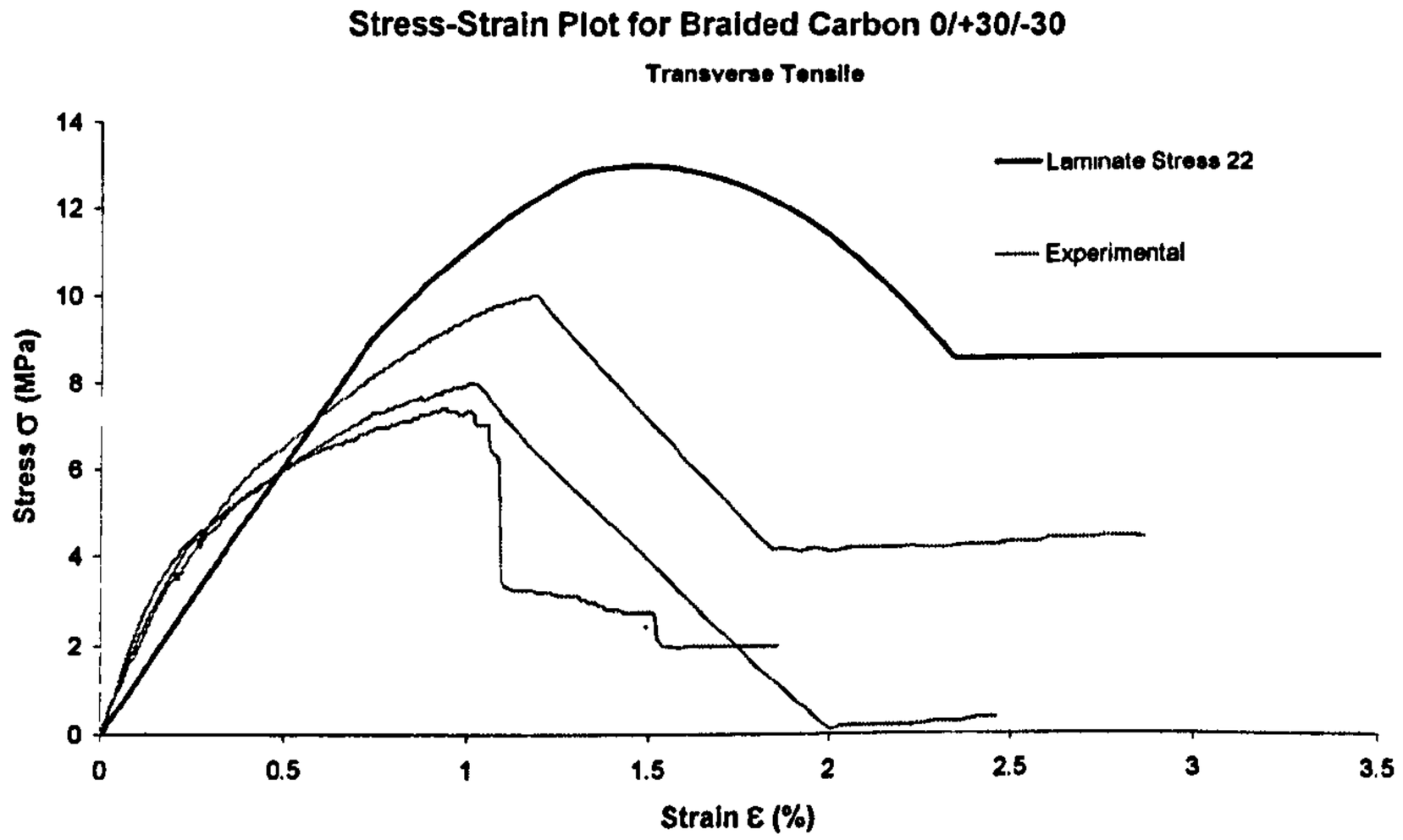
Stress-Strain Plot for Braided Carbon 0/+30/-30
Transverse Tensile
Laminate Stress 22
Experimental
Stress σ (MPa)
Strain ε (%)
0
2
4
6
8
10
12
14
0
0.5
1
1.5
2
2.5
3
3.5

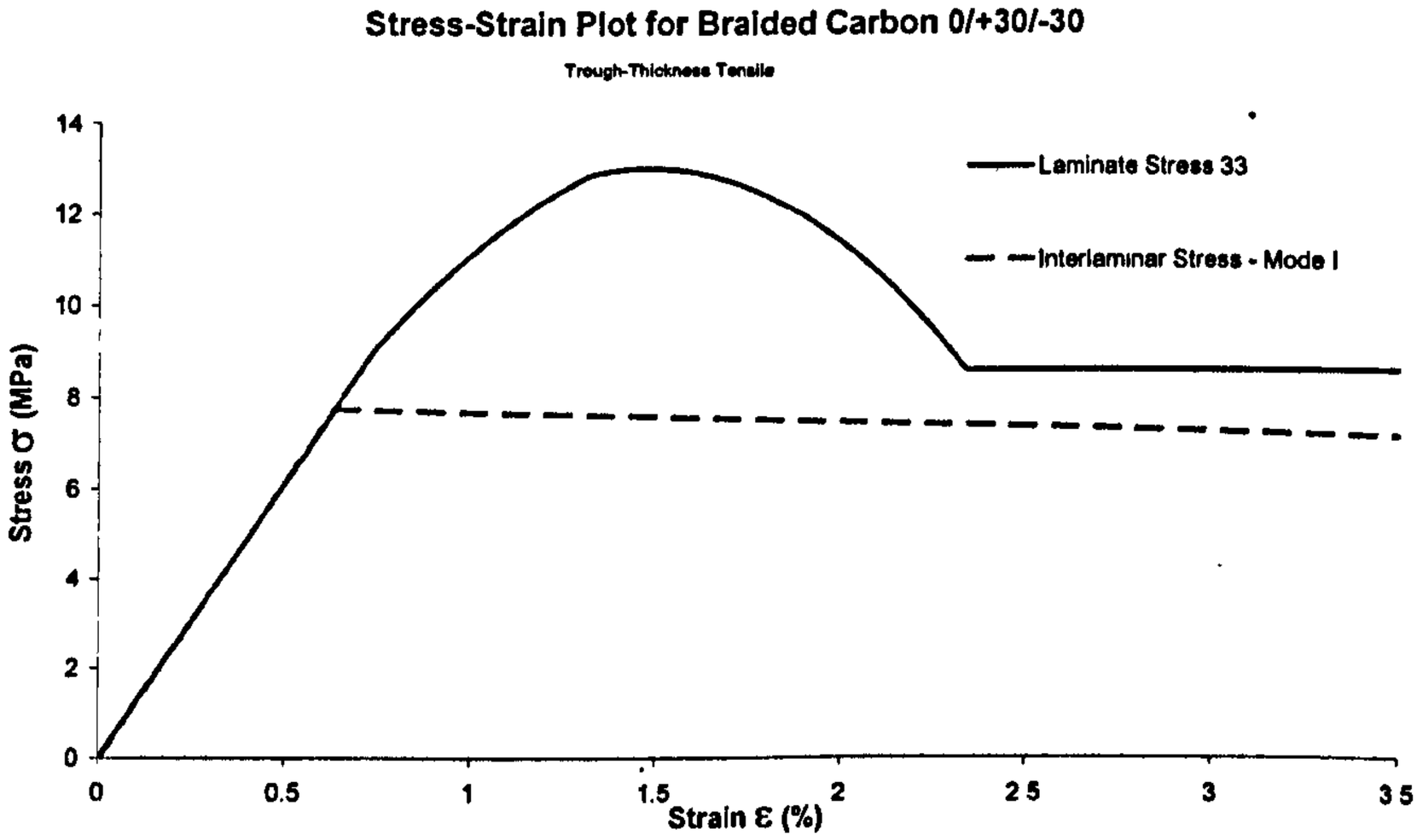
Stress-Strain Plot for Braided Carbon 0/+30/-30
Trough-Thickness Tensile
Laminate Stress 33
Interlaminar Stress - Mode I
Stress σ (MPa)
Strain ε (%)
0
2
4
6
8
10
12
14
0
0.5
1
1.5
2
2.5
3
3.5

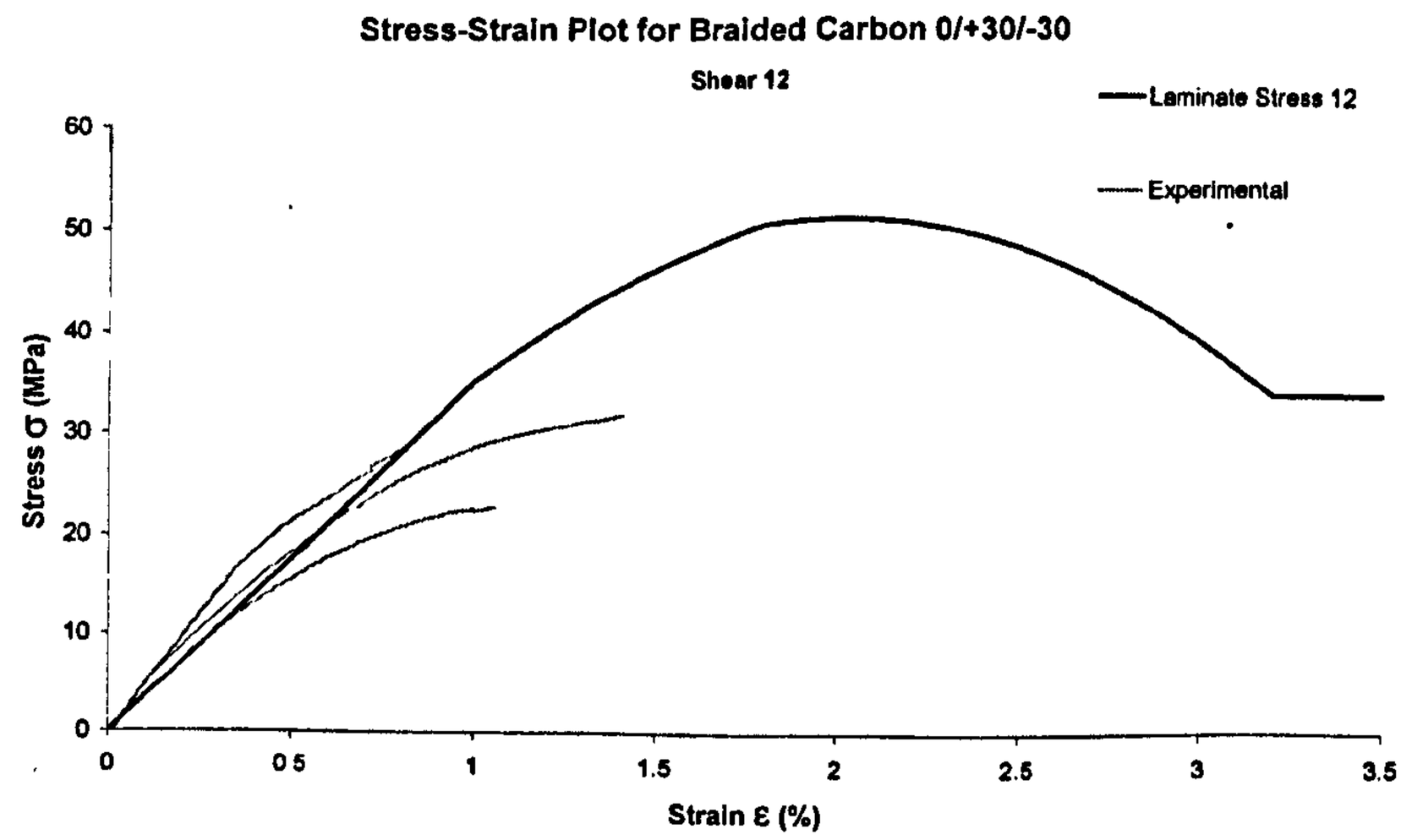
Stress-Strain Plot for Braided Carbon 0/+30/-30
Shear 12
Laminate Stress 12
Experimental
Stress σ (MPa)
Strain ε (%)
0
10
20
30
40
50
60
0
0.5
1
1.5
2
2.5
3
3.5

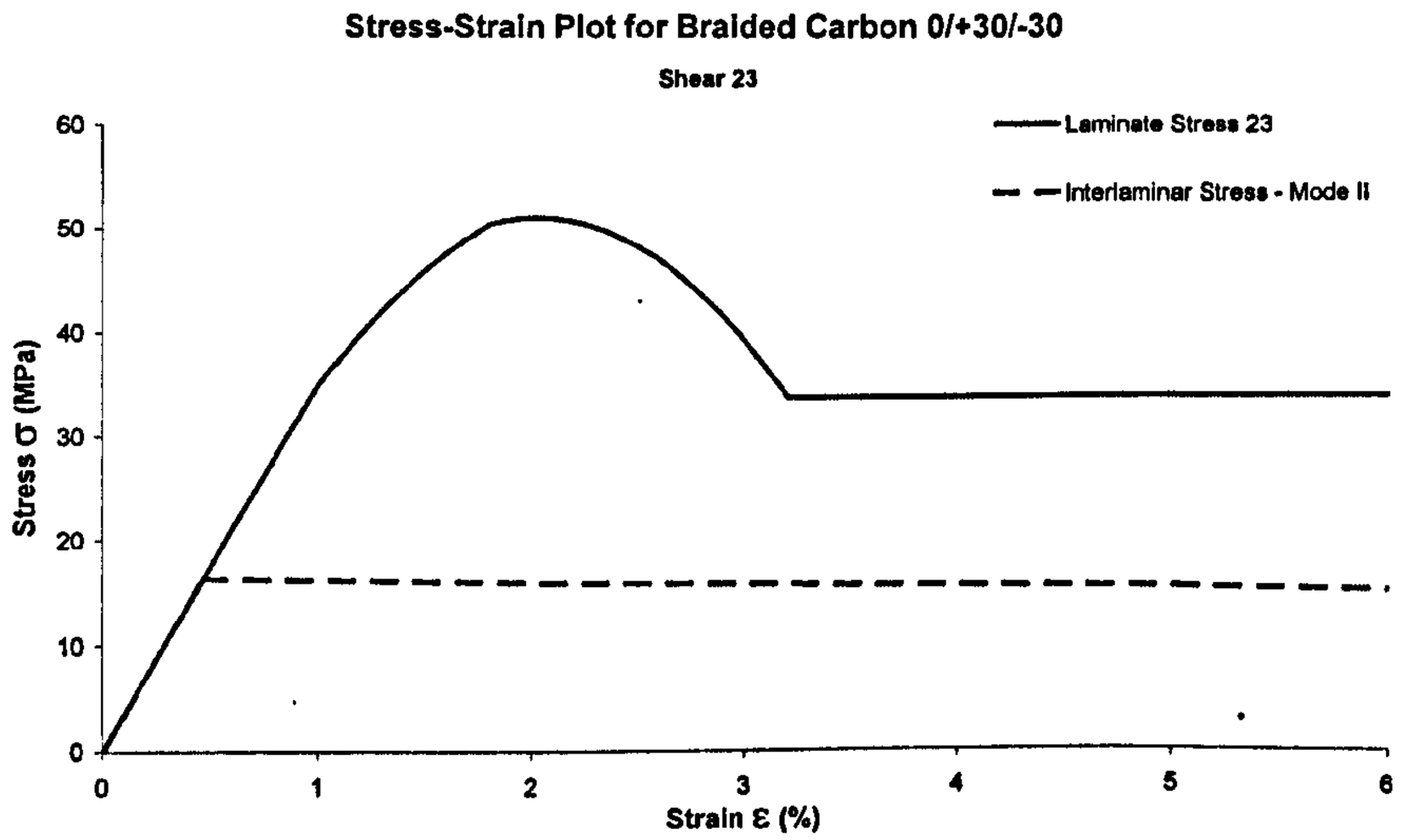
Stress-Strain Plot for Braided Carbon 0/+30/-30
Shear 23
Laminate Stress 23
Interlaminar Stress - Mode II
Stress σ (MPa)
Strain ε (%)
0
10
20
30
40
50
60
0
1
2
3
4
5
6

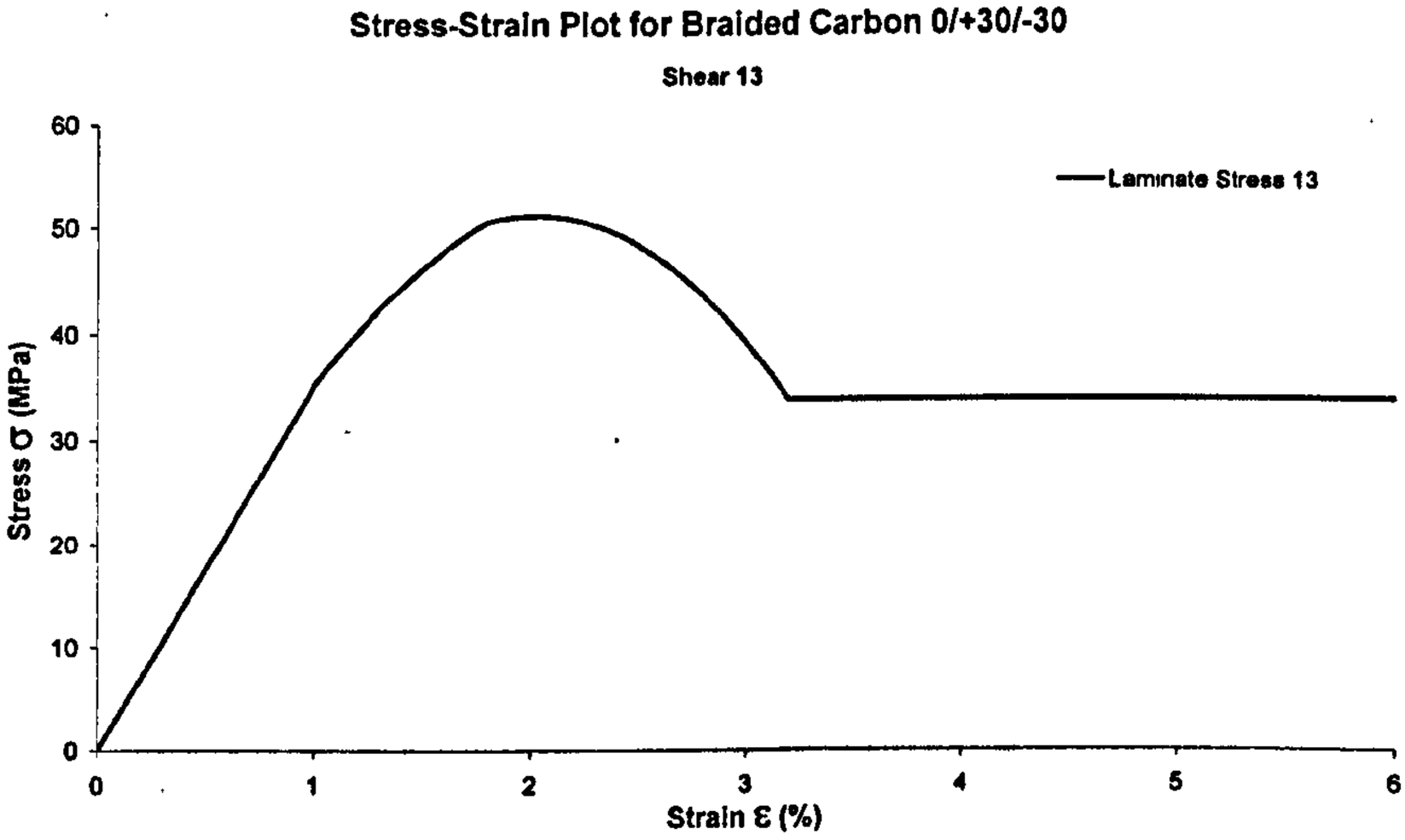
Stress-Strain Plot for Braided Carbon 0/+30/-30
Shear 13
Laminate Stress 13
Stress σ (MPa)
Strain ε (%)
0
10
20
30
40
50
60
0
1
2
3
4
5
6

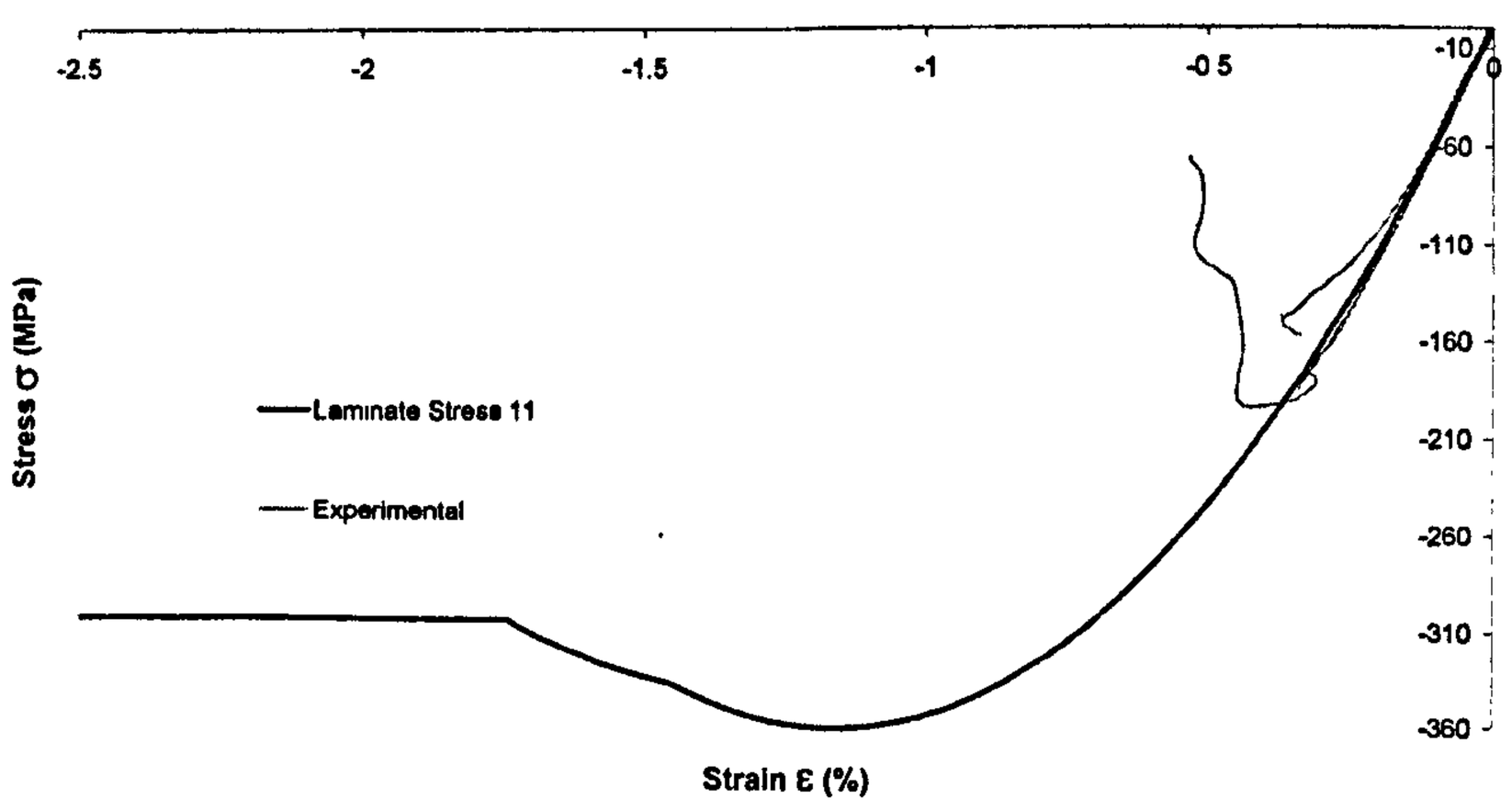
Stress-Strain Plot for Braided Carbon 0/+30/-30
Axial Compressive
Laminate Stress 11
Experimental
Stress σ (MPa)
Strain ε (%)
-2.5
-2
-1.5
-1
-0.5
0
-10
-60
-110
-160
-210
-260
-310
-360

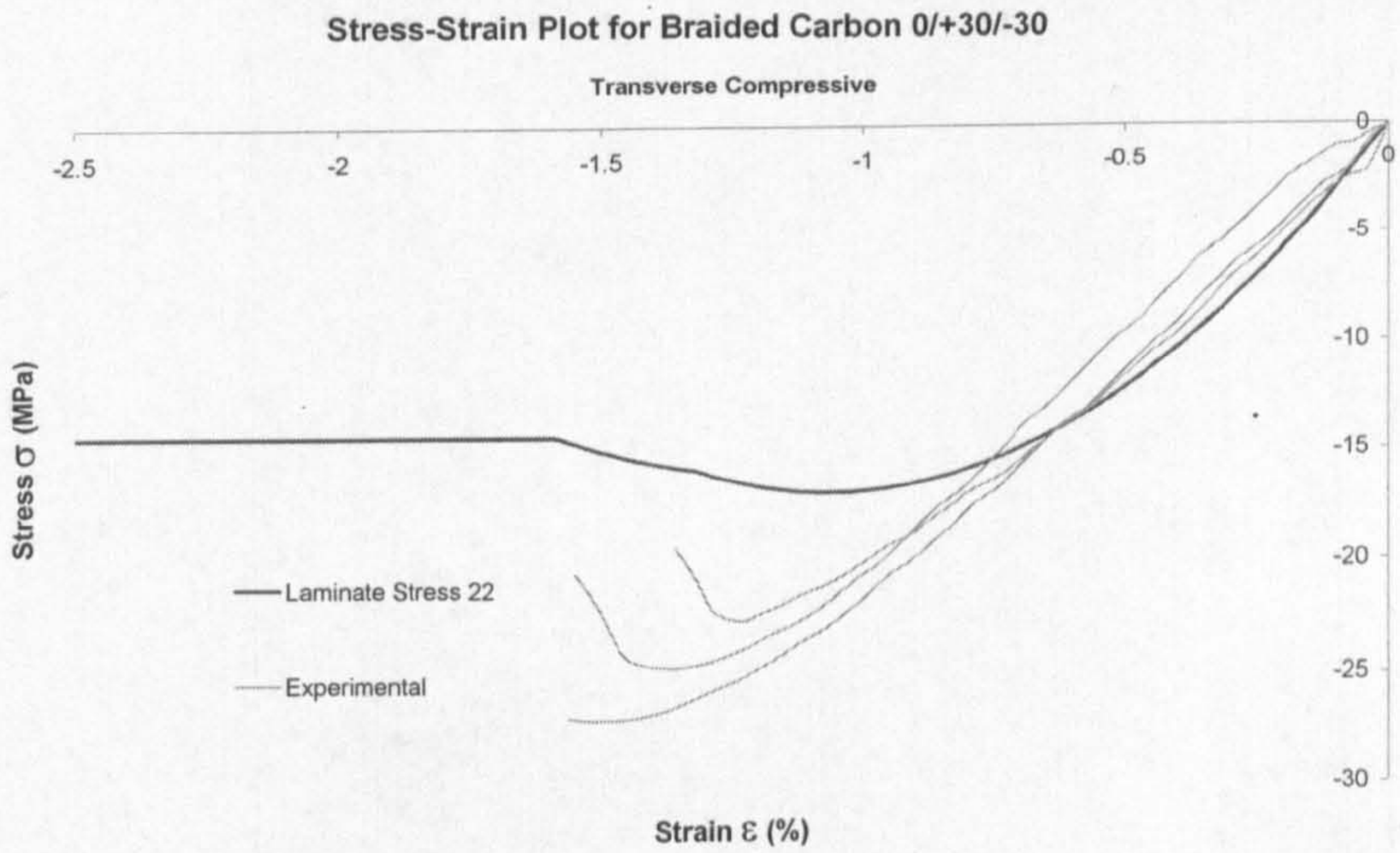

5.2.3 Braided Carbon 0/+45/-45

Fibre Tensile Properties				
		Volumetric Damage		
E (GPa)	0	εi (%)	0	
vf	0	ε1 (%)	0 d1	0
		εu (%)	0 du	0
Matrix Tensile Properties				
		Volumetric Damage		
E1 (GPa)	62.6	εi (%) volumet	0	
E2 (GPa)	5.74	ε1 (%) volume	0 d1	0
E3 (GPa)	5.74	εu (%) volume	0 du	0
G12 (GPa)	3.9	Shear Damage		
G23 (GPa)	3.9	εi (%) deviator	0.5	
G13 (GPa)	3.9	ε1 (%) deviato	1 d1	0.2
		εu (%) deviato	2.1 du	0.7
ν12	0.312			
ν23	0.312			
ν13	0.312			

Fibre Compressive Properties				
		Volumetric Damage		
E (GPa)	0	εi (%)	0	
vf	0	ε1 (%)	0 d1	0
		εu (%)	0 du	0
Matrix Compressive Properties				
		Volumetric Damage		
E1 (GPa)	70.6	εi (%) volumet	0	
E2 (GPa)	10	ε1 (%) volume	0 d1	0
E3 (GPa)	10	εu (%) volume	0 du	0
G12 (GPa)	3.9	Shear Damage		
G23 (GPa)	3.9	εi (%) deviator	-0.1	
G13 (GPa)	3.9	ε1 (%) deviato	-0.6 d1	0.6
		εu (%) deviato	-0.65 du	0.7
ν12	0.312			
ν23	0.312			
ν13	0.312			

Interlaminar Properties	
E0 (GPa)	5.74
G0 (GPa)	3.9
σ1max (GPa)	0.00772
σ2max (GPa)	0.016359
G1c (kN/mm)	1.00E-03
G2c (kN/mm)	4.00E-03
Lm (mm)	0.08

= thickness of Interlaminar Region

= values calculated automatically

Figure 5-10 - Input Parameters of Braided Carbon 0/+45°/-45°

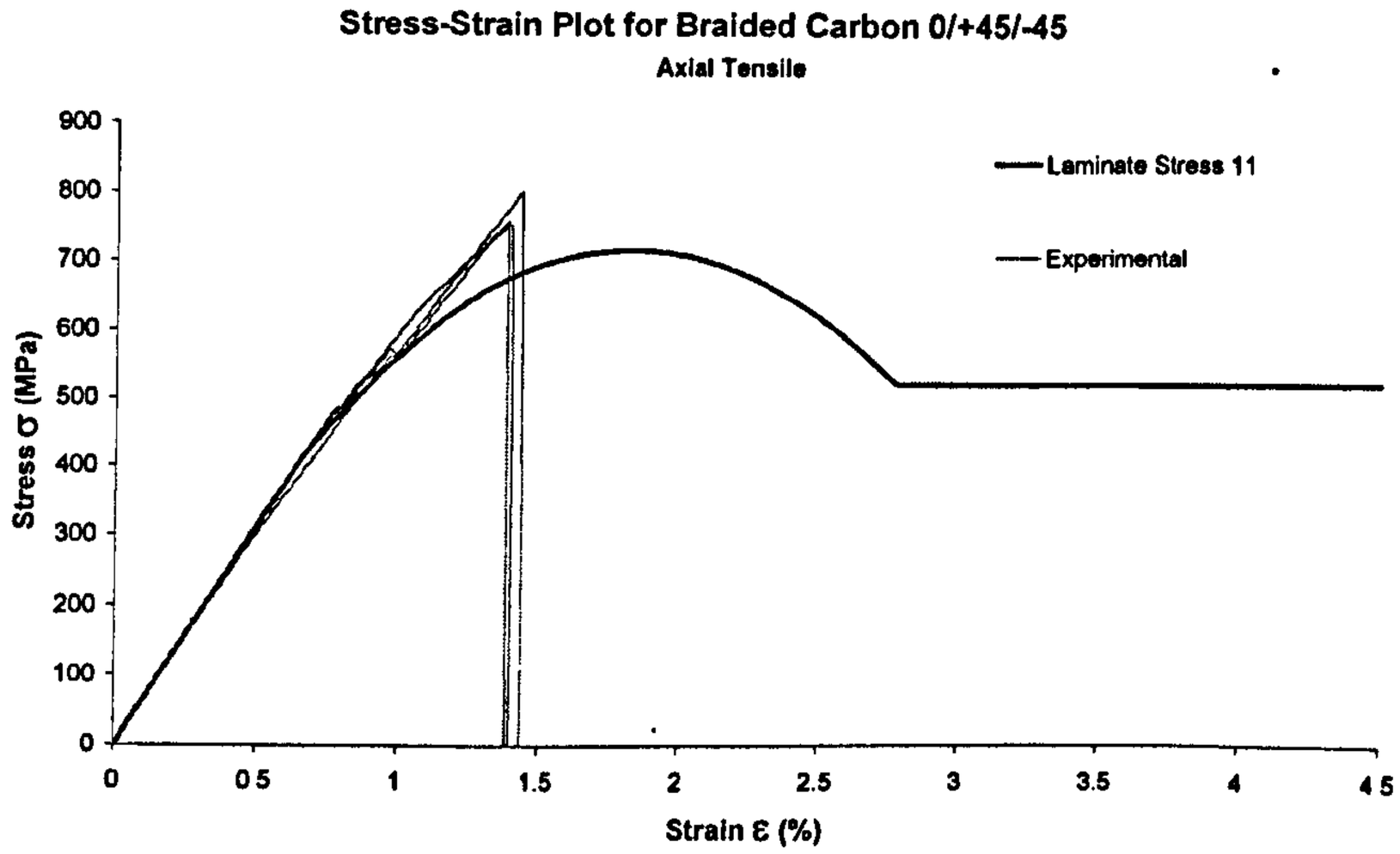
Stress-Strain Plot for Braided Carbon 0/+45/-45
Axial Tensile
Laminate Stress 11
Experimental
Stress σ (MPa)
900
800
700
600
500
400
300
200
100
0
0
0 5
1
1.5
2
2.5
3
3.5
4
4 5
Strain ε (%)

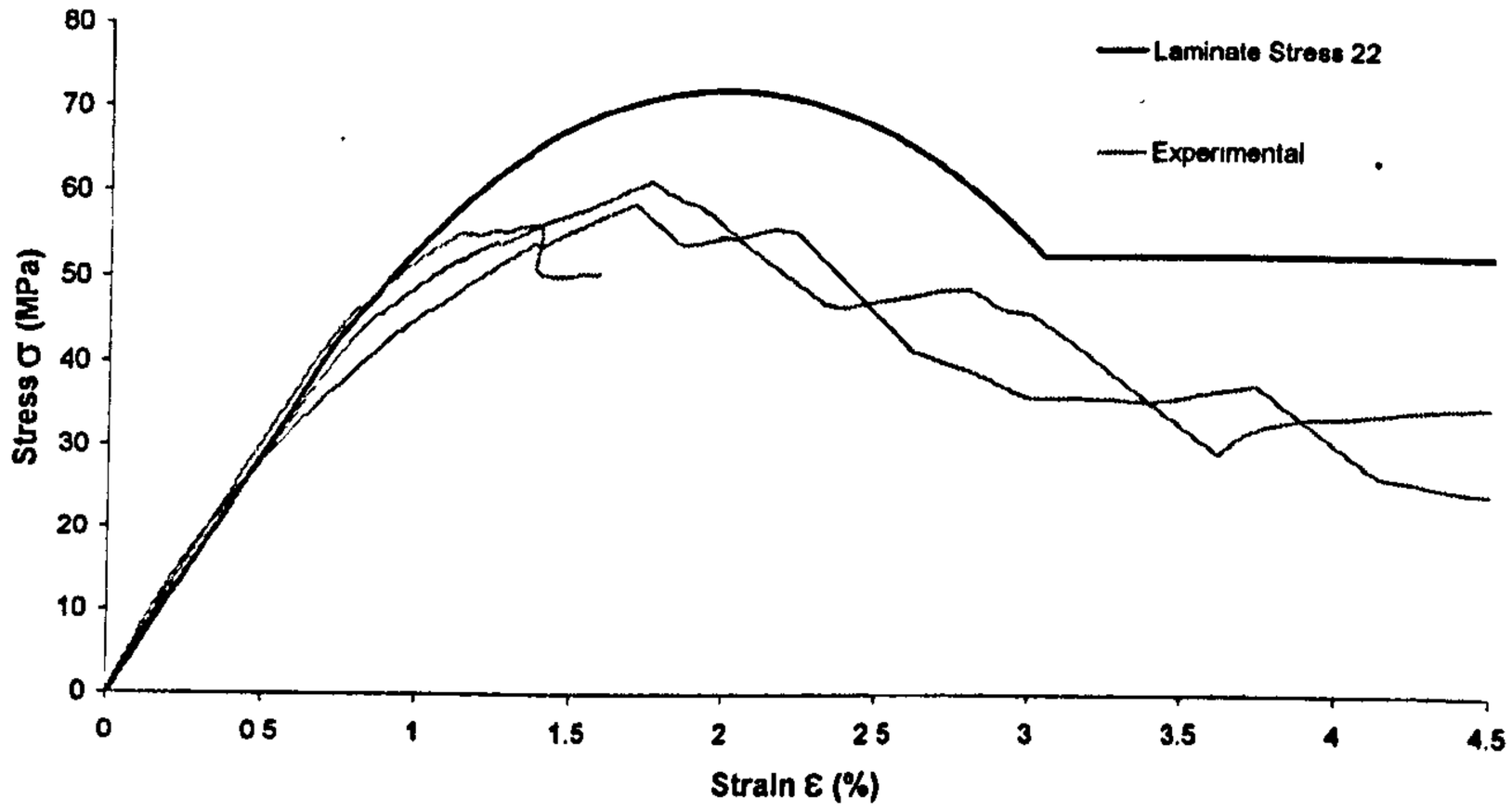
Stress-Strain Plot for Braided Carbon 0/+45/-45
Tranverse Tensile
Laminate Stress 22
Experimental
Stress σ (MPa)
80
70
60
50
40
30
20
10
0
0
0 5
1
1.5
2
2 5
3
3.5
4
4.5
Strain ε (%)

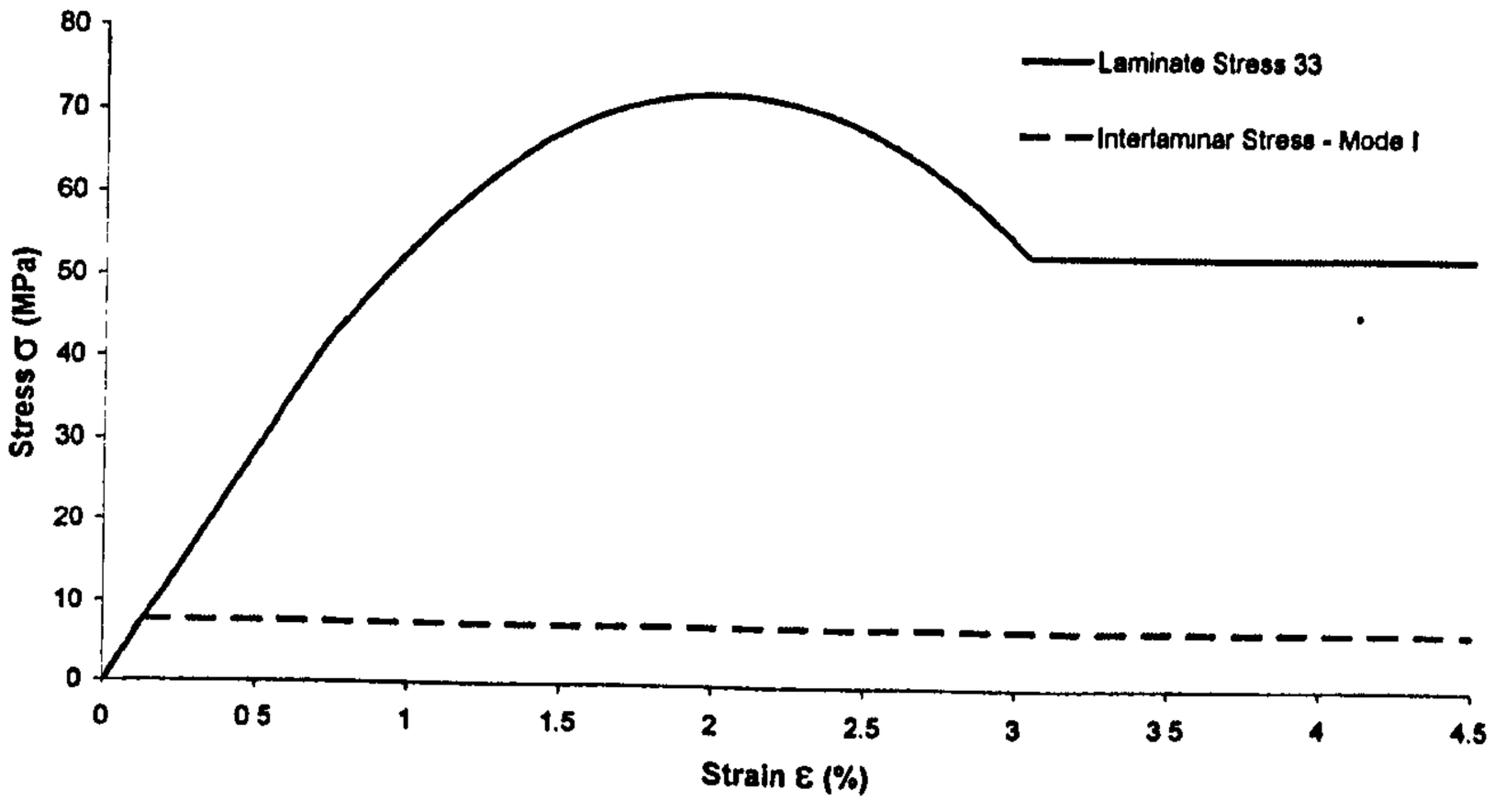
Stress-Strain Plot for Braided Carbon 0/+45/-45
Through Thickness Tensile
Laminate Stress 33
Interlaminar Stress - Mode I
Stress σ (MPa)
80
70
60
50
40
30
20
10
0
0
0 5
1
1.5
2
2.5
3
3 5
4
4.5
Strain ε (%)

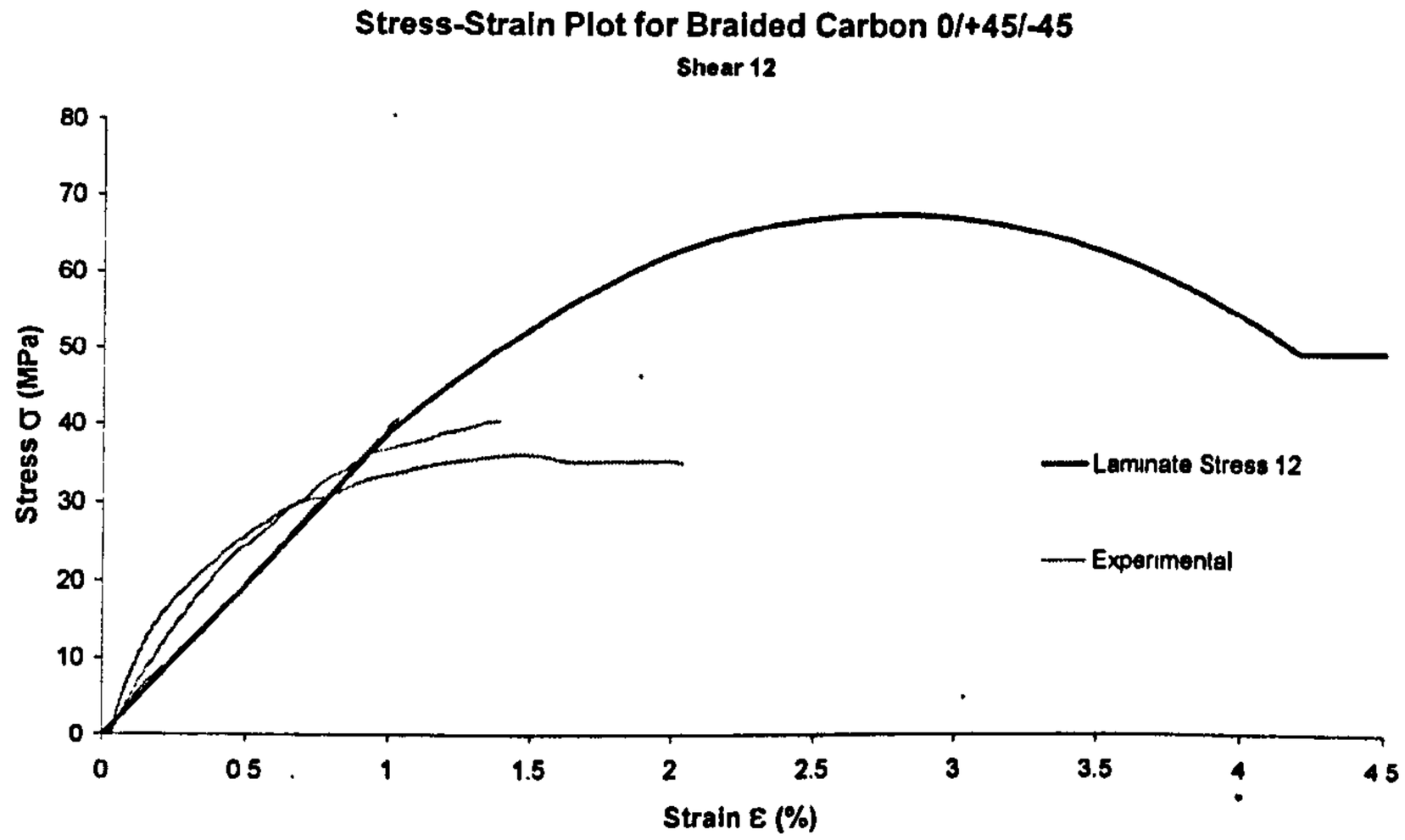
Stress-Strain Plot for Braided Carbon 0/+45/-45
Shear 12
Stress σ (MPa)
Strain ε (%)
Laminate Stress 12
Experimental
0
10
20
30
40
50
60
70
80
0
0 5
1
1.5
2
2.5
3
3.5
4
4 5

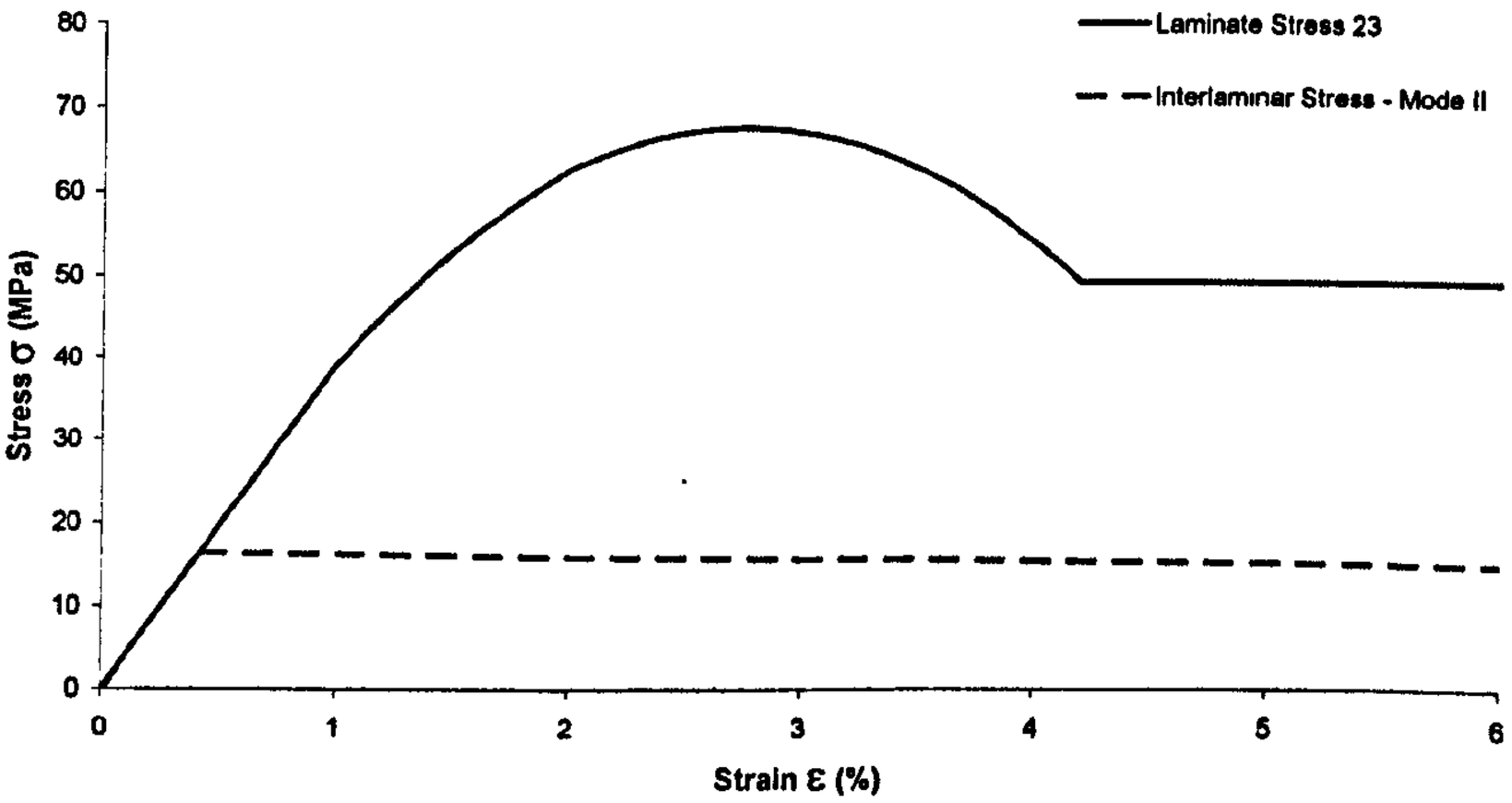
Stress-Strain Plot for Braided Carbon 0/+45/-45
Shear 23
Stress σ (MPa)
Strain ε (%)
Laminate Stress 23
Interlaminar Stress - Mode II
0
10
20
30
40
50
60
70
80
0
1
2
3
4
5
6

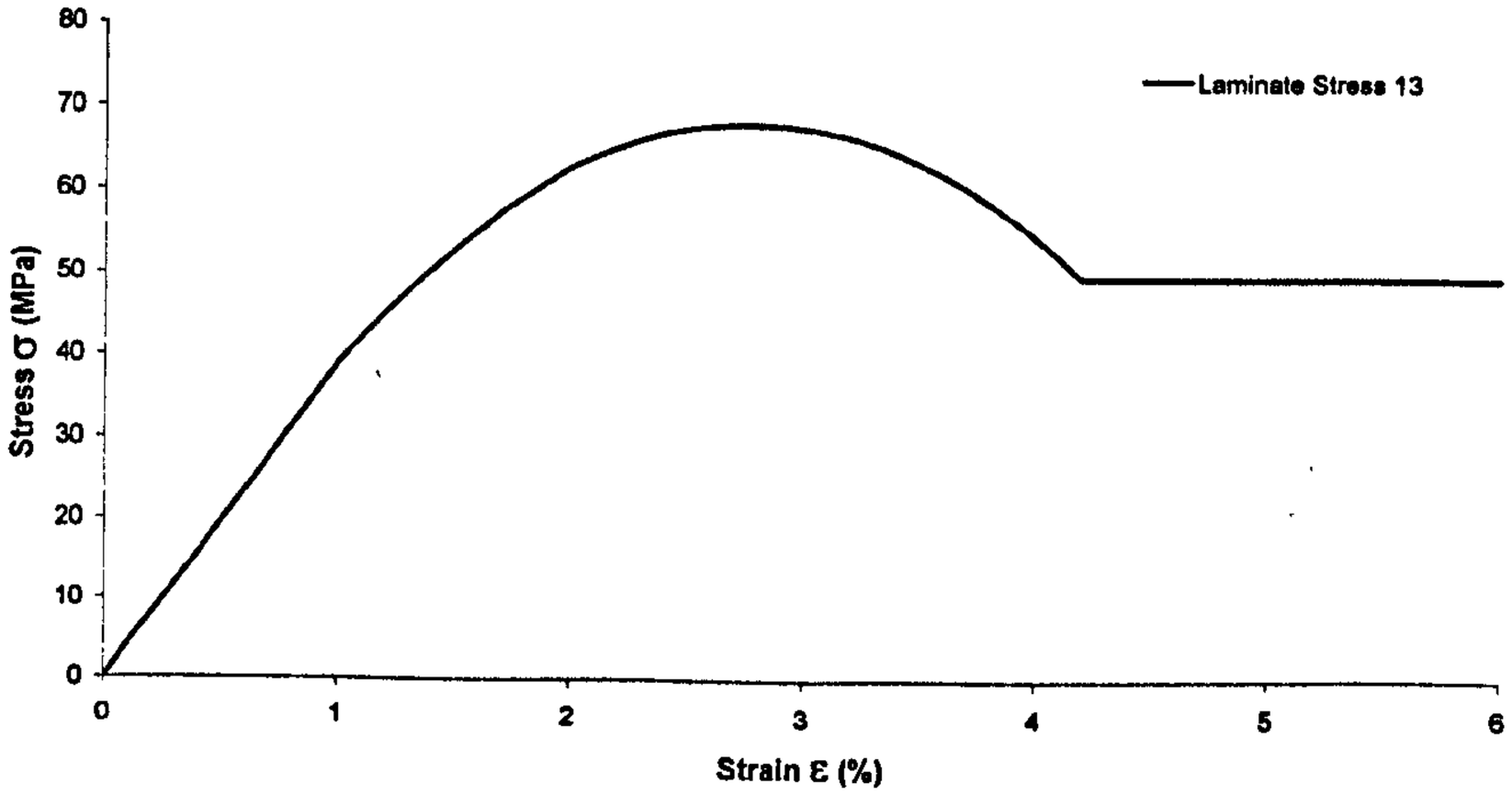
Stress-Strain Plot for Braided Carbon 0/+45/-45
Shear 13
Stress σ (MPa)
Strain ε (%)
Laminate Stress 13
0
10
20
30
40
50
60
70
80
0
1
2
3
4
5
6

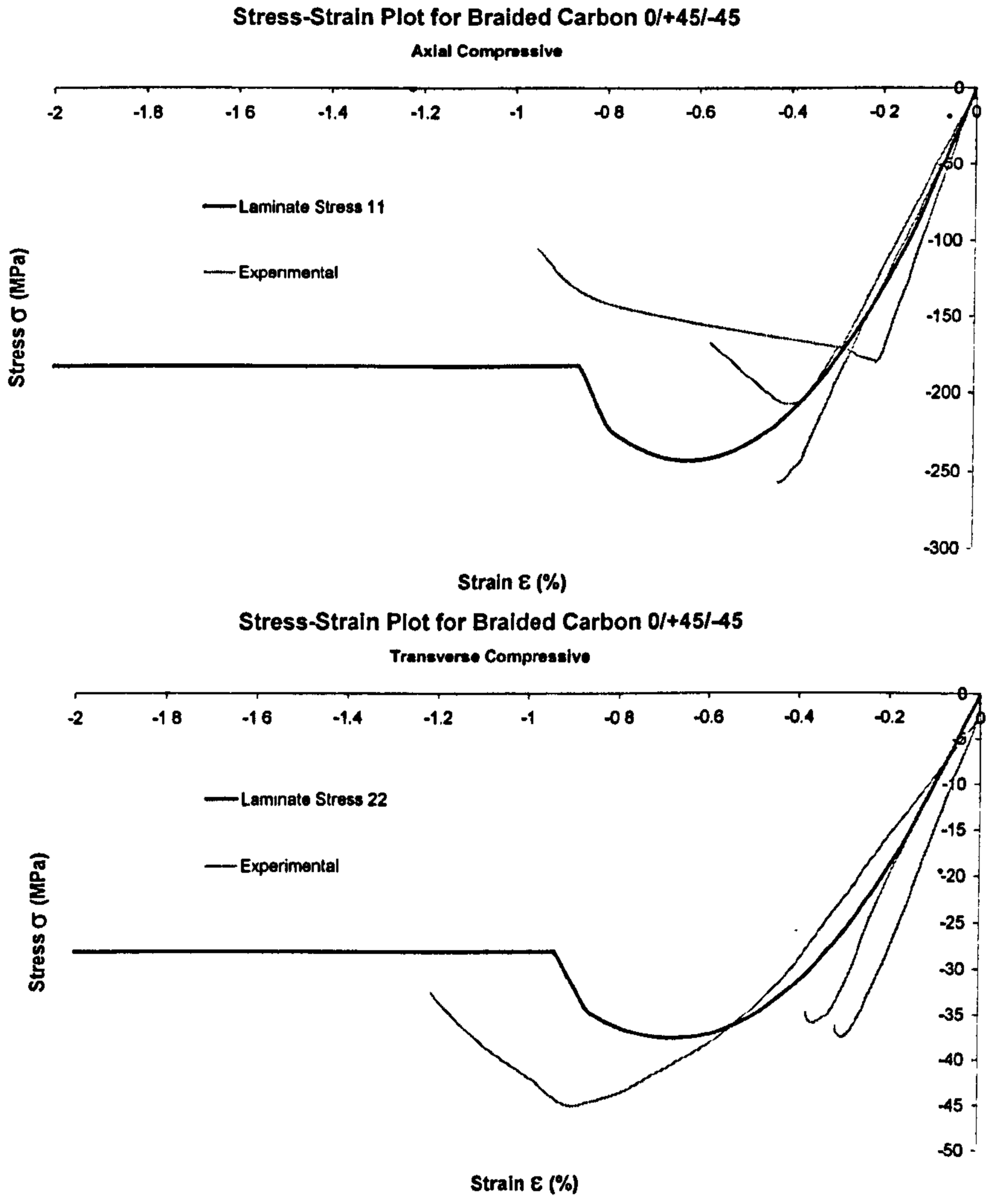
Stress-Strain Plot for Braided Carbon 0/+45/-45
Axial Compressive
Laminate Stress 11
Experimental
Stress σ (MPa)
Strain ε (%)
-2
-1.8
-1.6
-1.4
-1.2
-1
-0.8
-0.6
-0.4
-0.2
0
-50
-100
-150
-200
-250
-300
Stress-Strain Plot for Braided Carbon 0/+45/-45
Transverse Compressive
Laminate Stress 22
Experimental
Stress σ (MPa)
Strain ε (%)
-2
-1.8
-1.6
-1.4
-1.2
-1
-0.8
-0.6
-0.4
-0.2
0
-10
-15
-20
-25
-30
-35
-40
-45
-50

5.2.4 Braided Carbon 0/+60/-60

Fibre Tensile Properties				
		Volumetric Damage		
E (GPa)	0	εi (%)	0	
vf	0	ε1 (%)	0 d1	0
		εu (%)	0 du	0
Matrix Tensile Properties				
		Volumetric Damage		
E1 (GPa)	58.9	εi (%) volumet	0	
E2 (GPa)	16.74	ε1 (%) volume	0 d1	0
E3 (GPa)	16.74	εu (%) volume	0 du	0
G12 (GPa)	5.1	**Shear Damage**		
G23 (GPa)	5.1	εi (%) deviator	0.5	
G13 (GPa)	5.1	ε1 (%) deviato	1 d1	0.15
		εu (%) deviato	2.1 du	0.7
V12	0.38			
V23	0.398			
V13	0.149			

Fibre Compressive Properties				
		Volumetric Damage		
E (GPa)	0	εi (%)	0	
vf	0	ε1 (%)	0 d1	0
		εu (%)	0 du	0
Matrix Compressive Properties				
		Volumetric Damage		
E1 (GPa)	53.5	εi (%) volumet	0	
E2 (GPa)	18	ε1 (%) volume	0 d1	0
E3 (GPa)	18	εu (%) volume	0 du	0
G12 (GPa)	5.1	**Shear Damage**		
G23 (GPa)	5.1	εi (%) deviator	-0.1	
G13 (GPa)	5.1	ε1 (%) deviato	-0.6 d1	0.6
		εu (%) deviato	-0.65 du	0.7
V12	0.225			
V23	0.482			
V13	0.151			

Interlaminar Properties	
E0 (GPa)	16.74
G0 (GPa)	5.1
σ1max (GPa)	0.00772
σ2max (GPa)	0.016359
G1c (kN/mm)	1.00E-03
G2c (kN/mm)	4.00E-03
Lm (mm)	0.08

= thickness of Interlaminar Region

= values calculated automatically

Figure 5-11 - Input Parameters of Braided Carbon 0/+60°/-60°

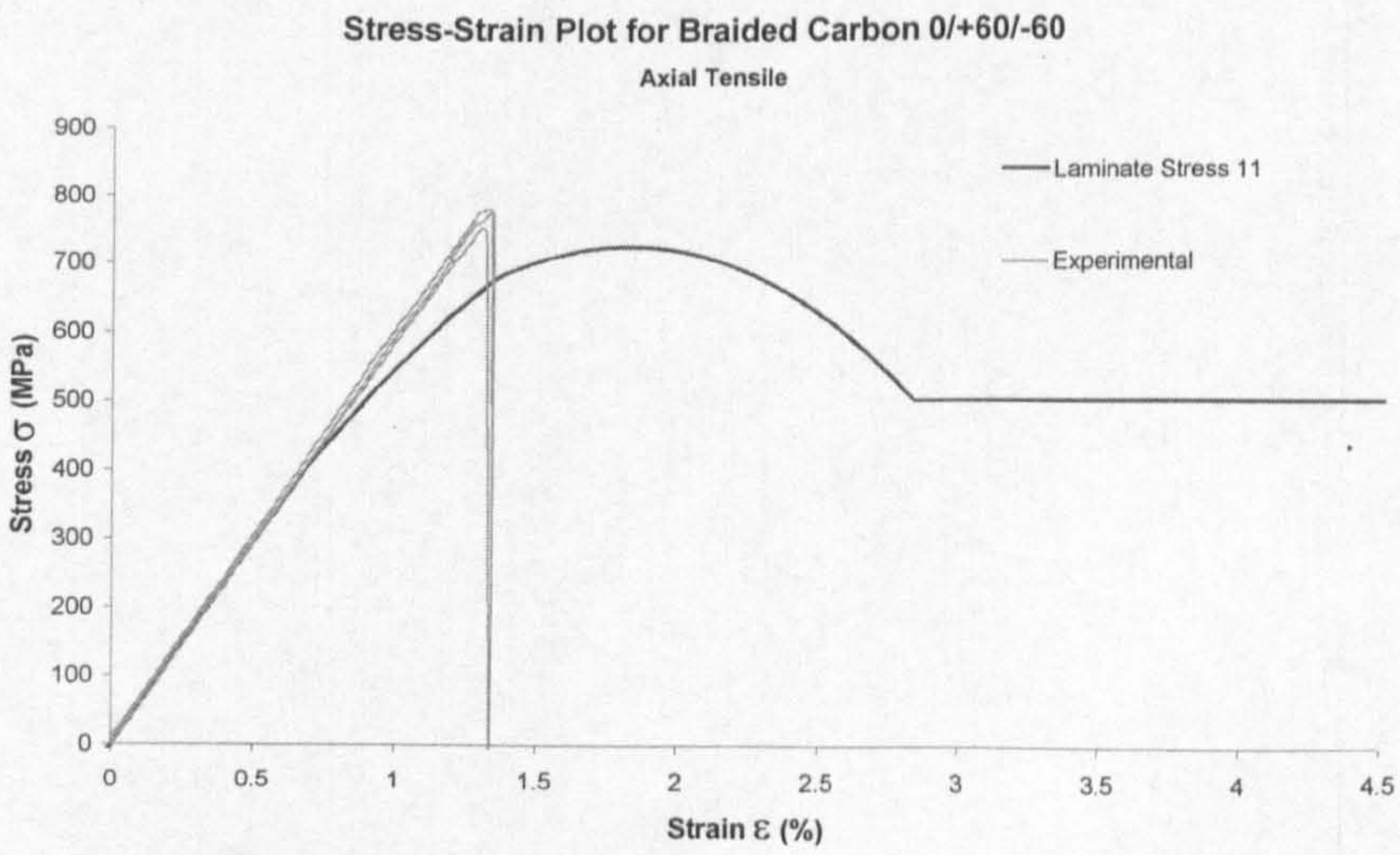

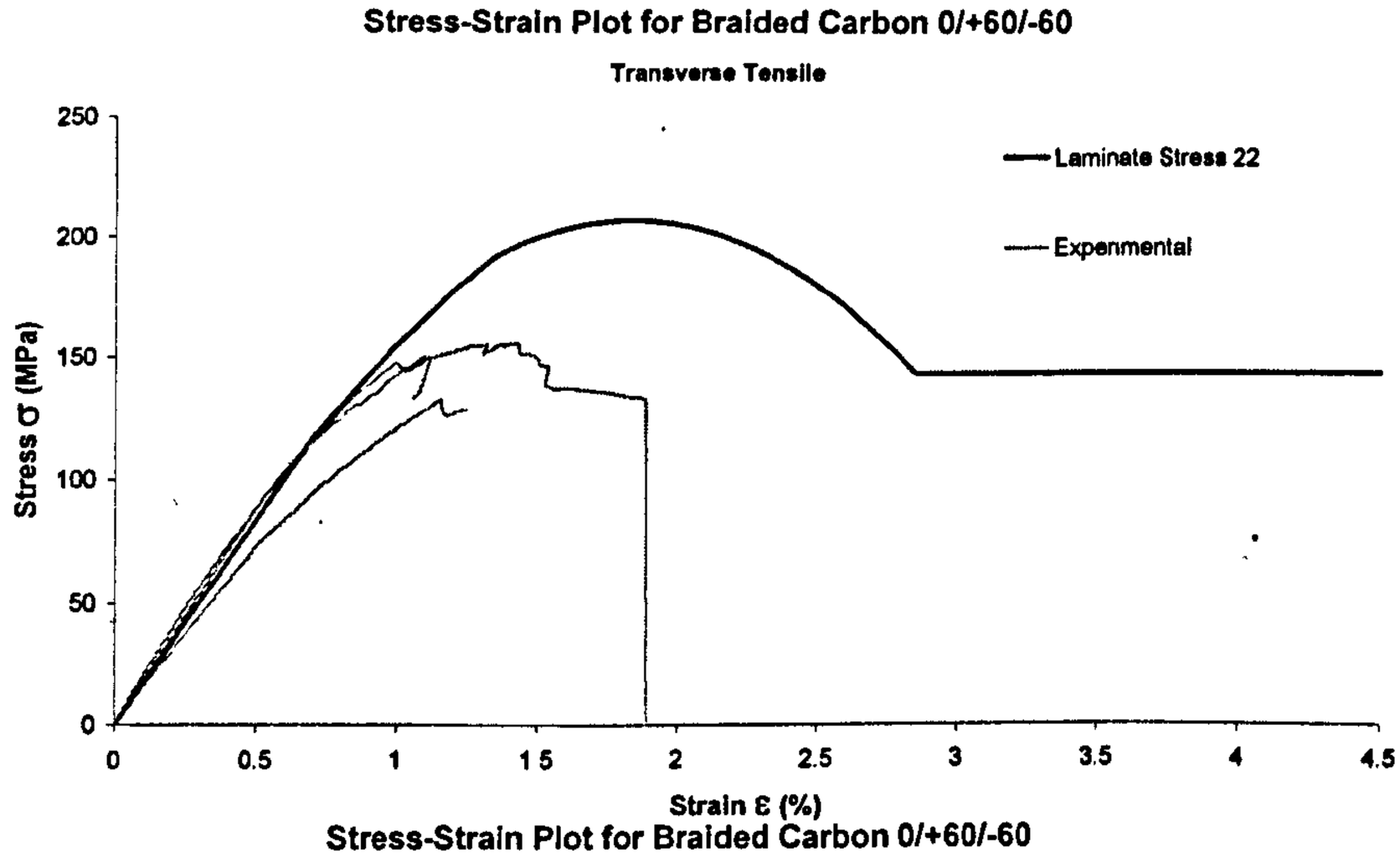
Stress-Strain Plot for Braided Carbon 0/+60/-60
Transverse Tensile
Laminate Stress 22
Experimental
Stress σ (MPa)
Strain ε (%)
250
200
150
100
50
0
0
0.5
1
1.5
2
2.5
3
3.5
4
4.5

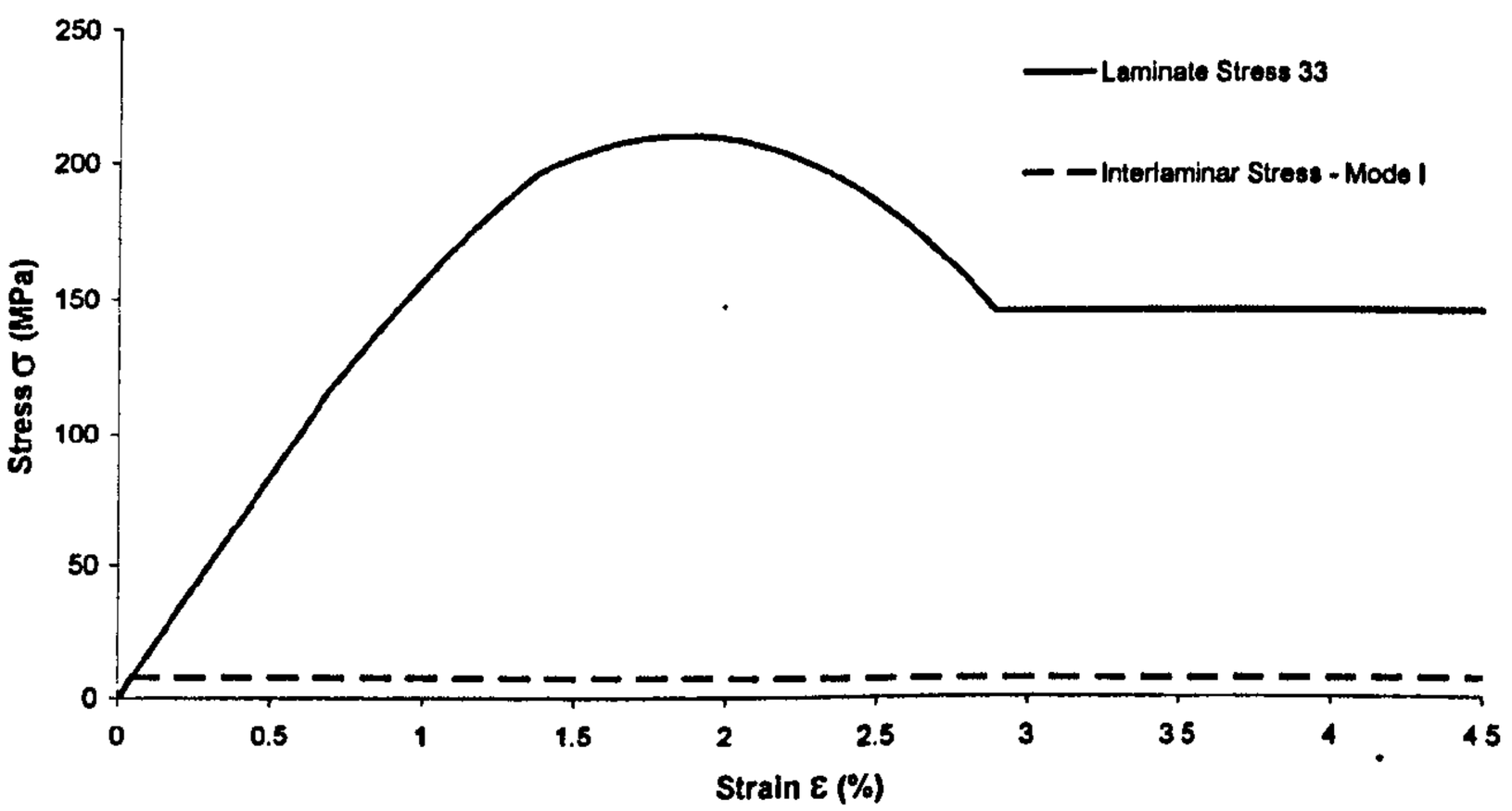
Stress-Strain Plot for Braided Carbon 0/+60/-60
Through-Thickness Tensile
Laminate Stress 33
Interlaminar Stress - Mode I
Stress σ (MPa)
Strain ε (%)
250
200
150
100
50
0
0
0.5
1
1.5
2
2.5
3
3.5
4
4.5

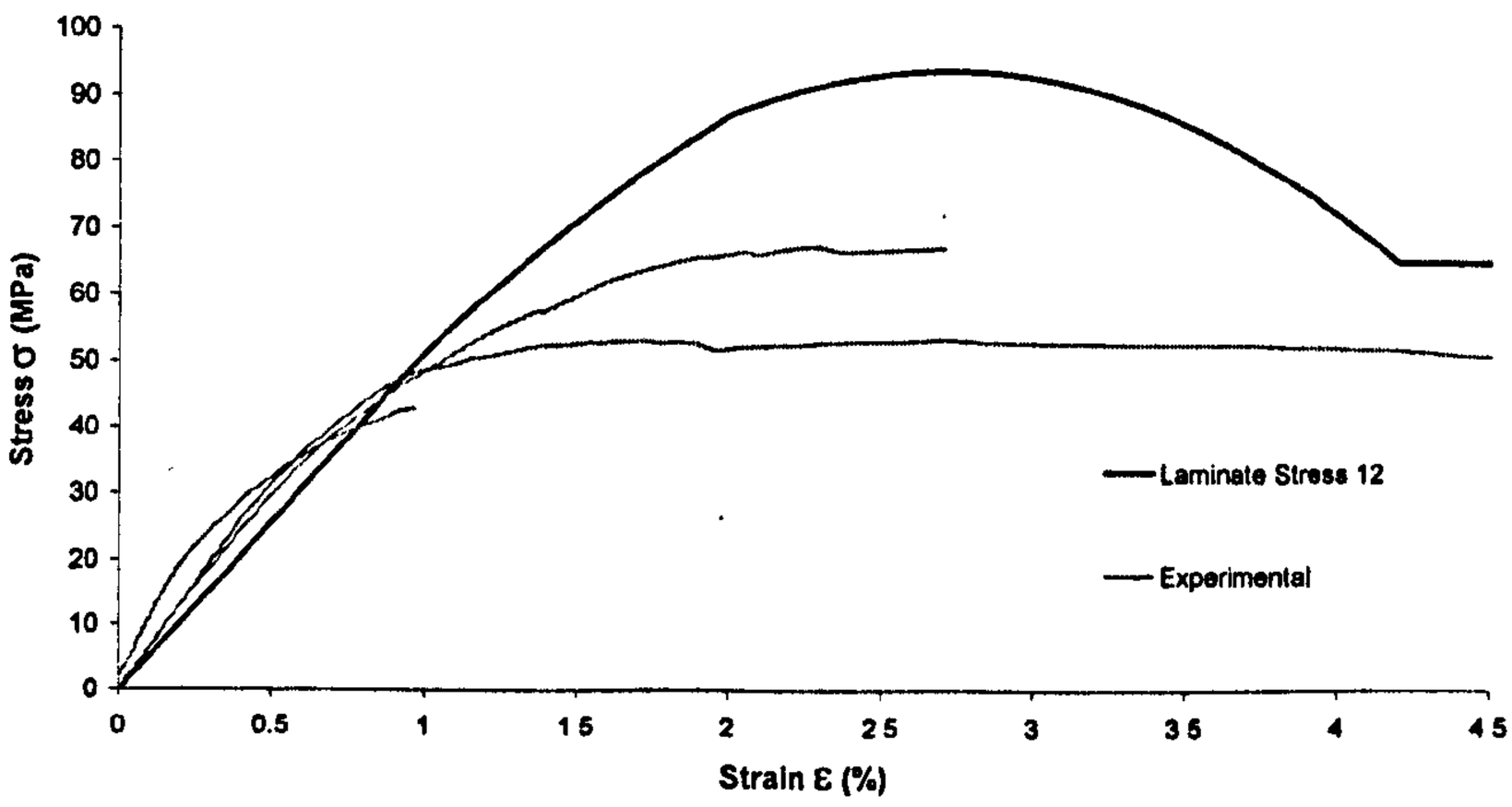
Stress-Strain Plot for Braided Carbon 0/+60/-60
Shear 12
Laminate Stress 12
Experimental
Stress σ (MPa)
Strain ε (%)
100
90
80
70
60
50
40
30
20
10
0
0
0.5
1
1.5
2
2.5
3
3.5
4
4.5

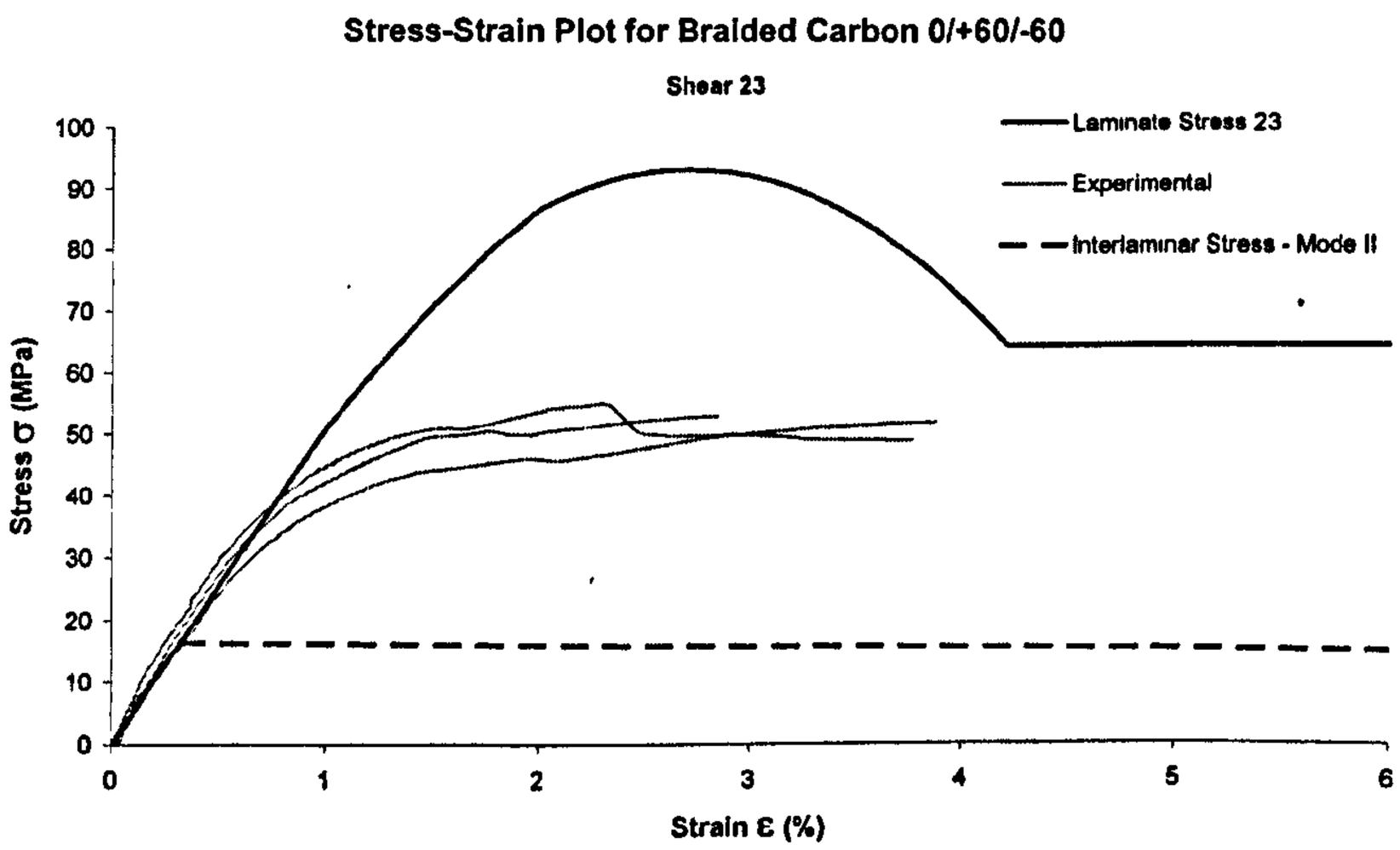
Stress-Strain Plot for Braided Carbon 0/+60/-60
Shear 23
Laminate Stress 23
Experimental
Interlaminar Stress - Mode II
Stress σ (MPa)
Strain ε (%)
100
90
80
70
60
50
40
30
20
10
0
0
1
2
3
4
5
6

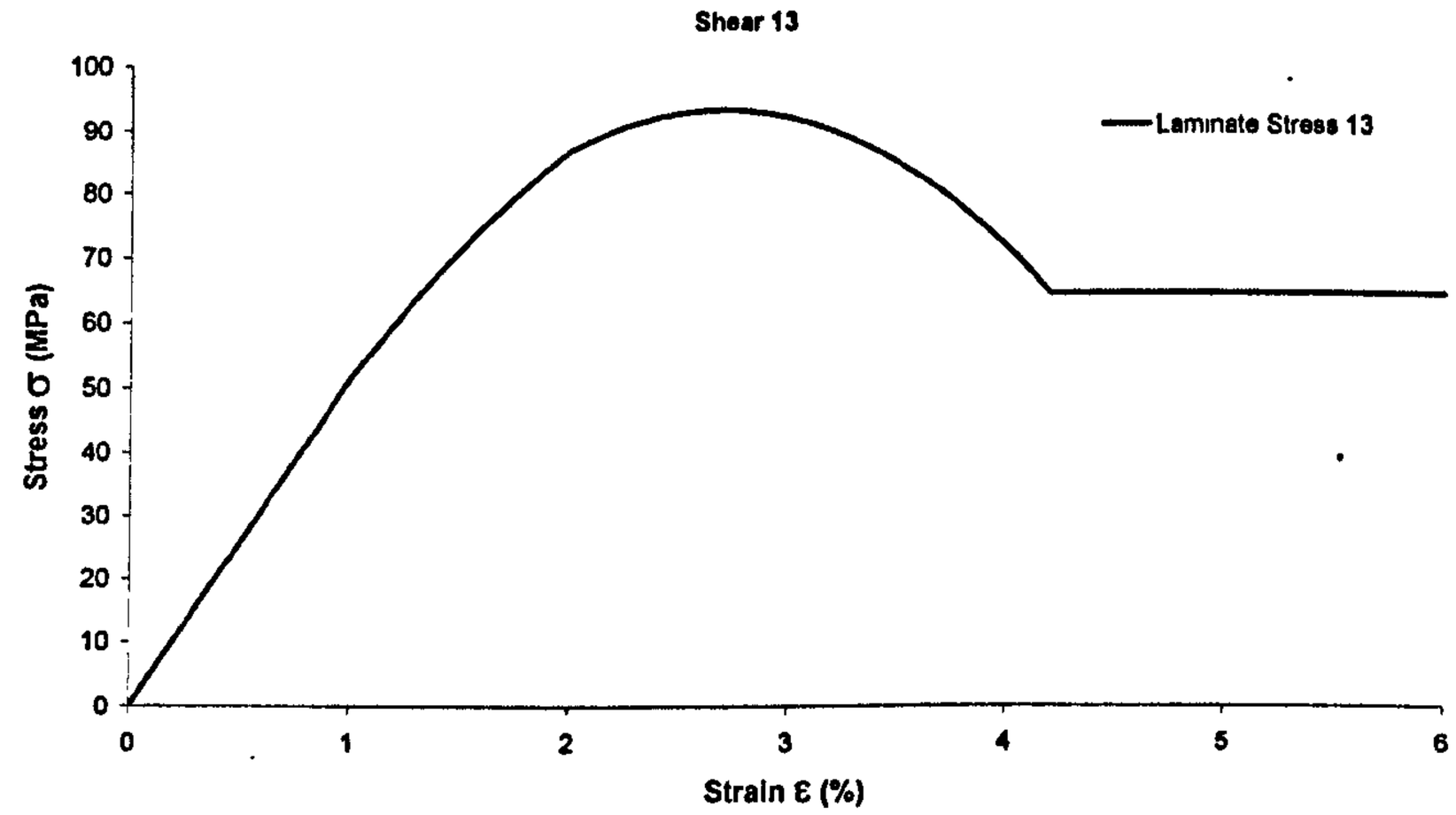
Stress-Strain Plot for Braided Carbon 0/+60/-60
Shear 13
Laminate Stress 13
Stress σ (MPa)
Strain ε (%)
100
90
80
70
60
50
40
30
20
10
0
0
1
2
3
4
5
6

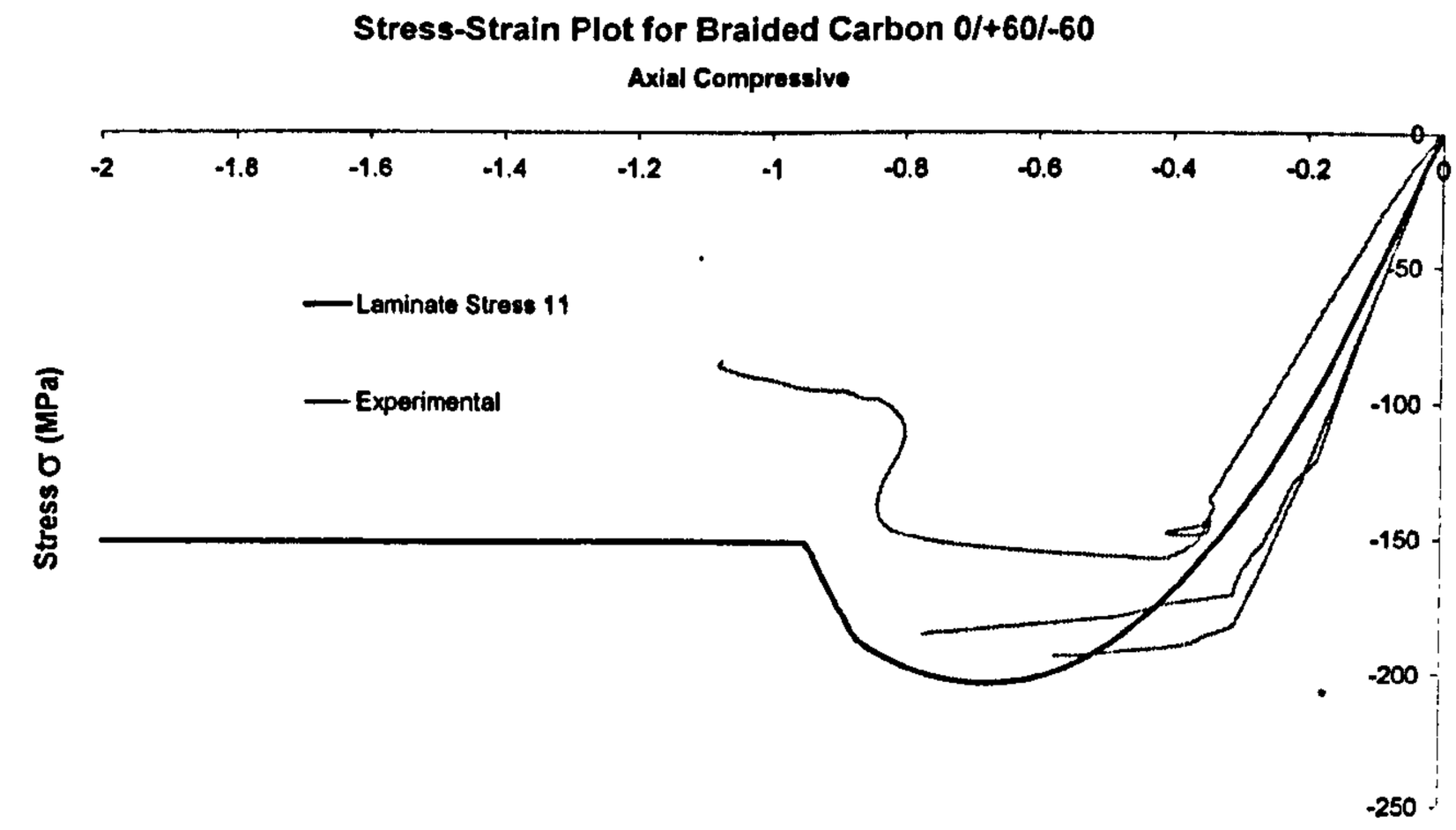
Stress-Strain Plot for Braided Carbon 0/+60/-60
Axial Compressive
Laminate Stress 11
Experimental
Stress σ (MPa)
Strain ε (%)
-2
-1.8
-1.6
-1.4
-1.2
-1
-0.8
-0.6
-0.4
-0.2
0
0
-50
-100
-150
-200
-250

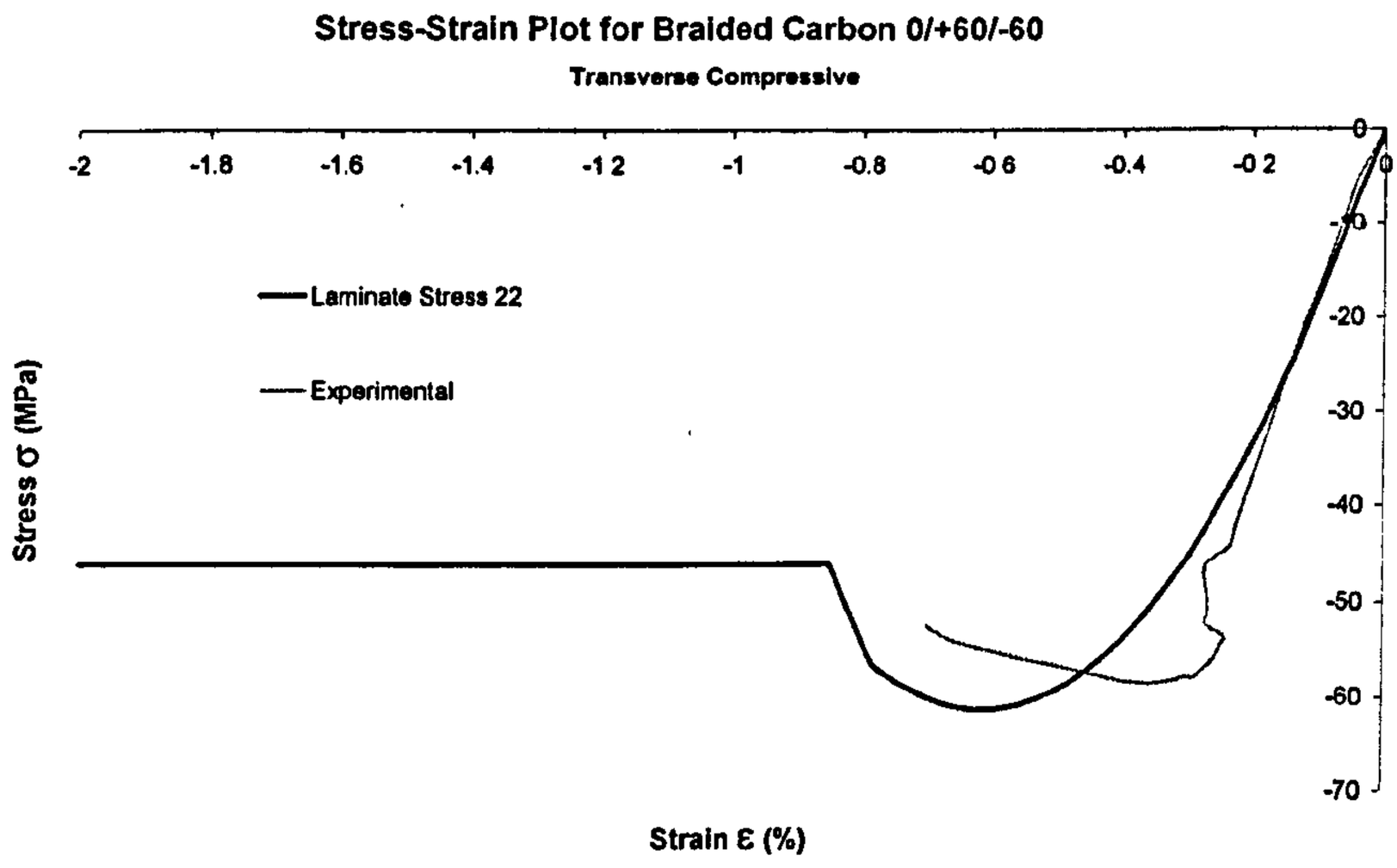
Stress-Strain Plot for Braided Carbon 0/+60/-60
Transverse Compressive
-2
-1.8
-1.6
-1.4
-1 2
-1
-0.8
-0 6
-0.4
-0 2
0
-10
-20
-30
-40
-50
-60
-70
Laminate Stress 22
Experimental
Stress σ (MPa)
Strain ε (%)

6.0 Coupon Finite Element Modelling

To validate the material modelling described in the previous chapters, the experimental coupon tests were modelled. For all tests, the representation of the crosshead displacement of the test machine was by means of an imposed displacement boundary condition at the rate of 0.1mm/ms. Intralaminar tests of braided carbon were modelled as these showed anisotropic in-plane behaviour, which required a more careful assessment of the material model's performance. Interlaminar tests for CoFRM were modelled to validate the delamination model.

6.1 Intralaminar Tests

For each of the tests, three modelling techniques were used:

- single shell
- bi-shell with one contact interface (delamination model)
- multi-shell (6 shells) with five contact interfaces (delamination model)

Modelling the Interlaminar Region

For the bi-shell and multi-shell models, the interlaminar region is represented by the delamination model described in Chapter 4. Nodes on adjacent elements are connected through the contact interface. One of the plies contains the slave nodes while the adjacent ply is consisted of the slave elements, Figure 6-1.

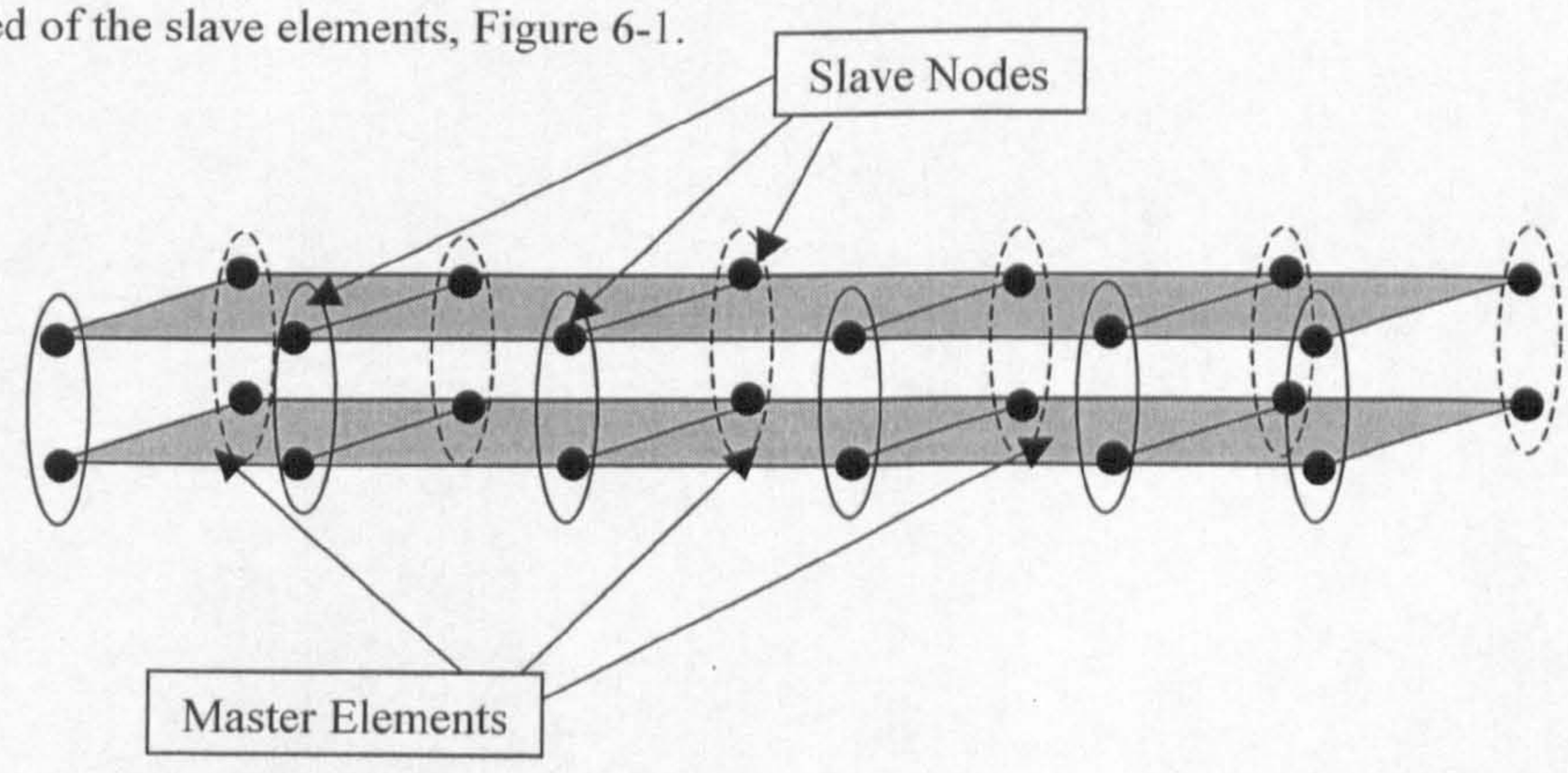

Figure 6-1 – Interlaminar modelling between adjacent plies for bi-shell and multi-shell tests

Details of the models and respective results are shown in the following sections.

6.1.1 Tensile Tests

A total of 18 tensile tests were modelled as we have 3 different braid architectures, 2 types of test for each architecture (axial and compressive) using the 3 different modelling approaches described in the previous paragraph.

6.1.1.1 FE Models

Figure 6-2 shows the three different FE models used for the tensile test, while Figure 6-4 shows details of the boundary conditions imposed.

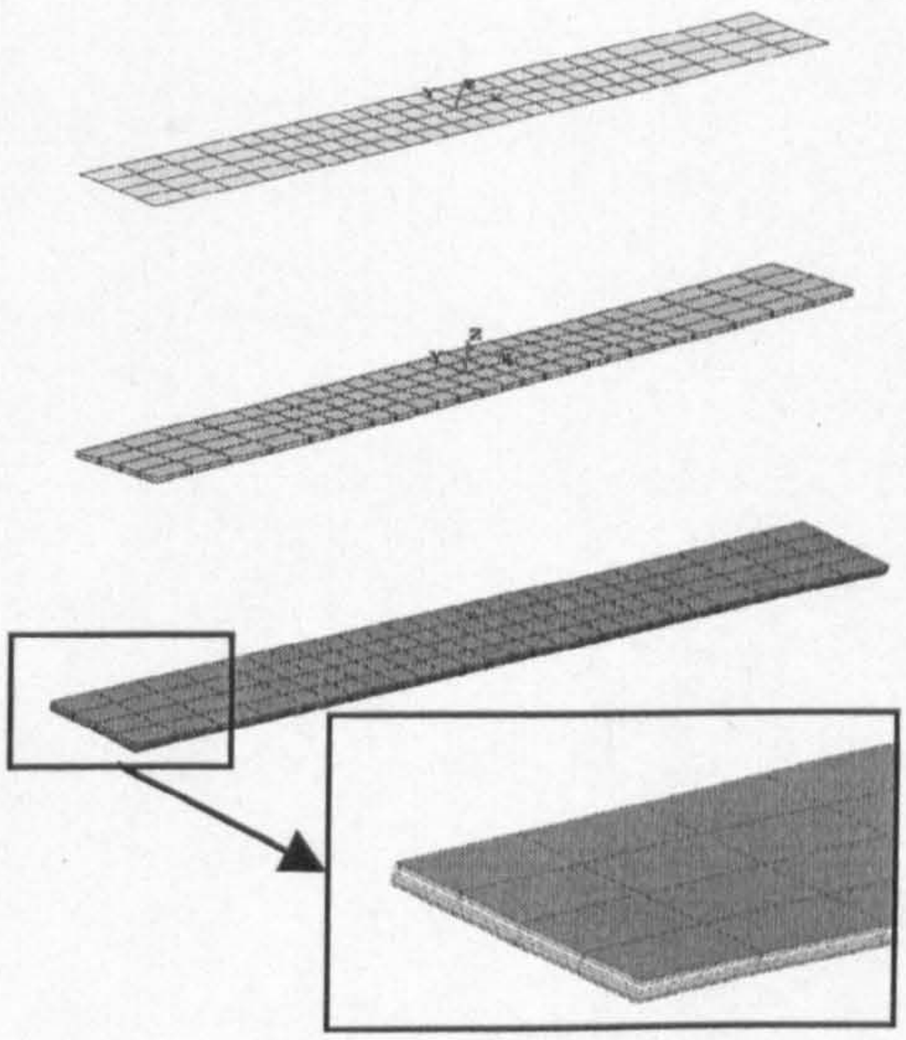

Figure 6-2 - FE Models for Tensile Test - single shell (top), Bi-shell (middle) and multi-shell (bottom)

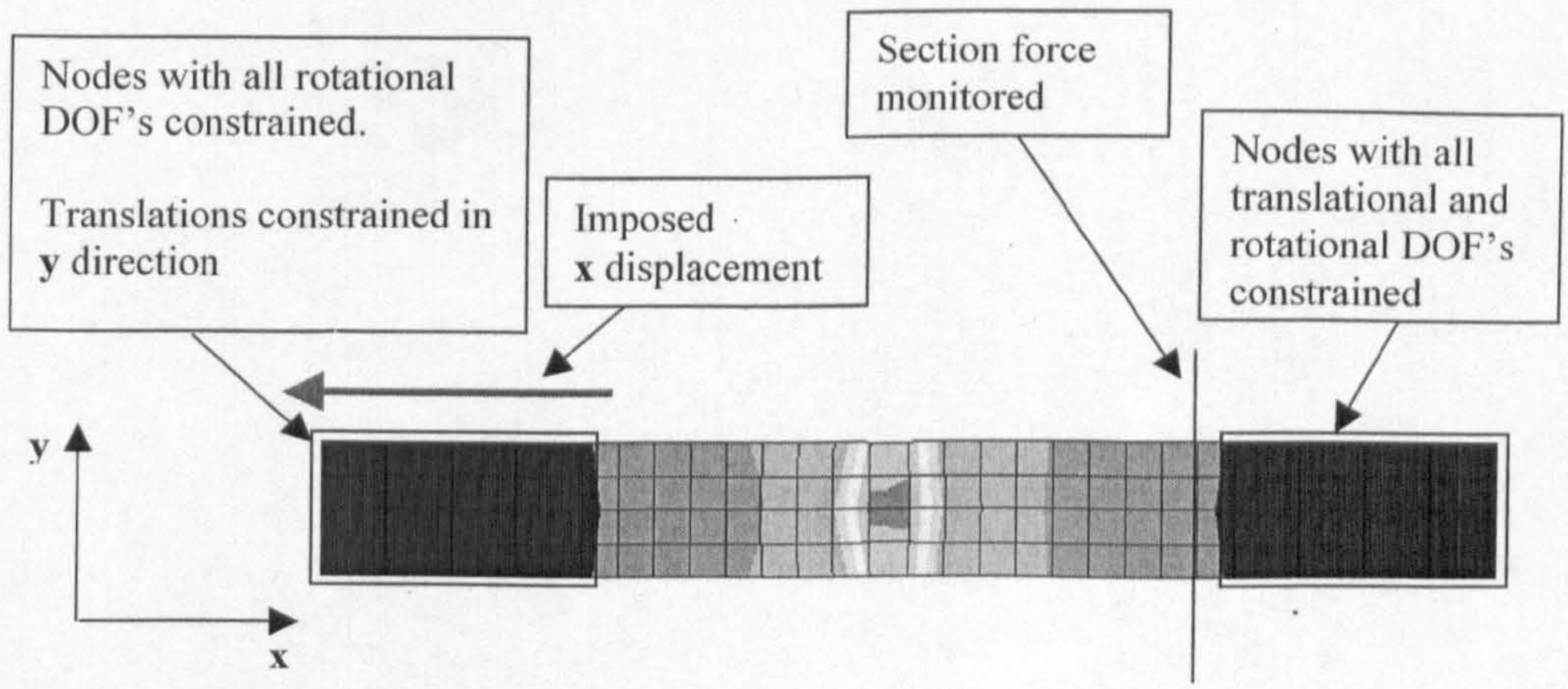

Figure 6-3 – Boundary Conditions in Tensile Test

6.1.1.2 Axial Tensile Results

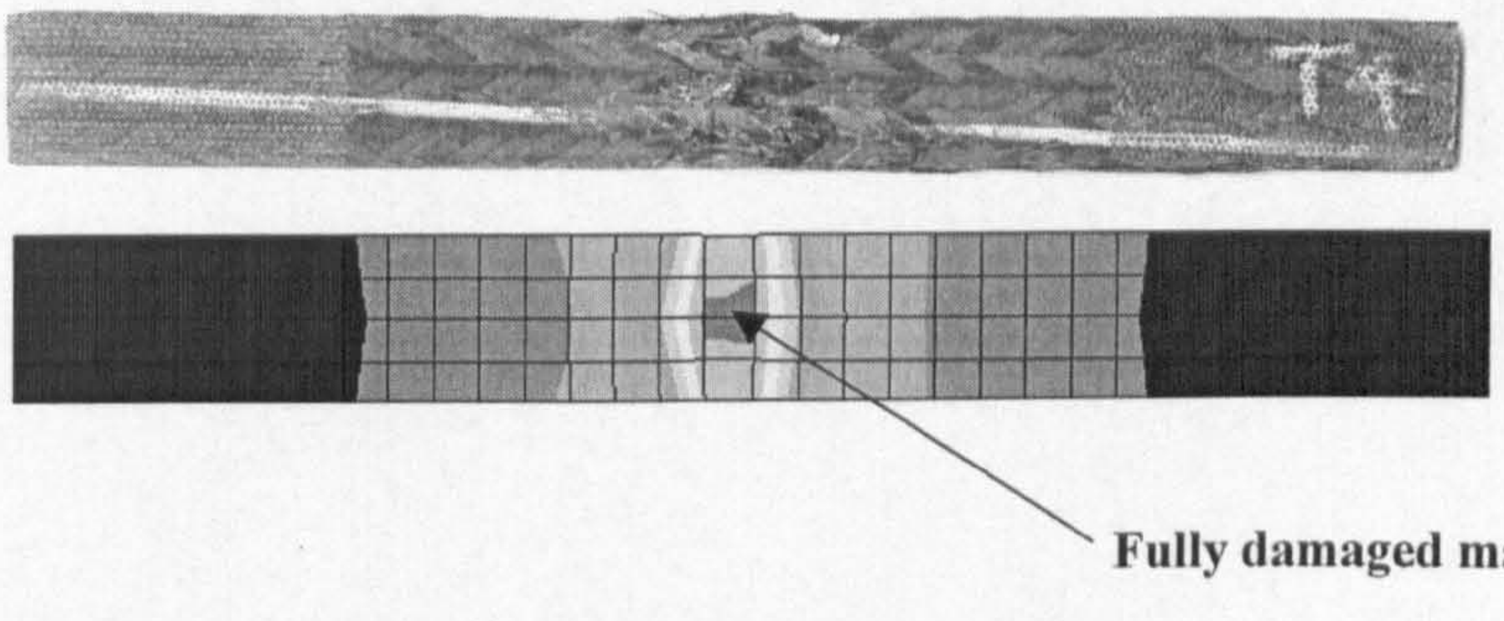

Figure 6-4 - Damage and failure of Single-shell Axial Tensile Test

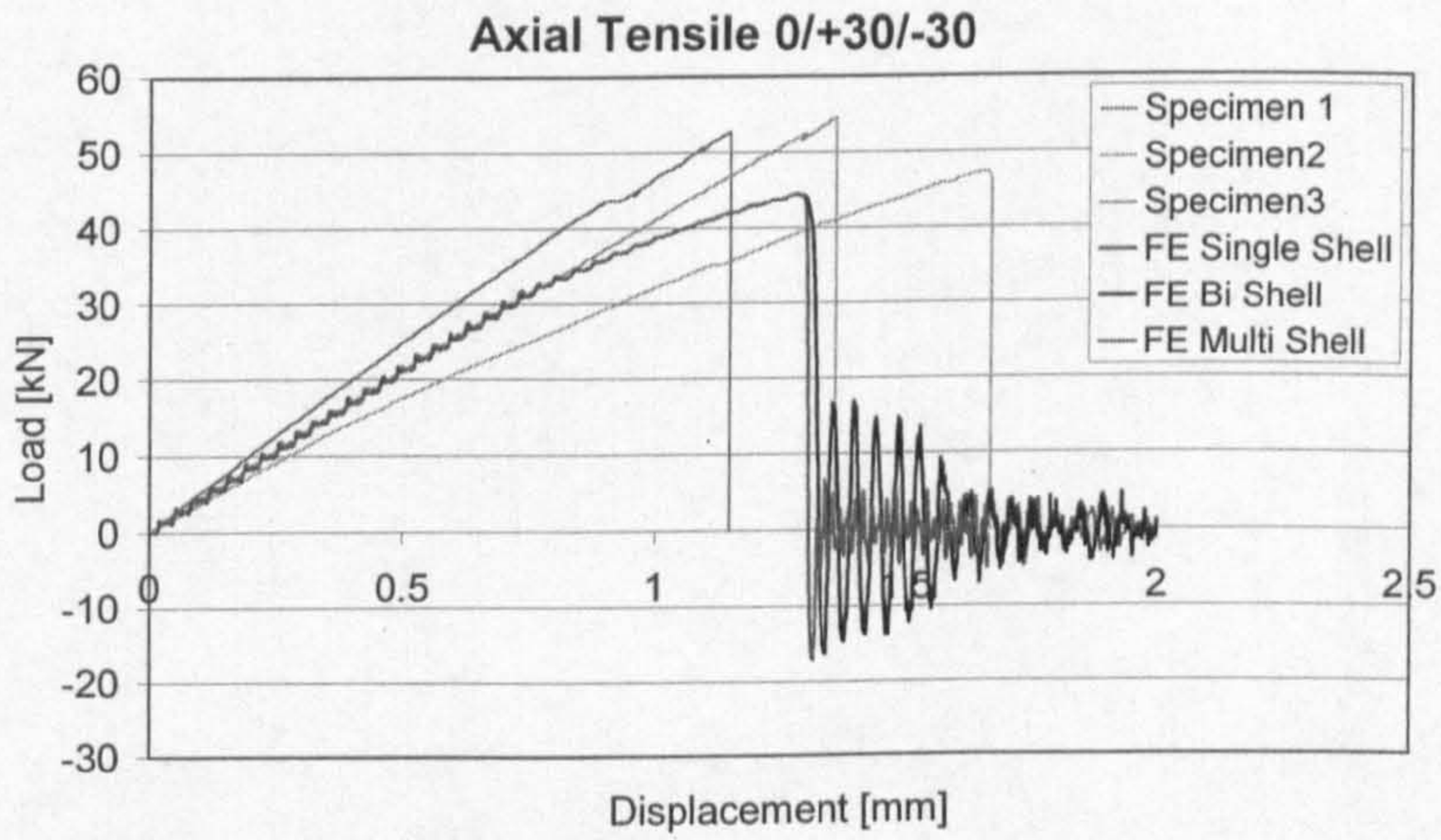

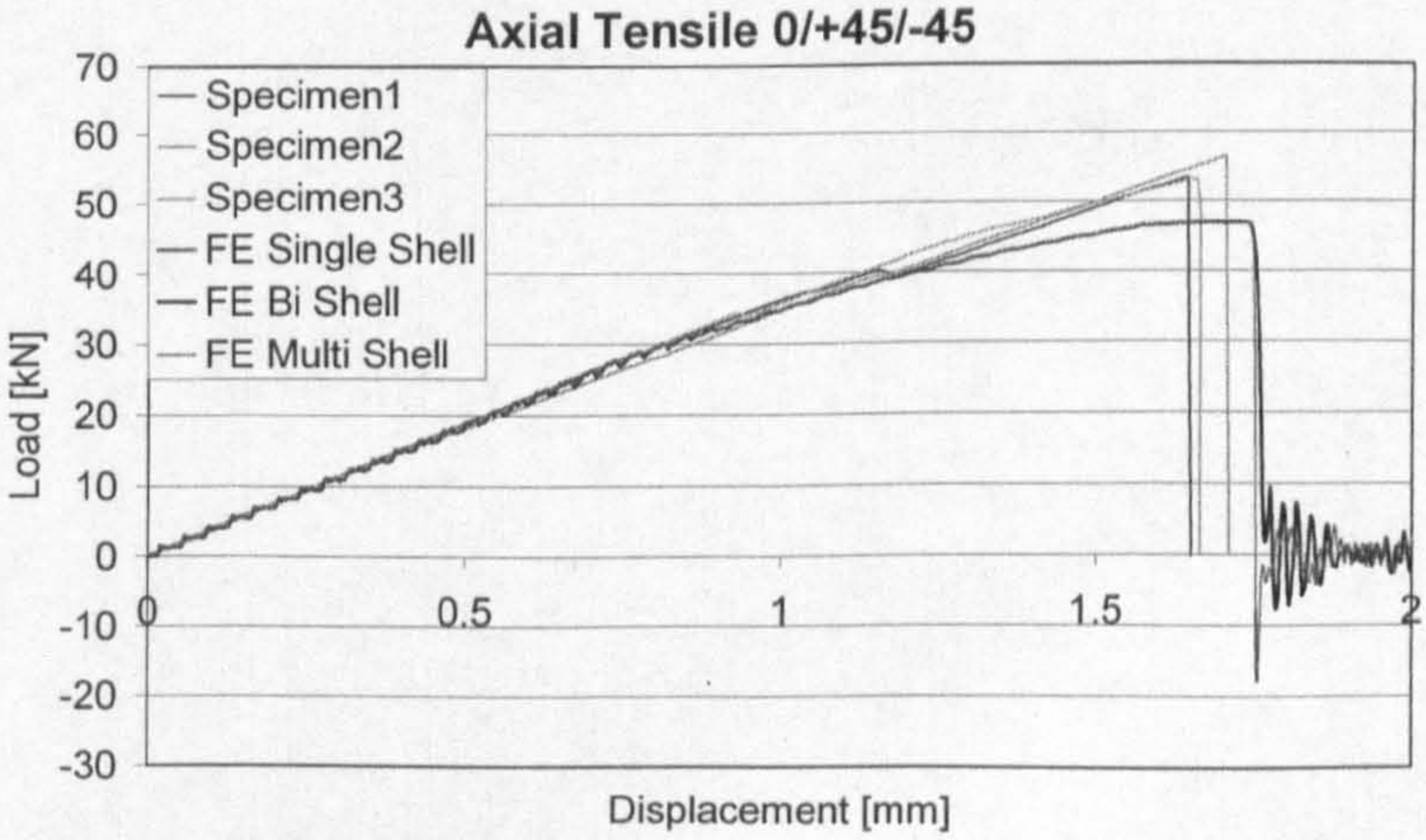

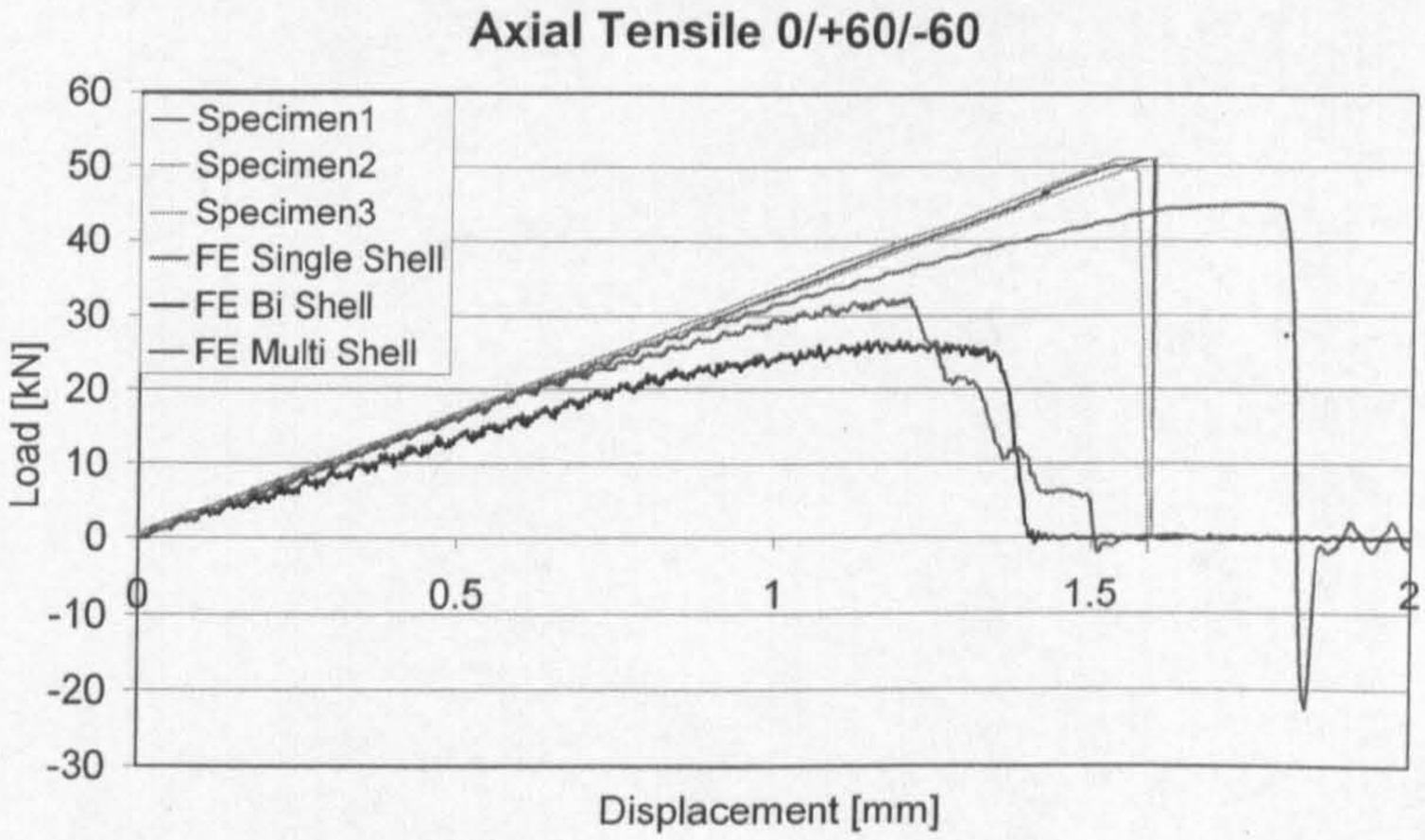

Observations

The agreement between the FE and experimental curves is generally good. The contribution of interlaminar behaviour to determine the failure strain of the specimen can be observed mostly on the 0°/+60°/-60° test, where the bi-shell and multi-shell models are damaged at an earlier stage than the single-shell one.

6.1.1.3 Transverse Tensile Results

Figure 6-5 shows the better accuracy of the multi-shell approach to model the failure mechanism of the specimen. The bi-shell model exhibited premature element elimination due to a propagation of the interlaminar failure.

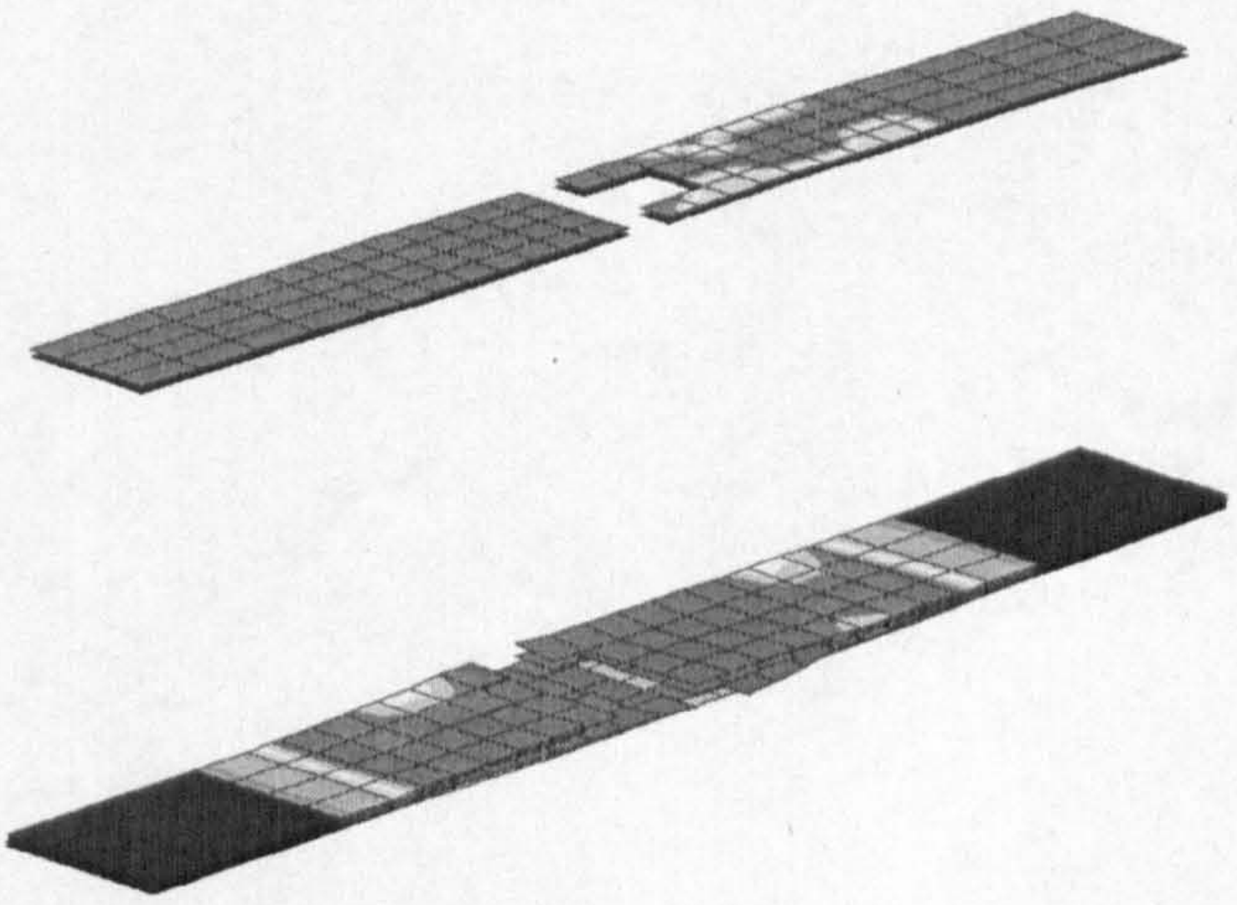

Figure 6-5 – Delamination in Bi-shell and Multi-Shell Transverse Tensile Test

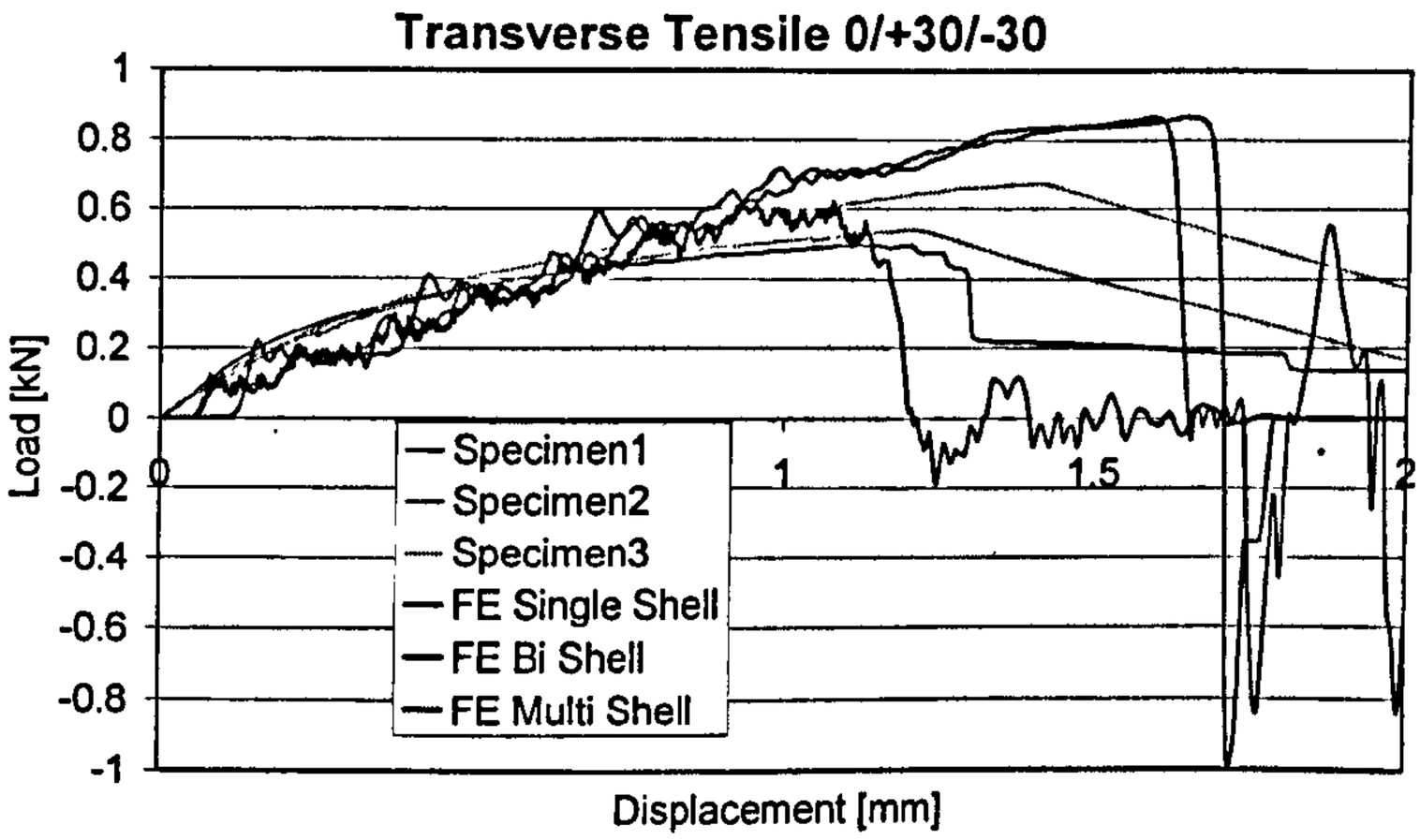
Transverse Tensile 0/+30/-30
Load [kN]
Displacement [mm]
Specimen1
Specimen2
Specimen3
FE Single Shell
FE Bi Shell
FE Multi Shell

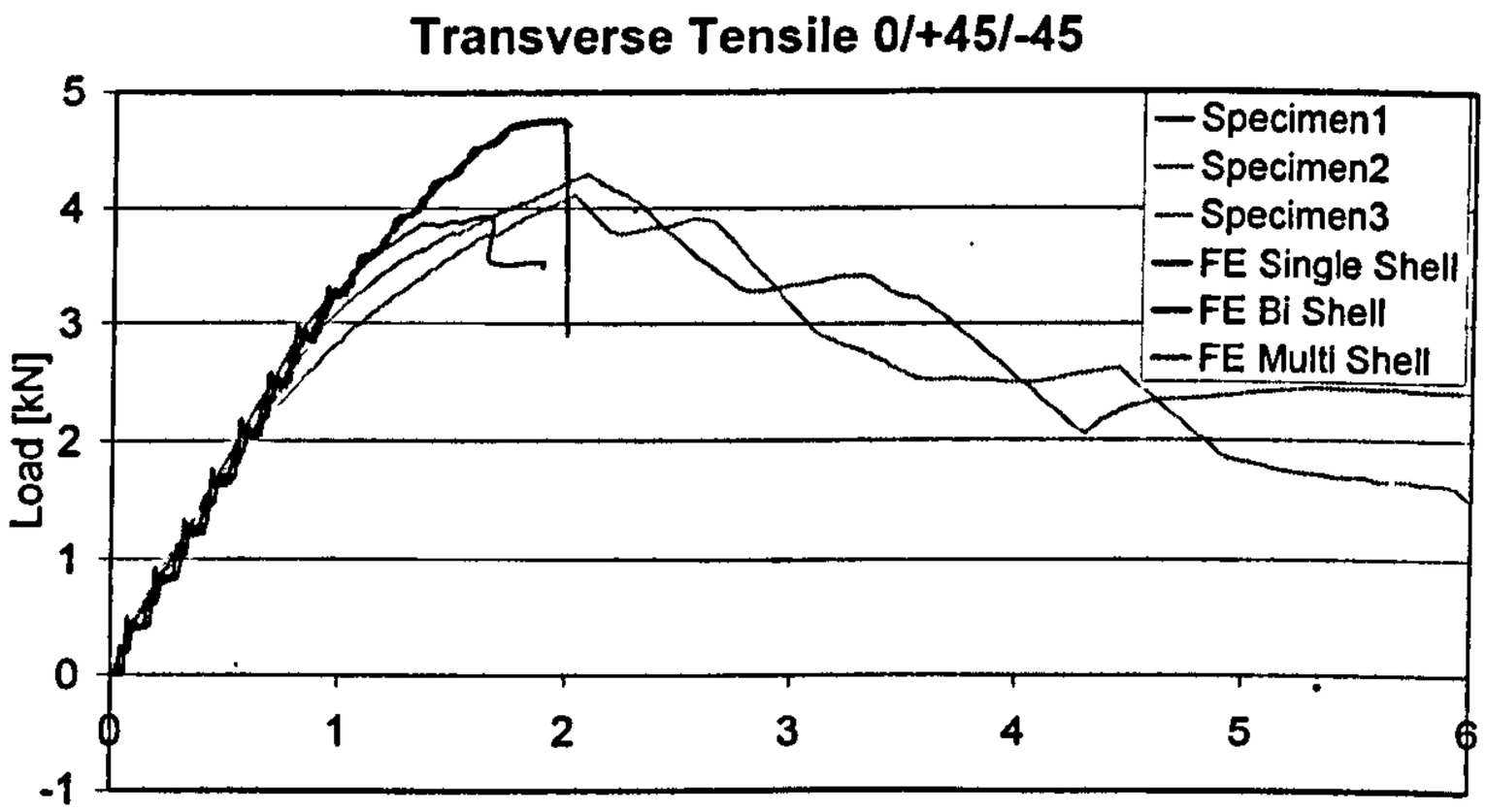
Transverse Tensile 0/+45/-45
Load [kN]
Displacement [mm]
Specimen1
Specimen2
Specimen3
FE Single Shell
FE Bi Shell
FE Multi Shell

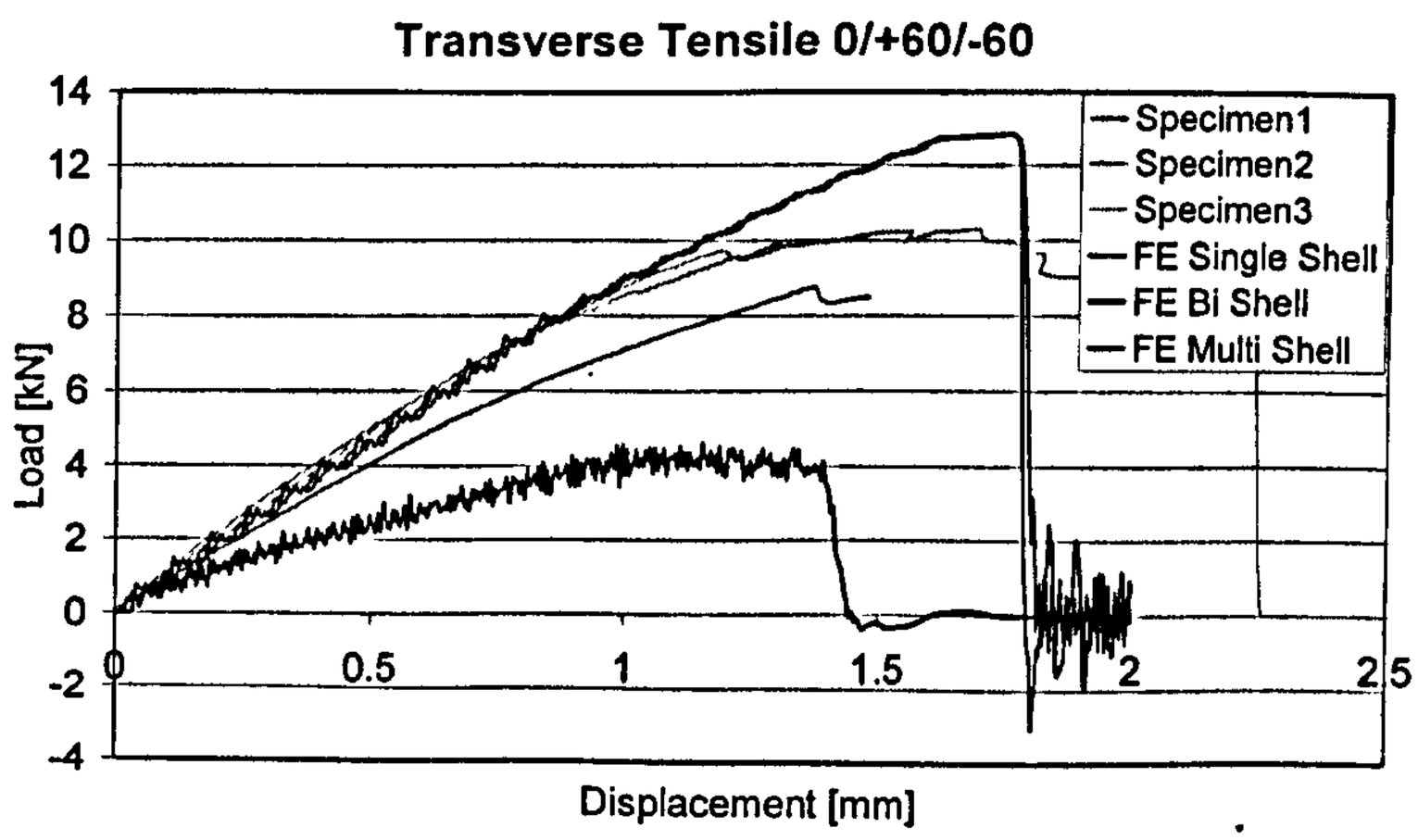
Transverse Tensile 0/+60/-60
Load [kN]
Displacement [mm]
Specimen1
Specimen2
Specimen3
FE Single Shell
FE Bi Shell
FE Multi Shell

Observations

As with the Axial Tensile test, there is generally reasonable agreement between the numerical and experimental results. The Bi-shell model for the 0°/+60°/-60° exhibits excessive damage leading to a decrease in stiffness followed by premature failure. Such may be attributed to an inaccurate definition of interlaminar properties for which only data for the 0°/+30°/-30° architecture was available. This inaccuracy is not so relevant for the 0°/+45°/-45° model as the properties for this architecture are expected to be closer to the 0°/+30°/-30° ones.

6.1.2 Compressive Tests

A total of 18 tensile tests were modelled as we have 3 different braid architectures, 2 types of test for each architecture (axial and compressive) using the 3 different modelling approaches.

6.1.2.1 FE Models

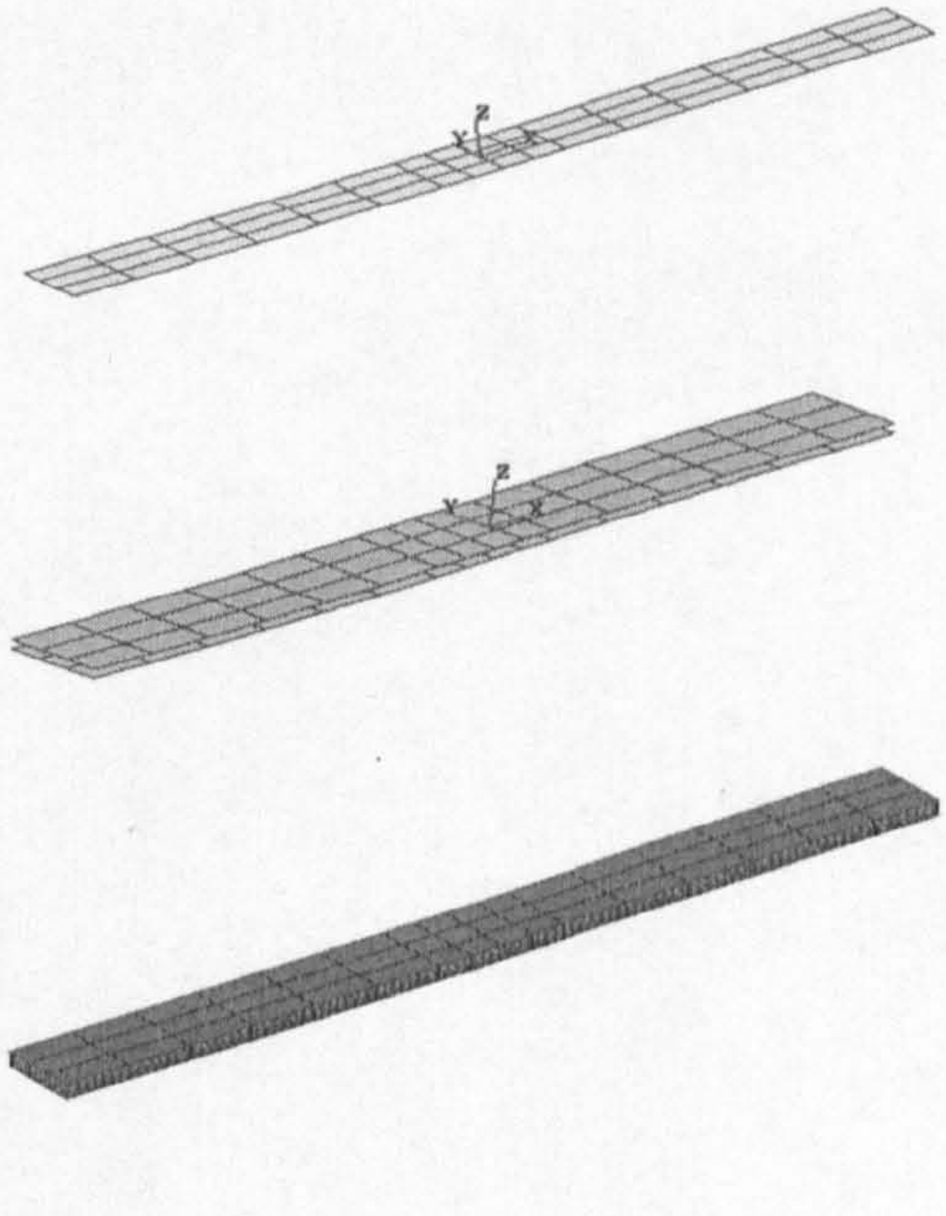

Figure 6-6 – FE Models for Compressive Test

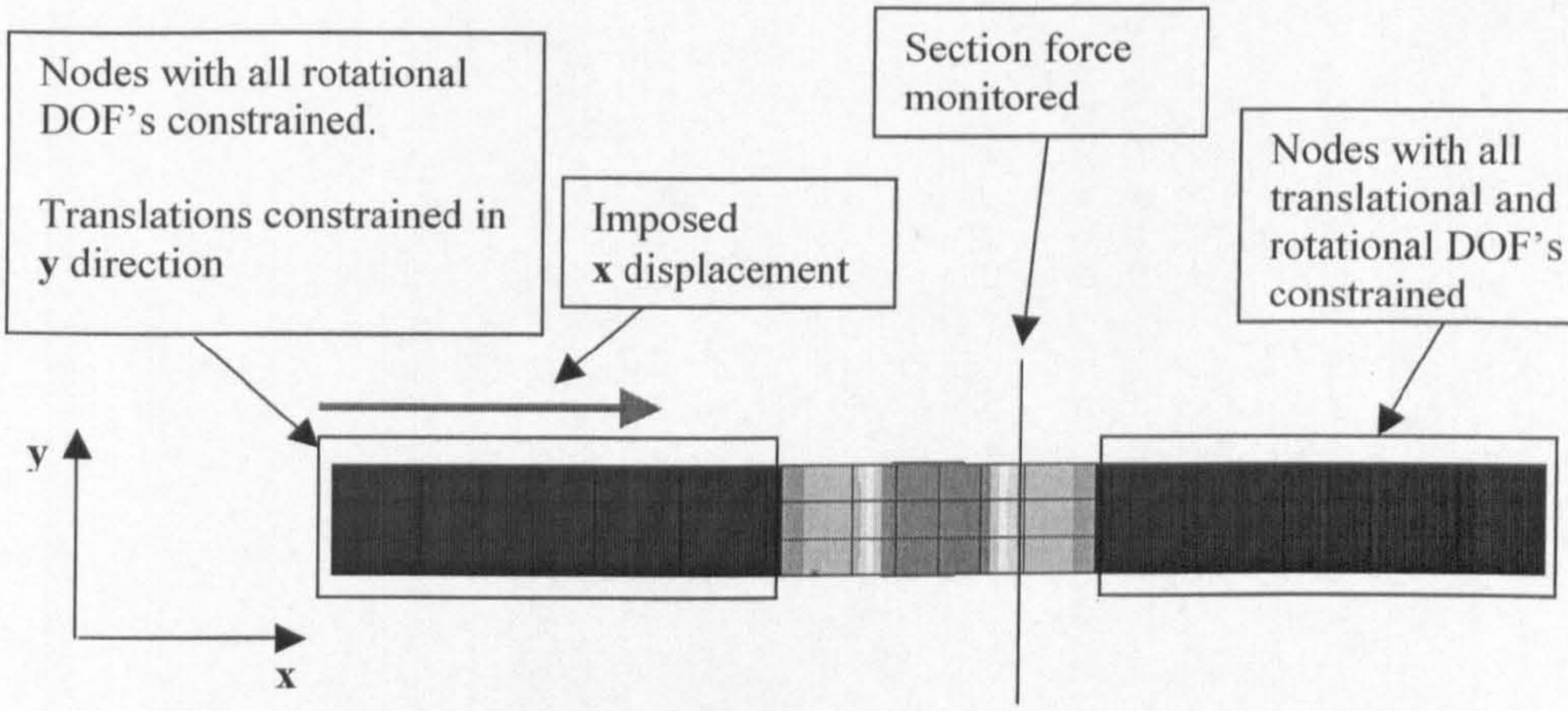

Figure 6-7 - Boundary Conditions in Compressive Test

6.1.2.2 Axial Compressive Results

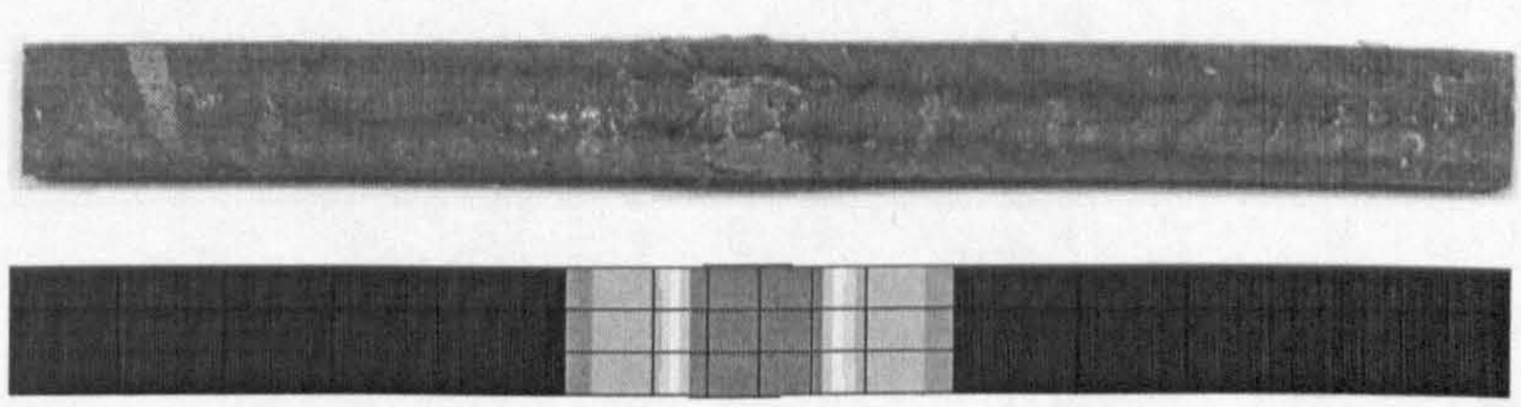

Figure 6-8 Damage and failure of Single-shell Axial Compressive Test

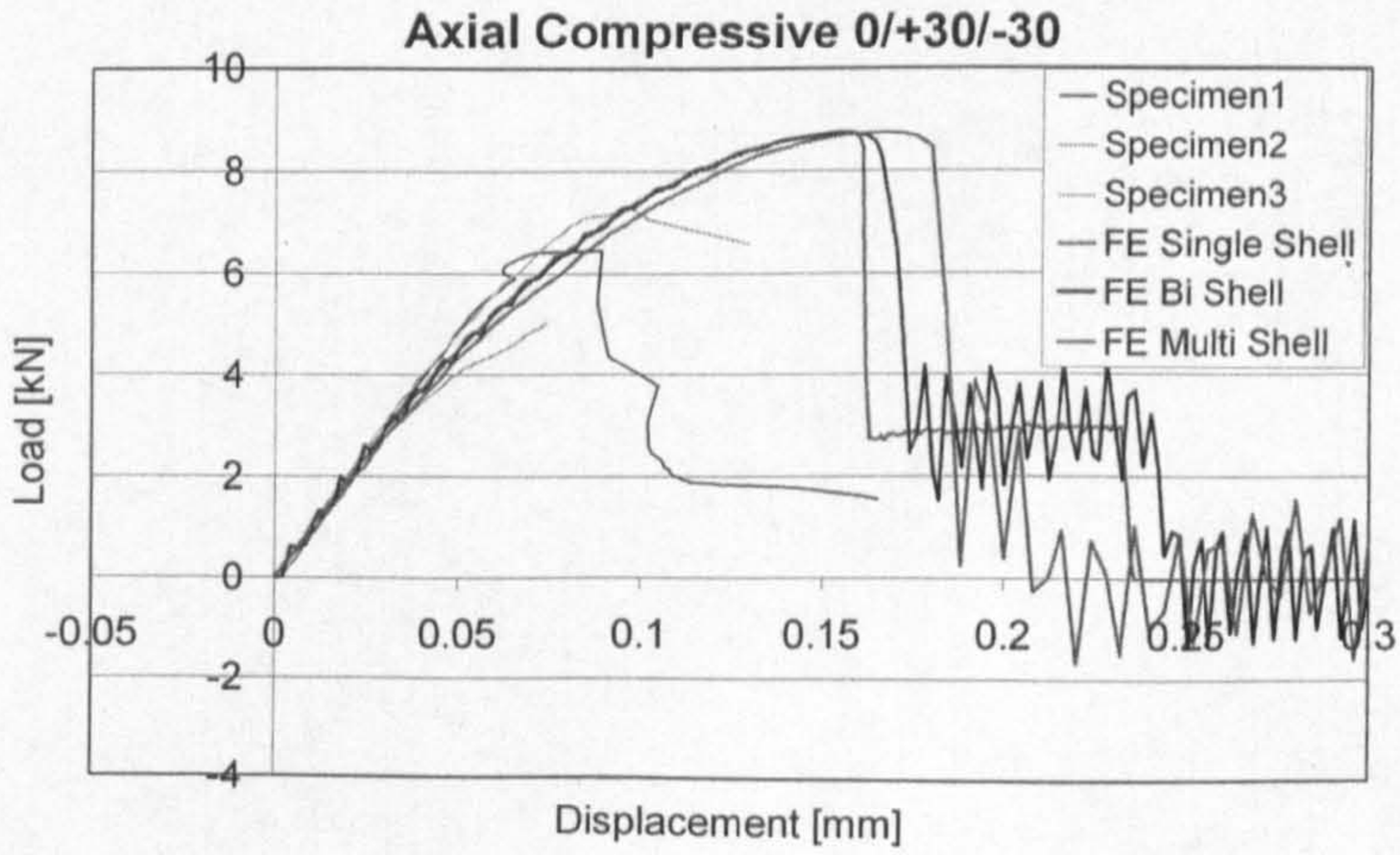

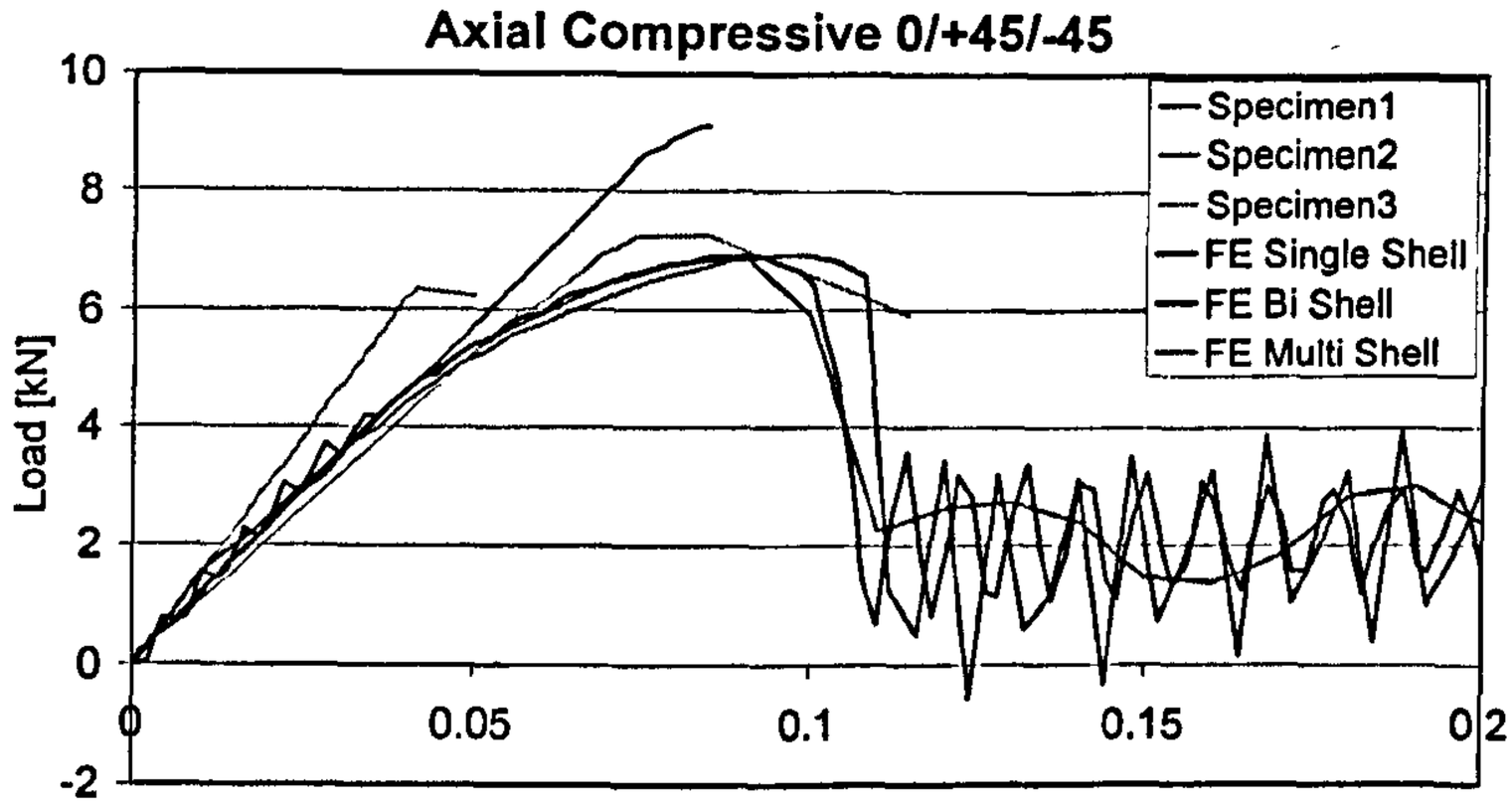
Axial Compressive 0/+45/-45
Load [kN]
Displacement [mm]
Specimen1
Specimen2
Specimen3
FE Single Shell
FE Bi Shell
FE Multi Shell
10
8
6
4
2
0
-2
0
0.05
0.1
0.15
0.2

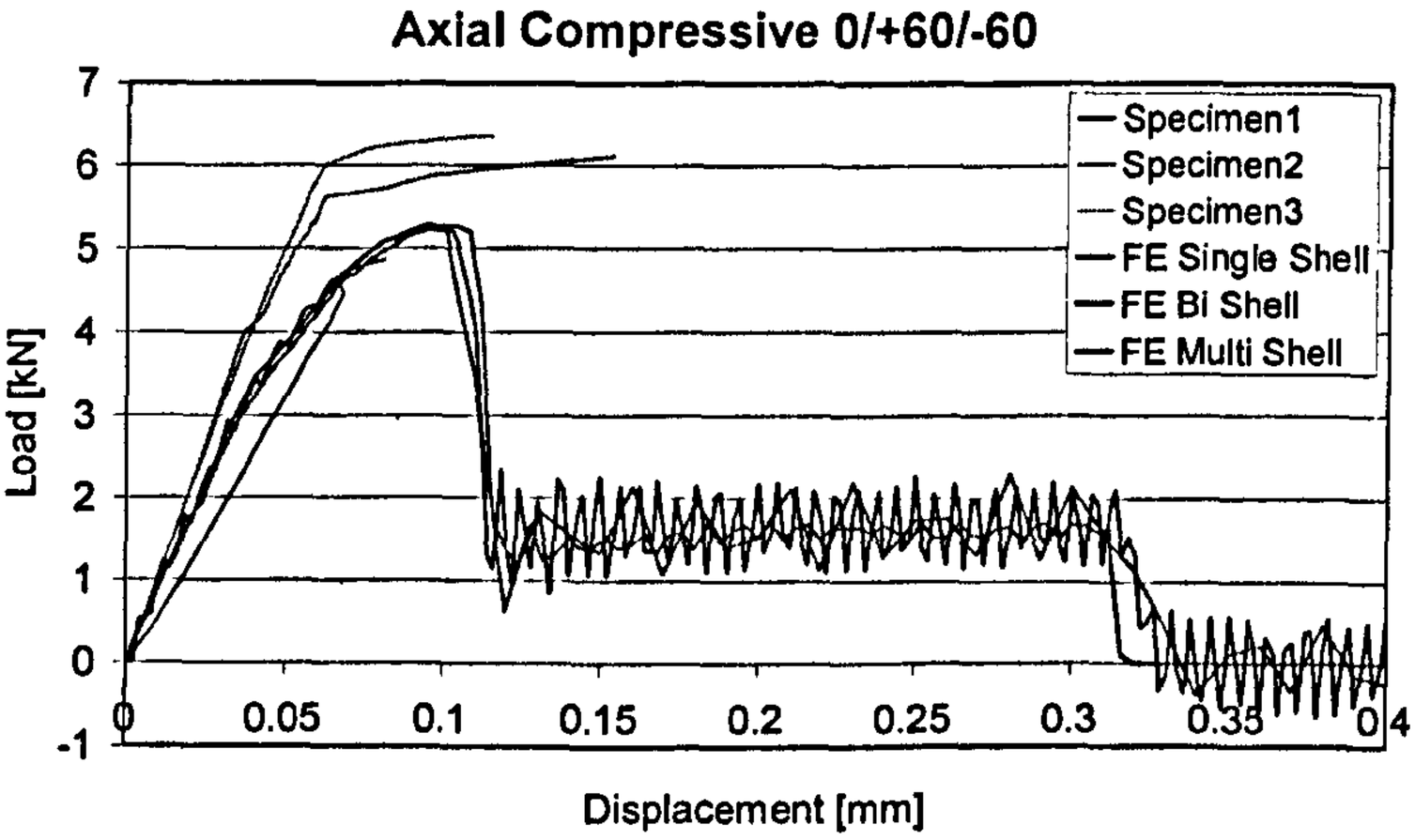
Axial Compressive 0/+60/-60
Load [kN]
Displacement [mm]
Specimen1
Specimen2
Specimen3
FE Single Shell
FE Bi Shell
FE Multi Shell
7
6
5
4
3
2
1
0
-1
0
0.05
0.1
0.15
0.2
0.25
0.3
0.35
0.4

6.1.2.3 Transverse Compressive Results

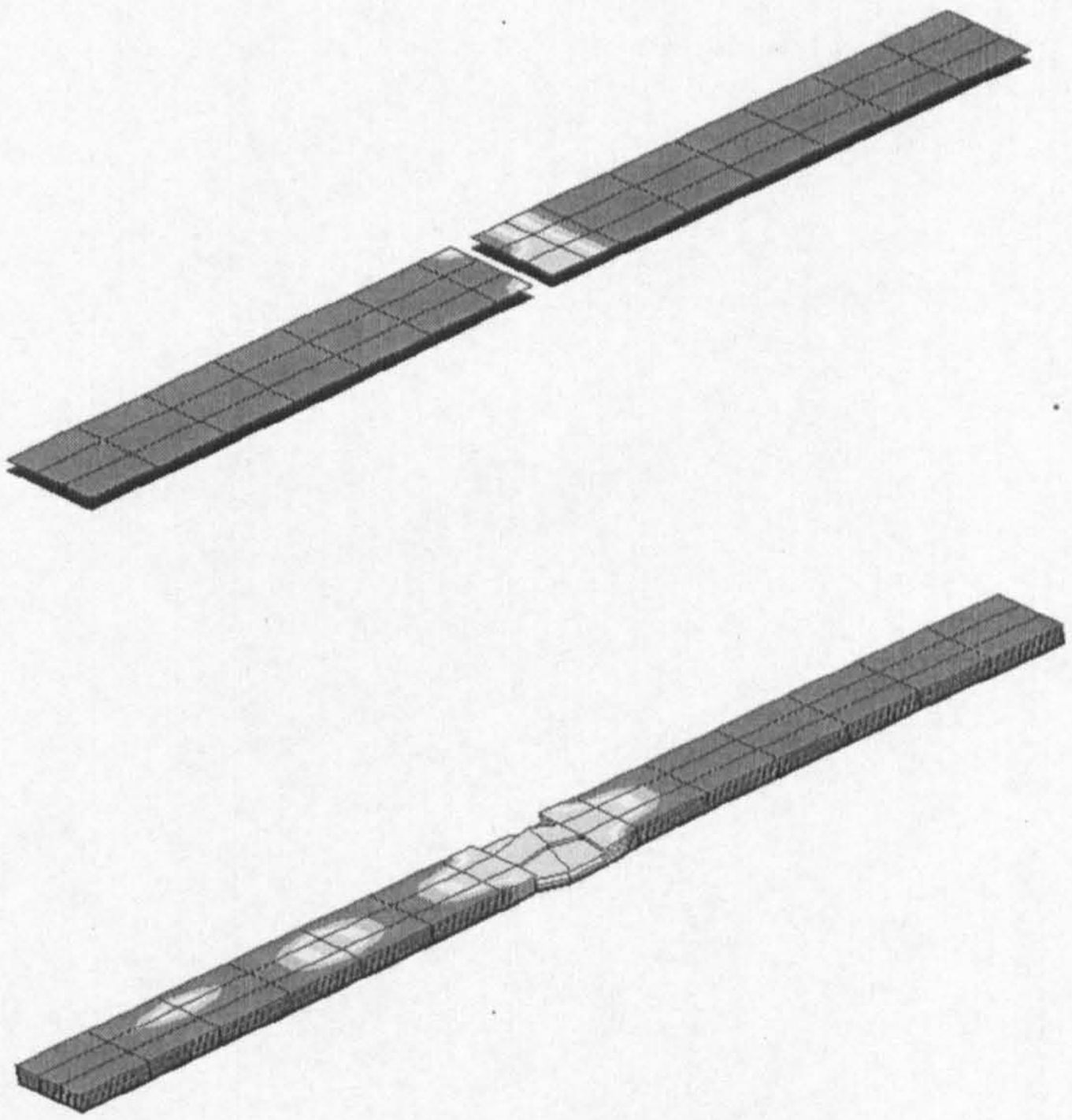

Figure 6-9 - Delamination in Bi-shell and Multi-Shell Transverse Compressive Test

As with the tensile test, the multi-shell model also allowed a better simulation of the interlaminar failure that occurred in the test specimen. However, the difference in results arising from the more accurate interlaminar modelling of the multi-shell approach is less noticeable for the compressive tests when compared with the axial. That can be seen on the load displacement curves, which show reasonable agreement for all three modelling approaches.

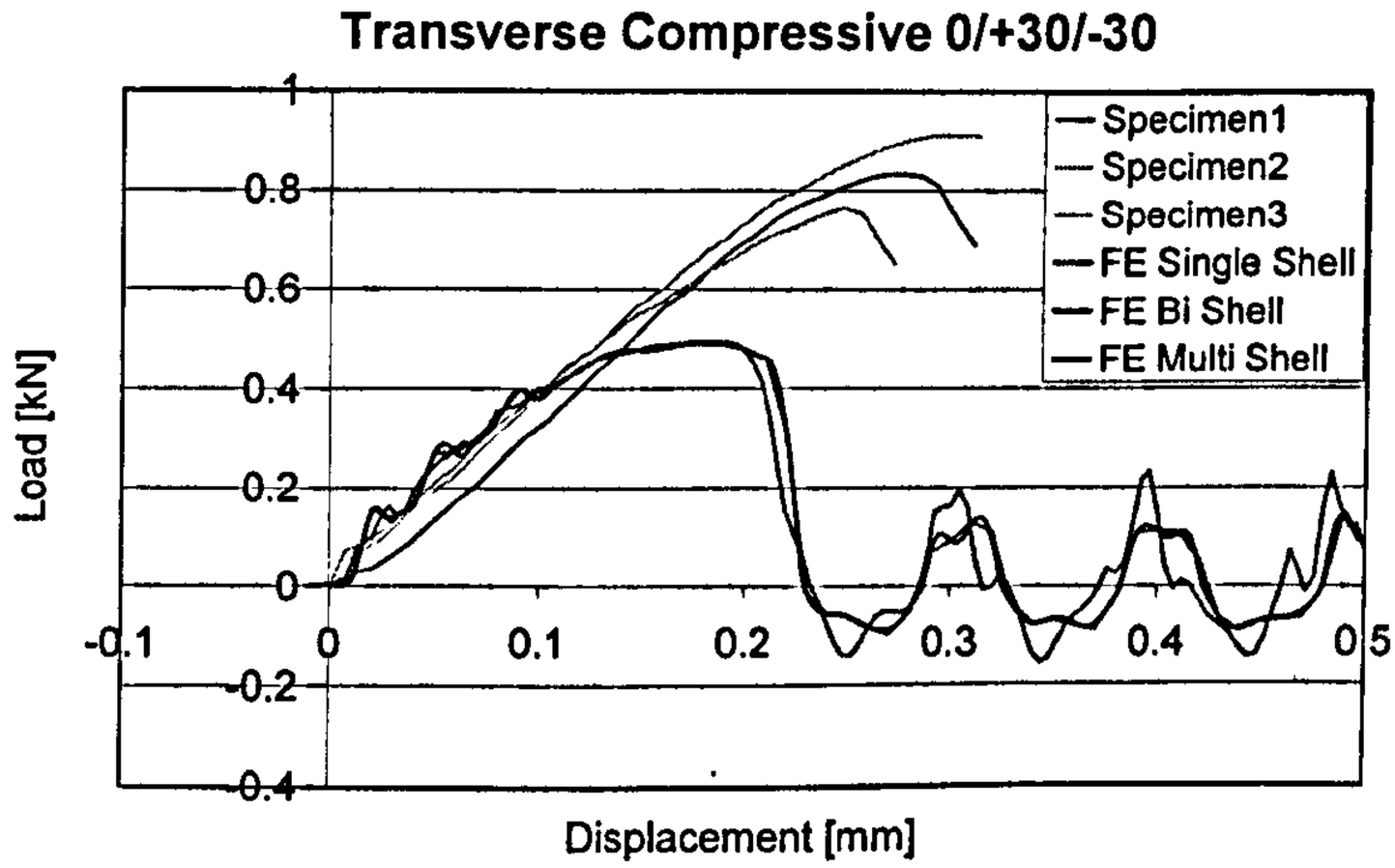
Transverse Compressive 0/+30/-30
Load [kN]
Displacement [mm]
Specimen1
Specimen2
Specimen3
FE Single Shell
FE Bi Shell
FE Multi Shell
1
0.8
0.6
0.4
0.2
0
-0.2
0.4
-0.1
0
0.1
0.2
0.3
0.4
0.5

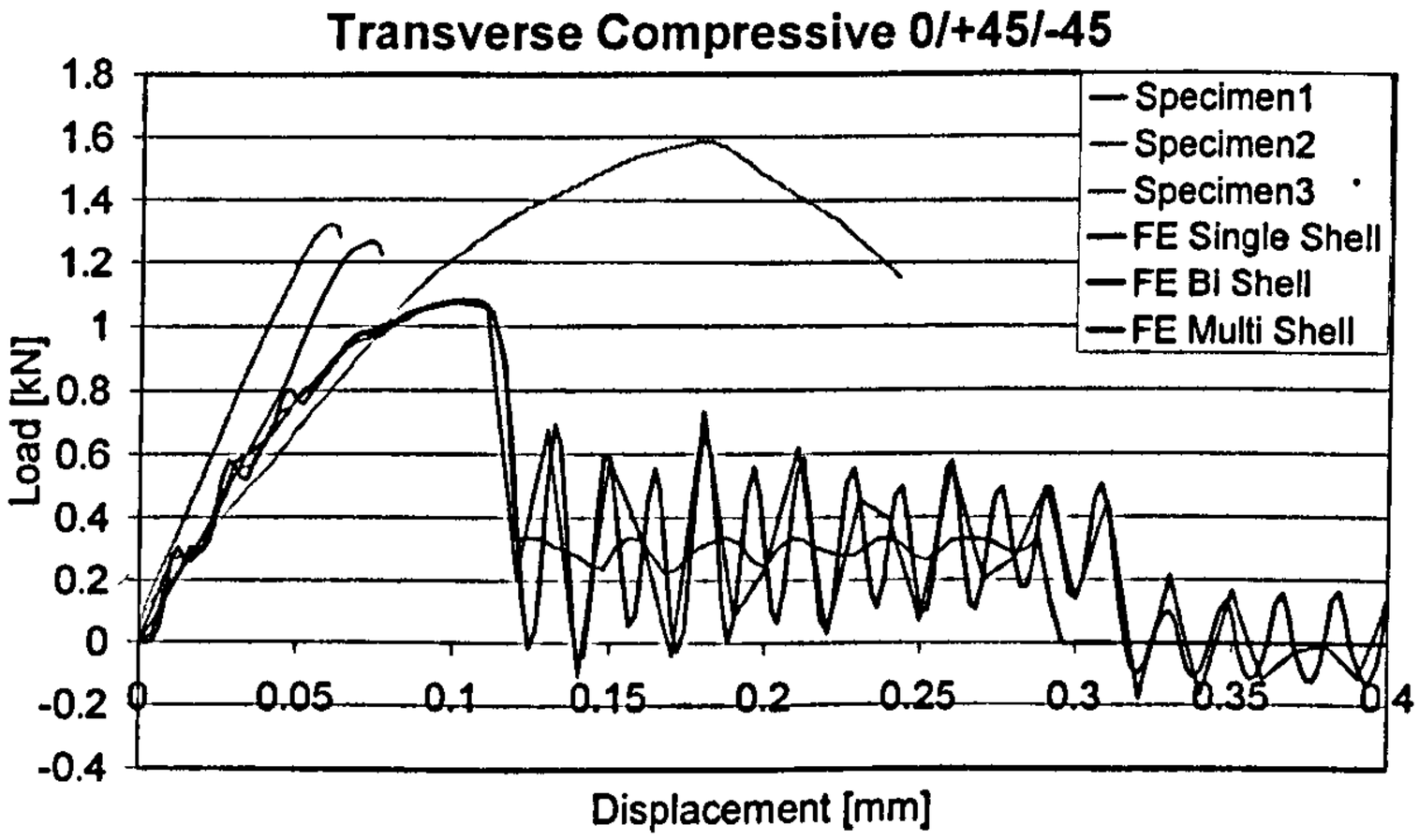
Transverse Compressive 0/+45/-45
Load [kN]
Displacement [mm]
Specimen1
Specimen2
Specimen3
FE Single Shell
FE Bi Shell
FE Multi Shell
1.8
1.6
1.4
1.2
1
0.8
0.6
0.4
0.2
0
-0.2
-0.4
0
0.05
0.1
0.15
0.2
0.25
0.3
0.35
0.4

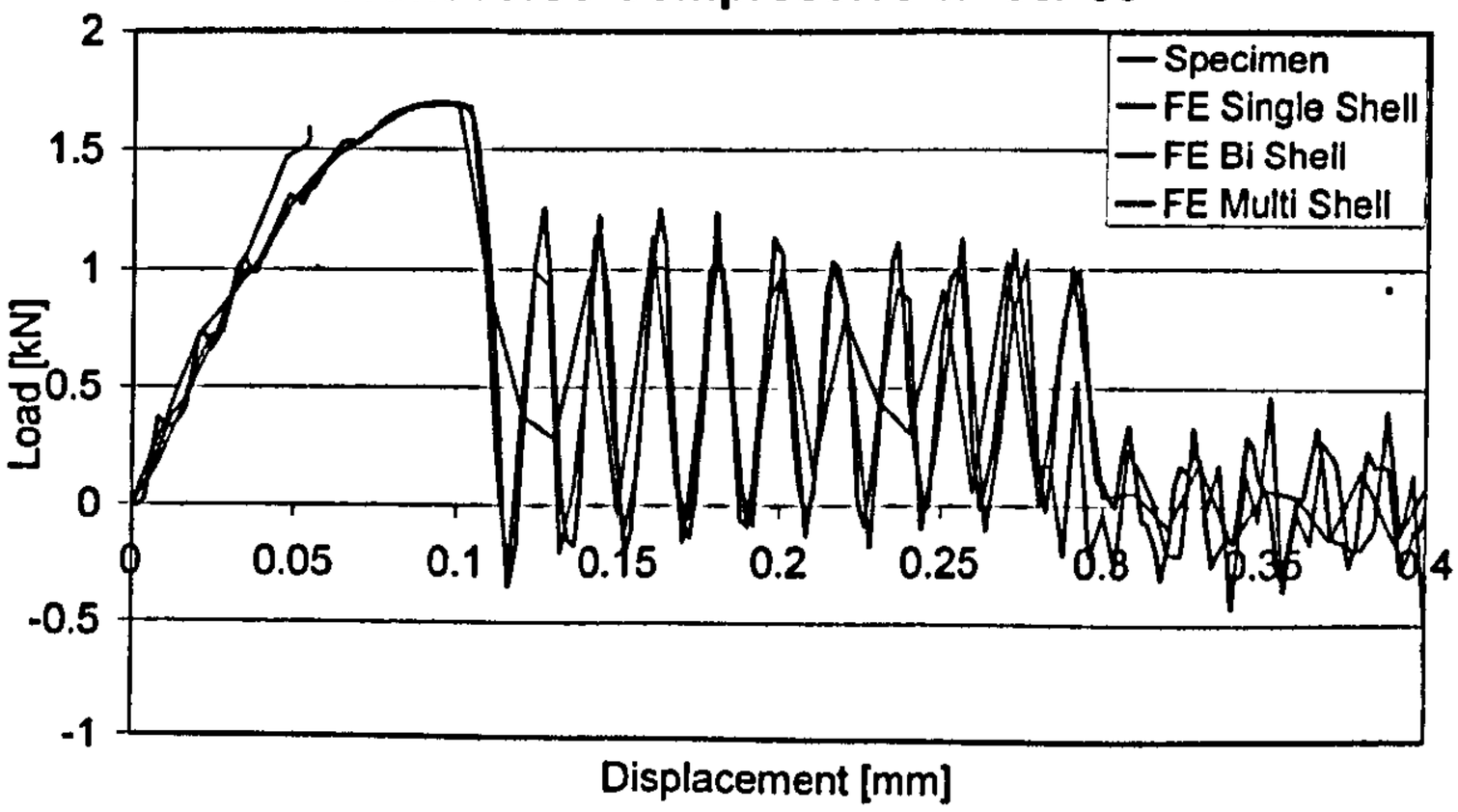
Transverse Compressive 0/+60/-60
Load [kN]
Displacement [mm]
Specimen
FE Single Shell
FE Bi Shell
FE Multi Shell
2
1.5
1
0.5
0
-0.5
-1
0
0.05
0.1
0.15
0.2
0.25
0.3
0.4

Observations

The main conclusion to be drawn from the compressive modelling is that the interlaminar properties seems to have little influence in the compressive behaviour of the material and that the driving mechanisms for the failure come from the intralaminar material properties.

6.1.3 Shear Tests

A total of 18 tensile tests were modelled as we have 3 different braid architectures, 2 types of test for each architecture (axial and compressive) using the 3 different modelling approaches. Only the test in direction 12 was modelled, as this is the only value used for the PAM-CRASH material input.

6.1.3.1 FE Models

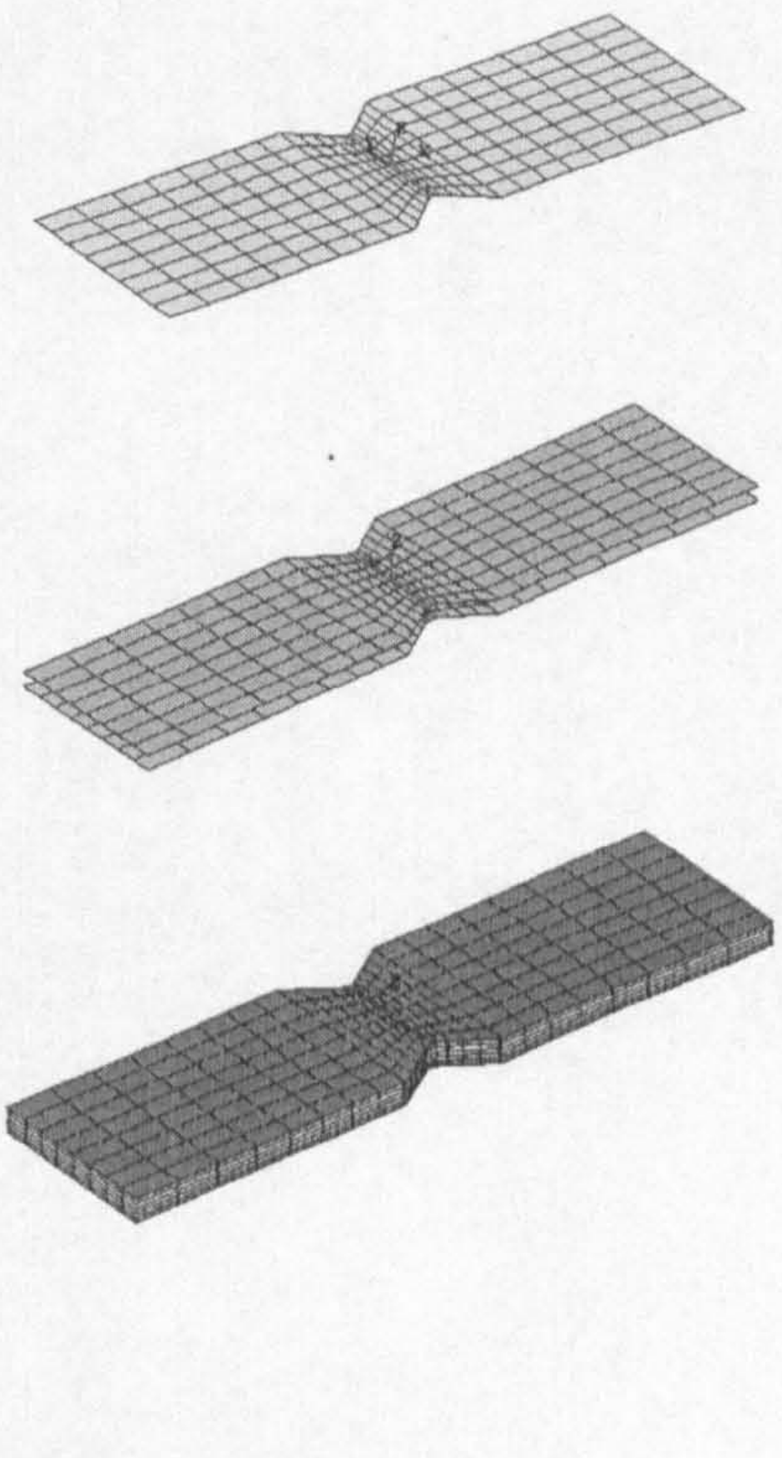

Figure 6-10 - FE Models for Shear Test

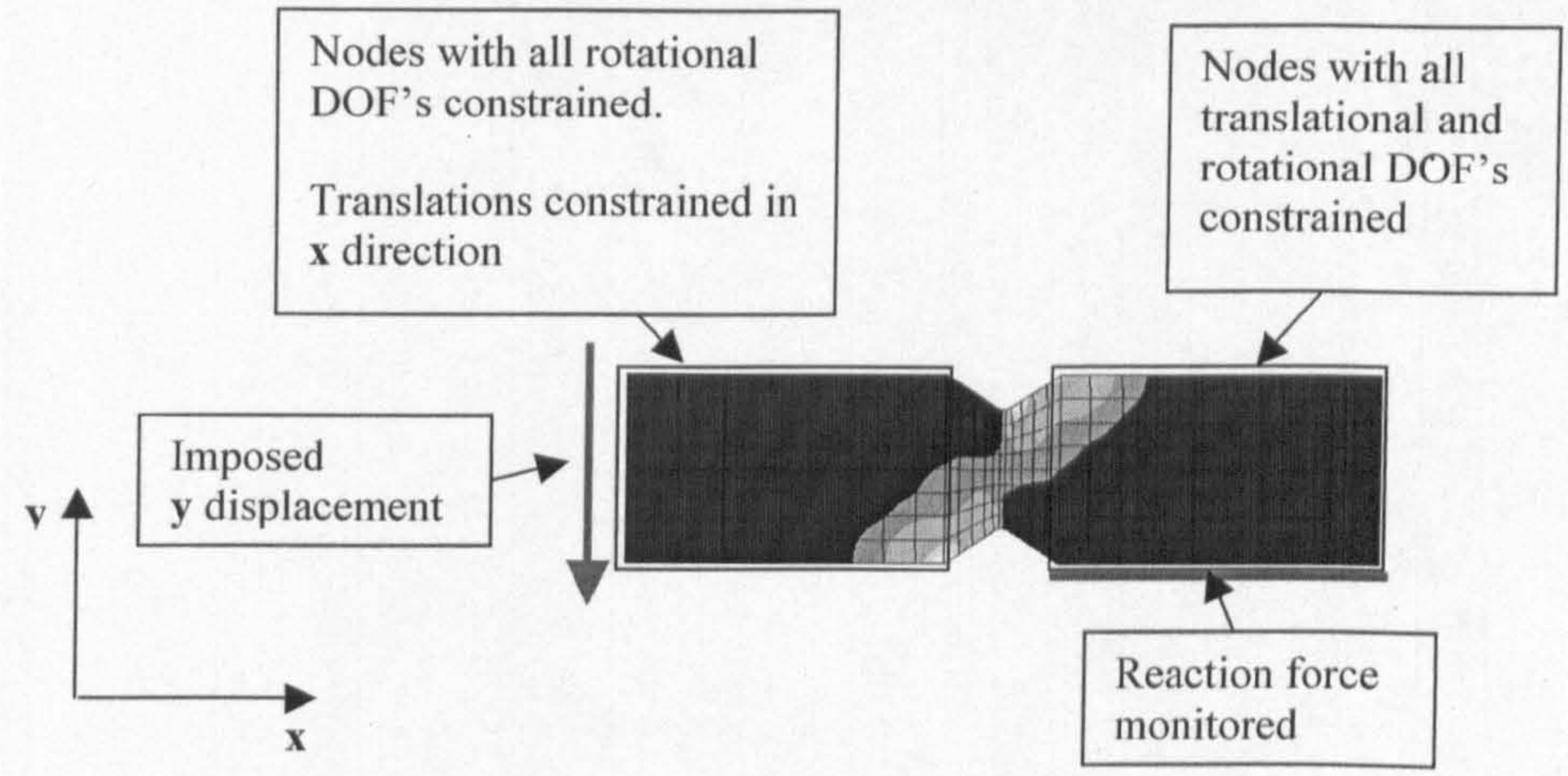

Figure 6-11 - Boundary Conditions in Compressive Test

6.1.3.2 Shear 12 Results

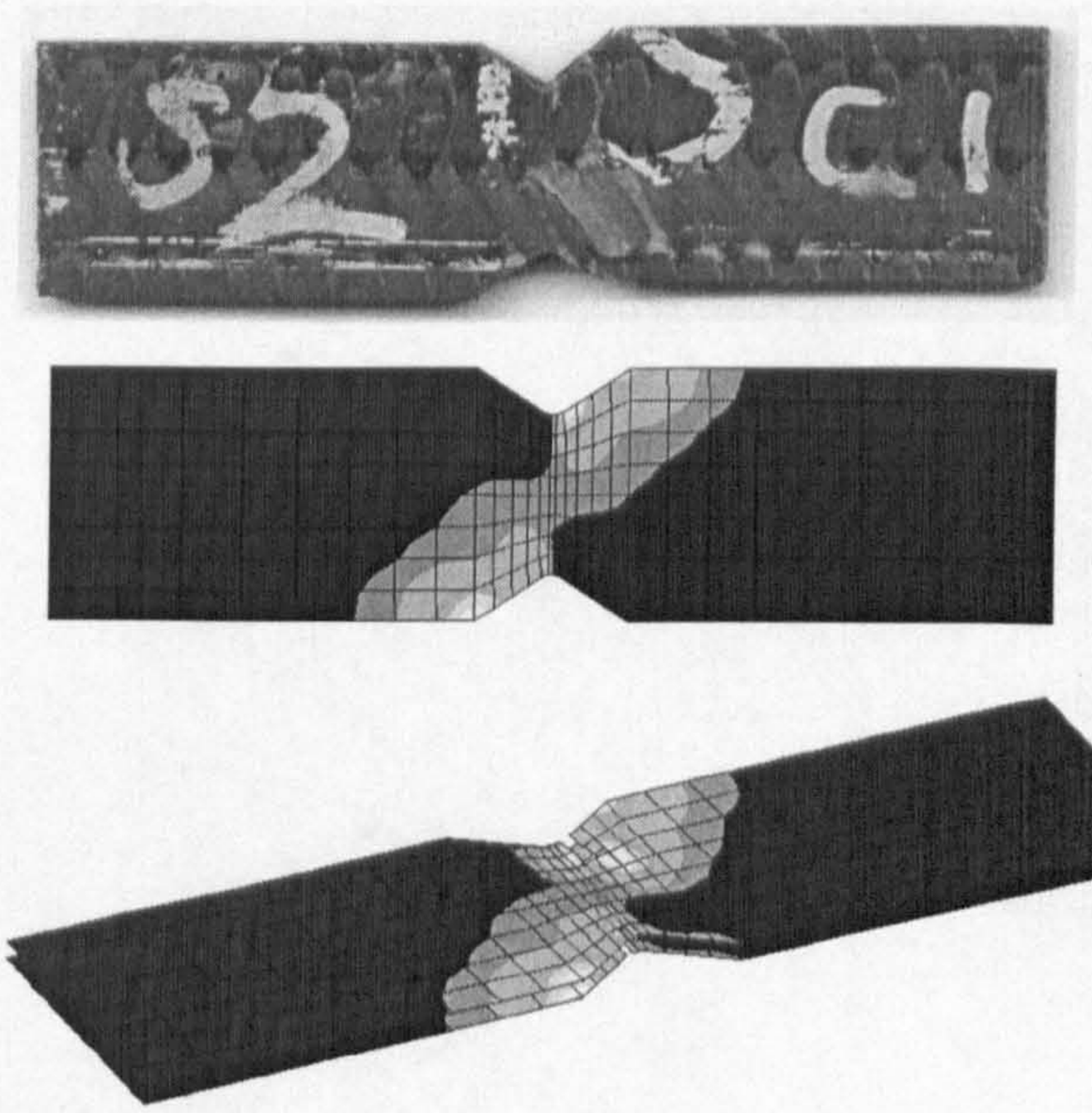

Figure 6-12 - Damage and failure of Shear 12 Test

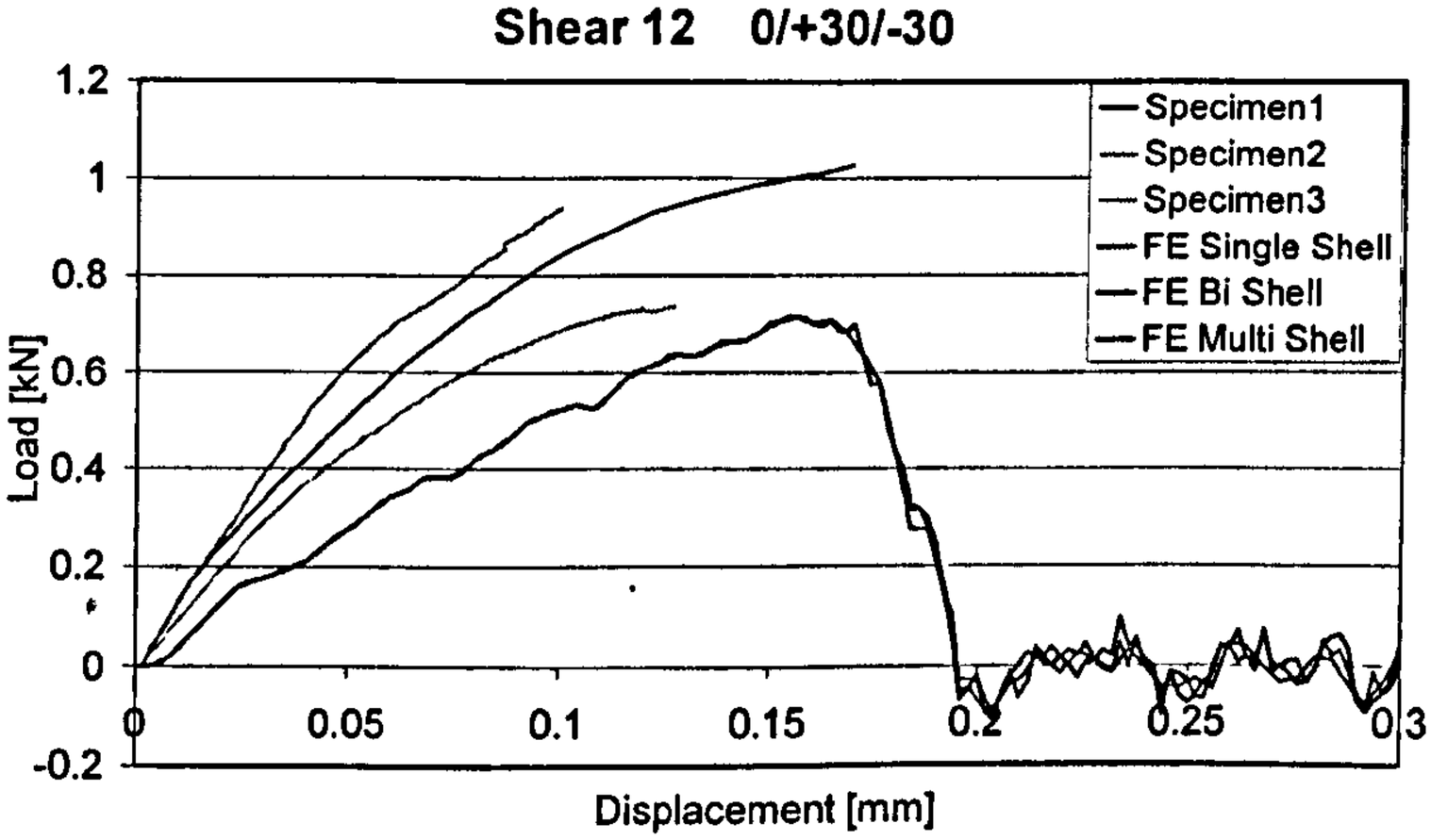
Shear 12 0/+30/-30
Load [kN]
Displacement [mm]
Specimen1
Specimen2
Specimen3
FE Single Shell
FE Bi Shell
FE Multi Shell
1.2
1
0.8
0.6
0.4
0.2
0
-0.2
0
0.05
0.1
0.15
0.2
0.25
0.3

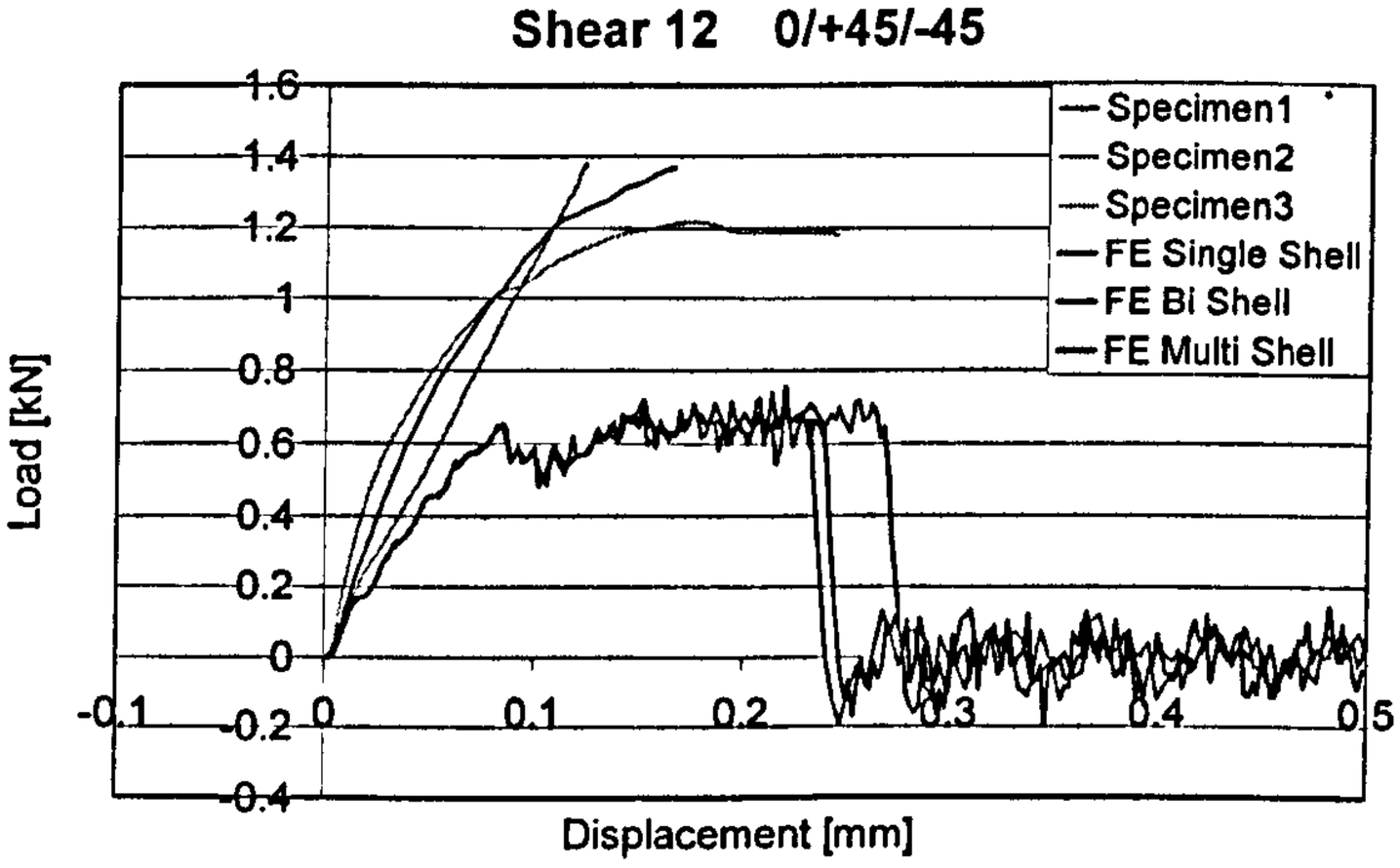
Shear 12 0/+45/-45
Load [kN]
Displacement [mm]
Specimen1
Specimen2
Specimen3
FE Single Shell
FE Bi Shell
FE Multi Shell
1.6
1.4
1.2
1
0.8
0.6
0.4
0.2
0
-0.2
-0.4
-0.1
0
0.1
0.2
0.3
0.4
0.5

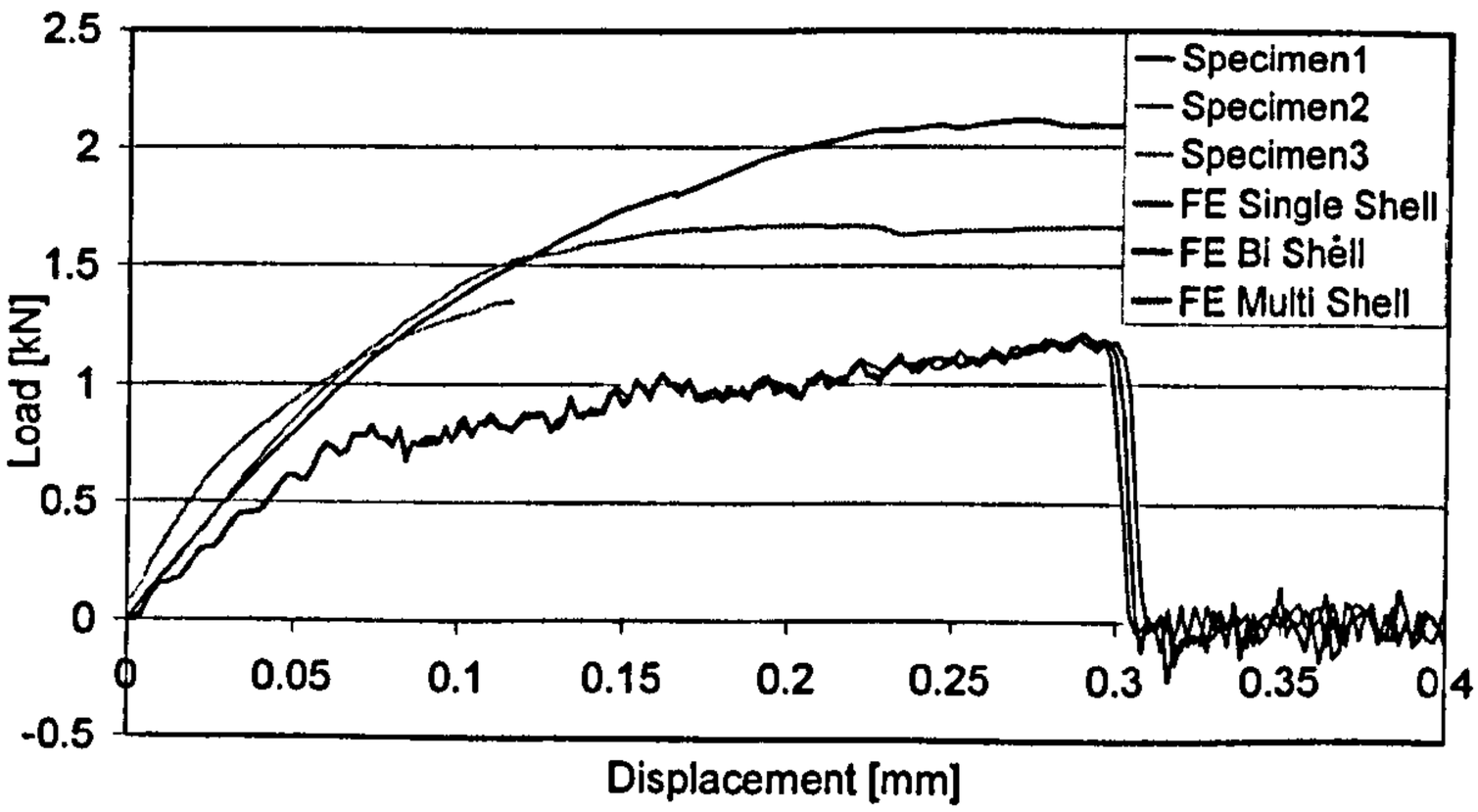
Shear 12 0/+60/-60
Load [kN]
Displacement [mm]
Specimen1
Specimen2
Specimen3
FE Single Shell
FE Bi Shell
FE Multi Shell
2.5
2
1.5
1
0.5
0
-0.5
0
0.05
0.1
0.15
0.2
0.25
0.3
0.35
0.4

Observations

As shown on the load-displacement response of the several tests, shear modelling exhibits the lowest accuracy of all the tests, but can still be considered to have a reasonable agreement with the experimental data.

As with the compressive tests, the in-plane properties drive the mechanical behaviour of the material in shear. However, the Iosipescu Shear test has shown limitations due to damage of the load surfaces by the testing apparatus. For this reason, no major conclusions can be drawn regarding the decrease in stiffness observed for all the FE models run.

6.2 Interlaminar Tests

Finite Element models of all the fracture toughness tests were built. The models for DCB, ENF and MMB tests are shown in Figure 6-13

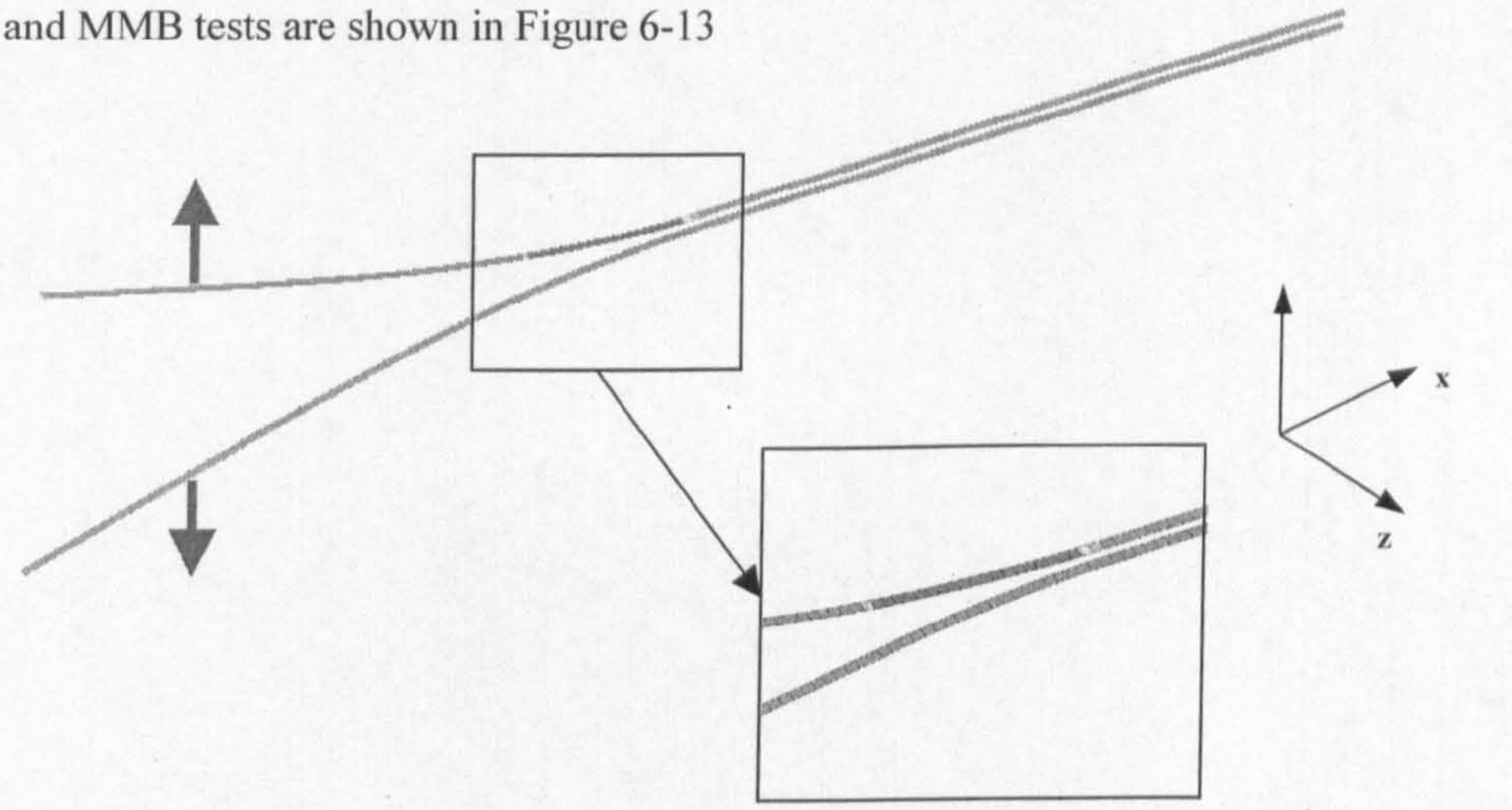

a) DCB

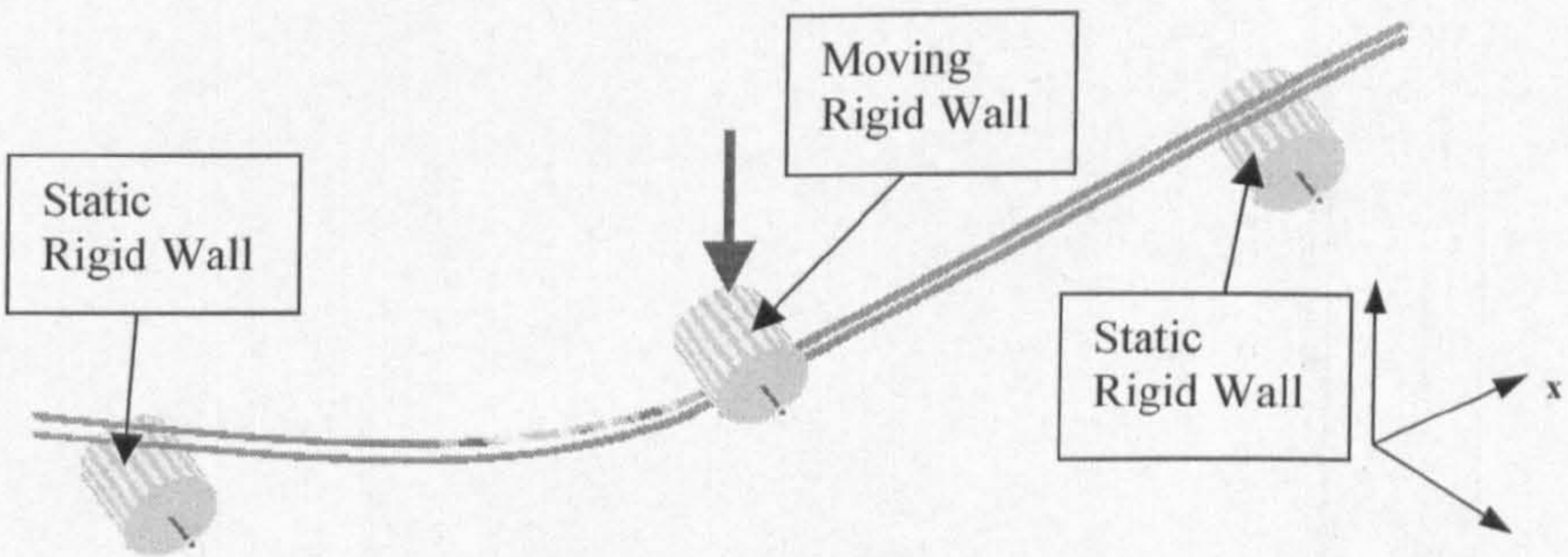

b) ENF

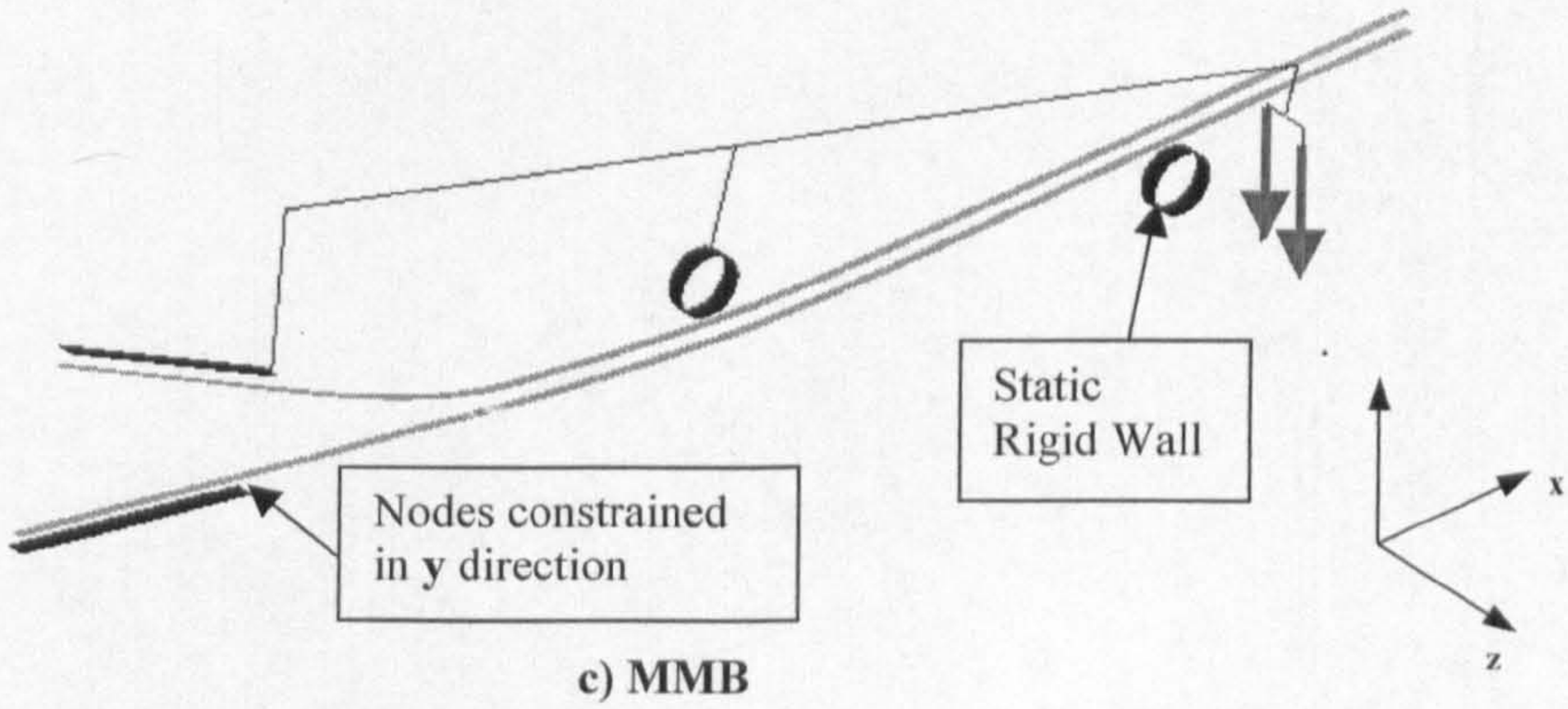

c) MMB

Figure 6-13 - Finite Element Models of Interlaminar Fracture Tests

The arrows in Figure 6-13 represent the loading boundary condition. All models consist of 2 layers of shell elements, each representing 3 plies of the 6-ply laminate composite. A contact interface (i.e. the delamination model described in this chapter) connects the two layers of shells. Only a 1mm wide strip of the specimens was modelled while the experimental tests were conducted on 25mm wide specimens. This modelling ignores the effect of plane strain, which is shown in Figure 3-10. This was done for CPU economy purposes, as the loads measured for a 1mm specimen are $1/25^{th}$ of the loads measured for a 25mm one.

Modelling the Interlaminar Region

For the DCB, ENF and MMB coupon models, the interlaminar region has a pre-crack which is represented by having "disconnected" nodes, i.e. which are not included in the contact interface definition, Figure 6-14.

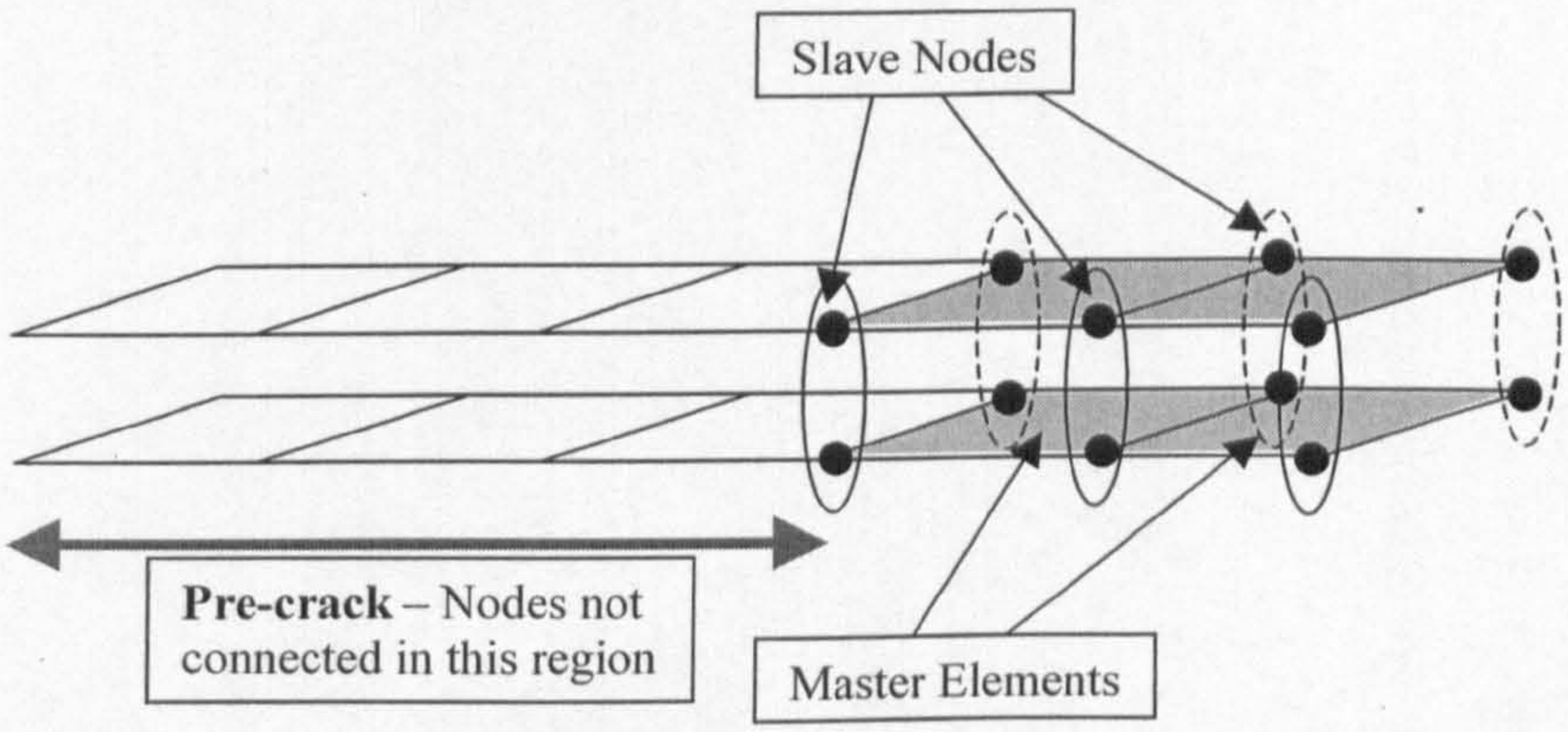

Figure 6-14 – Interlaminar modelling between adjacent plies for DCB, ENF and MMB tests

The Finite Element results for the interlaminar fracture toughness tests are shown in Figure 6-15 to Figure 6-19. These graphs show the experimental and Finite Element load-displacement plots as well as the beam theory solutions for DCB and ENF test. Those solutions are described in Appendix 1.

6.2.1 DCB Test

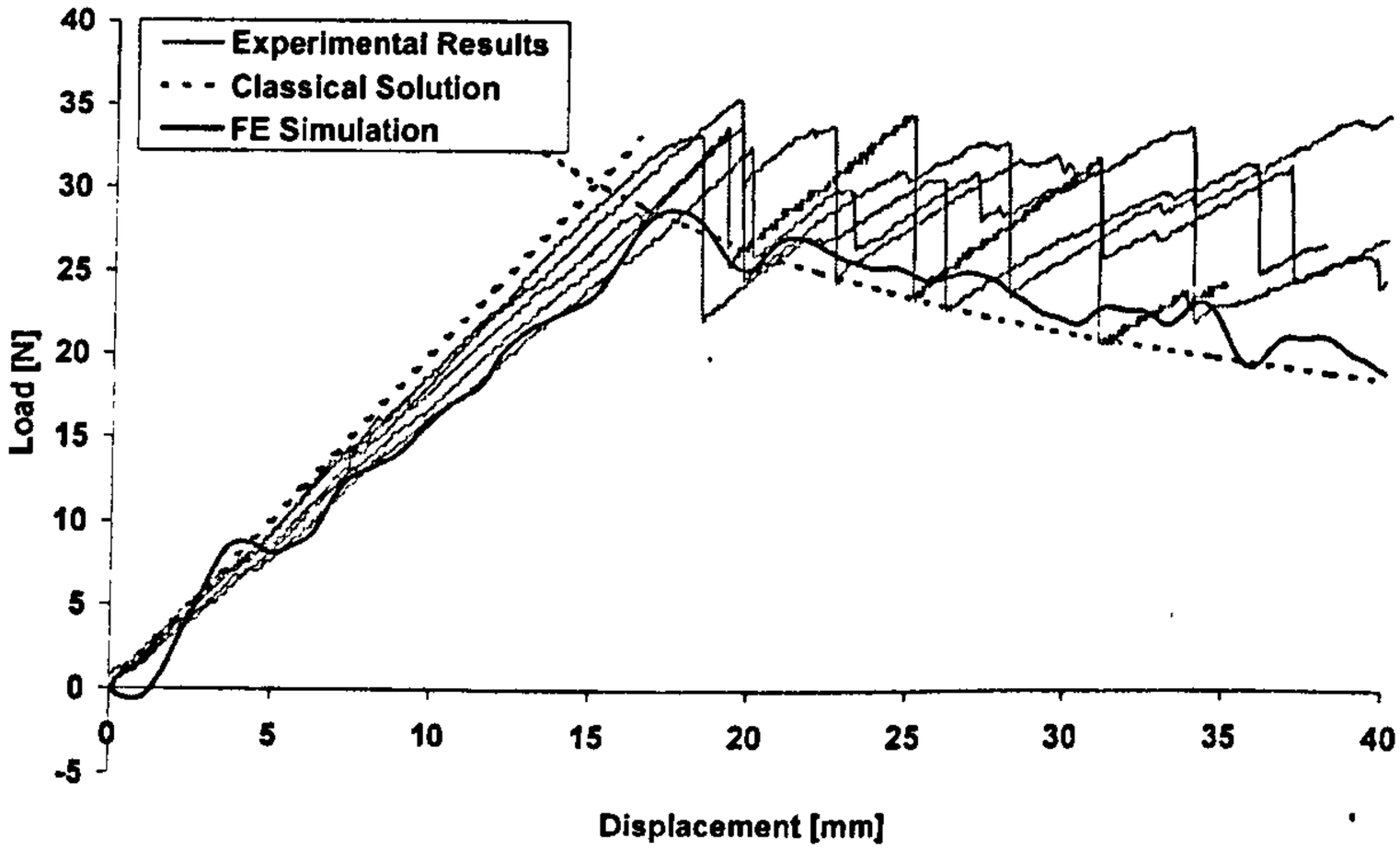

Figure 6-15 - DCB Results

6.2.2 ENF Test

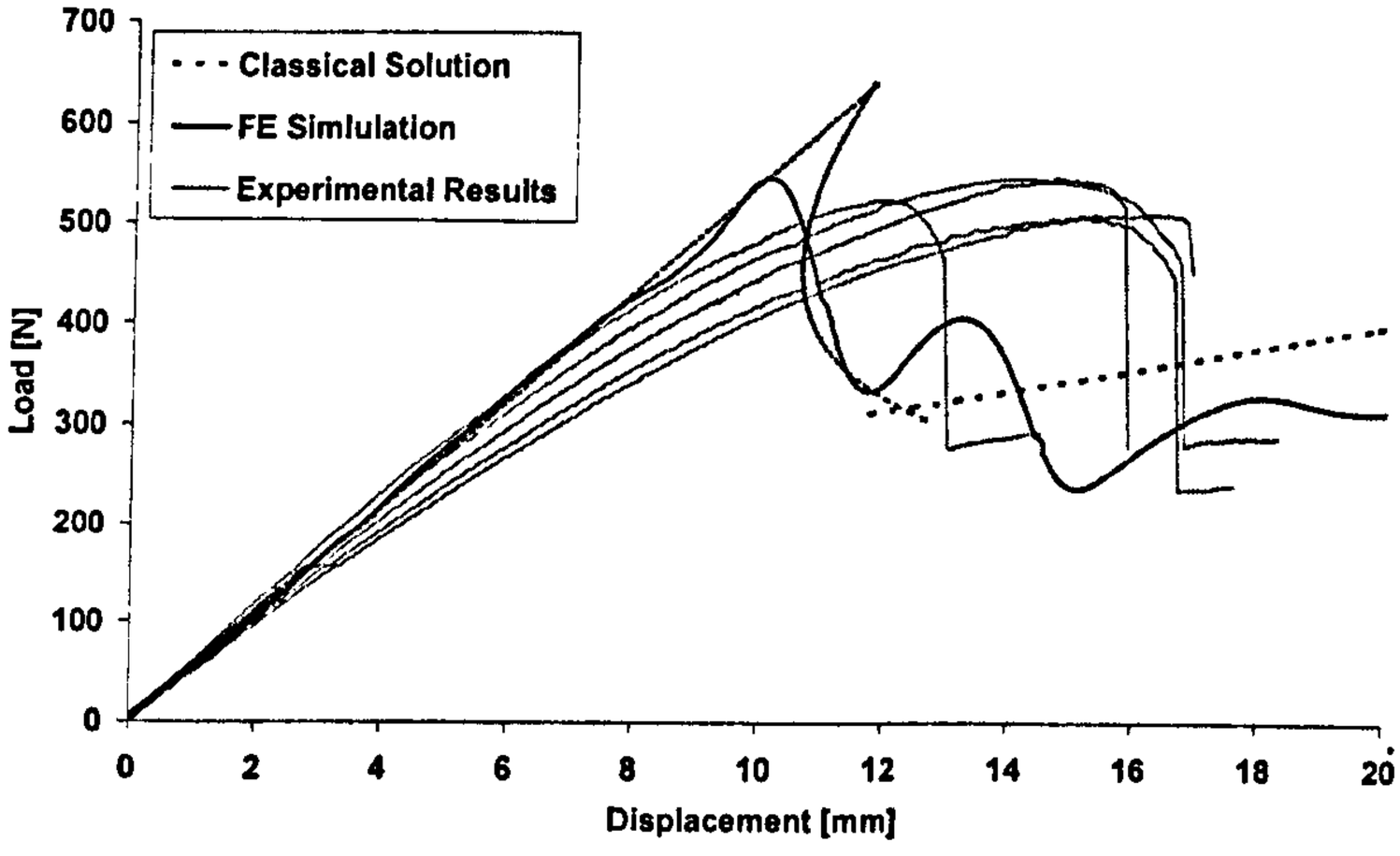

Figure 6-16 - ENF Results

6.2.3 MMB Tests

6.2.3.1 Mixed-Mode Ratio 0.5

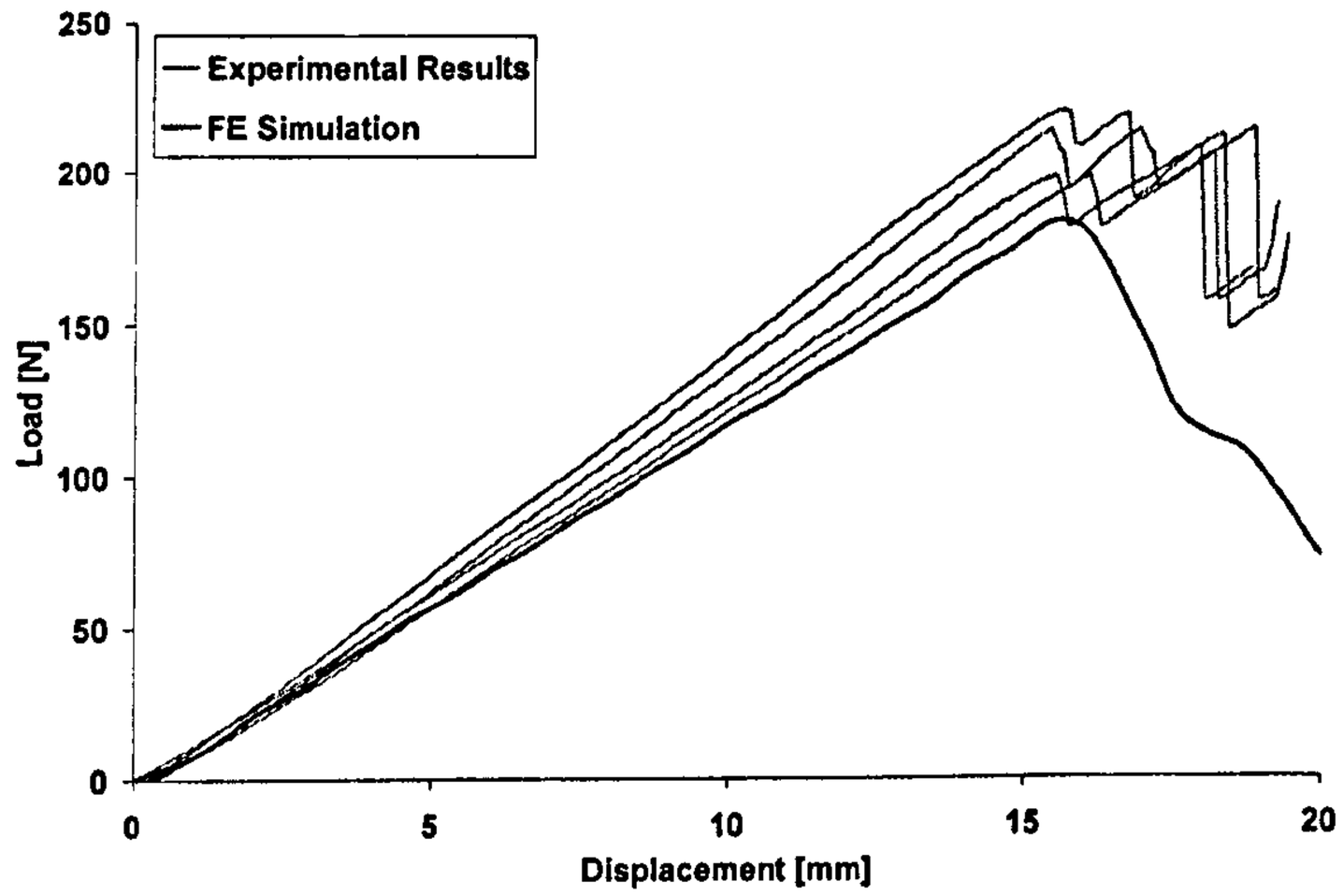

Figure 6-17 - MMB Results – Mixed-Mode Ratio 0.5

6.2.3.2 Mixed-Mode Ratio 2.0

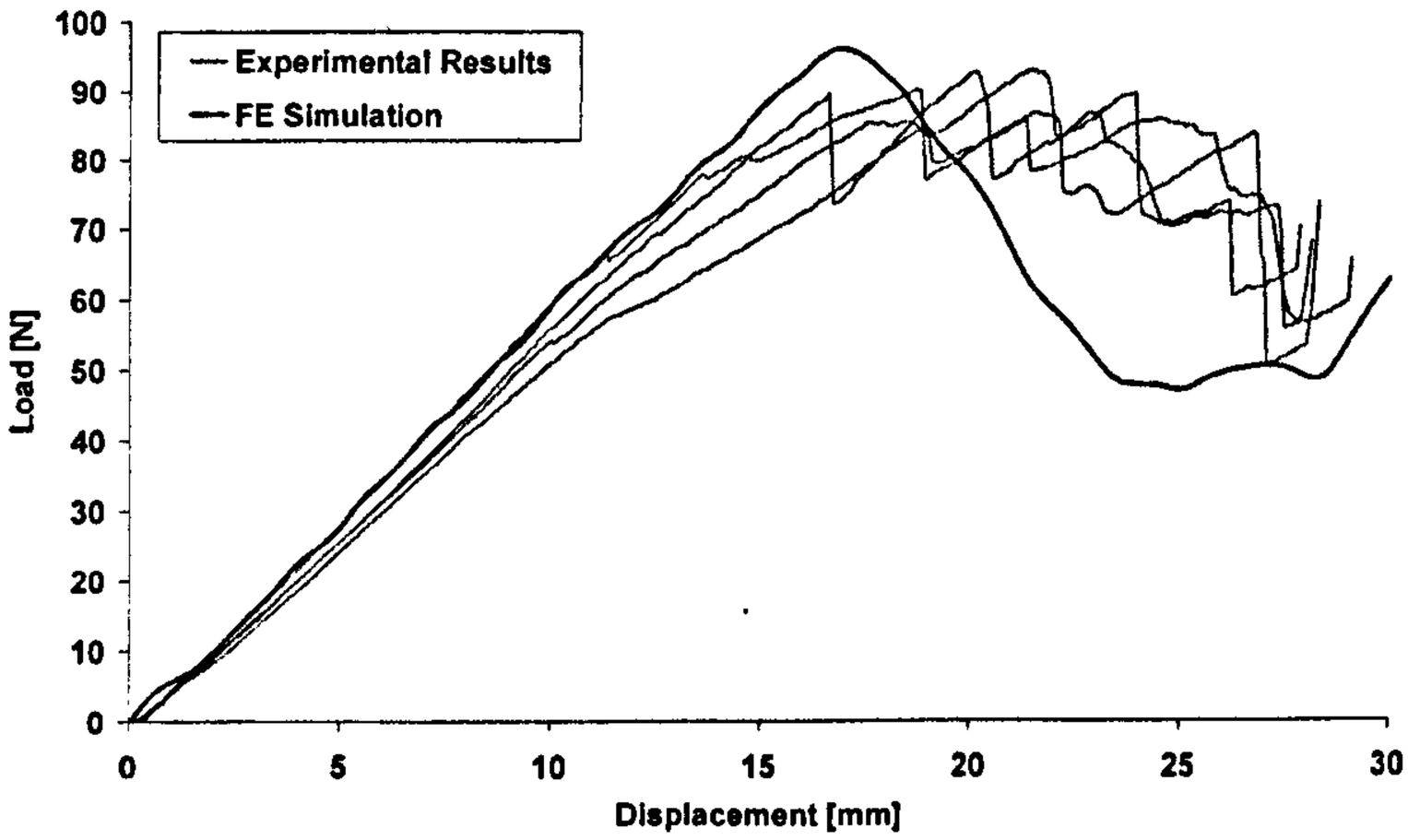

Figure 6-18 - MMB Results - Mixed-Mode Ratio 2.0

6.2.3.3 Mixed-Mode Ratio 3.7

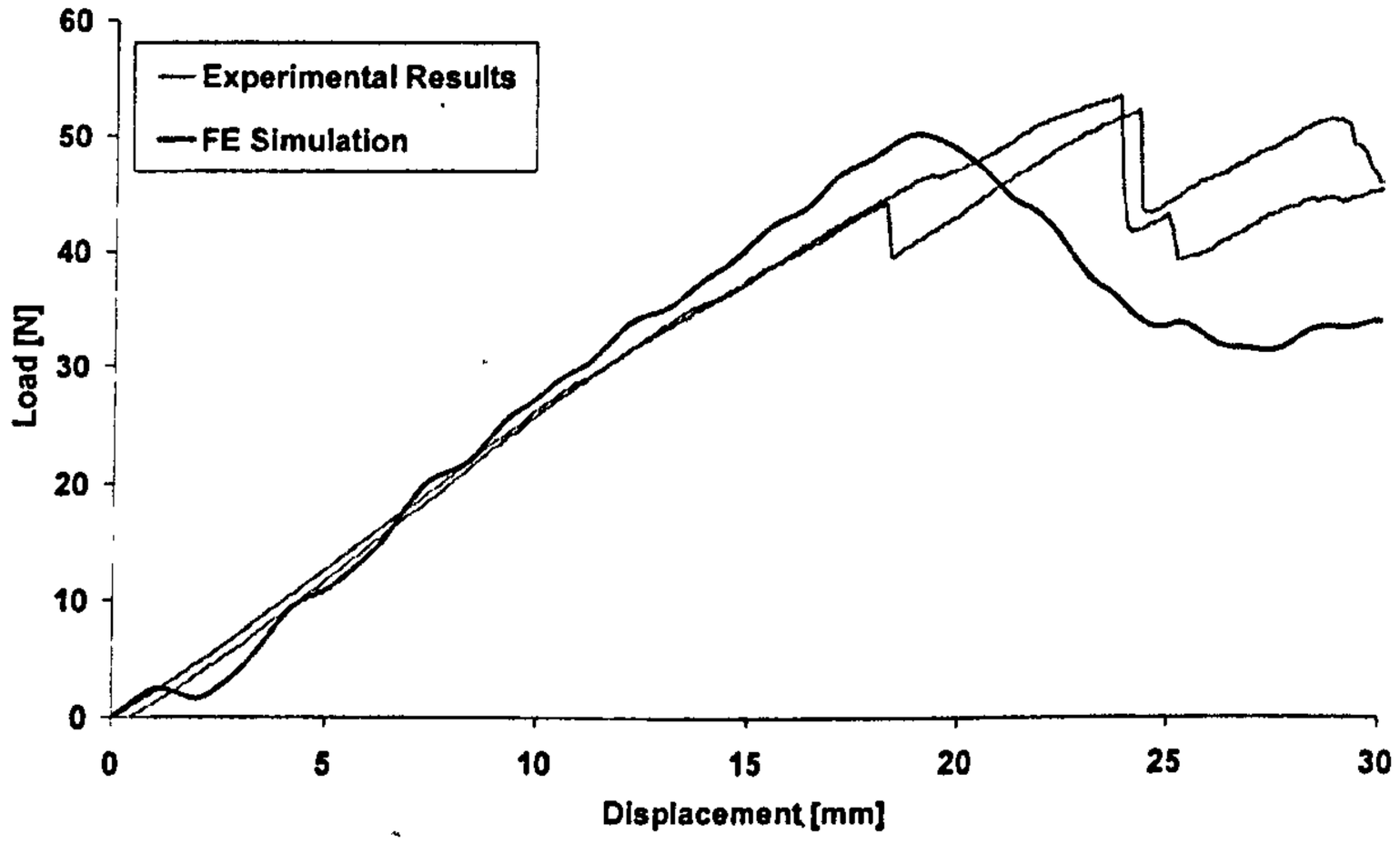

Figure 6-19 - MMB Results - Mixed-Mode Ratio 3.7

Mode Ratio G1/G2=2.0

Specimen No.	Fracture Toughness (J/sq.m)
1	1878.751111
2	1888.311579
3	1798.315556
4	1697.572
Average	1815.737561
Std. Dev. (%)	4.87483764

% G2	G	
0	546.146	
11.30468	1210.873	3.074864
29.05784	1815.738	88.51426
74.57076	2330.366	127.6194
100	2795	

Mode RatioG1/G2= 0.5

Specimen No.	Fracture Toughness (J/sq.m)
5	2464.192
6	2160.135038
7	2322.98049
8	2374.156761
Average	2330.366072
Std. Dev. (%)	5.47636827

Mode RatioG1/G2= 3.7

Specimen No.	Fracture Toughness (J/sq.m)
9	1208.6992
10	1213.047714
Average	1210.873457
Std. Dev. (%)	0.253937678

Mixed Mode Graph Points

	G1 (J/sq.m)	G2 (J/sq.m)
Pure Mode 1	546.146	0
Mode Ratio G1/G2=3.7	1168.922608	315.965924
Mode Ratio G1/G2=2.0	1623.972999	812.1666018
Mode RatioG1/G2= 0.5	1042.351454	2084.252738
Pure Mode 2	0	2795

Table 6-1 – Mixed-Mode Fracture Toughness Results

Combining the three obtained values of Mixed-Mode fracture toughness with the previously obtained fracture toughness values for pure Mode I and Mode II, five points on the $G_I - G_{II}$ graph were identified. This allowed a good measure of the Mixed-Mode behaviour of the material to be obtained, as shown in Figure 6-20.

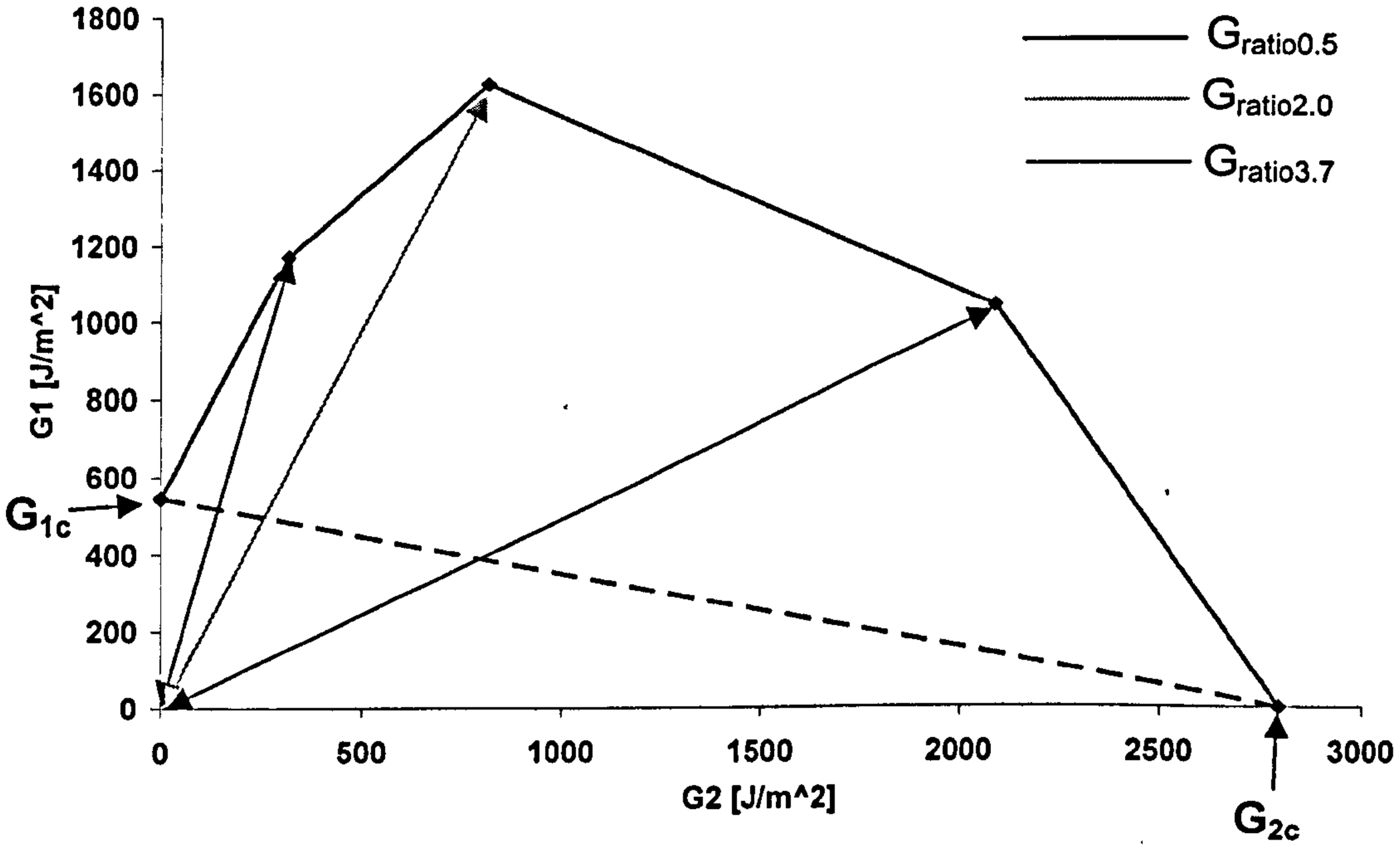

Figure 6-20 - Mixed-Mode Delamination Results – Fracture Energy Absorption

Observations

The agreement between experimental and numerical results is good, as shown in the load-displacement plots of the tests. The higher energy absorption observed in experimental ENF and MMB tests is believed to be the result of misreading the crack length in these tests, which leads to a lower value of fracture toughness. Indeed, it has been observed in tested specimens that the crack front does not have a rectangular shape (Figure 3-10) and the reading at the edge of the specimen (which is monitored during the tests) provides a lower value.

The coupling between the different fracture modes is not linear which can have a strong influence in modelling large structures, as in most loading situations the interlaminar deformation consists of a combination of modes I and II.

It must be noted that there are doubts concerning the validity of these results. It is not intuitive that it would require a higher amount of energy to propagate a crack by shear (mode II) when a certain amount of mode I tension is applied. The explanation for this apparent disparity in results could reside in geometric non-linearity intrinsic to the Mixed-Mode Bending test, which can affect the results.

7.0 Tube Modelling

In this chapter, tube crush analyses are described. Typically full vehicle crash modelling is based on shell elements. Preliminary work on shell models and conclusions drawn from their results led to the solid models proposed in this work as a predictive approach for tube crush.

7.1 Shell Models

This modelling approach consists of layers of shell elements connected by a delamination contact interface. Each ply is modelled with the degenerate bi-phase material model, as described in Chapter 5.

7.1.1 Bi-Shell Modelling Approach

For the bi-shell approach, a mesh with removed elements in the first row was chosen to trigger splaying of the plies. This is not a predictive approach but it allows the assessment of numerical stability of the delamination model for tube crush modelling.

The model consisted of 2 layers of shells connected by a contact interface (PAM-CRASH Contact Type 32).

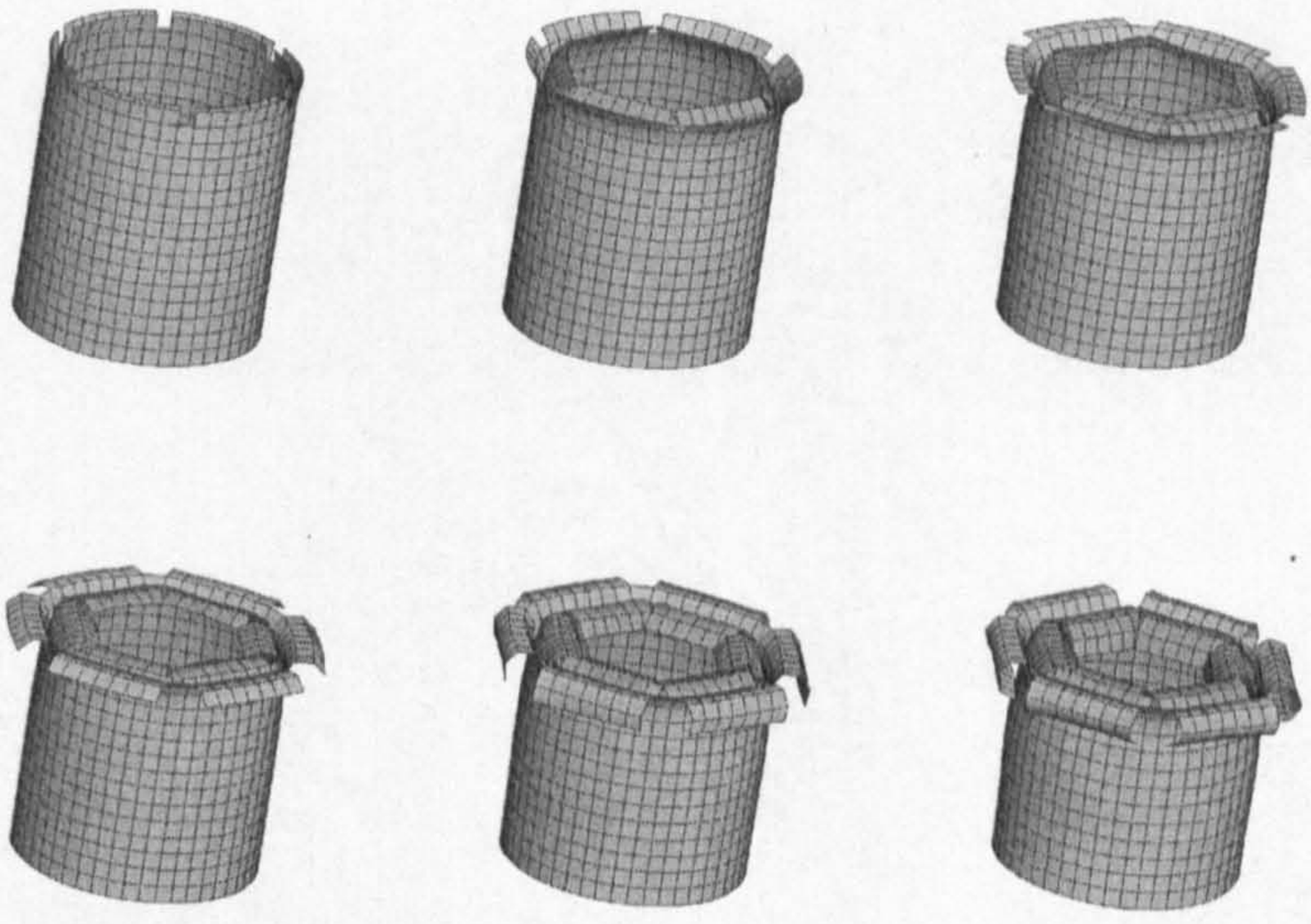

Figure 7-1 – Bi-Shell CoFRM Tube Model

7.1.1.1 Geometry

The dimensions of the model are shown in Figure 7-2.

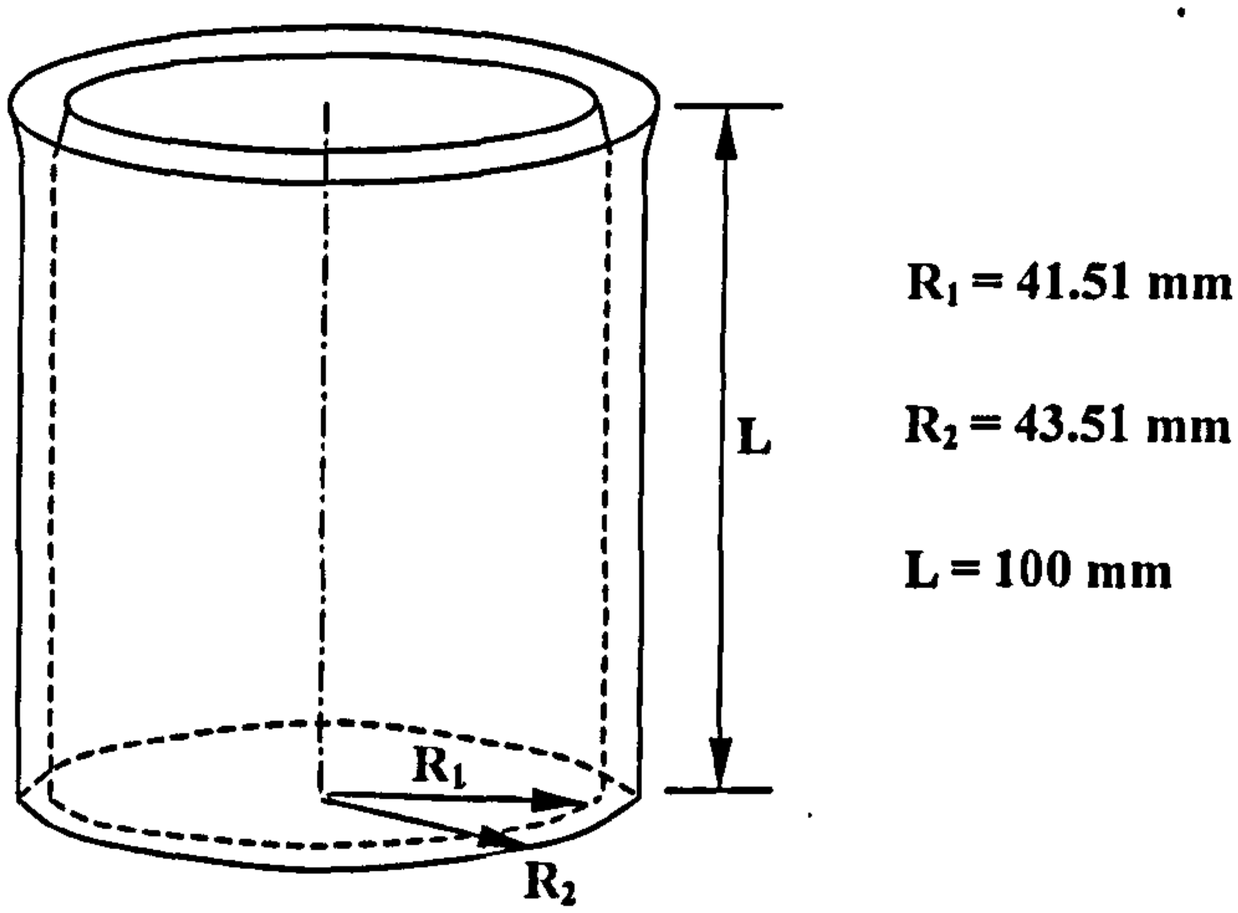

Figure 7-2 – Geometry of Bi-shell pre-splayed CoFRM Tube Model

The distance between the 2 layers of shells was such so that the total thickness of the model (including shells and interlaminar region) equalled the total thickness of the CoFRM tube, Figure 7-3.

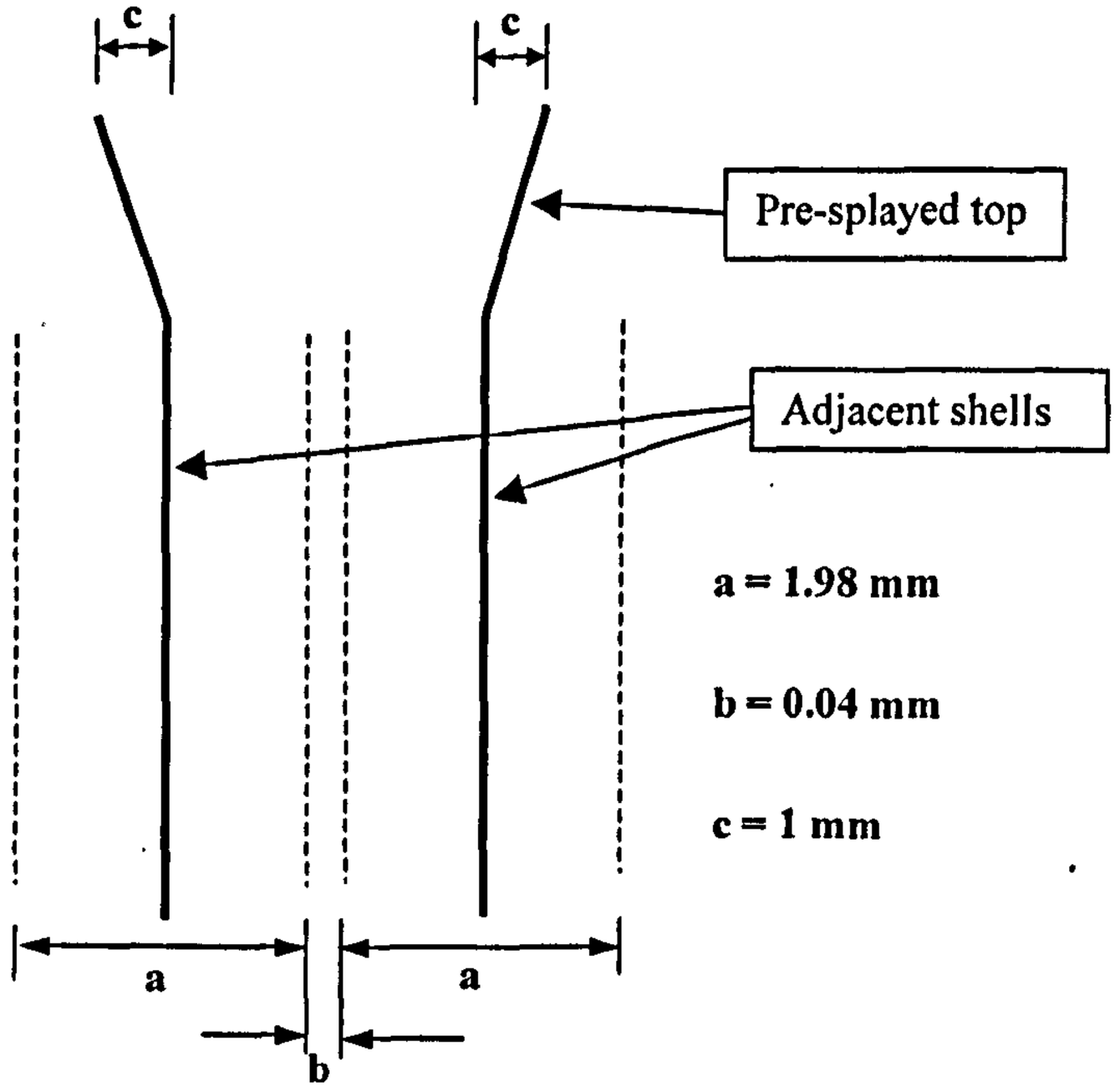

Figure 7-3 – Detailed Geometry of Bi-shell Tube Model

7.1.1.2 Boundary Conditions

Boundary conditions that represent the quasi-static crush of the tube were applied as shown in Figure 7-4.

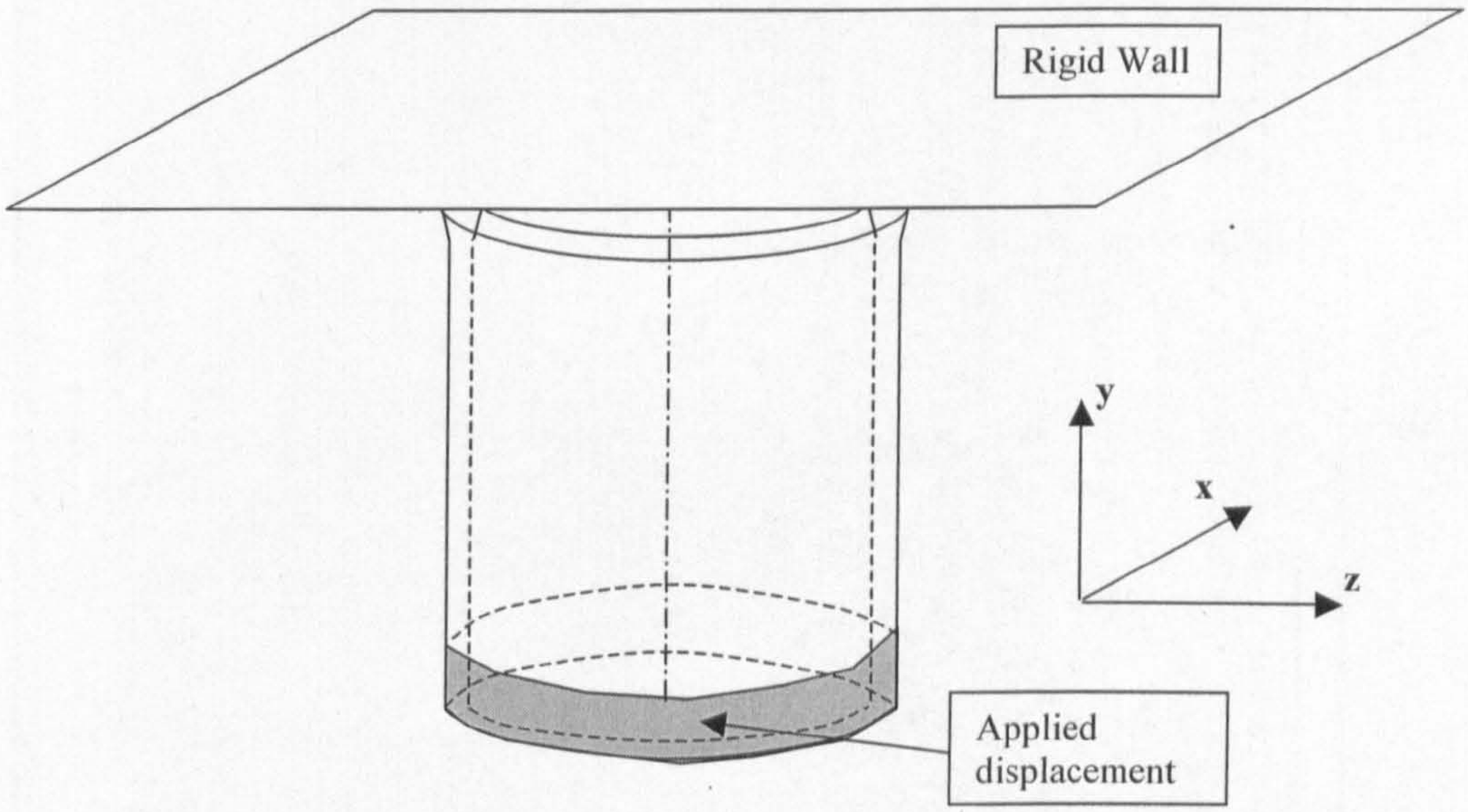

Figure 7-4 – Boundary conditions in Bi-shell Tube Model

A constant displacement rate of 1mm/ms was applied to the bottom two rows of nodes. Those nodes' degrees of freedom were constrained as described in Table 7-1.

x displacement	**y displacement**	**z displacement**	**x rotation**	**y rotation**	**z rotation**
Fixed	Free	Fixed	Fixed	Fixed	Fixed

Table 7-1 – Constraints Applied in Bi-shell Tube Model

7.1.1.3 Results

The vertical (y-direction) force on the rigid wall is monitored and its results are shown in Figure 7-5.

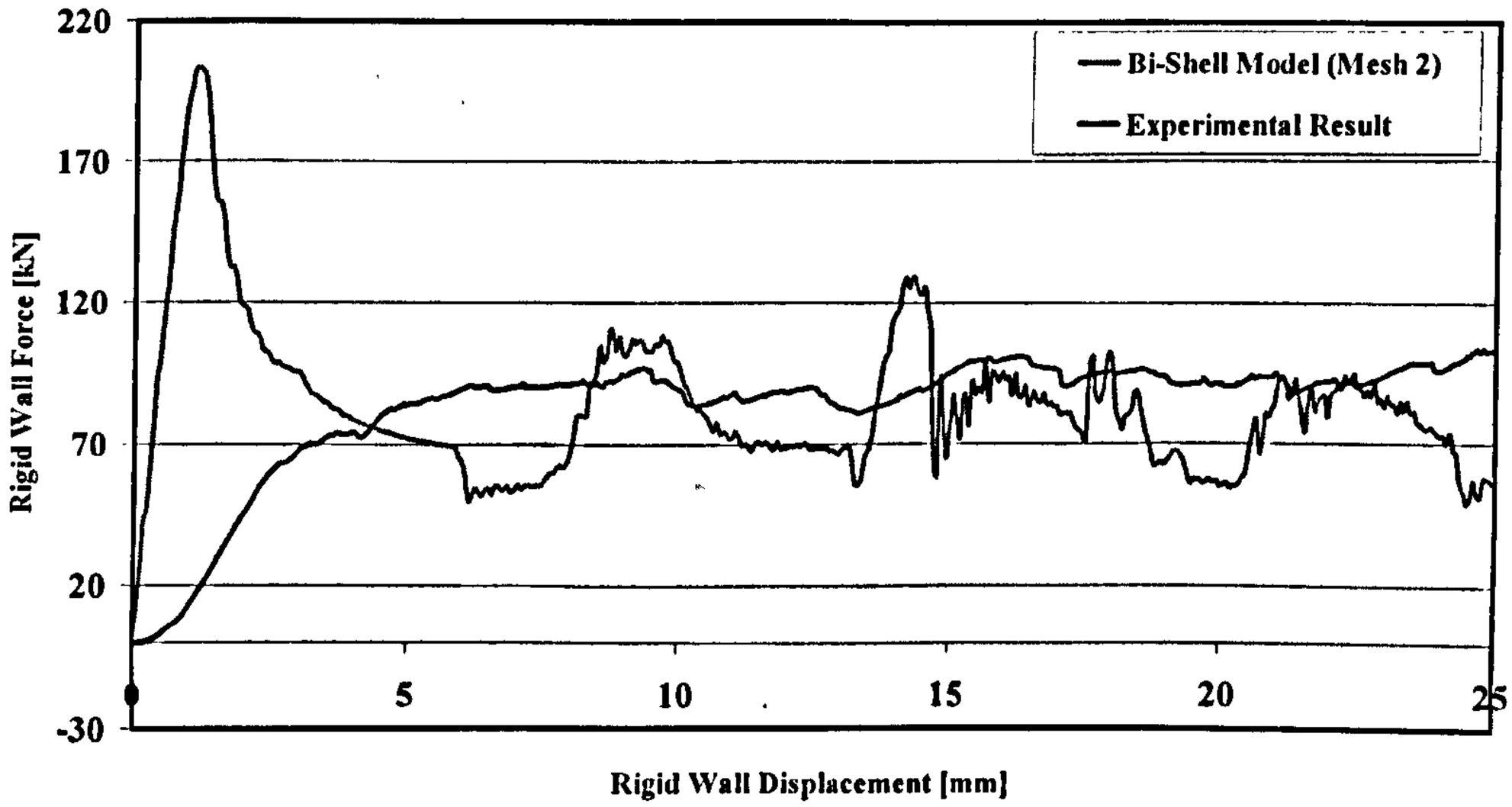

Figure 7-5 - Load-Displacement Plot for CoFRM Bi-Shell Model (Mesh Type 2)

This model shows a reasonable agreement with the steady state experimental result but greatly exceeding the peak load, as shown in Figure 7-5. In spite of not being truly predictive (the mesh is pre-splayed and some elements are removed to initiate the fronds), it is possible to conclude that a tube model consisting of several plies connected by the delamination contact interface allows for a geometrical representation of the splaying mode. Whereas single shell models tend to buckle (as shown in Chapter 2), a pre-splayed bi-shell model exhibits a stable progression of the crush front and crack propagation.

However, the inclusion of the contact interface had a negative effect on the stability of the analysis. This required careful control of the time-step was to prevent the job from crashing once the inner fronds started contacting each other.

7.1.2 Multi Shell Modelling Approach

This model has no pre-splayed geometry defined and consisted of 6 layers of shells (each representing one ply of the laminate) connected by a delamination contact interface. Only $1/8^{th}$ of the tube was modelled to reduce computational times.

7.1.2.1 Geometry

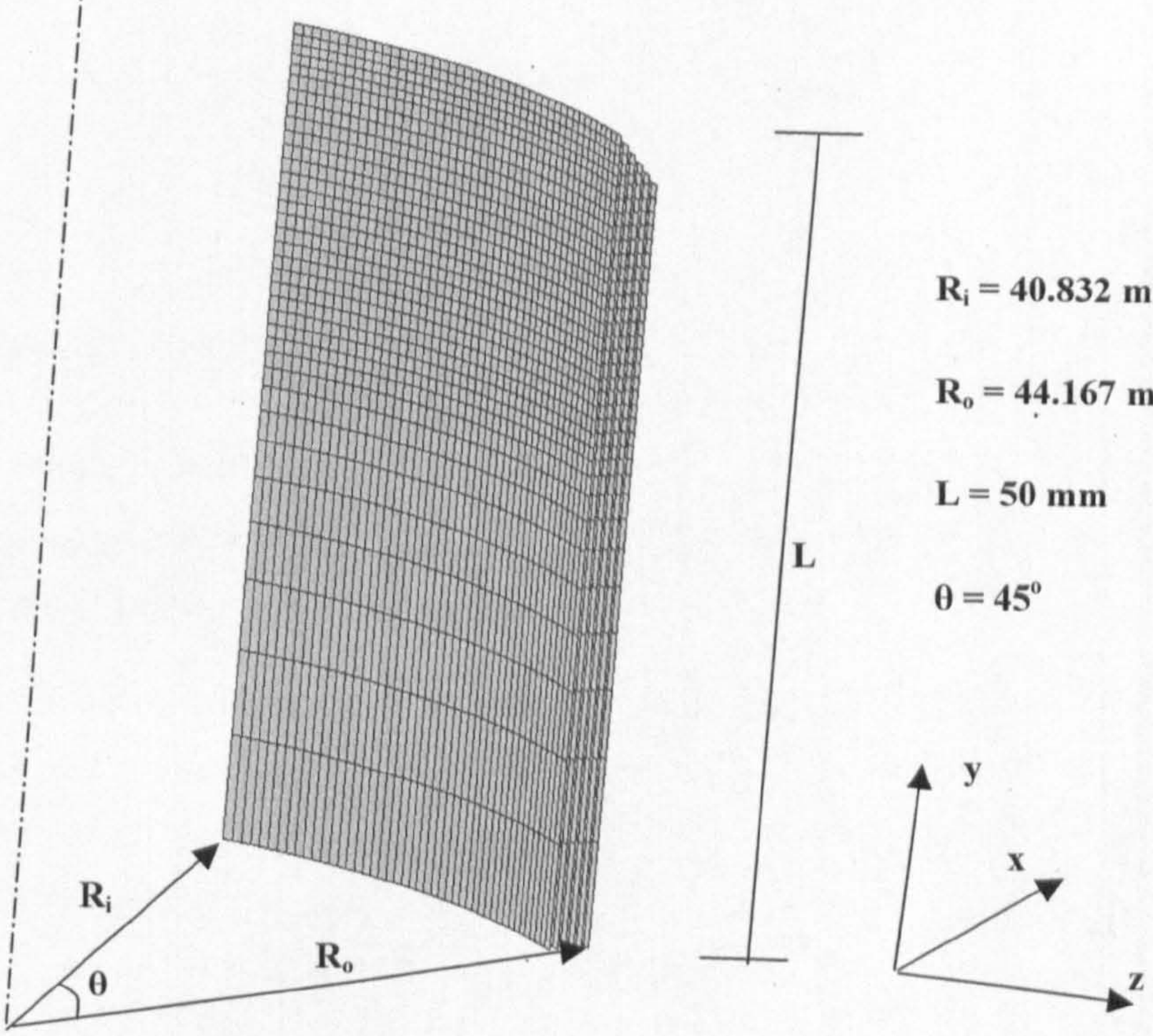

Figure 7-6 - Geometry of Multi-shell Tube Model

As in the pre-splayed bi-shell model, the distance between adjacent layers of shells was such so that the total thickness of the model (including shells and interlaminar region) equalled the total thickness of the CoFRM tube, Figure 7-3.

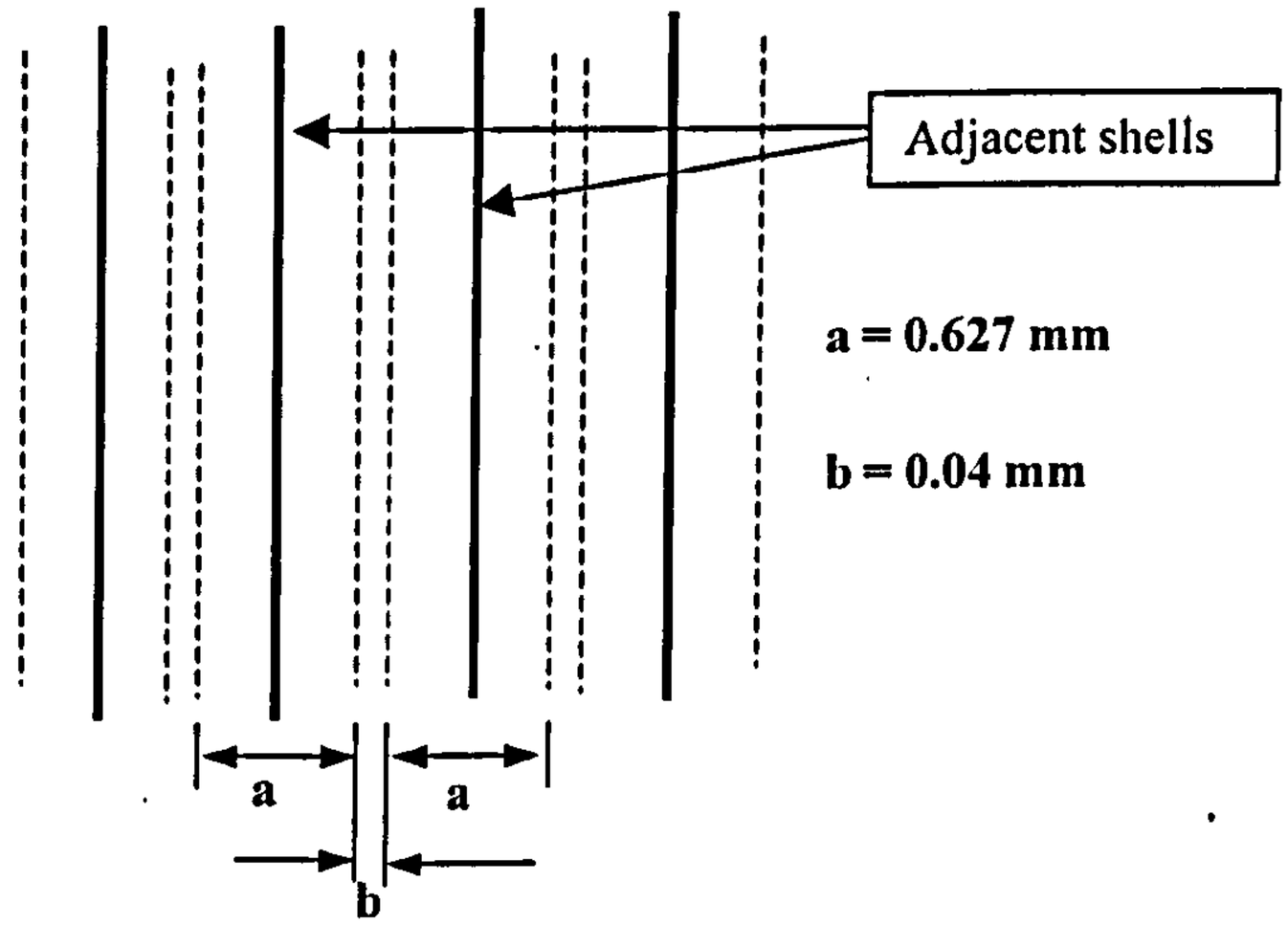

Figure 7-7 – Detailed Geometry of Multi-shell Tube Model

7.1.2.2 Boundary Conditions

As in the pre-splayed bi-shell tube model, the tube was crushed against a flat rigid wall by imposing a displacement at the bottom two rows of nodes.

Since only 1/8th of the tube is modelled, symmetry boundary conditions at the edges of the tube are imposed to represent the remaining material, Figure 7-8. Boundary conditions are defined for a global coordinate system **x,y** (in the case of Constraint **A**) and for a skewed coordinate system **x',y'** (in the case of Constraint **B**).

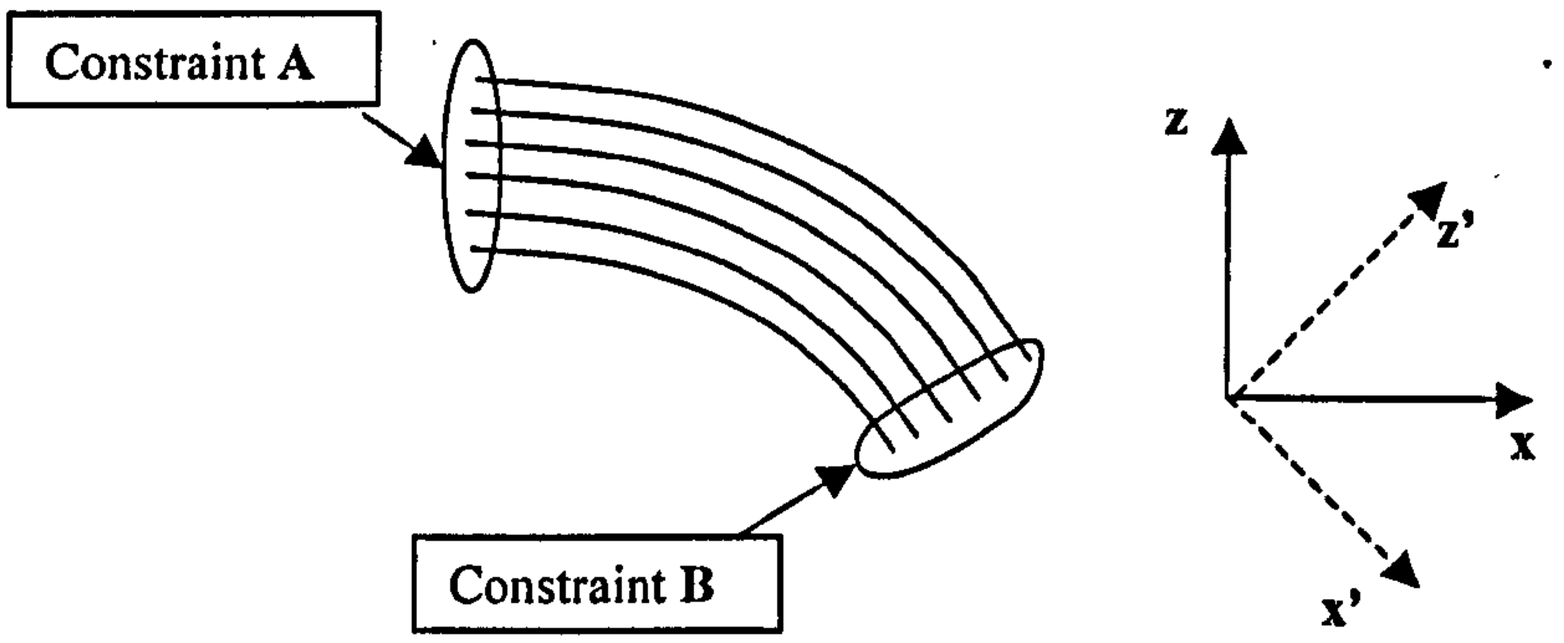

Figure 7-8 – Top View Showing Symmetry Boundary Conditions for Multi-shell 1/8th Tube Model

Symmetry boundary conditions for each constraint are shown in Table 7-2.

x displacement	**y displacement**	**z displacement**	**x rotation**	**y rotation**	**z rotation**
Fixed	Free	Free	Free	Fixed	Fixed

Table 7-2 – Symmetry Boundary Constraints Applied in Multi-shell 1/8th Tube Model

7.1.2.3 Results

This approach did not provide satisfactory results, due to numerical instability that caused elements to be eliminated prematurely (Figure 7-9). It is believed that the causes for this instability are related to the tendency of the plies to buckle, which in turn can cause out-of-plane oscillations responsible for premature element elimination.

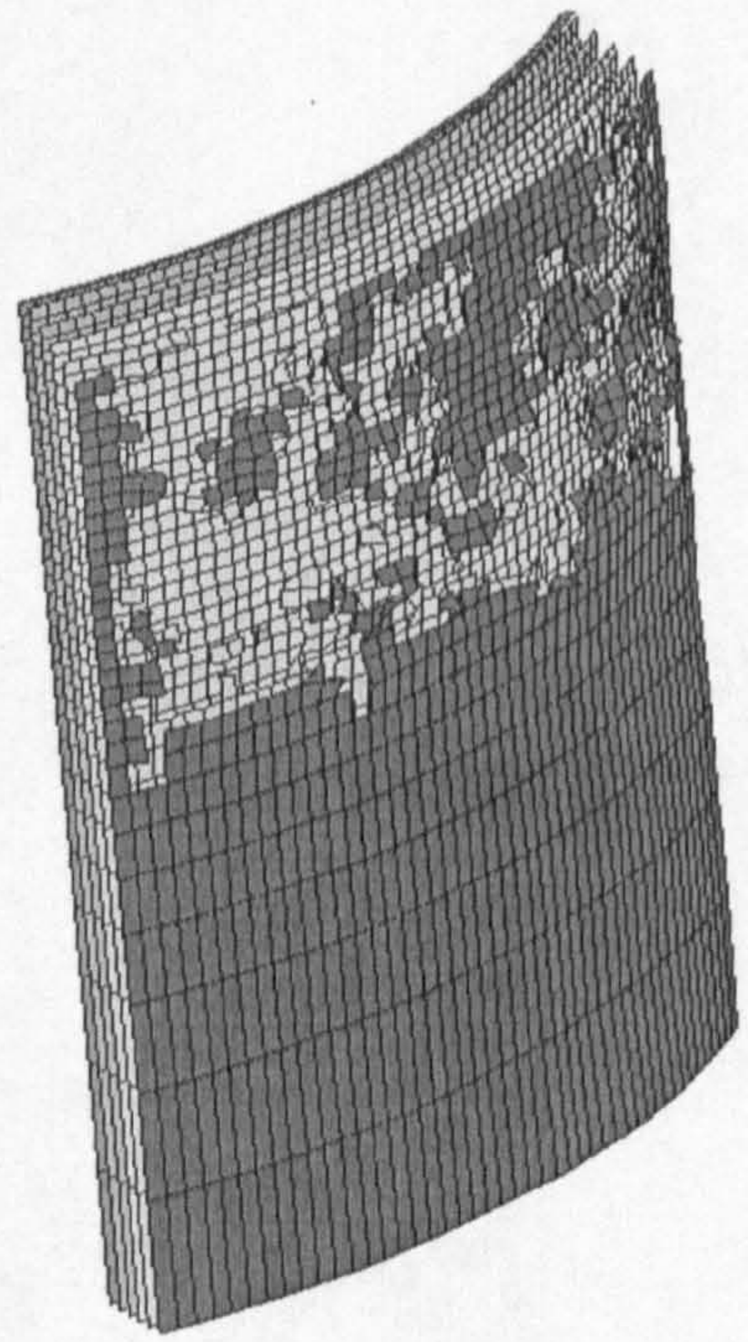

Figure 7-9 – Multi-shell Tube Model Showing Premature Element Elimination

A discussion of the reasons for the failure of the shell modelling approach is included in the section below.

7.1.3 Limitations of modelling the chamfer with shell elements

The nature of shell finite elements means that there is no geometrical representation of their thickness. Thickness is only accounted for out-of-plane stress and strain calculations but a shell element is always an infinitely thin plane defined by nodes at its corners.

Therefore, it is not possible to correctly model the chamfer, which has a "step" geometry, as illustrated in Figure 7-10.

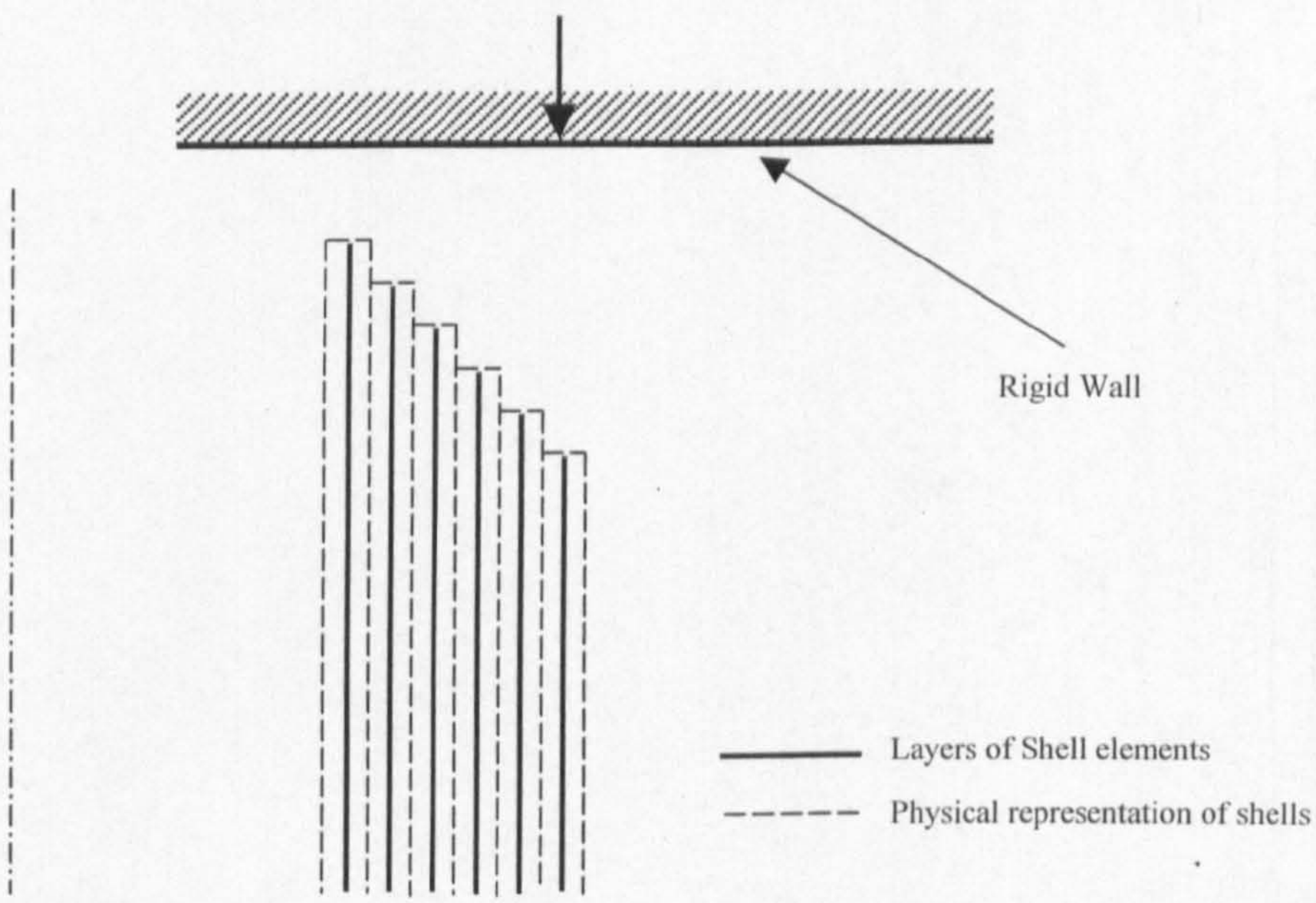

Figure 7-10 - Limitations of modelling the chamfer with shell elements

As a result, the perpendicular loading of the tube model as shown in Figure 7-10 will cause the shells to buckle, which in turn has a stress wave propagation effect leading to the premature elimination of elements, as seen in the model in Figure 7-9.

To conclude, a shell based modelling approach is not suitable for the kind of loading observed in tube crush as only solid elements can capture the geometry of the trigger and deal with the in-plane loading that the plies are subjected to. However there is a clear advantage in using an interlaminar behaviour model which allows correct modelling of splaying behaviour (as shown in the pre-splayed bi-shell model in Section 7.1.1).

It was therefore proposed that a suitable approach for tube crush modelling should consist of solid elements to model the individual plies, connected by a contact interface representing the interlaminar behaviour.

7.2 Solid Models

The finite element tube models consisted of one layer of solid elements to model each ply of the composite tube, Figure 7-11.

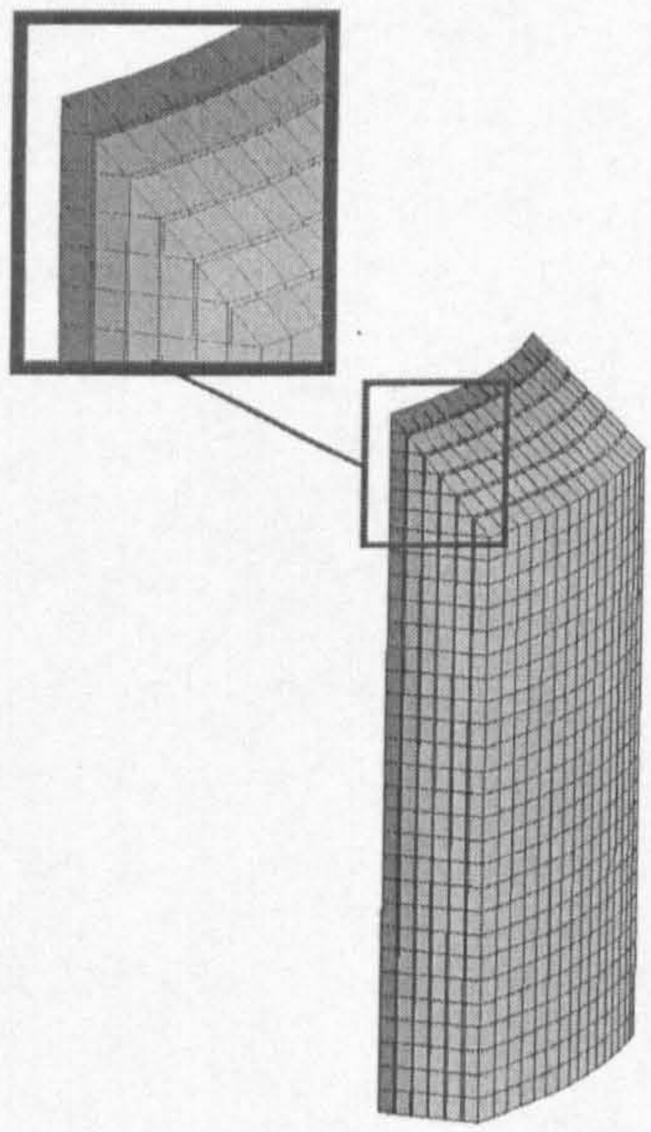

Figure 7-11 – Finite Element Tube Model of CoFRM.

The gap between two solid element layers represents the interlaminar resin-rich region. The two adjacent sides of those solid layers are connected by the delamination model described in Chapter 5, Figure 7-12.

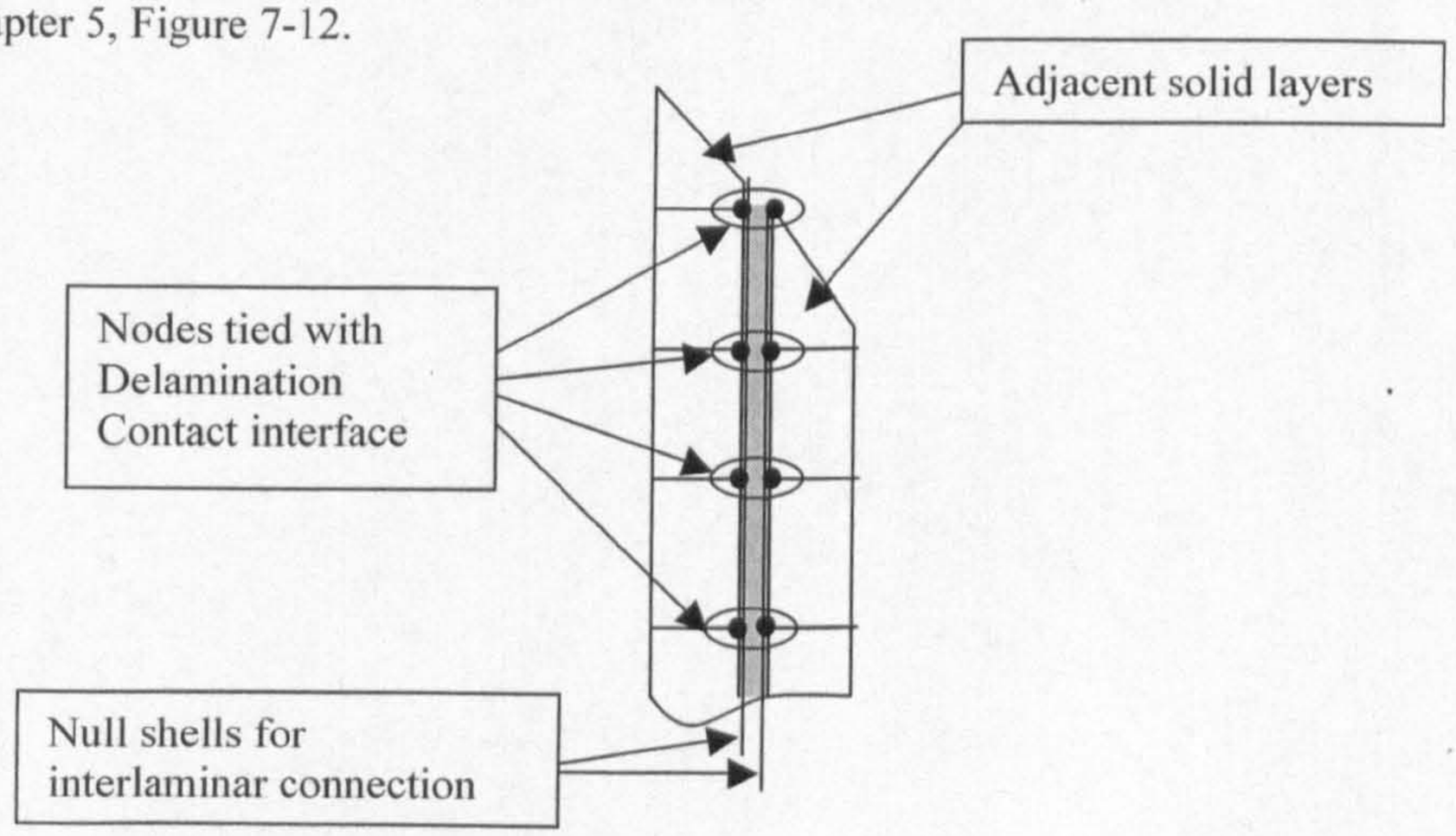

Figure 7-12 – Schematic detail of finite element model of composite tube

The delamination contact interface is defined between two adjacent shell layers. Each of these layers has coincident nodes with the respective solid ply. The shell elements have null material properties (Material Type #100) defined, which have no structural influence on the mechanical behaviour of the composite.

Each of the solid element layers contain coincident elements sharing nodes. Each of these coincident elements has one material model defined, namely degenerate bi-phase and elastic-plastic materials.

7.2.1 Elastic Plastic Data

One of the limitations of the current Bi-phase material model in PAM-CRASH is its numerical instability once damaged. This could be the result of non-linearities induced by the geometry of a crushed tube. This can have an impact in time-step, which is reduced to ensure stability of the solution. However, an excessive reduction in time-step can make the run-time impractical. To deal with this, it is usual in FEA analysis to define a criterion for element elimination. This is usually defined as a failure strain. A value of 90% axial strain was chosen for element elimination.

Eliminating finite elements poses a problem since, in a real structure, material does not simply disappear. Instead, it contributes to the overall strength of the structure, even if its properties have been degraded as a result of damage. To account for this residual strength post-elimination, the tubes modelled consisted of a double mesh of solid elements with the following material models:

- Degenerate-Bi-phase with element elimination (properties derived as described above)
- Elastic-Plastic to account for the residual stresses after Bi-phase are eliminated.

The material properties of the elastic plastic solids are related to the shear behaviour in direction *12* as this is the in-plane mode of deformation with the highest strain-energy absorption and therefore more likely to still be "active" at higher strains (when element elimination occurs).

The stress strain behaviour of the elastic-plastic solids is shown in Figure 7-13.

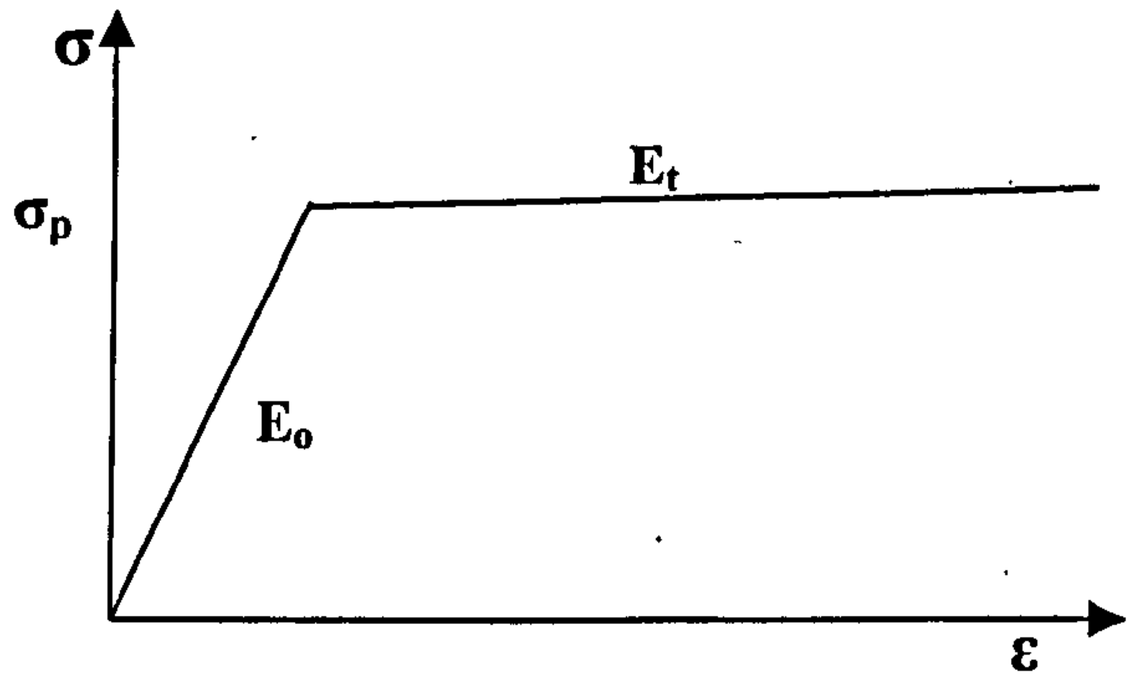

Figure 7-13 - Stress-strain behaviour of Elastic-Plastic material

As stated above, the properties of the elastic-plastic solids are related to the shear behaviour of the material in direction *12*, according to the following equations which define Young's Modulus E_o and Yield Stress σ_p:

$$E_o = 2 \cdot G_{12} \cdot (1 + \upsilon_{12})$$

$$\sigma_p = \sigma_{12_{max}}$$

where $\sigma_{12\ max}$ the maximum stress in the shear12 direction (see Figure 5-6).

The input parameters for the elastic-plastic material (Material Type #10) are the shear modulus G_{12} , the yield stress σ_p , the tangent modulus E_t , and the bulk modulus K, defined as:

$$K = \frac{E_o}{3(1 - 2\upsilon_{12})}$$

The behaviour of the material is elastic-perfectly plastic, which means that the tangent modulus E_t is zero. However, Material Type #10 in PAM-CRASH cannot accept such a value. Therefore a low value of E_t = 0.001 GPa was chosen. The elastic-plastic data for the composite materials investigated is shown in Table 7-3.

Elastic-Plastic Data	CoFRM	Braided Carbon		
		0/+30/-30	0/+45/-45	0/+60/-60
G [GPa]	4.246	3.5	3.9	5.1
σp [MPa]	96.7	51	67.5	92.9
Et [GPa]	0.001	0.001	0.001	0.001
K [GPa]	12.73	7.58	9.072	11.05

Table 7-3 – Elastic-Plastic Input Parameters for Composite Materials Investigated

7.2.2 Geometry

Figure 7-14 shows details of the geometry of the solid tube models, where ***a*** is the thickness of a ply, ***b*** is the thickness of the interlaminar region, ***c*** is the total thickness of the tube, ***d*** is the distance from the tube to the crush platen, and ***L*** is the length of the tube.

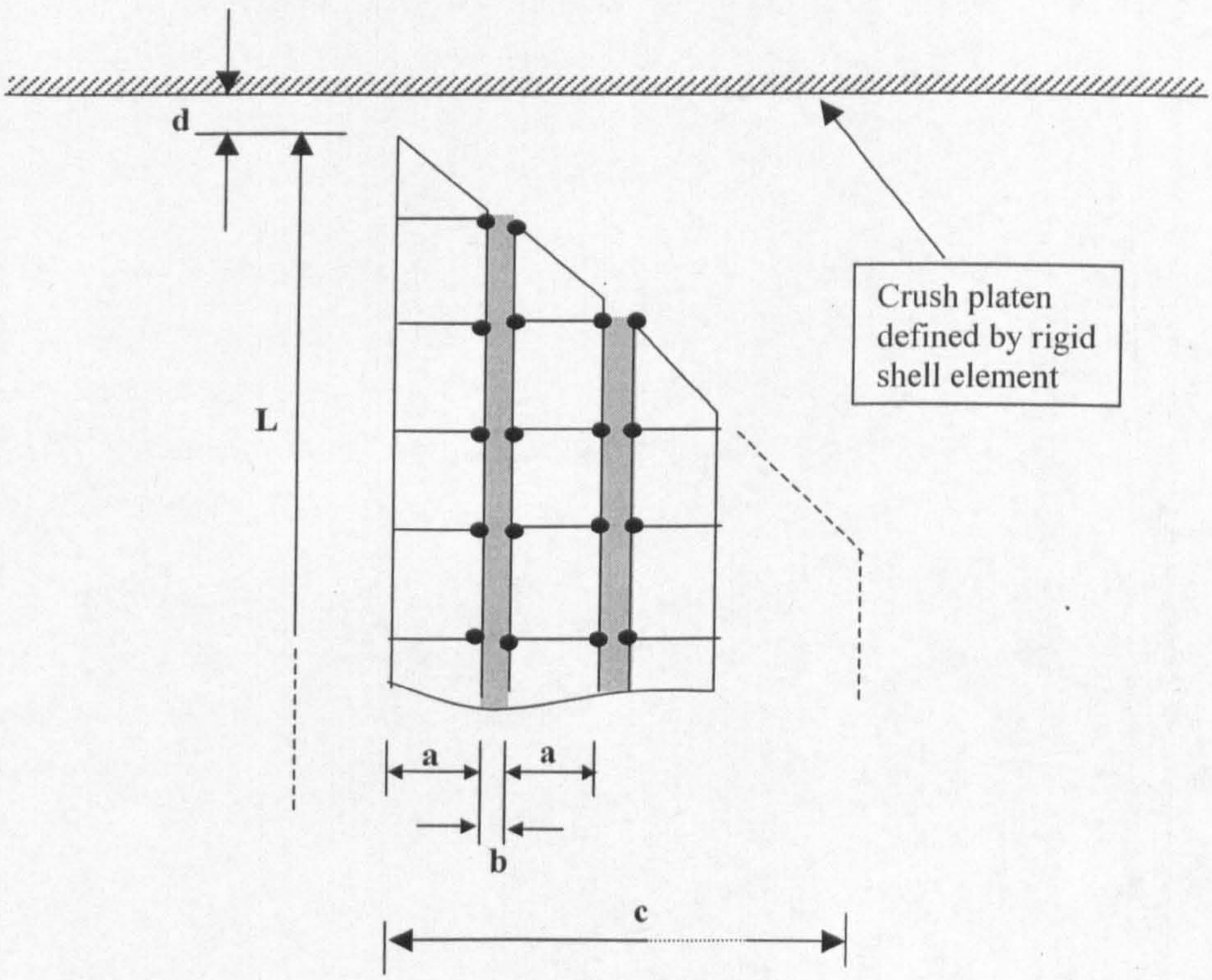

Figure 7-14 – Detailed Geometry of Solid Tube Model

Table 7-4 shows the dimensions of the tube models investigated.

Geometry	CoFRM	Braided Carbon		
	6-ply	2-ply	3-ply	4-ply
a [mm]	0.6	0.94	0.94	0.94
b [mm]	0.08	0.08	0.08	0.08
c [mm]	4	1.96	2.98	4
d [mm]	0.101	0.101	0.101	0.101
L [mm]	25	25	25	25

Table 7-4 – Dimensions of Solid Tube Models

7.2.3 Boundary Conditions

Only $1/16^{th}$ of the tube was modelled to reduce computational time. Boundary conditions at the free longitudinal edges of the tube were applied to represent the other $15/16^{th}$ of the tube structure. These symmetry boundary conditions are applied in similar manner to that described in 7.1.2.2 for the multi-shell tube model.

The tubes were crushed against a stationary rigid body defined by shell elements representing the crush platen . A contact interface between the tube and the rigid element was defined – this caused the deformation process to take place. The output force of this contact interface is the load-displacement characteristic of the tube. Load-displacement data output was filtered using a C180 filter [41].

An initial velocity of 5mm/ms was applied to the two lower rows of nodes of the tube to represent the crosshead displacement. The same group of nodes had its displacements constrained in the y-direction, i.e. for each time-step the y-coordinates of those nodes are the same, Figure 7-15.

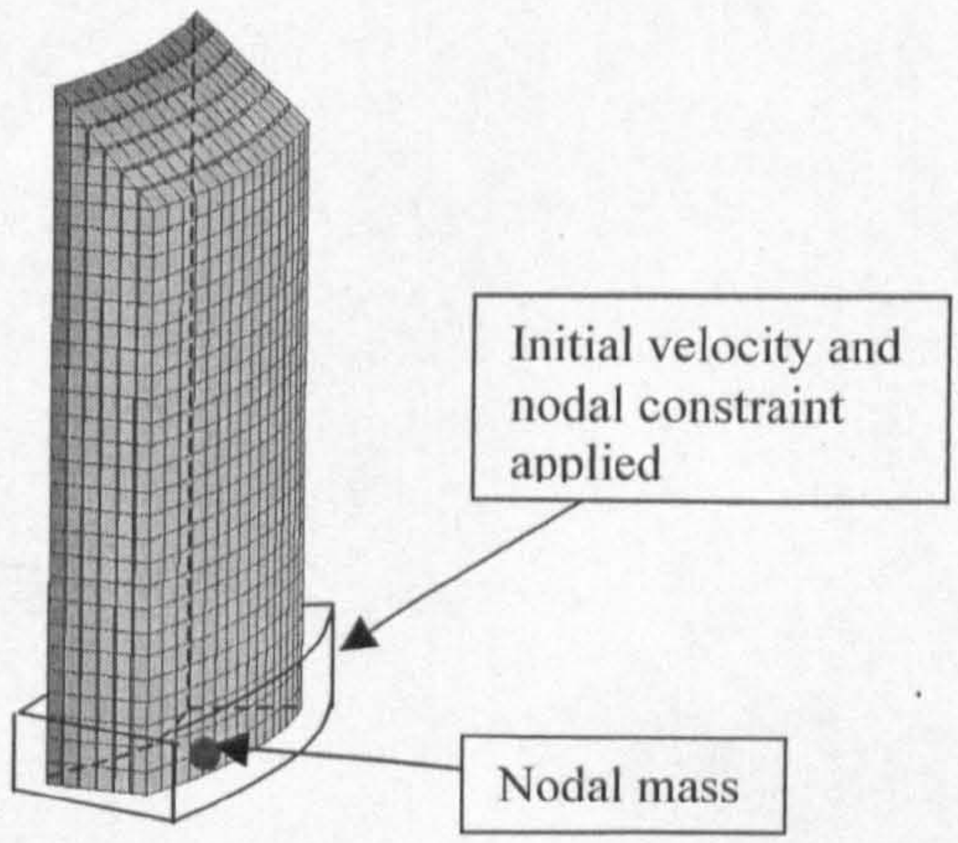

Figure 7-15 – Boundary Conditions on Solid Tube Model

A point mass of 24.4kg representing the crosshead was applied in one of the nodes at the bottom of the tube. To ensure quasi-static loading conditions, the kinetic energy of the analyses was measured below 5% of the internal energy which is common practice for FE analysis.

7.2.4 Global Control Parameters

The global control cards for the analysis where set to PAM-CRASH default values except for the following:

- Hourglass control based on stiffness using plastic modulus
- Scale factor for time-step set to 0.4
- Nodal time-step option active

An example of the control cards for a tube model is shown in Figure 7-16.

```
$
$ This file is generated by PAM-GENERIS version 2000 on 2000/12/01 at 5 :6 :8
$        PAM-GENERIS Version 2000 - Compiled 2000/04/28
$
FREE
TIMESTEP SMALL BEND
SOLVER CRASH
NOLIS
NOPRINT
SIGNAL YES
MNTR 3 2  0
FILE tube_braid_0_30_4ply
DATACHECK  YES
ALLOCATE 20000000
SHLPLOT DFLT
NODPLOT ALL
PIPE  NO
SHLTHP DFLT
SOLPLOT ALL
DEBUG  NO
TITLE /   Braided Carbon Tube - 0/+30/-30 4 Plies
$
$   CONTROL CARDS
$
$        TIME      TIOD      PIOD      IRD  NLOG DTO       SLFAC     ISTR IPHG IS
$
$---5---10----5---20----5---30----5---40----5---50----5---60----5---70----5---80
CTRL  /          2     0.001      0.01    0   10          0        0.1    0    1 0
$
$   SOLID VISCOSITY AND TIME STEP CARDS
$
$---5---10----5---20----5---30----5---40----5---50----5---60----5---70----5---80
               1.2      0.06         0       0.4          0        0.7          2
                 0         0         0         0    0          1    0    0    0
           1          0          0    0
$
```

Figure 7-16 – Control Cards for 4-ply Braided Carbon 0/+30/-30 Solid Tube Model

The options above, specifically time-step control were chosen to avoid diverging results and numerical instability, and were made following guidelines found in the PAM-CRASH manual [41].

7.2.5 Results

In the following sections results of tube crush analyses are shown. The format consists of images of successive states of deformation and corresponding load-displacement characteristics. The load-displacement curves for the experimental tests are also shown in the graphs. In the case of Braided Carbon analyses, only one set of plots is shown per each laminate type modelled (2-ply, 3-ply and 4-ply), as the deformed states for each of these tubes are similar for all three fibre architectures (0/+30/-30, 0/+45/-45, and 0/+60/-60), because 80k tows dominate the crush behaviour. For all the analyses, crack propagation (progression of delamination front) was monitored and is shown in the deformed states' plots.

7.2.5.1 CoFRM

This section shows results for CoFRM glass/polyester tube crush.

Degenerate Bi-phase Modelling

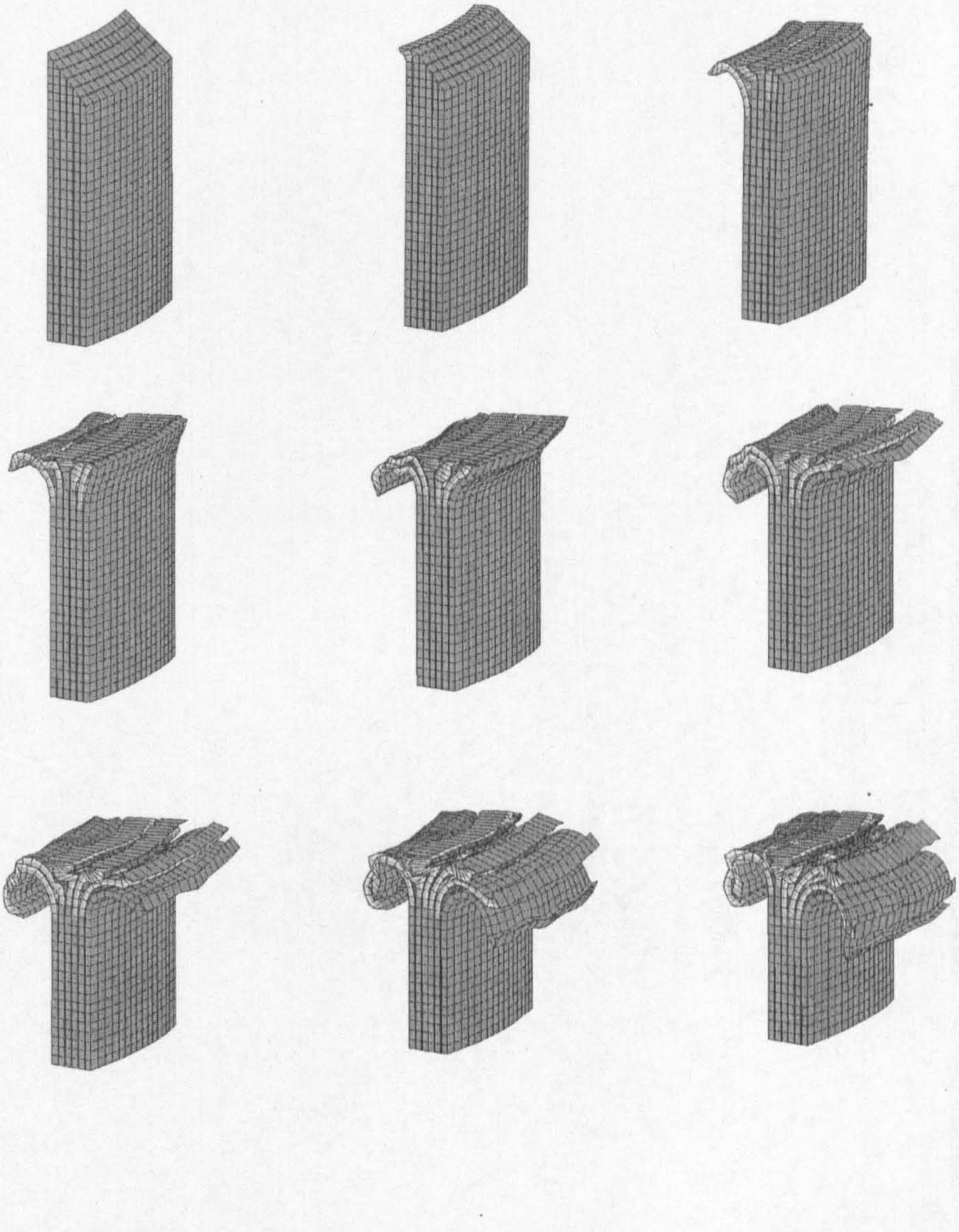

Figure 7-17 - CoFRM Tube Crush with Degenerate Bi-phase Modelling Approach

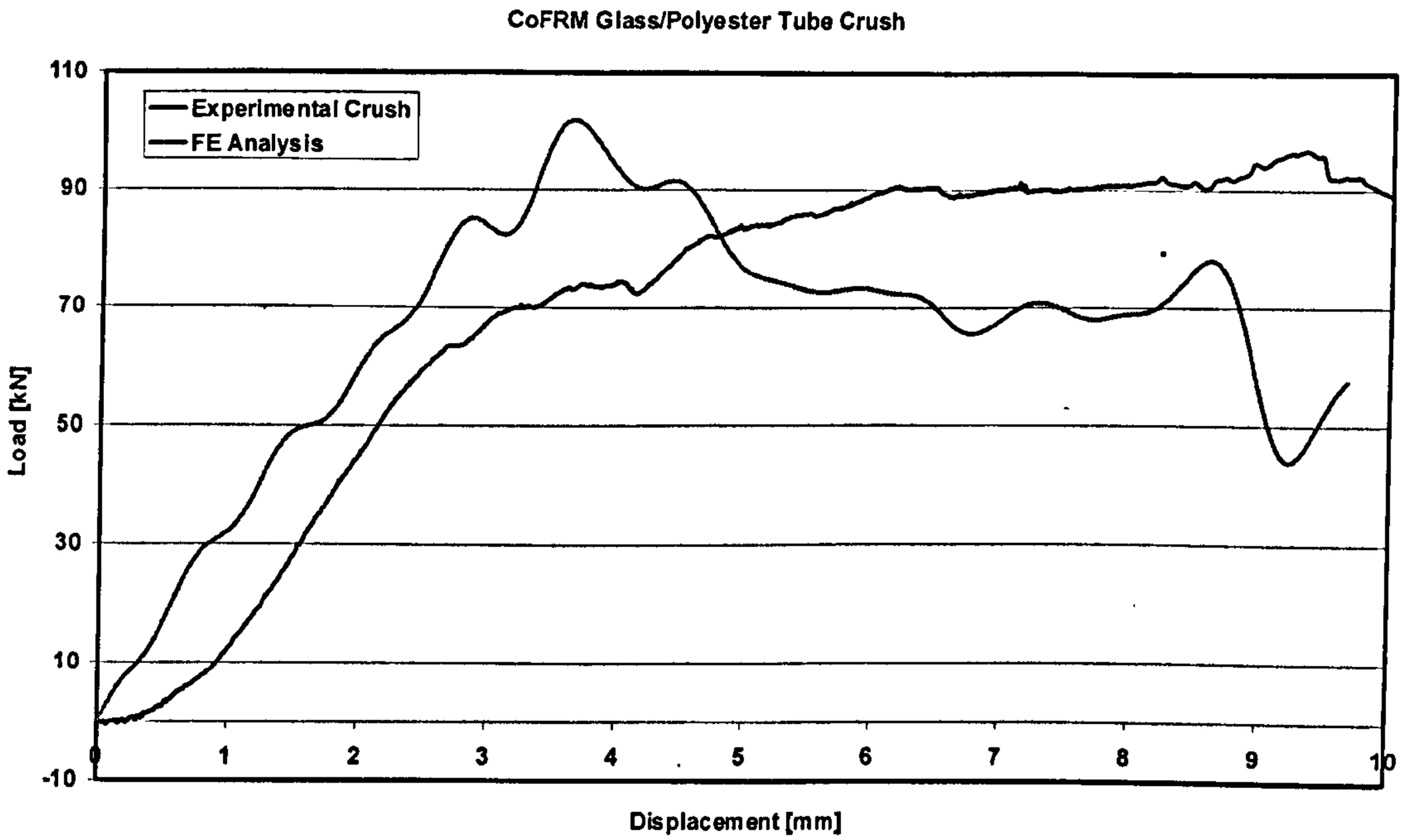

Figure 7-18 – Load-displacement of CoFRM Tube with Degenerate Bi-phase Modelling Approach

7.2.5.2 Braided Carbon

This section shows results for Braided Carbon tube crush, for the three fibre architectures tested.

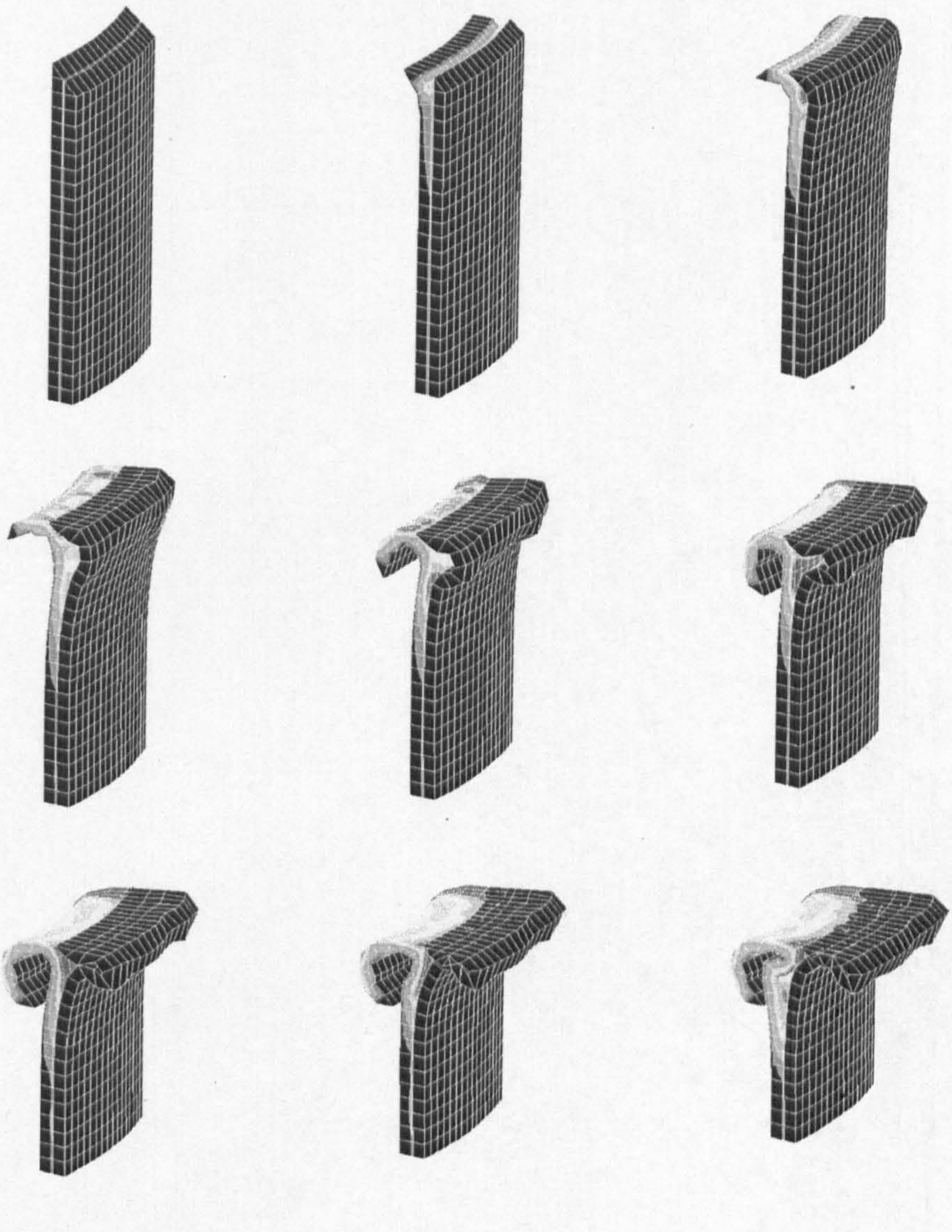

Figure 7-19 – 2-Ply Braided Carbon Tube Crush

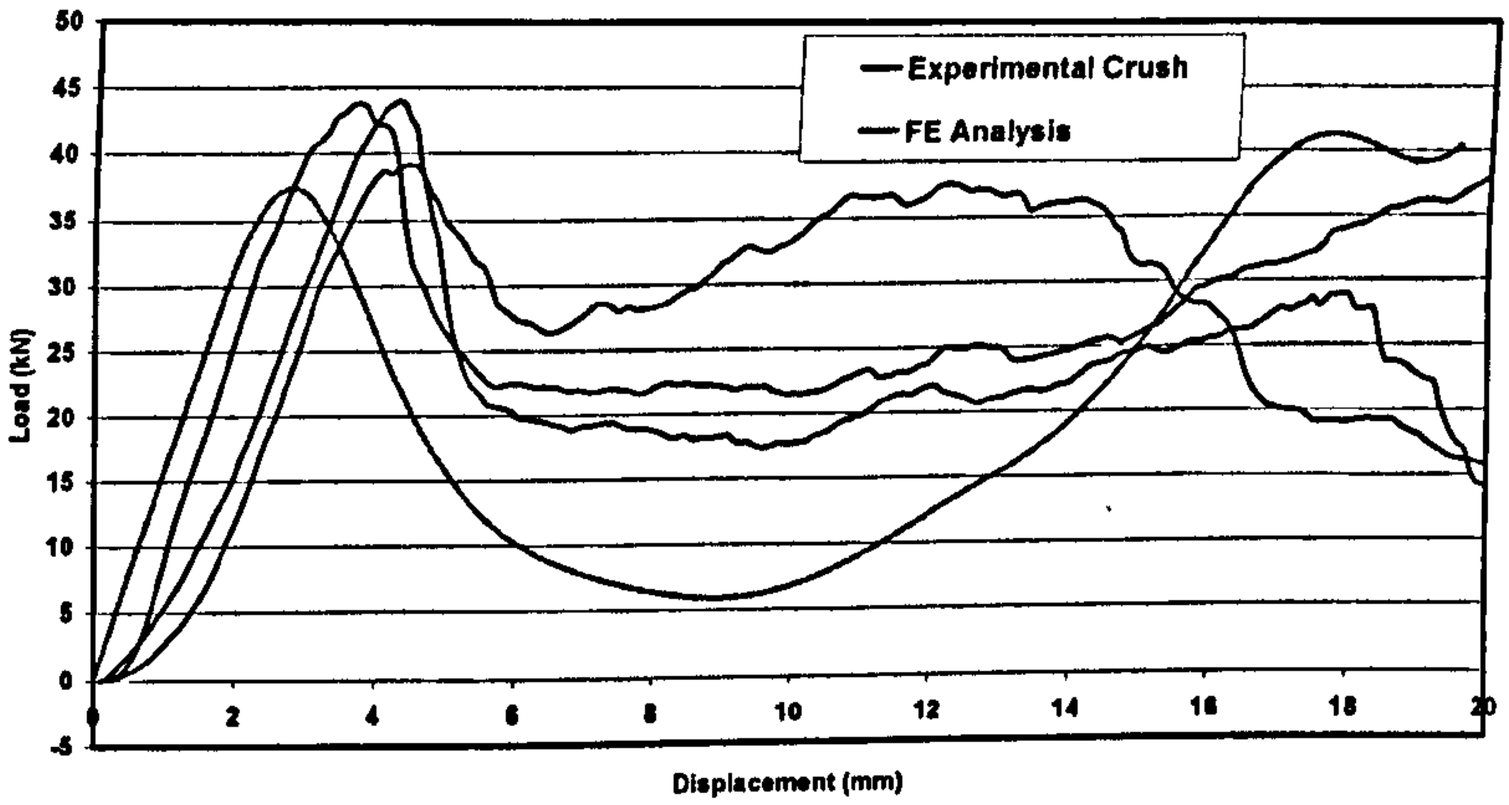

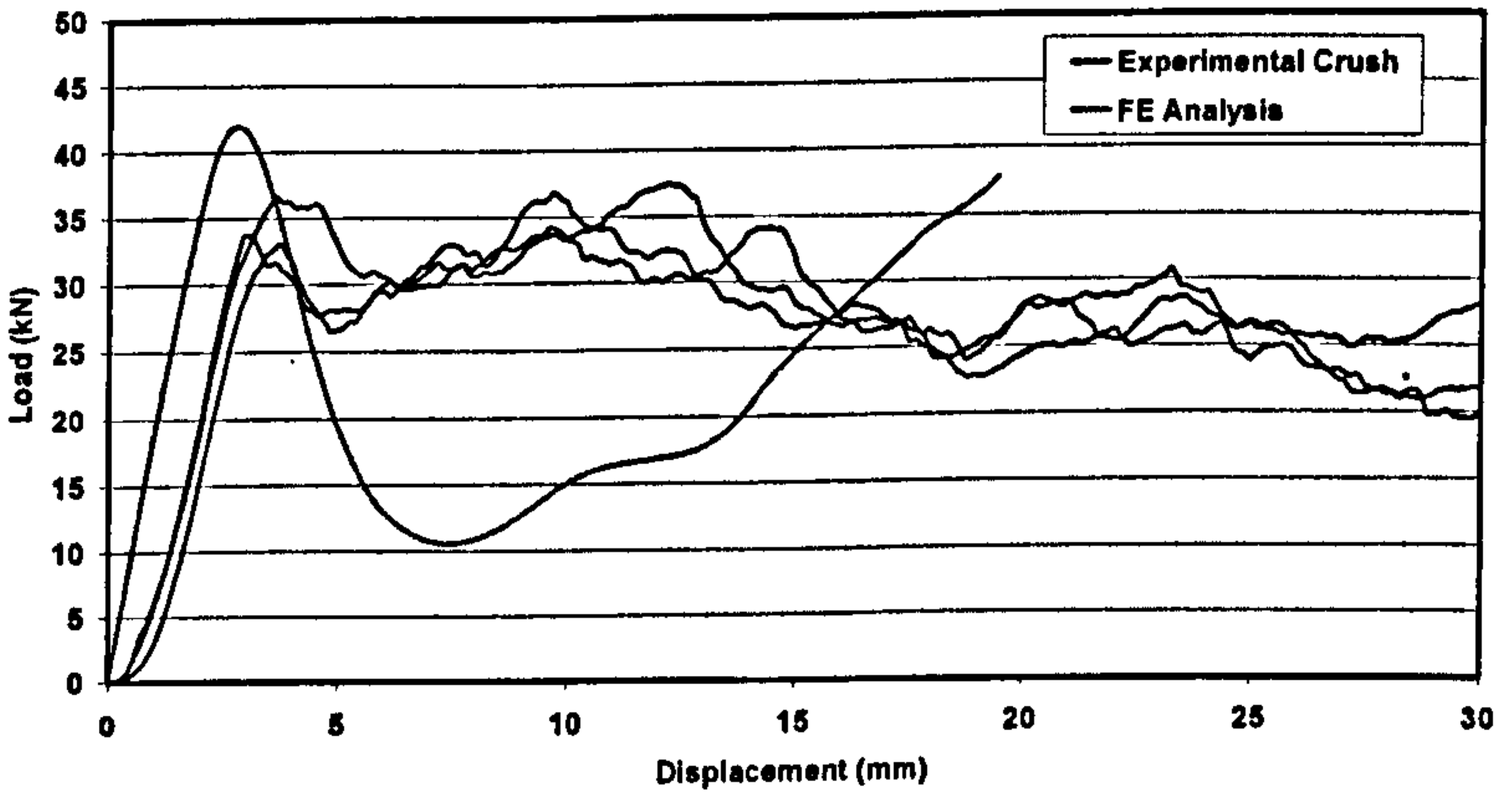

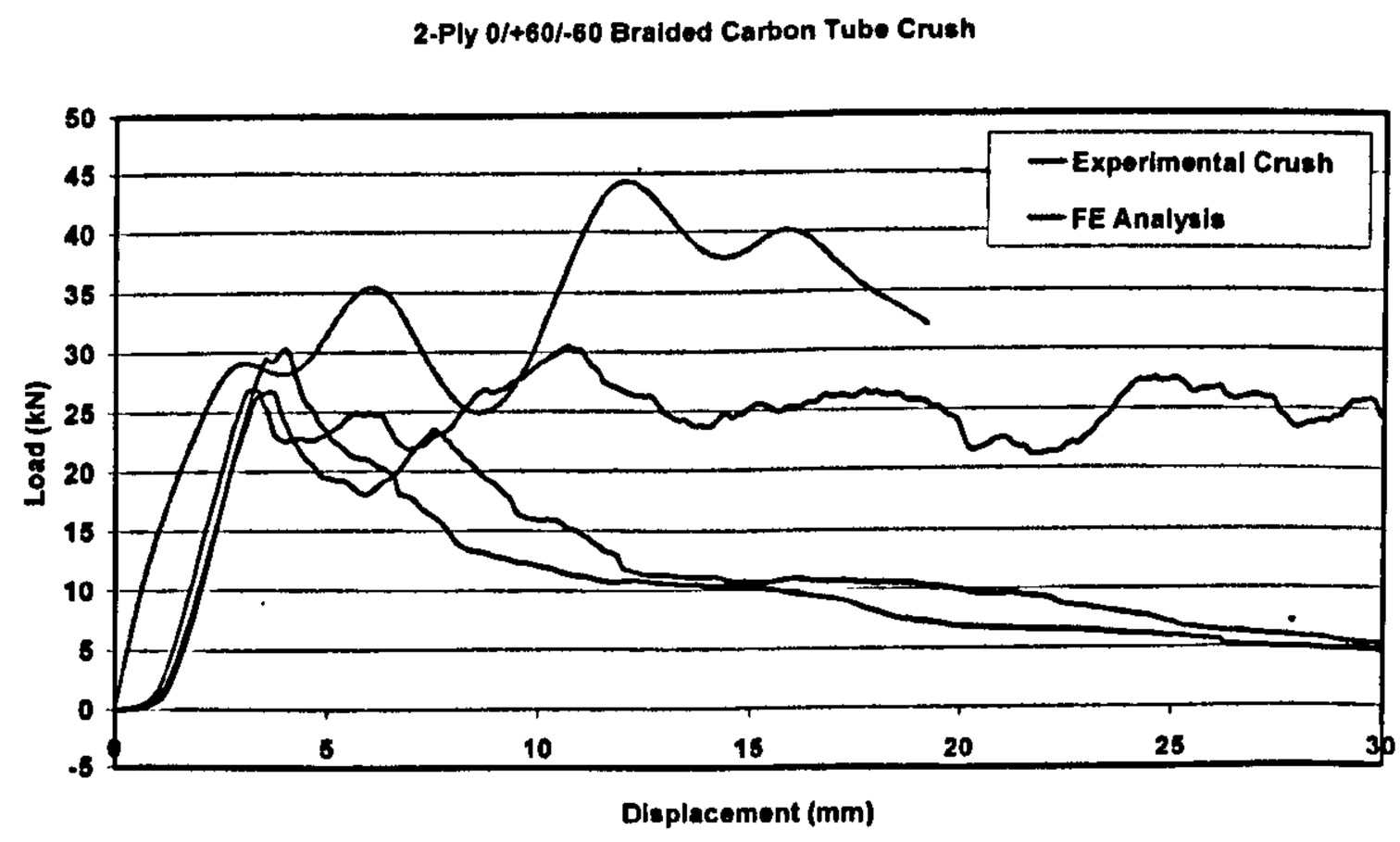

Figure 7-20 - 2-Ply load-displacement results for 3 fibre architectures

3-Ply Braid Architecture

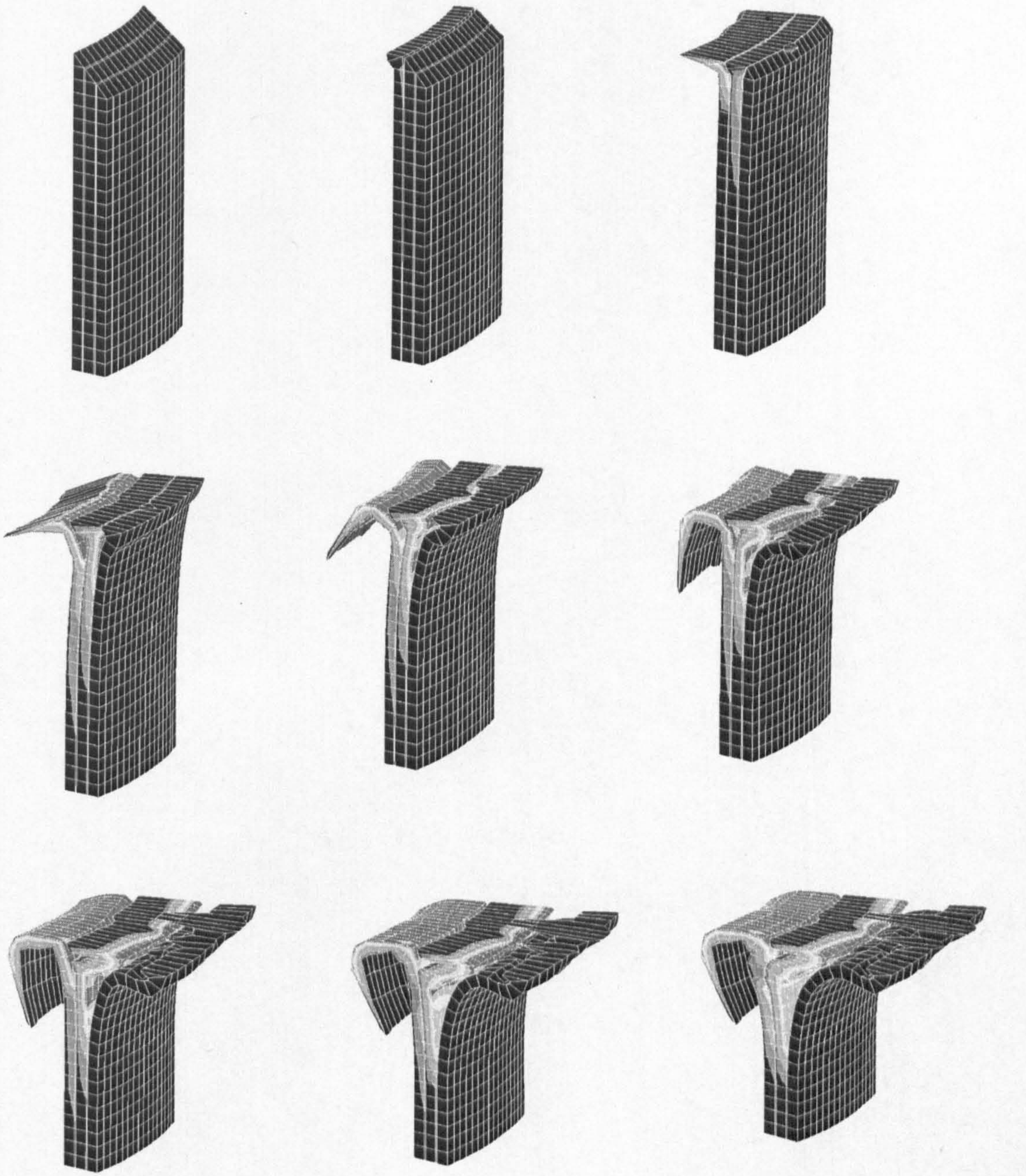

Figure 7-21 - 3-Ply Braided Carbon Tube Crush

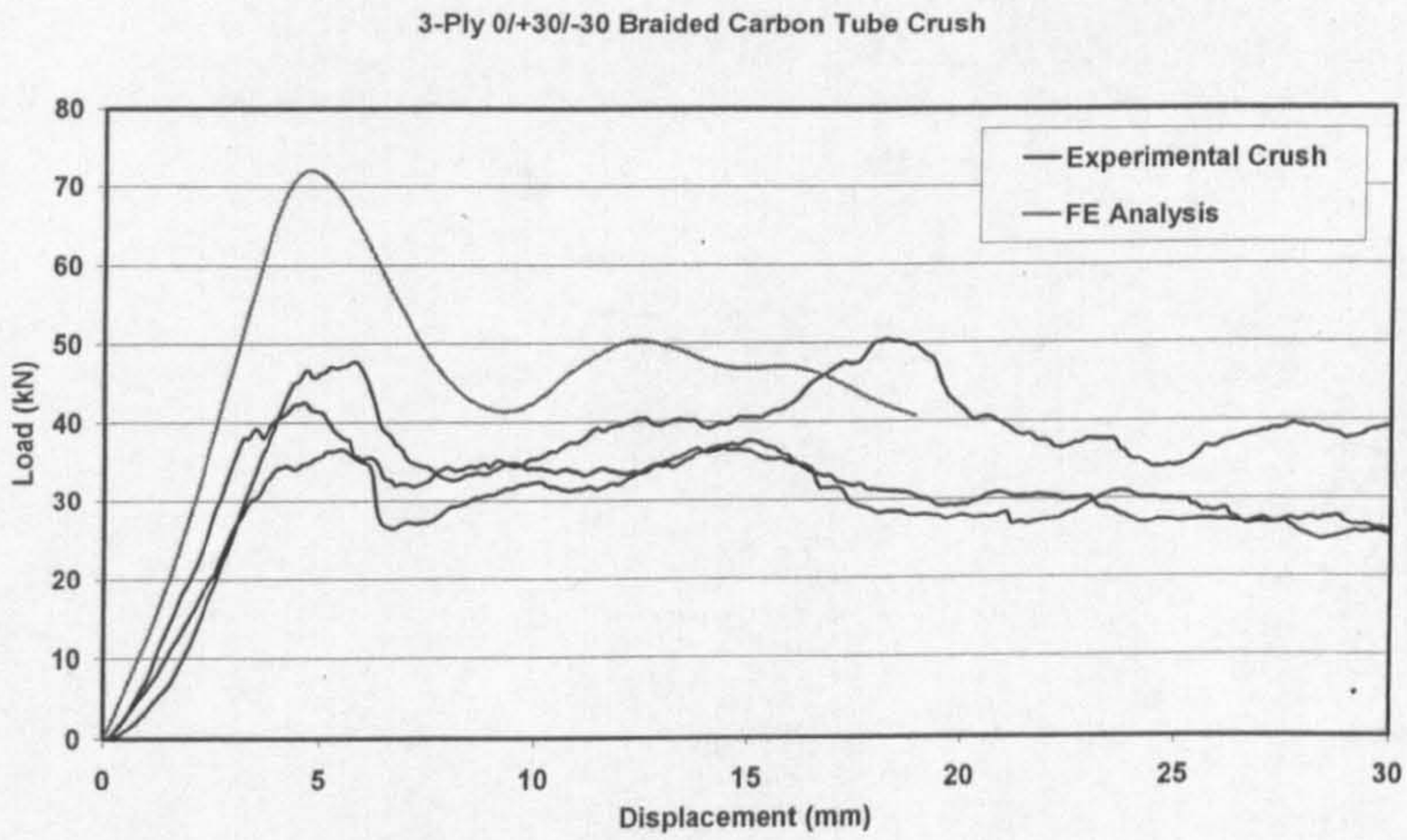

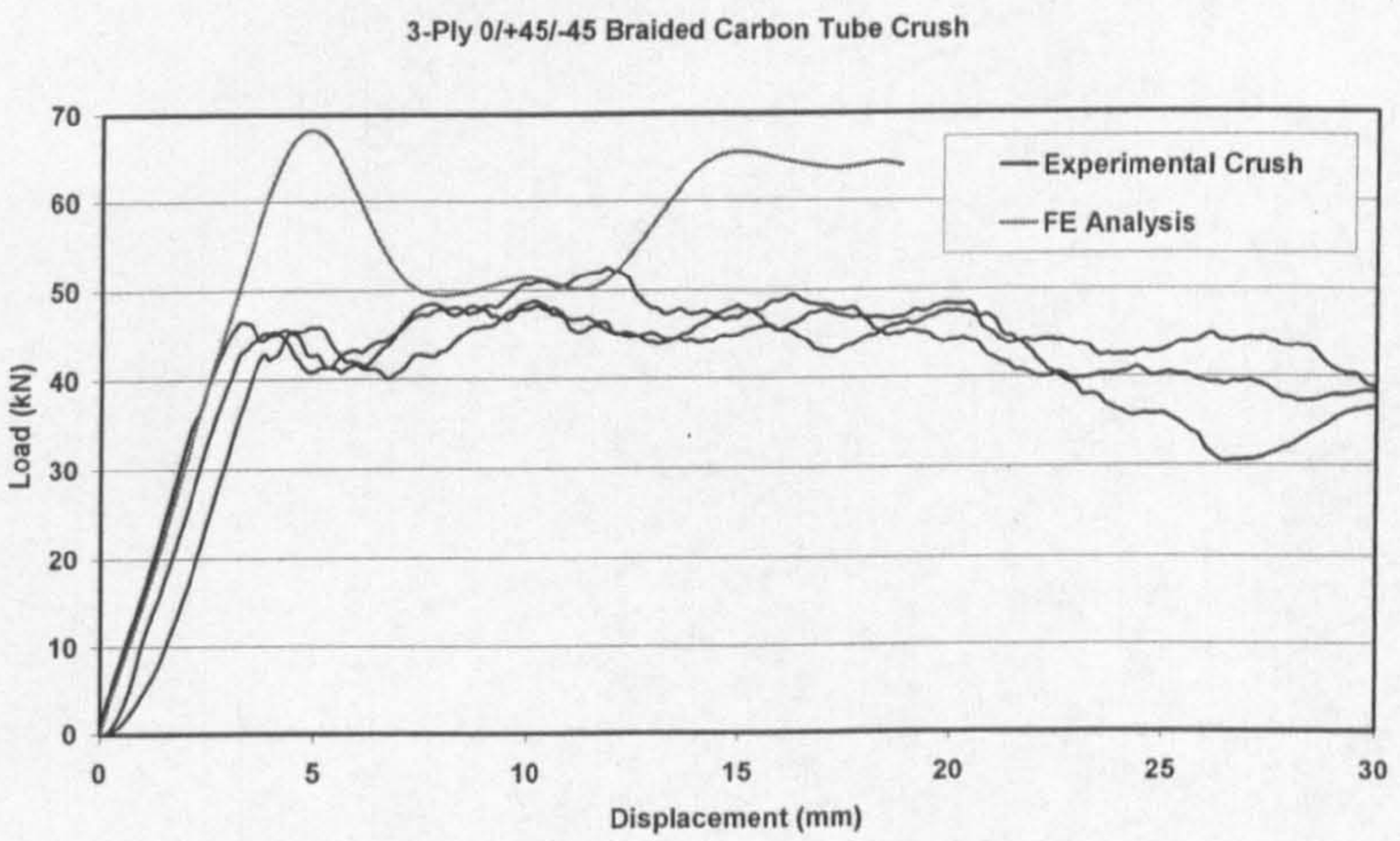

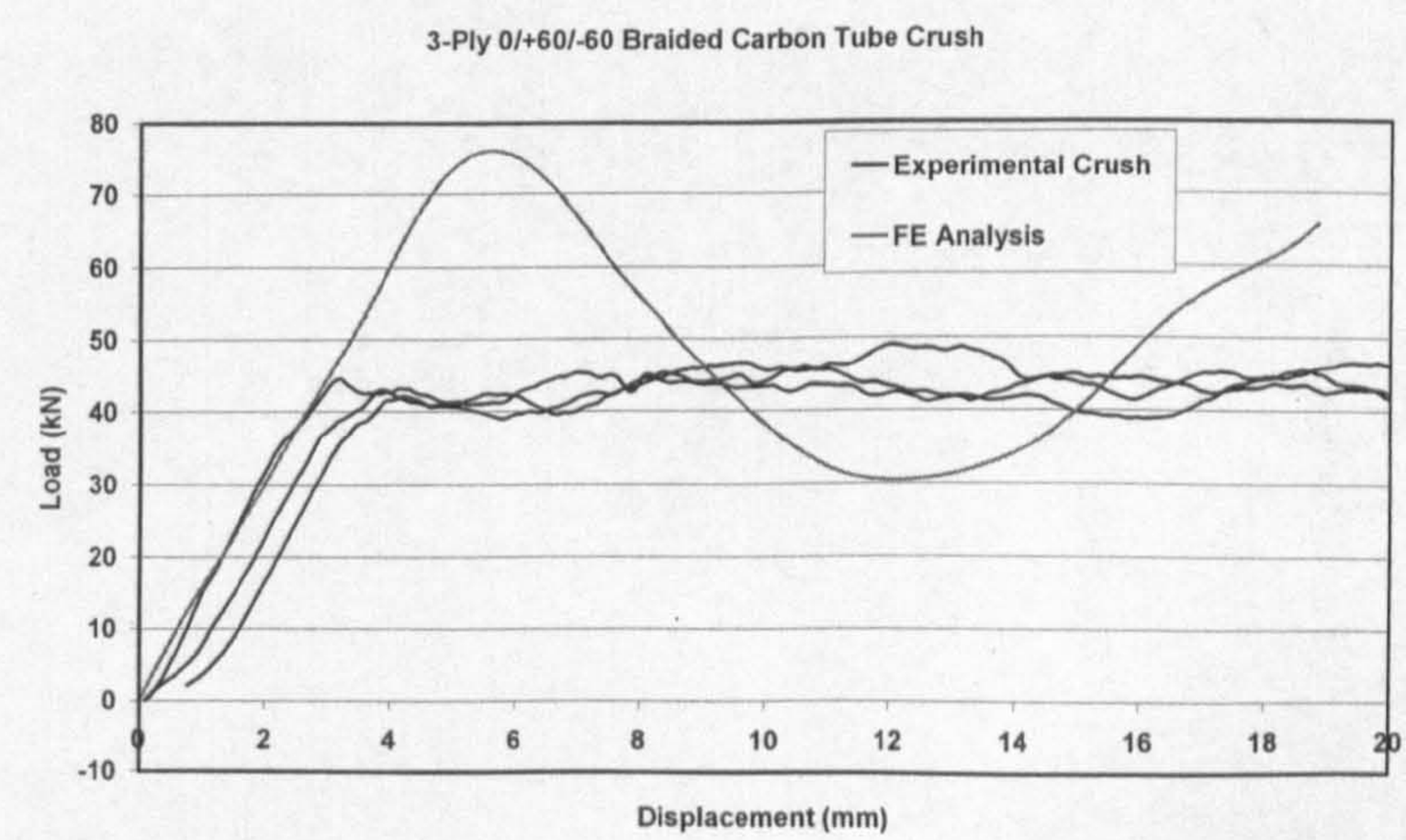

Figure 7-22 - 3-Ply load-displacement results for 3 fibre architectures

4-Ply Braid Architecture

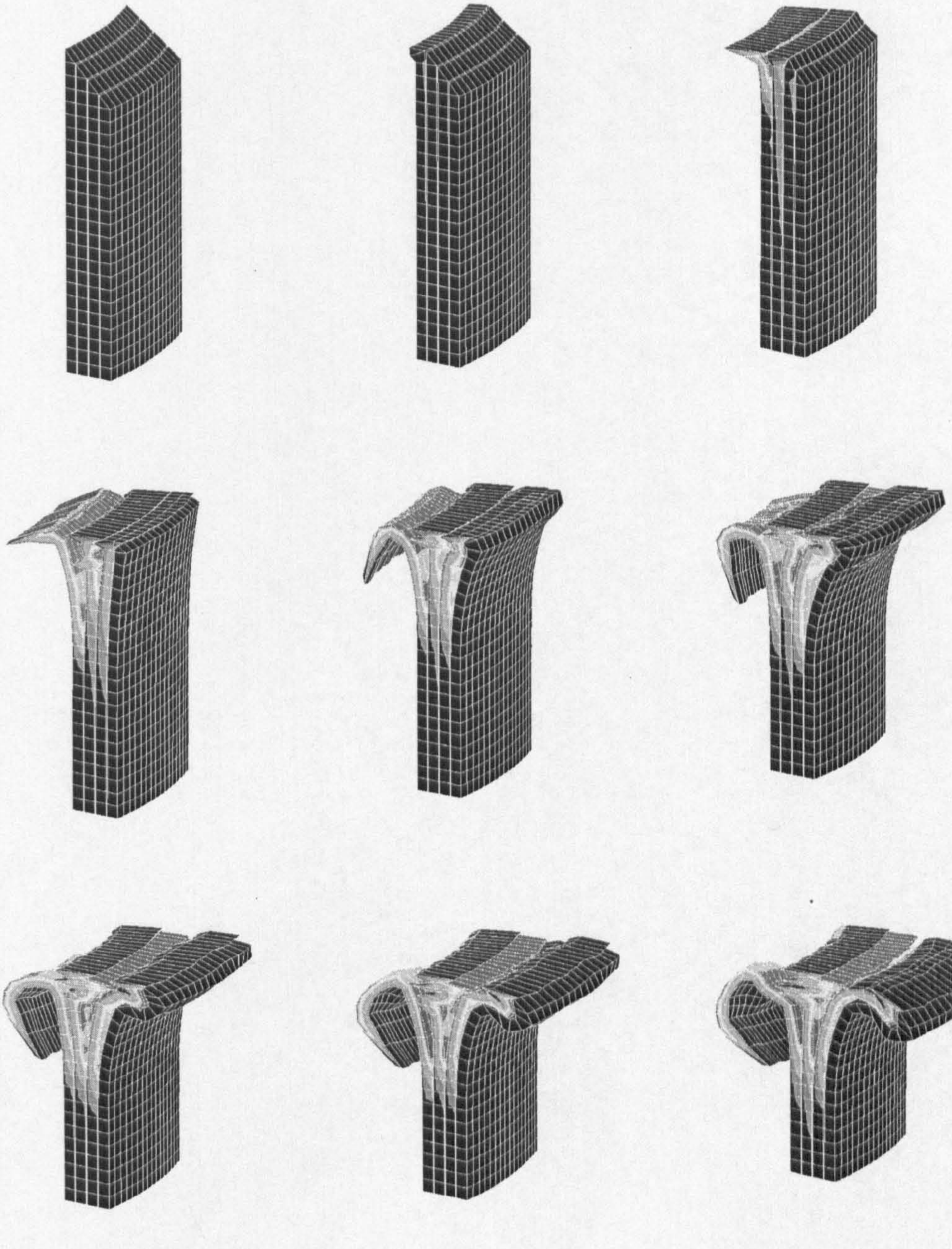

Figure 7-23 - 4-Ply Braided Carbon Tube Crush

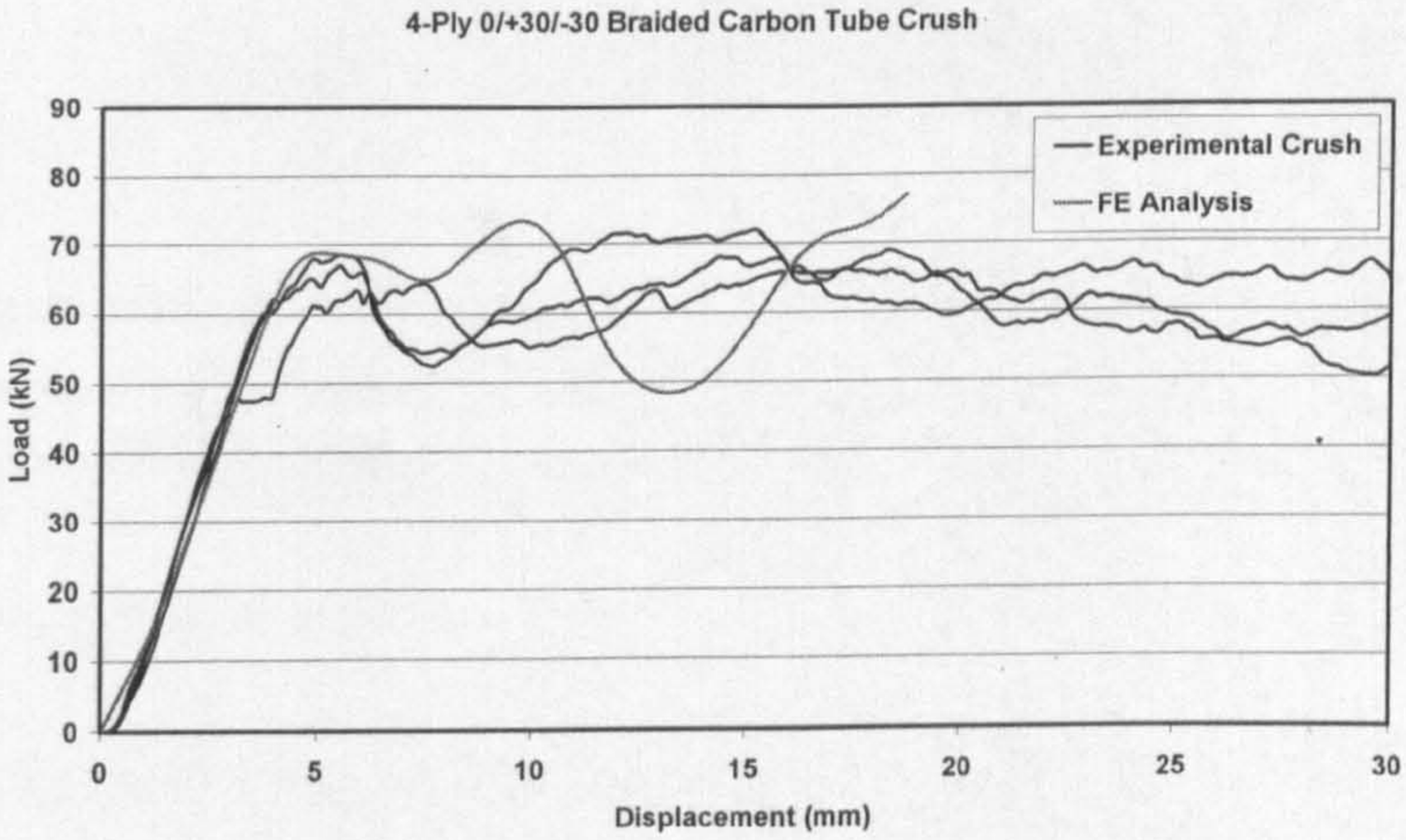

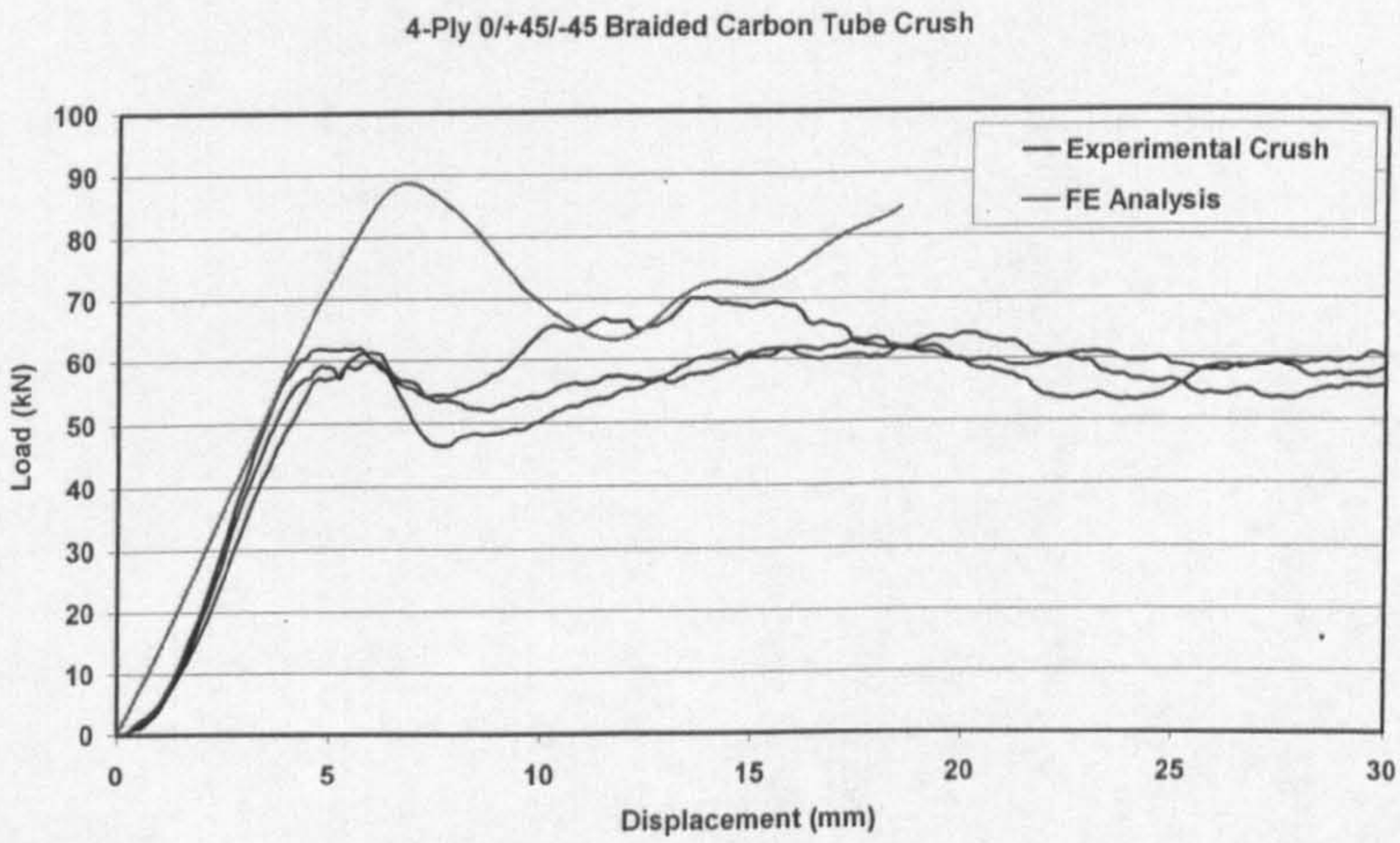

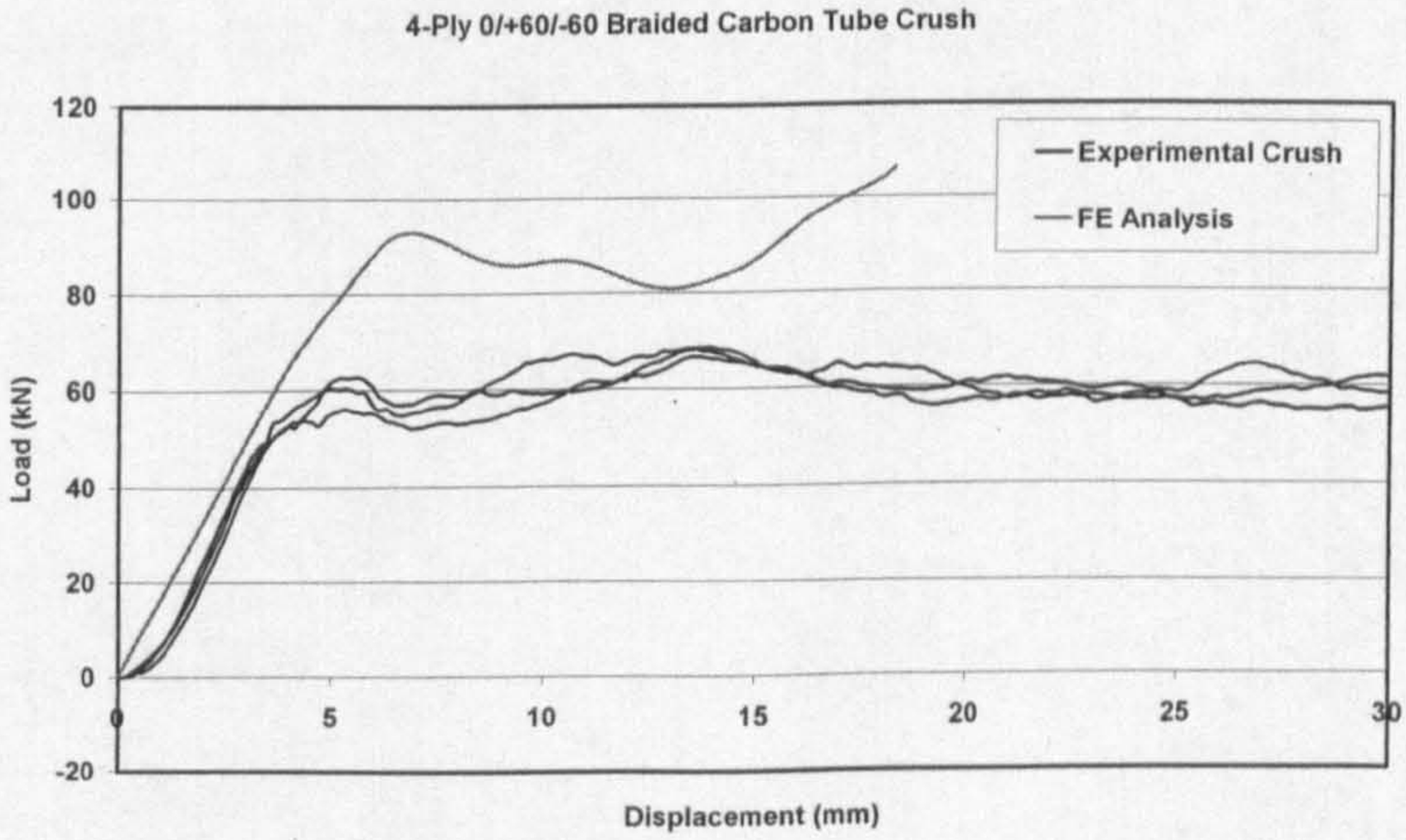

Figure 7-24 - 4-Ply load-displacement results for 3 fibre architectures

8.0 Discussion

In this chapter a discussion of the work covered in this thesis is given. This includes an assessment of the modelling approach proposed by the author and a discussion of its strengths and pitfalls. The following sections cover the results obtained in Chapters 4 to 7.

8.1 Intralaminar Results

8.1.1 Assessment of PAM-CRASH Degenerate Bi-phase Material Model

As previously stated in Chapter 4, this material model is recommended for bi-directional materials [41]. This is the case with CoFRM glass/polyester, which has quasi-isotropic in-plane properties and different behaviour through the thickness of the laminate. However, it is not the case with braided carbon, which exhibits considerable differences in stiffness and strength between the three principal axes. This is not a limitation though, if the proposed modelling approach is followed, as in-plane and out-of plane behaviour are treated separately. This means that the bi-directionality of the material model is valid in-plane whereas the delamination model described in Chapter 4 deals with the out-of-plane mechanical behaviour.

There are however limitations to this material model. Perhaps the main pitfall is the existence of only one set of (isotropic) damage parameters that affect the material properties. As a results, calibrating the material model to suit a particular laminate becomes a timeconsuming task, dependent on the experience of the analyst with the Excel Macro described in Chapter 5. Another limitation is the absence of rate dependency effects for this material model. It is anticipated that this will be addressed in a future version of the commercial code PAM-CRASH.

8.1.2 Validation of Degenerate Bi-phase Material Model

The purpose of this validation was to evaluate the performance of the material model with anisotropic structures. Therefore, these tests were performed on the 3 architectures of braided carbon studied. Three modelling techniques using shell elements were used:

- Single shell
- Bi-shell + delamination model
- Multi-shell + delamination

This work was carried out during initial stages of development of the delamination model described in Chapter 4 – as a result, the bi-shell and multi-shell models were run to test the numerical stability of the combined Degenerate Bi-phase material model and delamination subroutine.

The results generally show reasonable agreement with experimental tests. Bi-shell and Multi-shell models show premature failure in 0/+60/-60 axial tensile test and transverse tensile for 0/+30/-30 and 0/+60/-60. This can be attributed to two factors:

- Inaccurate interlaminar properties since only approximate fracture toughness test data was available for these materials
- Oscillation of slave nodes caused premature failure of adjacent elements.

The lower FE results observed in most tests are believed to be the consequence of eliminated elements. In a real structure, highly damaged material can still withstand load whereas they are eliminated in the Finite Element model to prevent numerical instability and excessive reduction in time-steps [41].

There is generally better agreement between numerical and experimental compressive tests. This suggests that interlaminar properties seem to have little influence in mechanical behaviour of the intralaminar coupon tests.

8.2 Interlaminar Results

8.2.1 Delamination Algorithm

In Chapter 4 the delamination model was developed and its implementation in the PAM-CRASH code was described in detail. This type of elastic damage law approach has been previously implemented in implicit codes [8] with encouraging results for fracture toughness tests. However, implicit codes are unable to deal with multiple delamination fronts because of the integration rule. Also, work carried out to date has not considered non-linear mixed-mode behaviour which is observed in many laminate composites. Hence the motivation of this work which was to develop a mixed-mode delamination model for an explicit FE code.

8.2.2 Validation of Delamination Model

A validation of the delamination model was carried out in Chapter 6 and consisted of modelling standard fracture toughness tests using a 2 layers of shell elements connected by

the developed contact interface. The tests analysed were Double Cantilever Beam (DCB), End Notch Flexure (ENF), and Mixed-Mode Bending (MMB), which are used to quantify respectively Mode I, Mode II and Mixed-Mode fracture toughness.

The mixed-mode coupling of the material was found to be highly non-linear. A high increase in critical fracture toughness was observed when a small component of Mode II loading was applied. Results showed an increase of 121% in critical fracture toughness with a Mixed-Mode ratio of 11.3% Mode II component. This means that previous delamination models which treat materials' mixed-mode behaviour as linear can be very conservative in their prediction of interlaminar fracture toughness Good agreement between FE and experimental results was achieved for all tests.

Further to the fracture toughness tests described above, a study was carried out to assess mesh dependency of the delamination model, as this phenomenon can affect the results of tube crush simulations [9]. This study consisted of modelling a 4-point bending test using two different mesh densities, which are shown in detail in Appendix 2. Comparison of results between two different meshes of the 4-point bending test showed no relevant differences.

8.3 Tube Crush Results

In Chapter 6 a procedure to model tube crush of composite circular tubes was described in detail. This included the required steps to calibrate PAM-CRASH material models using material properties measured from coupon tests. Details of FE models of the tubes were included.

The objective of this calibration was to build the required material cards using only data collected from coupon tests and avoid the inclusion of any parameters with no physical meaning. However, in the fitting process of the anisotropic damage, these material models do include damage parameters which could be described as non-physical. In the modelling approach proposed in this work, a relation between the damage parameters and in-plane shear properties was established, as described by Curtis [9].

8.3.1 Calibration of Degenerate Bi-phase Material Model

The calibration consisted of 3 basic steps:

- Inclusion of Elastic Moduli and Poisson's ratios collected from coupon tests.
- Calibration of damage parameters based on Shear 12 test.

- Inclusion of interlaminar data collected from fracture toughness tests.

Of the steps mentioned above, the calibration of damage parameters can vary depending on the experience of the analyst with the Excel macro described in Chapter 6. However, guidelines were given in the same chapter to allow the use of a similar strategy for other composite materials.

It can be observed in CoFRM results that the correlation between PAM-CRASH material behaviour and experimental results for out-of-plane tests (through-thickness tensile and Shear 23) is poor. This is the result of using anisotropic damage to define post-first ply failure behaviour of the laminate. However, the lower strength of the interlaminar contact interface ensures that out-of-plane damage and failure are controlled by the contact algorithm.

Elastic-Plastic Data

Results of preliminary analyses showed that elimination of degenerate bi-phase elements resulted in inaccurate modelling of splayed fronds and did not allow the formation of a debris wedge. To switch off element elimination for the degenerate bi-phase elements would be unreasonable as they introduce numerical instability once deformation is high. This is a result of excessive reduction in time-step for the analyses which would make them impractical for today's computing power.

As a countermeasure to this effect, a coincident mesh of elastic-plastic elements was introduced. This approach was previously tried by Pickett with encouraging results [33]. The purpose of this coincident mesh is to simulate the residual strength of the damaged composite material which the author believes to be responsible for the development of a debris wedge and subsequent splaying of fronds.

A relation between the elastic-plastic material properties and in-plane shear behaviour was established. This was based on the observation that this is the in-plane mode of deformation with the highest strain energy absorption and therefore more likely to control the mechanical behaviour of the plies for high strains.

8.3.2 Finite Element Models of Circular Tubes

A description of the meshing details and applied boundary conditions of the circular tube models was given in Chapter 7. Only one sixteenth of the tubes' circumferences were modelled to reduce computational time.

In the present work the crush platen was modelled with rigid shell elements with null material properties and the contact with the crushing tube was defined by a penalty-based contact interface to prevent penetration. The more traditional approach consists of modelling the crush platen as a RIGID WALL which imposes a constraint on the nodes with reach the rigid wall surface. In explicit codes, nodal constraints are generally more numerically unstable that penalty-based contact interfaces [41], which explains the choice of crush platen modelling in this work.

8.3.2.1 CoFRM Results

There was a good agreement between FE and experimental tube crush results using this modelling approach. A clear formation of a debris wedge and splaying fronds was observed. As described in Chapter 4, the delamination algorithm allows the monitoring of crack propagation which is shown in all tube crush models shown in Chapter 7. In the model no centre wall crack propagation was evident. An initial higher strength of the FE tube compared to experimental results was observed. This is believed to be a result of damage in the vicinity of the trigger, caused by the machining operation.

8.3.2.2 Braided Carbon Results

Braided Carbon FE tube results showed generally good agreement with experimental results, both at load-displacement level as well as crush modes. The correlation between finite element models and experimental results is gradually better as the number of plies increases. The cause for this is that 2- and 3-ply tubes are more prone to buckling as was shown by Duckett [11]. The same author concluded that there was more variability in experimental tube crush results for braided carbon tubes with a low number of plies as a result of manufacturing. A considerable number of voids and resin-rich areas was found in tested tubes which can dramatically change the crush mode.

These issues with manufacturing of braided carbon tubes can also be responsible for the absence of a high peak in the load-displacement response of 3- and 4-ply tubes. The machining effect on the trigger explained above can be more relevant for tubes with higher void content, which is this case of braided carbon when compared with CoFRM [11].

9.0 Conclusions

A predictive modelling approach was developed for the crushing of composite laminate circular tubes. Several materials were used in this study, varying fibre and resin types, and also different fibre architectures. These were:

- CoFRM Glass/Polyester 6-ply laminate
- Braided Carbon/Vinylester
  - 2-ply, 3-ply, and 4-ply tubes
  - 0/+30°/-30°, 0/+45°/-45°, and 0/+60°/-60° fibre architectures

The modelling approach consisted of treating in-plane and out-of-plane behaviour separately. The in-plane modelling was based on work developed by Curtis [9] and includes a clearly defined test programme to obtain the relevant material properties, which characterize the mechanical behaviour. Details of intralaminar modelling were described, which includes a validation of the PAM-CRASH Bi-phase material model used. In Chapter 4, a new delamination model was described and the details of the algorithm programmed in PAM-CRASH were explained. It is possible with this new sub-routine to describe the interlaminar behaviour of the composite materials using clearly defined physical parameters obtained from standard fracture toughness tests. A validation of the delamination model was included in Chapter 6.

This work contains a detailed description of the procedure used to obtain the input parameters for the PAM-CRASH material model, which were collected from the coupon tests. A description of the modelling technique for the tubes is included, which comprises geometry, meshing details, boundary and loading conditions, and output readings.

The approach can be considered predictable as only coupon test data is used for the input parameters of PAM-CRASH material models and delamination contact interface. There is no required prior knowledge of the mechanical behaviour of a composite tube to carry out the simulation.

The present modelling approach is applicable to current crash models of complete vehicles in that it uses a widely used commercial explicit finite element code and standard modelling tools for the assembly of the tube structure. A high number of elements is required for an

accurate prediction of crush modes and SEA since each ply has to be modelled separately but this is possible considering the current processing power of computer clusters in the automotive industry. As an example, currently a model of a crash test dummy contains an average of 20000 elements.

Johnson and Pickett [33] successfully predicted the interlaminar damage of aircraft composite structures subjected to high velocity impact, using the delamination model presented in this work. In the work by those authors the structures were modelled as layers of shells connect by a delamination contact interface. Shells are the preferred elements to be used in crash models for automotive applications. However, the tendency for single ply buckling exhibited by shells loaded in in-plane compression proves impractical for predicting the initiation of splaying, formation of a debris wedge, and subsequent steady state crush observed in composite circular tubes.

9.1 Future Work

There is currently no option to model rate effects for the Degenerate Bi-phase material in PAM-CRASH, which is a further requirement for a complete feasible application of the approach proposed in this work in current automotive crash simulation.

Future work required in the scope of this thesis will have to be concentrated on modelling of strain rate effects. This includes the development of a testing programme which will provide data for inclusion in the PAM-CRASH material and delamination input parameters. Some of that work has been developed by Duckett [11] and Fernie [18].

10.0 References

[1] ASTM D5528 94a Standard Test Method for Mode I Interlaminar Fracture Toughness of Unidirectional Fibre-Reinforced Polymer Matrix Composites, 1994.

[2] Allix O., Ladeveze P. and Corigliano A., "Damage Analysis of Interlaminar Fracture Specimens", *Composite Structures*, 31, pp 61-74, 1995.

[3] Bolukbasi AO and Laananen DH, Analytical and Experimental Studies of Crushing Behaviour in Composite Laminates, *Journal of Composite Materials*, Vol. 29, No. 8, pp 1117-1139, 1995.

[4] Botkin M, Johnson N, Zywicz E, Simunovic S, Crashworthiness Simulation of Composite Automotive Structures, *SAE/Advanced Composites Conference and Exposition*, Detroit, Michigan, USA, 1998.

[5] Castejon L., Cuartero J., Clemente R. and Larrode E., Energy Absorption Capability of Composite Materials Applied to Automotive Crash Absorbers Design, SAE 980964, 1998.

[6] Chen JH, Sernow R, Schulz E and Hinrichsen G, A Modification of the Mixed-Mode Bending Test Apparatus, *Composites:Part A,* Vol. 30, pp 871-877, 1999.

[7] Corigliano A, Formulation, Identification and Use of Interface Models in the Numerical Analysis of Composite Delamination, *International Journal of Solids and Structures*, Vol. 30, No. 20, pp 2779-2811, 1993.

[8] Crisfield MA, Mi Y, Davies GAO and Hellweg H-B, Finite Element Methods and Progressive Failure Modelling of Composite Structures, Computational Plasticity – Fundamentals and Applications, ed DRJ Owen et al, CIMNE Barcelona, Part 1, pp 239-254, 1997

[9] Curtis, CD, Energy Absorption and Crush Behaviour of Composite Tubes, Ph.D. Thesis, University of Nottingham, UK, 2000.

[10] Delsen Testing Laboratories Test Report T34773, Tensile, Compressive, V-Notch Shear Testing, End Notch Flexure and Double Cantilever Beam on the Submitted Material, Prepared for the Automotive Composites Consortium by Delsen Testing Laboratories, 1024 Grand Central Avenue, Glendale, California 91201, USA, 1st February 1999.

[11] Duckett, MJ, Rate Dependent Effects on the Energy Absorption and Material Properties of Polymer Composites, Ph.D. Thesis, University of Nottingham, UK, October 2001.

[12] *European Transport Safety Council*, Reducing Traffic Injuries Through Vehicle Safety Improvements – The Role of Car Design – Technical Annexes, 1993

[13] Fairfull AH and Hull D, Energy Absorption of Polymer Matrix Composite Structures: Frictional Effects, Symposium on Structural Failure, Chapter 8, pp 255-279, June 1998.

[14] Farley GL, Effect of Fibre and Matrix Maximum Strain on the Energy Absorption of Composite Materials, Journal of Composite Materials, Vol. 20, 1986, pp 322-334.

[15] Farley GL, Energy Absorption of Composite Material and Structure, Proceedings of the 43rd American Helicopter Society Annual Forum, St Louis, Missouri, USA, 1987, Vol. 2, pp 613-627

[16] Farley GL, Relationship between mechanical-property and energy absorption trends for composite tubes, NASA Report TP-3284, December 1992, pp 1-13. Downloaded from http://techreports.larc.nasa.gov/cgi-bin/NRTS

[17] Farley GL and Jones RM, Prediction of the Energy Absorption Capability of Composite Tubes, *Journal of Composite Materials*, Vol. 26, No. 3, pp 388-404, 1992.

[18] Fernie R, Ph.D. Thesis, University of Nottingham, UK, October 2002 (*to be submitted*).

[19] Gouri MIA and Newaz GM, Energy dissipation due to various failure modes in axial compression of unidirectional PMC tubes, *Advanced Composites Conference Proceedings*, Detroit, Michigan, USA, 7th-10th April 1997, Pub. ESD – The Engineering Society, pp 35-45, 1997.

[20] Hamada H., Coppola J. and Hull D., Effect of Surface Treatment on Crushing Behaviour of Glass Cloth/Epoxy Composite Tubes, *Composites*, 23/2, pp 93-99, 1992

[21] Hamada H., Ramakrishna S., Nakamura M., Maekawa Z. and Hull D., Progressive Crushing Behaviour of Glass/Epoxy Composite Tubes with Different Surface Treatment, *Composite Interfaces*, 2/2, pp 127-142, 1994

[22] Hamada H., Ramakrishna S., Nishiwaki T., and Maekawa Z., Energy Absorption Characteristics of Composite Tubes with Different Cross-Sectional Shapes, *Proceedings of 10th ASM/ESD Conference*, Michigan, USA, pp 523-534, 1994.

[23] Hamada H and Ramakrishna S, A FEM Method for Prediction of Energy Absorption Capability of Crashworthy Polymer Composite Materials, Journal of Reinforced Plastics and Composites, Vol. 16, No. 3, 1997.

[24] Hart-Smith LJ, Should Fibrous Composite Failure Modes be Interacted or Superimposed?, *Composites*, Vol. 24, No. 1, pp 53-55, 1993.

[25] Hart-Smith LJ, The Truncated Maximum Strain Composite Failure Model, *Composites*, Vol. 24, No. 7, pp 587-591, 1993.

[26] Hart-Smith LJ, The First Fair Dinkum Macro-Level Fibrous Composite Failure Criteria, *Eleventh International Conference on Composite Materials ICCM-11*, Gold Coast, Queensland, Australia, 14th-18th July 1997, Volume I, Ed. Scott ML, pp I-52 to I-87, 1993.

[27] Hashin Z, Failure Criteria for Unidirectional Fiber Composites, *Journal of Applied Mechanics*, Vol. 47, pp 329-334, June 1980.

[28] Haug E, Fort O, Tramecon A, Watanabe M, Nakada I, Numerical Crashworthiness Simulation of Automotive Structures and Components Made of Continuous Fibre Reinforced Composite and Sandwich Assemblies, *SAE International Conference and Exhibition*, Detroit, Michigan, USA, 25th Feb-1st March 1991, pp 245-258.

[29] Hull D., Energy Absorbing Composite Structures, *Science and Technology Review,* University of Wales, 3, pp 22-30, 1988.

[30] Hull D., A Unified Approach to Progressive Crushing of Fibre-Reinforced Composite Tubes, *Composites Science and Technology,* 40, pp 377-421, 1991.

[31] Hull D. and Clyne T.W., *An Introduction to Composite Materials*, 2nd Edition, Cambridge University Press, 1996

[32] International Standard EN ISO 14125:1998, Fibre Reinforced Plastic Composites – Determination of Flexural Properties

[33] Johnson AF and Pickett AK, Impact and Crash Modelling of Composite Structures: A Challenge for Damage Mechanics, ECCM'99 European Conference on Computational Mechanics, Munich, 31Aug – 3Sept 1999

[34] Krajcinovic D, Damage Mechanics: Accomplishments, Trends and Needs. *International Journal of Solids and Structures*, Vol. 37, Nos. 1-2, pp 267-277, 2000.

[35] Mamalis AG, Yuan YB and Viegelahn GL, Collapse of Thin-Wall Composite Sections Subjected to High Speed Axial Loading, *International Journal of Vehicle Design*, Vol. 13, Nos. 5/6, pp 564-579, 1992.

[36] Mamalis A.G., Manolakos D.E., Demosthenous G.A. and Ioannidis M.B., *Crashworthiness of Composite Thin-Walled Structural Components*, Technomic Publishing Company Inc., U.S.A. 1998

[37] Mechanics of Materials. Hearn EJ. Volume I, First Edition 1977, Pergamon Press Ltd, pp340-342. Volume II, Third Edition 1997, Butterworth-Heinemann, pp246-247

[38] Mori T., Hamada H., Ikuta N., Desaeger M. and Verpoest I., Effect of Silane Treatment on Mechanical Properties of Hydrothermal Aged Glass Fabric/Epoxy Laminates, *Proceedings of ICCM-10*, VI, pp 613-620, 1995

[39] National Research Council (U.S.), Shopping for Safety, *Committee for Study of Consumer Automotive Safety Information, Special Report 248*, Washington 1996

[40] Nonlinear Failure Simulation of Thick Composite Structures, H-B Hellweg, PhD Thesis, Department of Aeronautics, Imperial College of Science Technology and Medicine, London 1994

[41] PAM-CRASH/PAM-SAFE Solver Notes and Reference Manual, ESI Group, PAM-CRASH™ FE Code, Engineering Systems International S.A., 20 Rue Saarinen, Silic 270, 94578 Rungis-Cedex, France. 1998

[42] Philipps M, Patberg L, Dittmann R, Adam H, Structural Analysis and Testing of Composites in Automotive Crashworthiness Application, SAE 981140, 1998.

[43] Popov EP, Engineering Mechanics of Solids, Prentice Hall, 1990.

[44] Puck A, Strength Proof of Design for FRPC Based Components, *Fibre Composites*, pp 24-25, June 1996. {Translated from "Festigkeitsnachweis von FKV-Bauteilen" Kunststoffe Plast Europe, Vol. 86, No. 6, pp 828-829, 1996.

[45] Quek SC, Waas AM, Hoffman J, Agaram V, The Crushing Response of Braided and CSM glass reinforced composite tubes, *Composite Structures*, 52, pp 103-112, 2001.

[46] Reeder JR, Evaluation of Mixed-mode Delamination Failure Criteria, NASA Technical Memorandum 104210,1992.

[47] Reeder JR and Crews JR, Mixed-Mode Bending Method for Delamination Testing, *AIAA Journal*, Vol. 28, No. 7, pp 1270-1276, 1990.

[48] Reedy E.D. Jr., Mello F.J. and Guess T.R., Modelling the Initiation and Growth of Delaminations in Composite Structures, *Journal of Composite Materials*, Vol. 31, No. 8, pp 812-831, 1997

[49] Shahid I and Chang FK, An Accumulative Damage Model for Tensile and Shear Failures of Laminated Composite Plates. *Journal of Composite Materials*, Vol. 29, No. 7, pp 926-981, 1995

[50] Tsai SW and Wu M, A General Theory of Strength for Anisotropic Materials, *Journal of Composite Materials*, Vol. 5, pp 58-80, 1971.

[51] Wisheart M and Richardson MOW, The Finite Element Analysis of Impact Induced Delamination in Composite Materials Using a Novel Interface Element, *Composites Part A*, Vol. 29A, pp 301-313, 1998.

[52] Lourenço N, Warrior NA, Pickett AK, Mixed-Mode Delamination – Experimental and Numerical Studies, 2002, (*submitted for publication*).

Appendix 1. Beam Theory Solutions for DCB, ENF and 4-point Bending Tests

Some results of LEFM (Linear Elastic Fracture Mechanics) applied to delamination specimens [1] [2] are presented here.

Hypothesis

Global behaviour of the specimens is linear for each fixed crack length *a*. According to this statement, the *Energy Release Rate* is:

$$G = \frac{P^2}{2B}\frac{dC}{da} \tag{1}$$

where C is the compliance of the beam, i.e.:

$$C = \frac{\delta}{P} \tag{2}$$

The crack propagates when G reaches a critical value G_{Ic}.

DCB Test

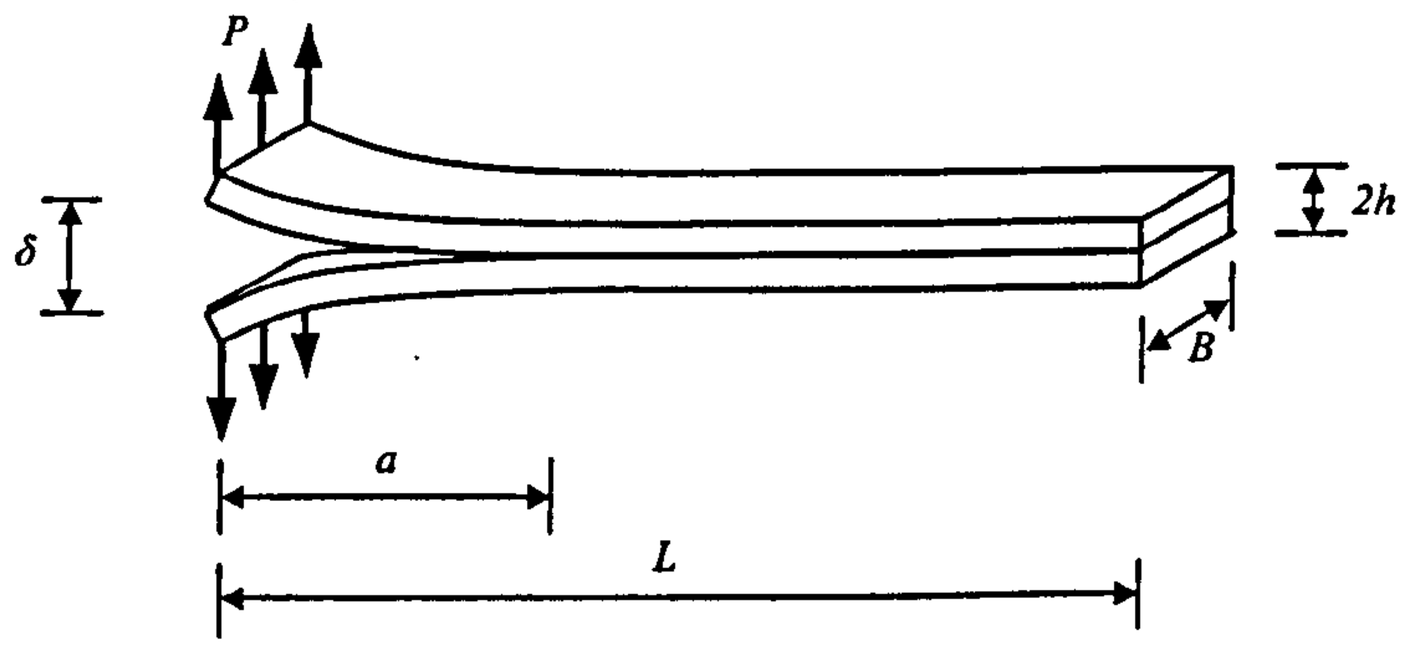

Figure 1 - DCB specimen

Compliance for DCB

The compliance for the Double Cantilever Beam is:

$$C = \frac{2a^3}{3EI} \tag{3}$$

where

$$I = \frac{Bh^3}{12} \tag{4}$$

Using equation (2):

$$P = \frac{3EI}{2a_0^{\ 3}}\delta \tag{5}$$

Equation (5) represents the linear behaviour of the Double Cantilever Beam. During this stage the displacement δ is due to the deflection of the beams; no crack propagation has occurred yet.

Crack Propagation Stage

Using equations (1) and (3), the energy release rate is:

$$G = \frac{Pa^2}{BEI} \tag{6}$$

Setting $G=G_{Ic}$ and using equation (5) (with a instead of a_0), we can eliminate a from equation (6).

$$G_{Ic} = \frac{Pa^2}{BEI} \Leftrightarrow a^2 = \frac{G_{Ic}BEI}{P} \Leftrightarrow a = \frac{(G_{Ic}BEI)^{\frac{1}{2}}}{P^{\frac{1}{2}}} \tag{7}$$

From equation (5):

$$P = \frac{3EI\delta}{2\left[\frac{(G_{Ic}BEI)^{\frac{1}{2}}}{P^{\frac{1}{2}}}\right]^3} = \frac{3EIP^{\frac{3}{2}}\delta}{2(G_{Ic}BEI)^{\frac{3}{2}}} \qquad (8)$$

After the start of crack propagation, the behaviour of the Double Cantilever Beam is represented by:

$$\delta = \frac{2}{3}\frac{(G_{Ic}BEI)^{\frac{3}{2}}}{EIP^2} \qquad (9)$$

Load Displacement Curve

The Load-displacement curve for the DCB test is shown in Figure 2. Curve **A** is given by equation (5) and curve **B** by equation (9).

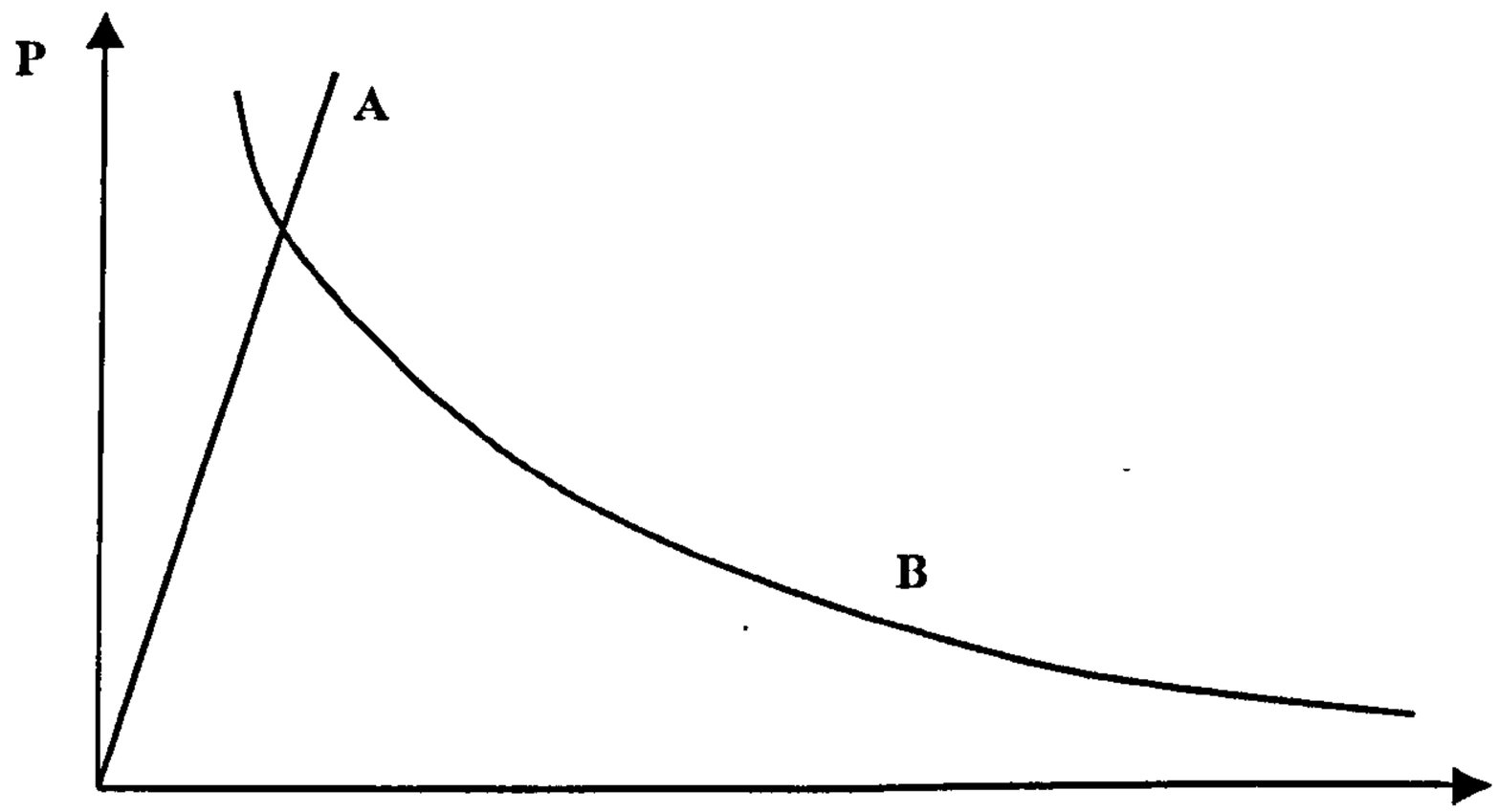

Figure 2 Load-displacement curve for Double Cantilever Beam test

ENF Test

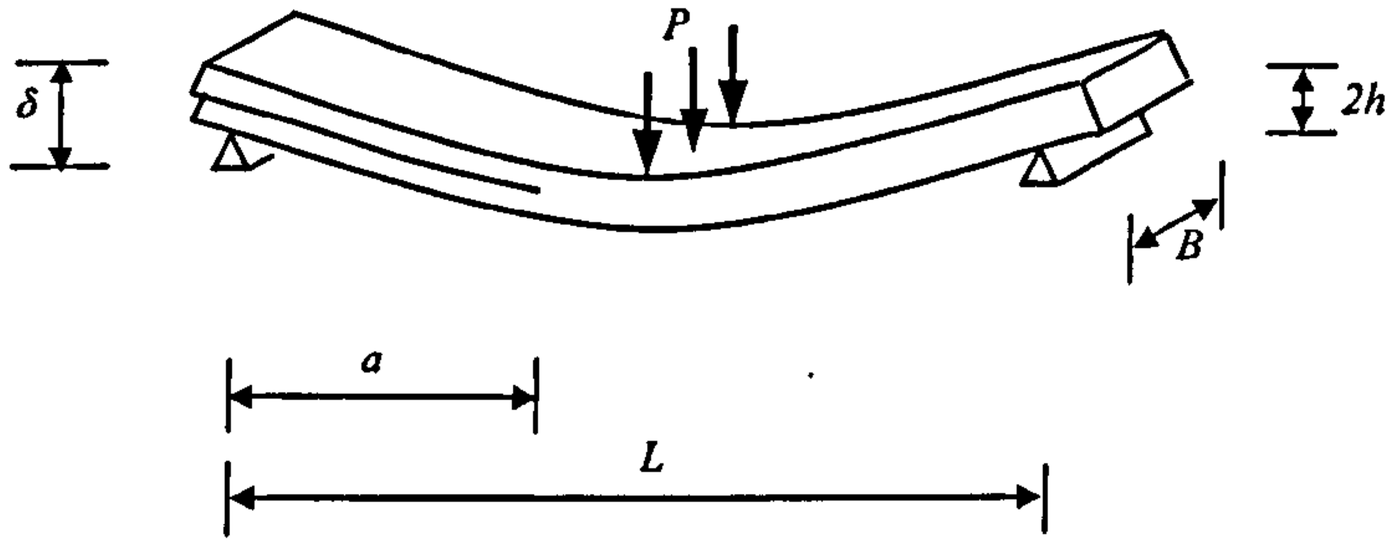

Figure 3 - ENF specimen

Equations

The classical solution for the ENF test, consists of four different stages:

1. Initial loading stage (linear behaviour)
2. Crack propagation stage, valid for $0<a<L/2$
3. Crack propagation stage, valid for $L/2<a<L$
4. Final loading stage of the completely split beam.

The curves for the previous four stages of loading are given by the four following equations [8].

For stage **1.**, the loading line is given by equation (10), line **A** in Figure 4.

$$\delta = \frac{P\left(\frac{L^3}{4} + 3a_0^3\right)}{96EI} \tag{10}$$

For the crack propagation stage **2**, which results in decreasing load (line **B**):

$$\delta = \frac{P}{96EI}\left[\frac{L^3}{4} + \frac{\left(64G_{II_c}BEI\right)^{\frac{3}{2}}}{\sqrt{3}P^3}\right] \tag{11}$$

For stage **3**, line **C** is given by equation (12)

$$\delta = \frac{P}{24EI}\left[\frac{L^3}{4} - \frac{\left(64G_{II_c}BEI\right)^{\frac{3}{2}}}{4\sqrt{3}P^3}\right] \tag{12}$$

Finally curve **D** relates to the completely split beam for which:

$$\delta = \frac{PL^3}{96EI} \tag{13}$$

Load Displacement Curve

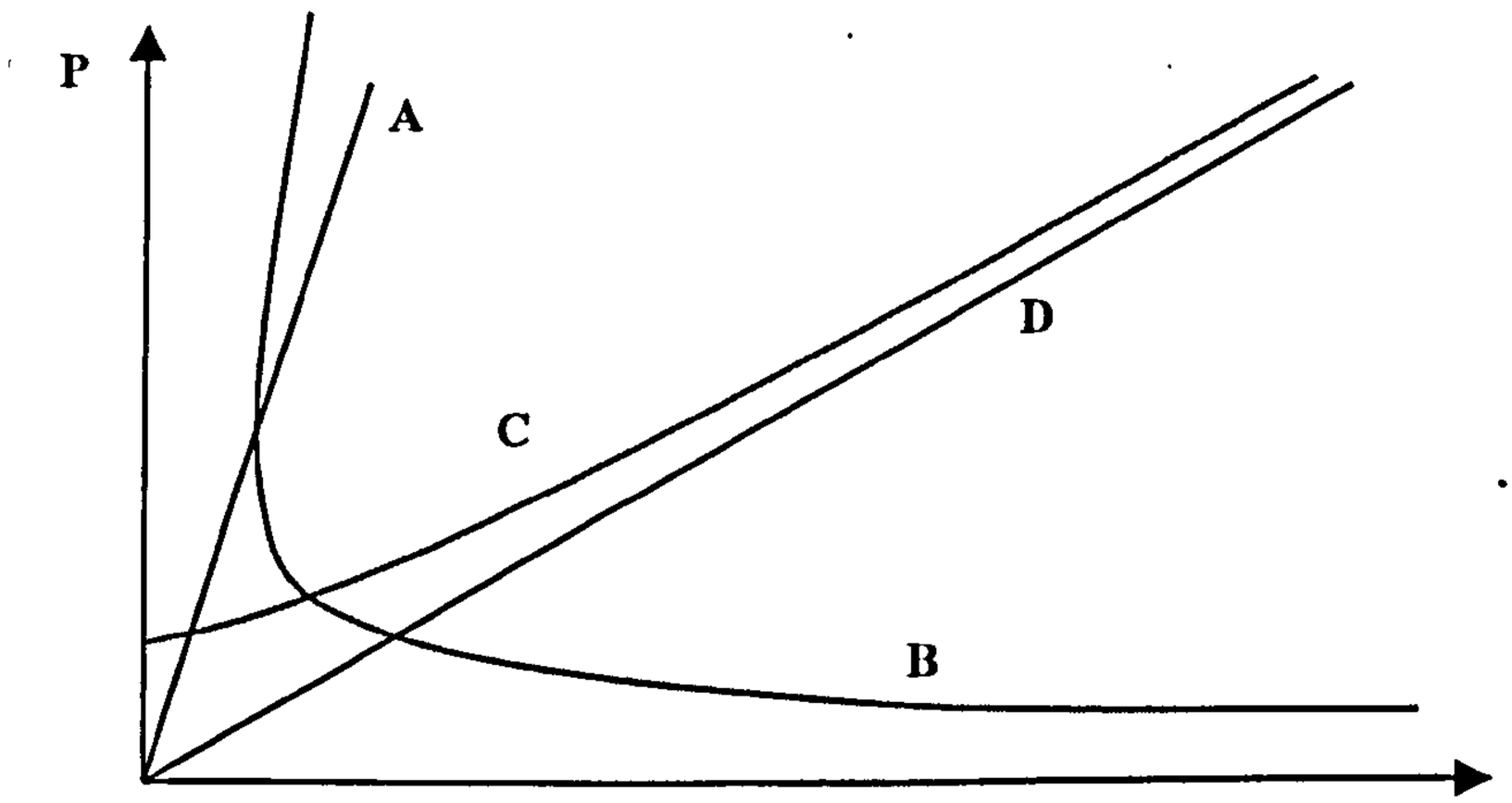

Figure 4 - Load-displacement curve for End Notched Flexure test

Beam Theory Solution for 4-point Bending Test

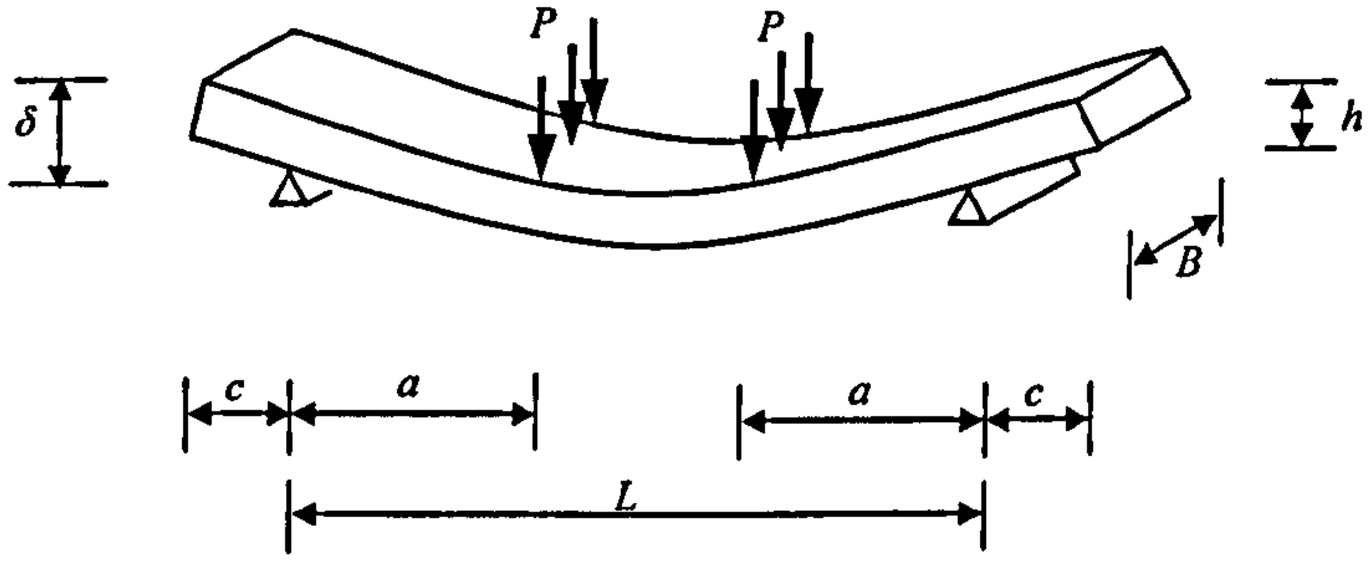

Figure 5 – 4-Point bending specimen

The load applied to the specimen is given by Popov [43] equation (14).

$$P = \frac{6EI}{a^2(3L-4a)}\delta \qquad (14)$$

Load Displacement Curve

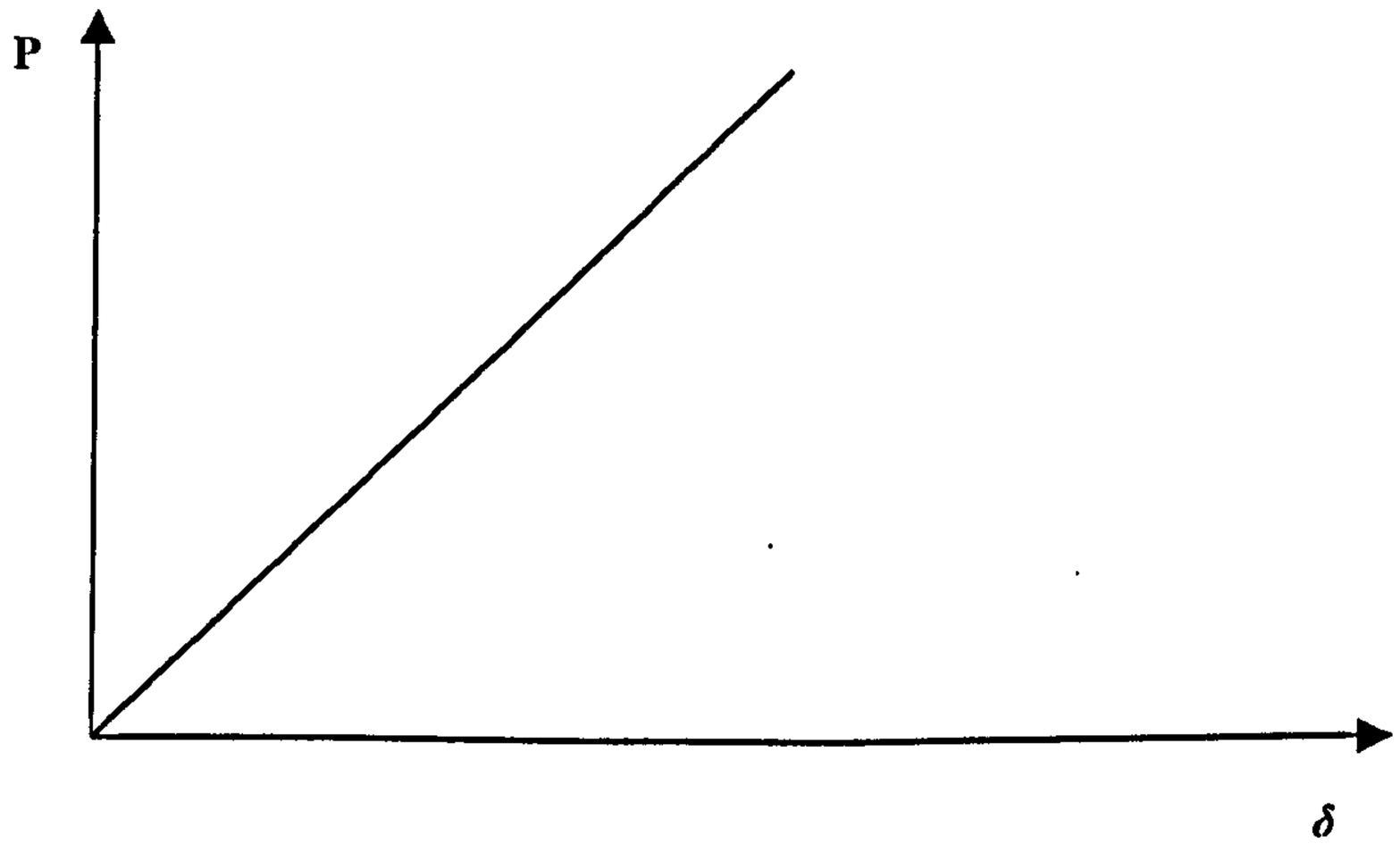

Figure 6 - Load-displacement curve for 4-point Bending test

Appendix 2. Mesh Dependency Study – 4-Point Bending Test

Further to the validation work on the delamination model, a study was performed to assess mesh dependency. This is usually a concern with finite element models, which are discrete representation of a continuous medium. The study consisted of a 4 point bending test. The test configuration is shown in Figure 7 and details of the test procedure are described in [32] and Appendix 1.

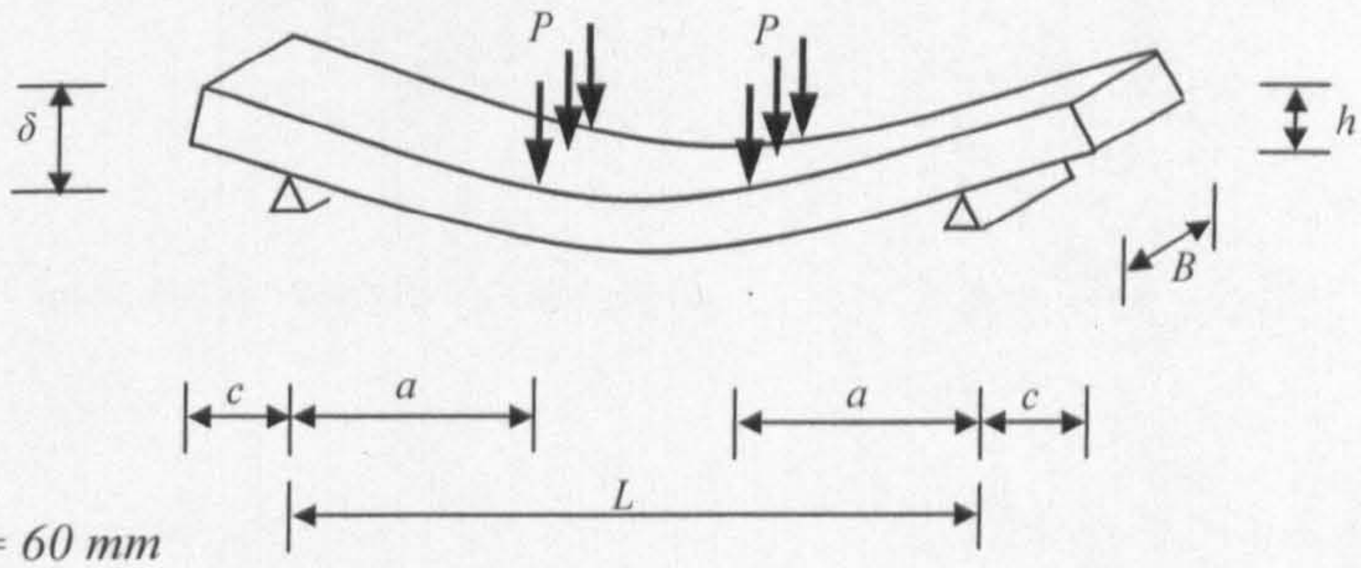

$L = 60\ mm$

$B = 15\ mm$

$h = 4\ mm$

$a = 19\ mm$

$c = 10\ mm$

Figure 7 - 4-point Bending Test Configuration

This study was performed with 2 different meshes of the 4-point Bending test, shown in Figure 8. The purpose was to compare the two resulting load-displacement curves. The models are considered mesh-dependent if there is a clear difference between those curves.

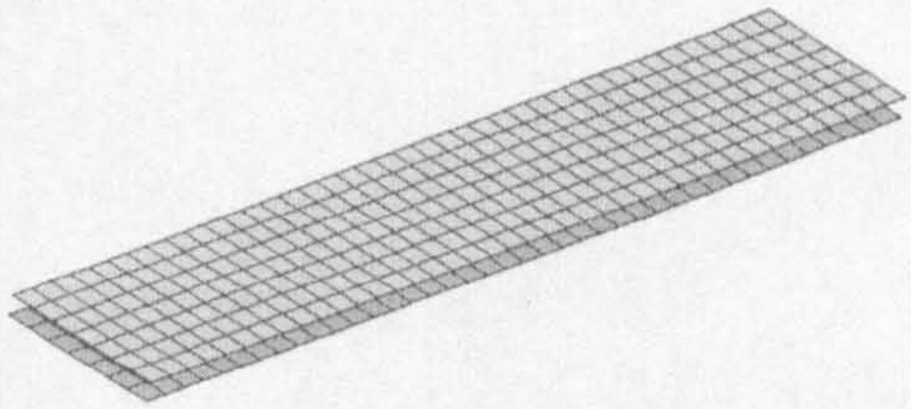

40 by 7 Element

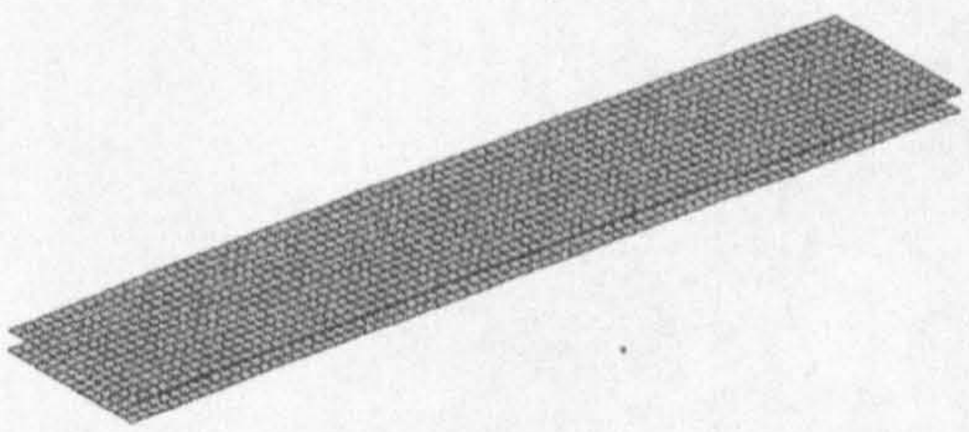

80 by 14 Element

Figure 8 – Bi-Shell Finite Element Models for Mesh Dependency Study

The model to duplicate the test is shown in Figure 9 and the progressive deformation in Figure 10.

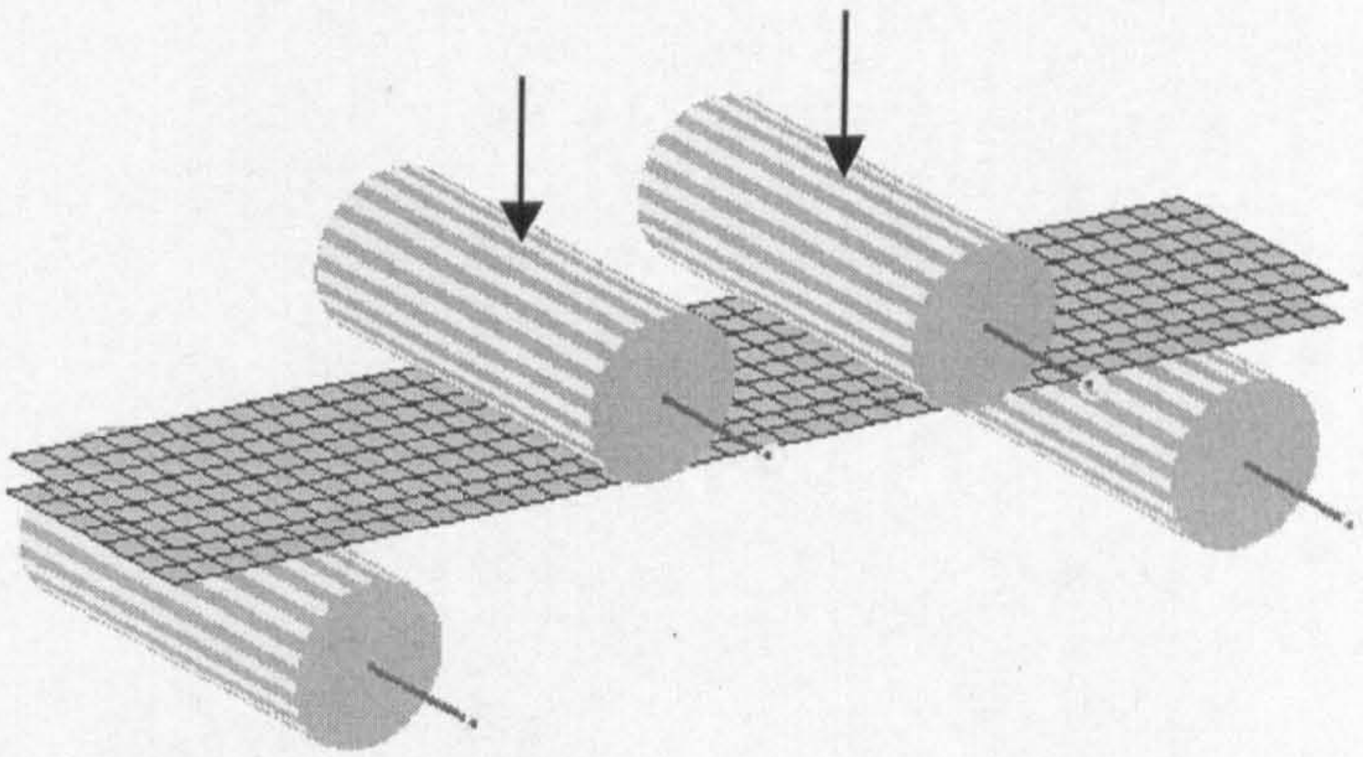

Figure 9 – Finite Element Model of 4-point Bending Test - Geometry and Loading

Figure 10 – Bi-Shell Finite Element Model Results of 4-point Bending Test

5.1.1 Mesh Dependency Study

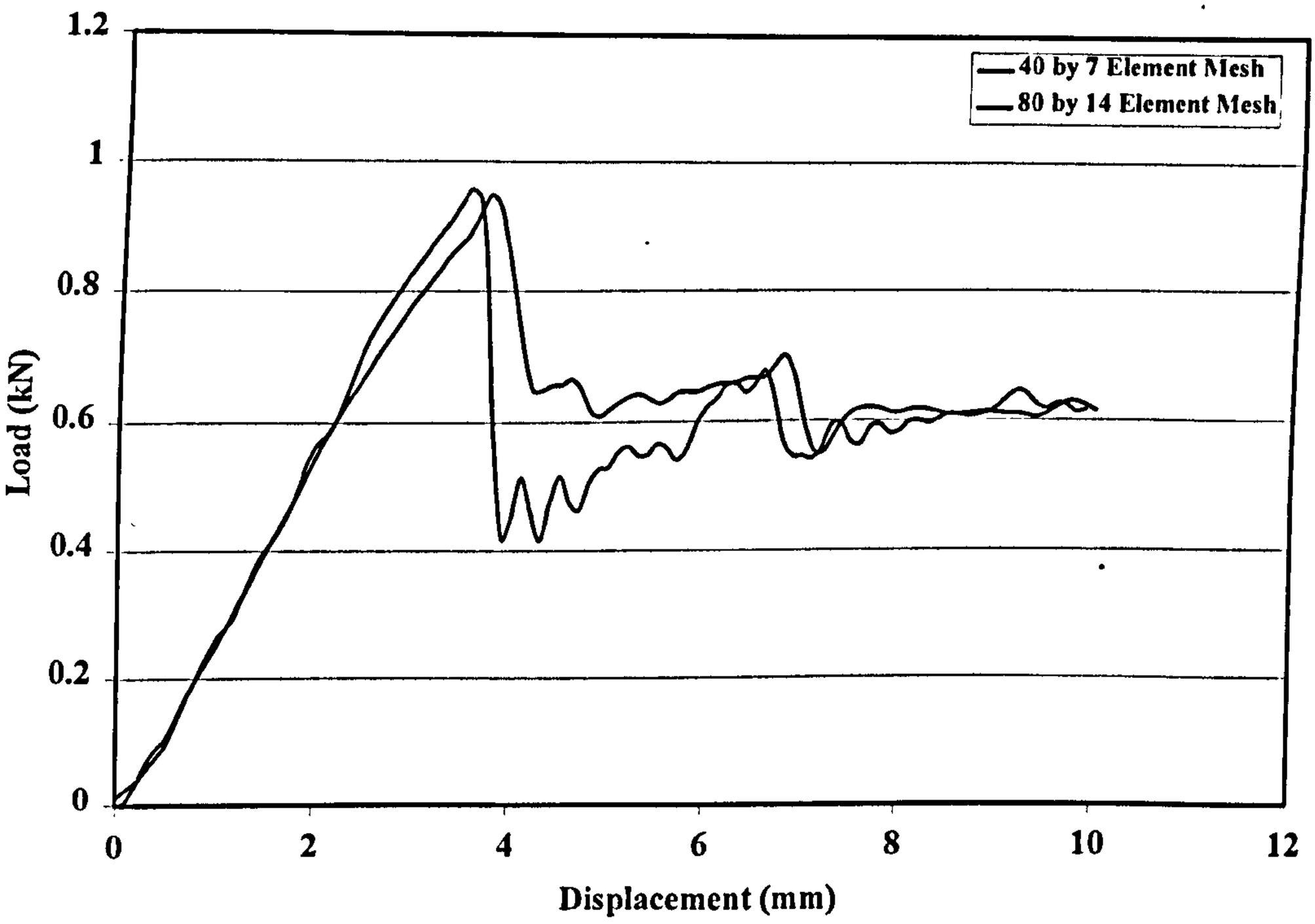

Figure 11 – 4-point Bending Mesh Dependency Study - Results

The results shown in Figure 11 show a very good agreement and the differences in the curves are can be attributed to the different time steps used[1], as this has a direct influence in the sample frequency of the analysis, which can be more visible in transient stages such as the one between 4 and 6 mm of displacement.

It can be stated that the analyses presented in this report are independent of mesh. This is valid for the delamination model since it is used to model the interlaminar region of the 4-point Bending test.

[1] Time step calculation is based on the size of the smallest element of the structure.

Appendix 3. PAM-CRASH Material Type #41

Material Type 41 was originally developed to represent Side Impact Barriers for automotive crash simulation. It has an arbitrary orthotropic material frame definition (Figure 12), where damage and strain rate effects can be considered [41].

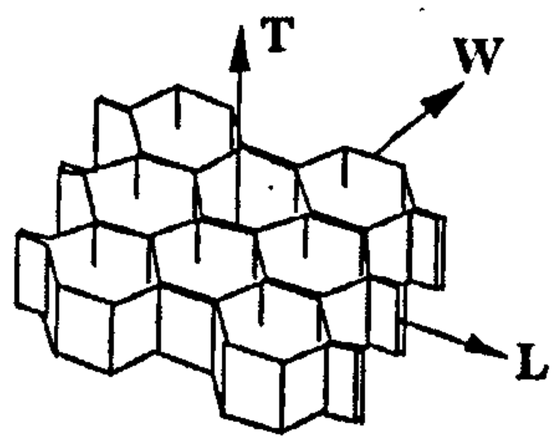

Figure 12 - Material 41 Orthotropic Definition for Honeycomb Barrier

From its basic features described above, this model appears to be ideally suited to the modelling of the anisotropic behaviour of composite laminates.

Input Data for Material Type 41

The three orthotropy directions of material type 41 are related to the experimental data of the composite as described in Figure 13 and Table 1.

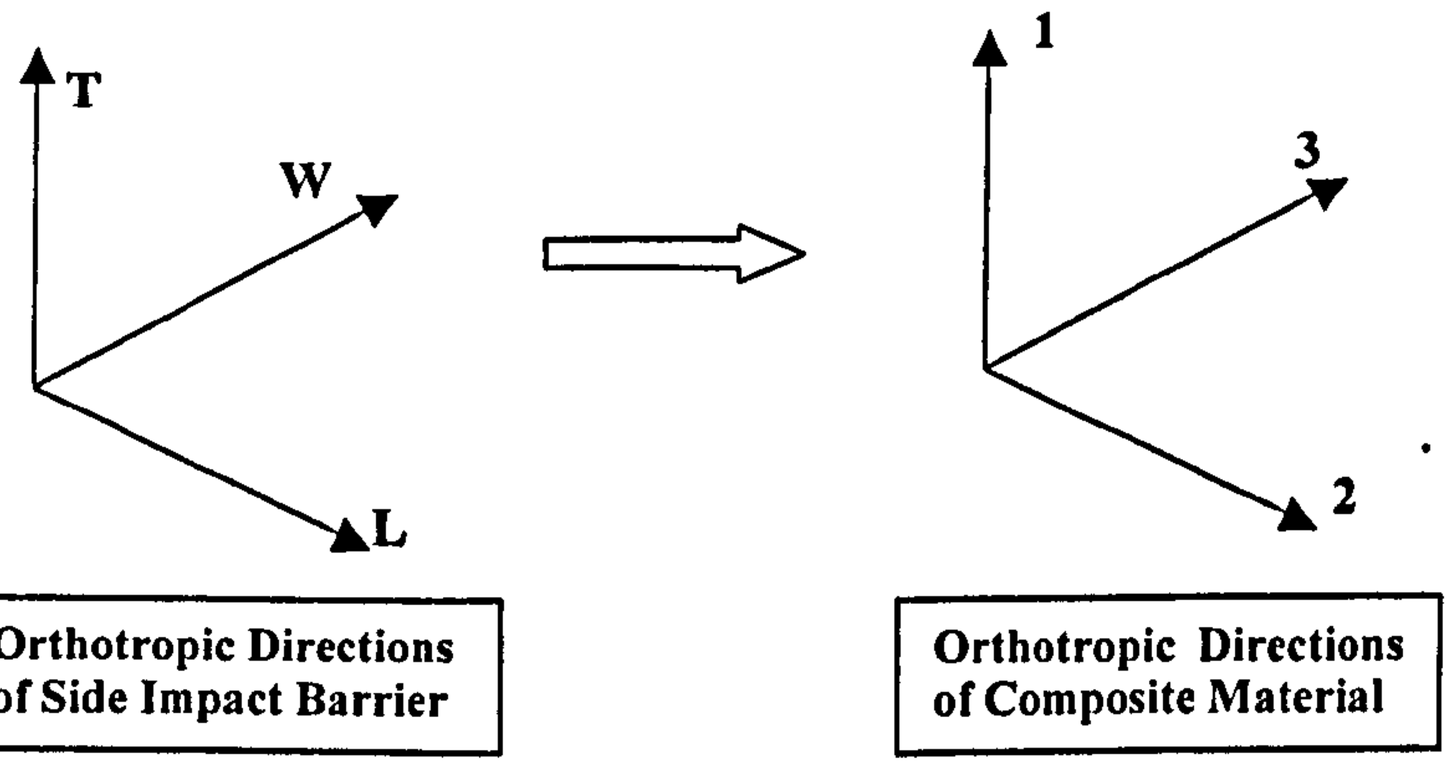

Figure 13 - Orthotropy Directions of Material Type 41 and Composite Material

Material Type 41 Input Data	Composite Material Property
E_T	E_{11}
E_L	E_{22}
E_W	E_{33}
G_{TL}	G_{12}
G_{LW}	G_{23}
G_{WT}	G_{13}

Table 1 - Material 41 Input Moduli and Equivalent Experimental Data

Compression/Tension Behaviour

In each of the three orthotropic directions (T, L, and W), uniaxial tensile and compressive behaviour can be represented by the curve in Figure 14.

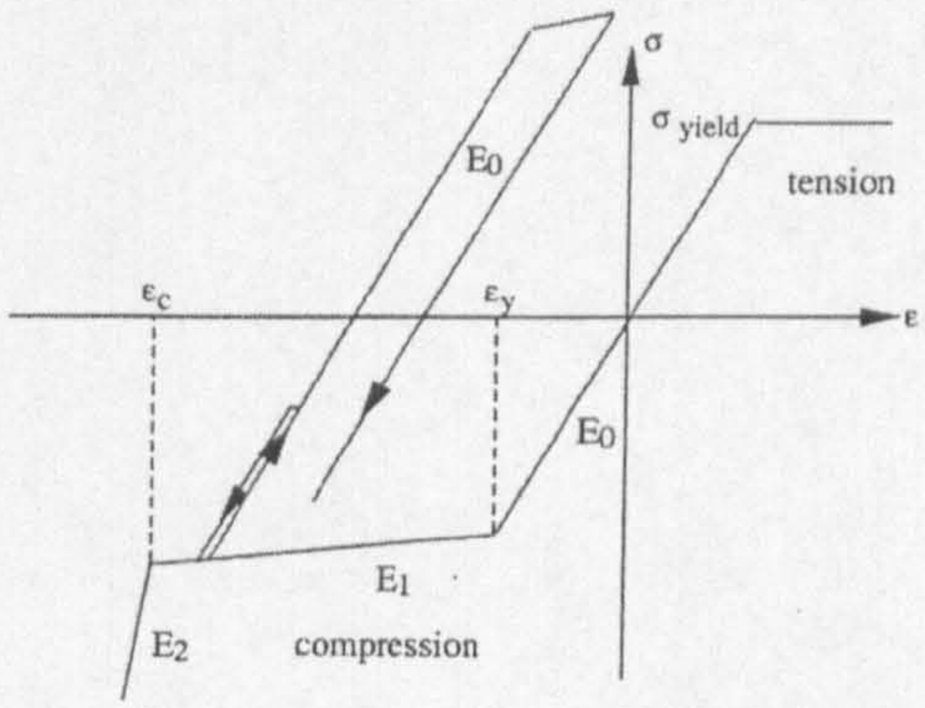

Figure 14 - Compressive/Tensile Behaviour of Material Type 41

Shear Behaviour

For each of the three shear components (TL, LW, and WT), shear stresses can be represented by the curve in Figure 15.

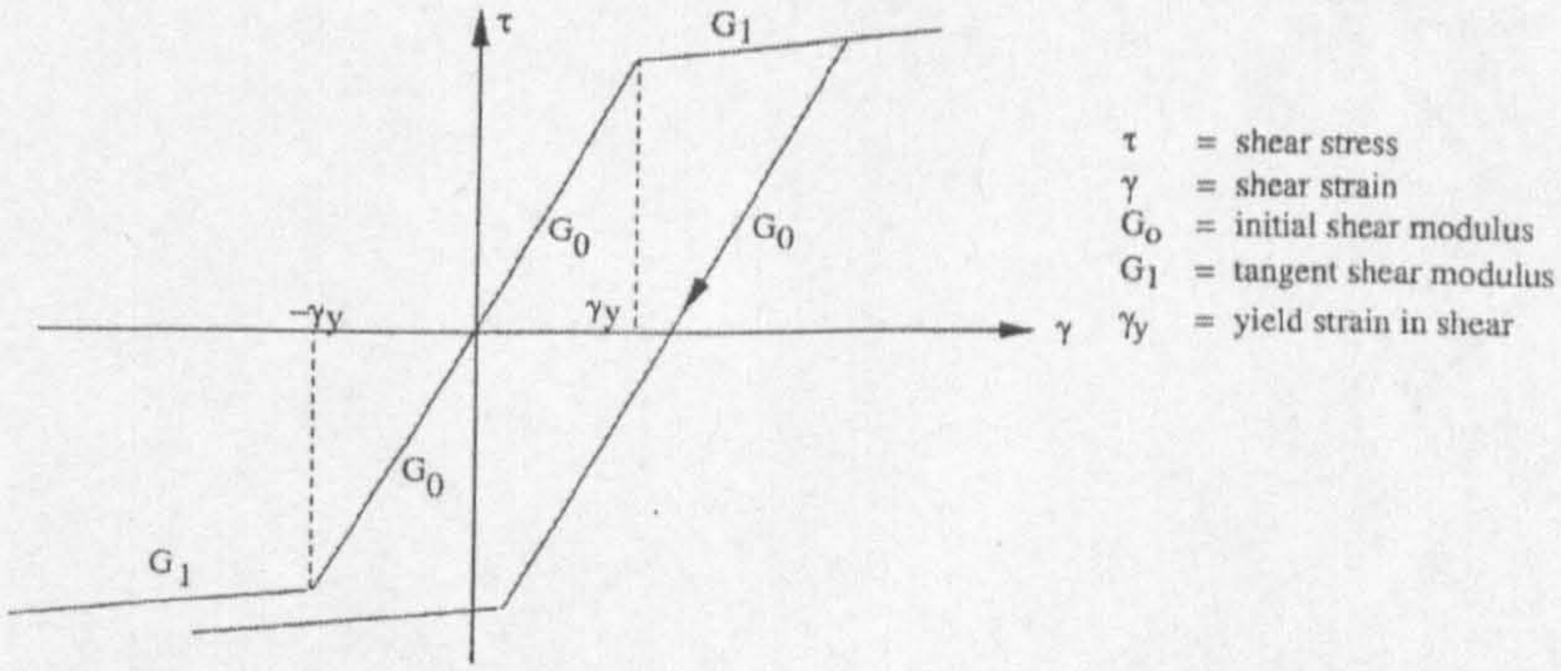

Figure 15 - Shear Behaviour of Material Type 41

Damage Behaviour

The implemented damage law is described in Figure 16 below.

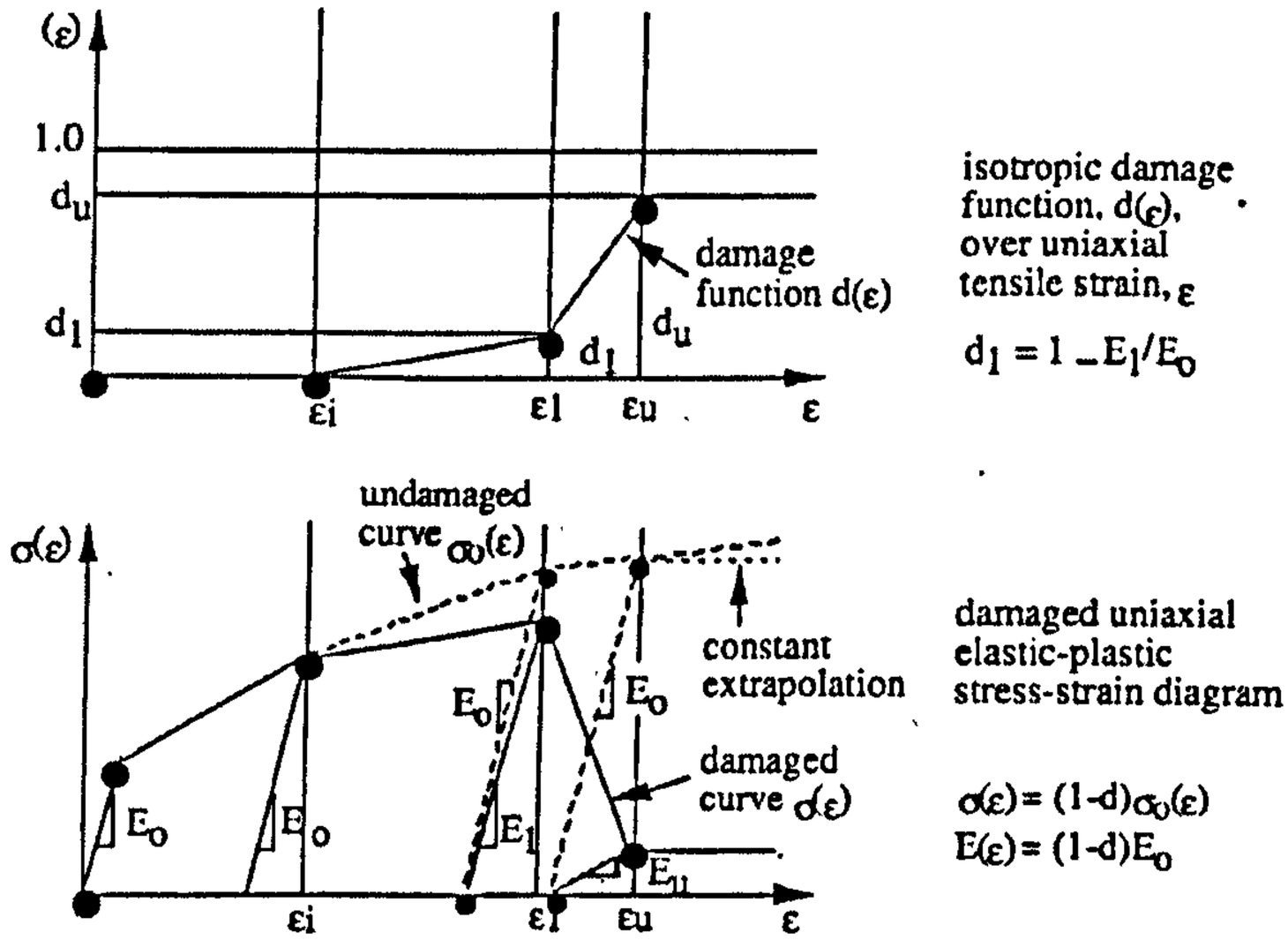

Figure 16 - Damage Behaviour in Material Type 41

Calibration of Material Model

The calibration procedure for obtaining the input data of Material Type #41 is in all similar to the approach for the degenerate bi-phase model in that it uses the same material source data from coupon tests and the input values are obtained through the use of an Excel® macro. Interlaminar data is input as for the Degenerate Bi-phase model. The calibration process did not include damage modelling as the material model proved numerically unstable in such case

Pam-Crash Material Input Deck for Material 41

= input these values into Pamcrash

Orthotropic Properties in T-direction	
E0T (GPa)	10.08
εyT (%)	2.01
E1T (GPa)	0.1
E2T (GPa)	10.08
G0TL (GPa)	4.246
εyTL (%)	3.2
G1TL (GPa)	0.1
σyT(GPa)	0.151

Orthotropic Properties in L-direction	
E0L (GPa)	10.08
εyL (%)	2.01
E1L (GPa)	0.1
E2L (GPa)	10.08
G0LW (GPa)	1.759
εyLW (%)	0.93
G1LW (GPa)	0.1
σyL(GPa)	0.151

Orthotropic Properties in W-direction	
E0W (GPa)	6.49
εyW (%)	6.35
E1W (GPa)	0.1
E2W (GPa)	6.49
G0WT (GPa)	1.684
εyWT (%)	3
G1WT (GPa)	0.1
σyW(GPa)	0.00772

Compaction Strain	
εc (%)	66

Damage Parameters	
σ1T	0.15
σuT	0.15
εi (%)	1.5
ε1 (%)	3
εu (%)	4
d1	0.01640624
du	0.022813934

= damaged stress values to be achived - Direction 11

Interlaminar Properties	
E0 (GPa)	6.49
G0 (GPa)	1.759
σ1max (GPa)	0.00772
σ2max (GPa)	0.0163587
G1c (kN/mm)	5.46E-04
G2c (kN/mm)	2.80E-03
Lm (mm)	0.08

= thickness of Interlaminar Region

= values calculated automatically

Figure 17 – Input Parameters for Material Type #41

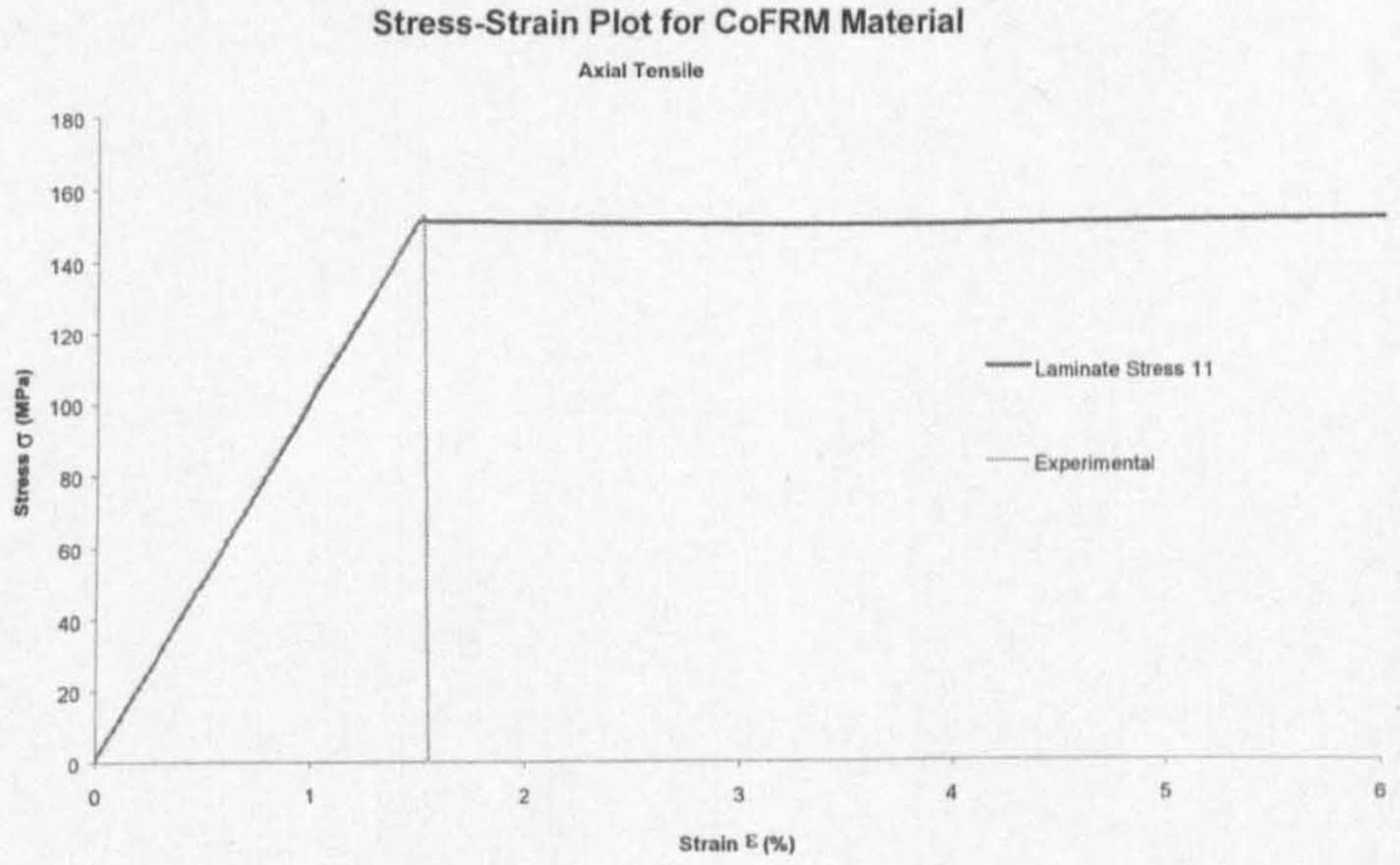

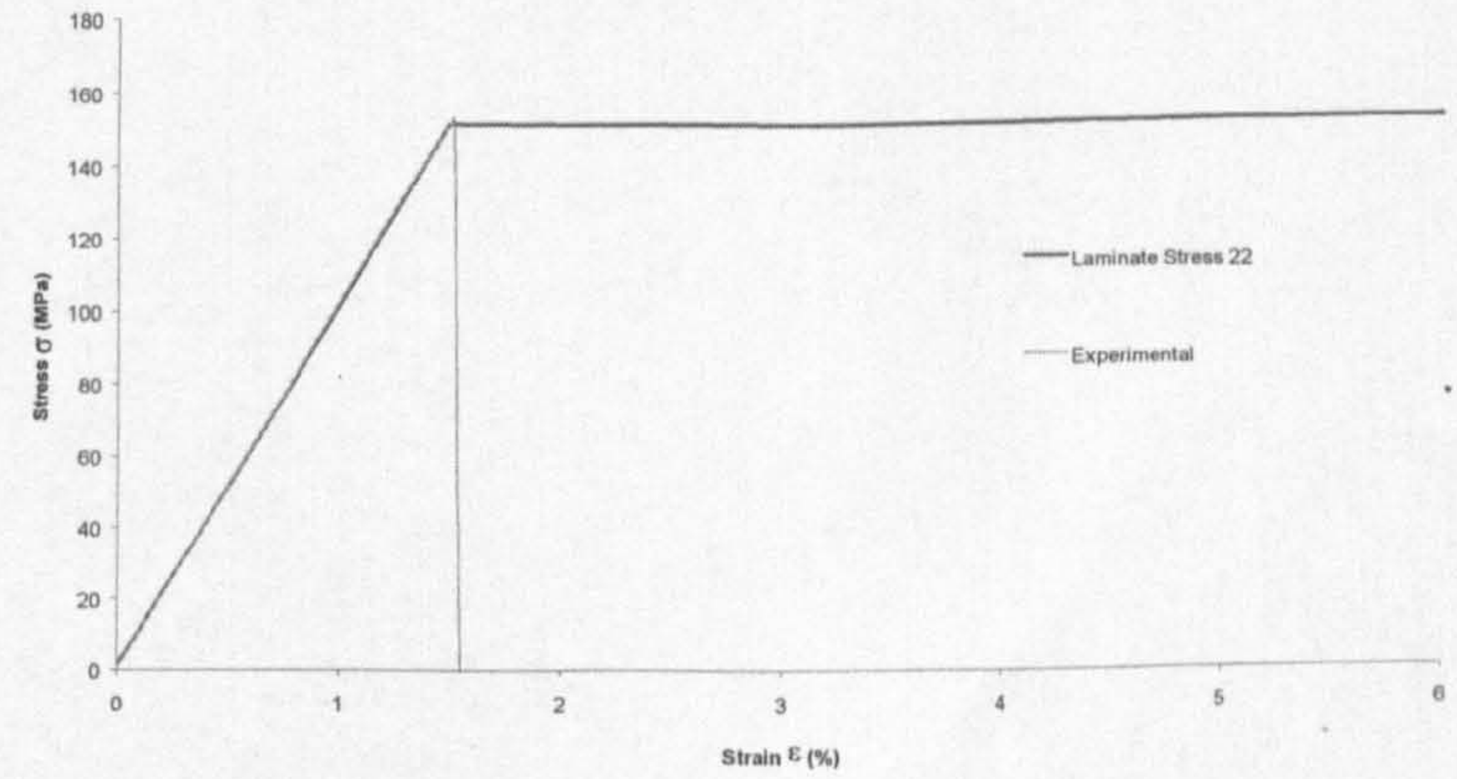

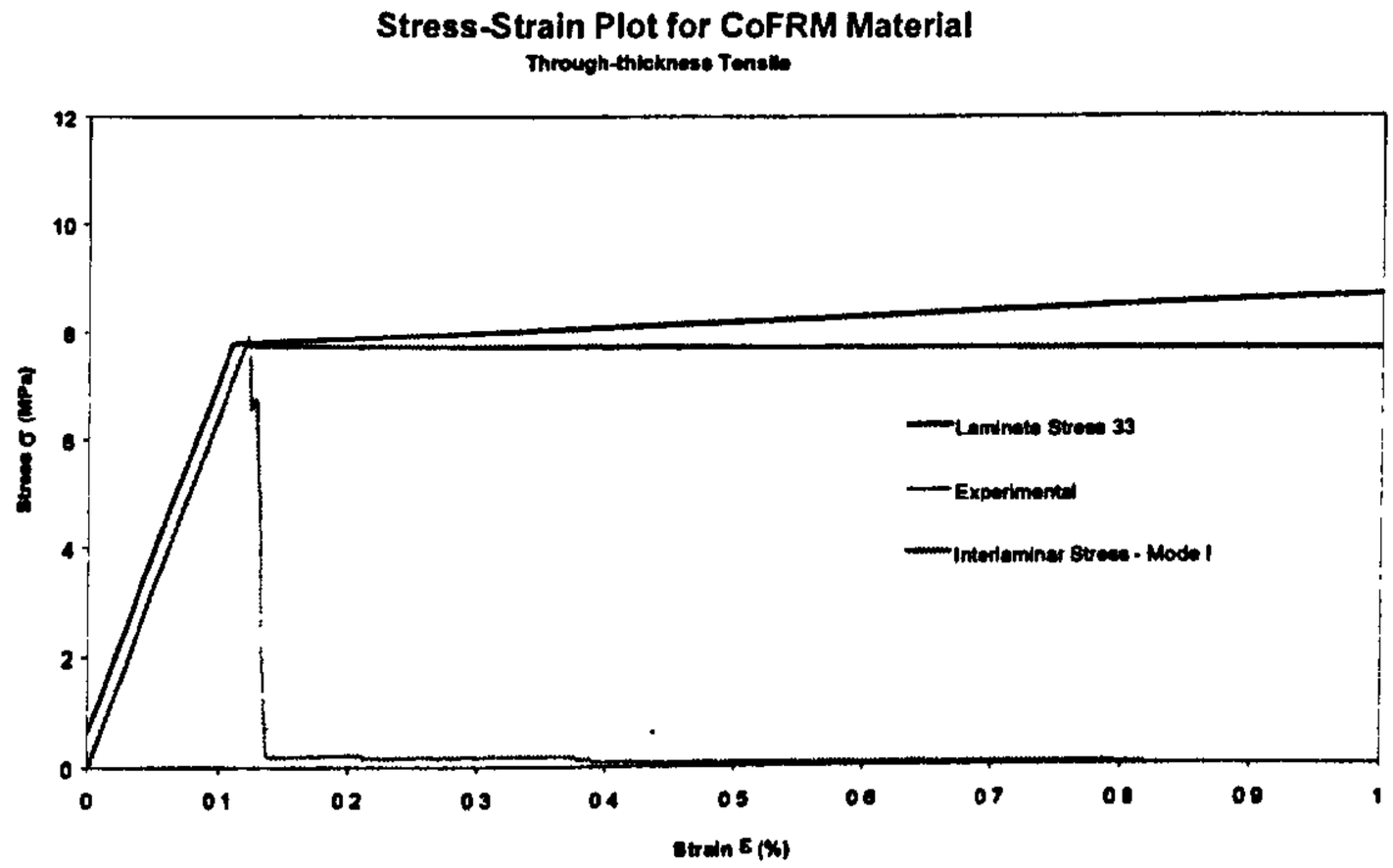
Stress-Strain Plot for CoFRM Material
Through-thickness Tensile
Stress σ (MPa)
Strain ε (%)
Laminate Stress 33
Experimental
Interlaminar Stress - Mode I
0
2
4
6
8
10
12
01
02
03
04
05
06
07
08
09
1

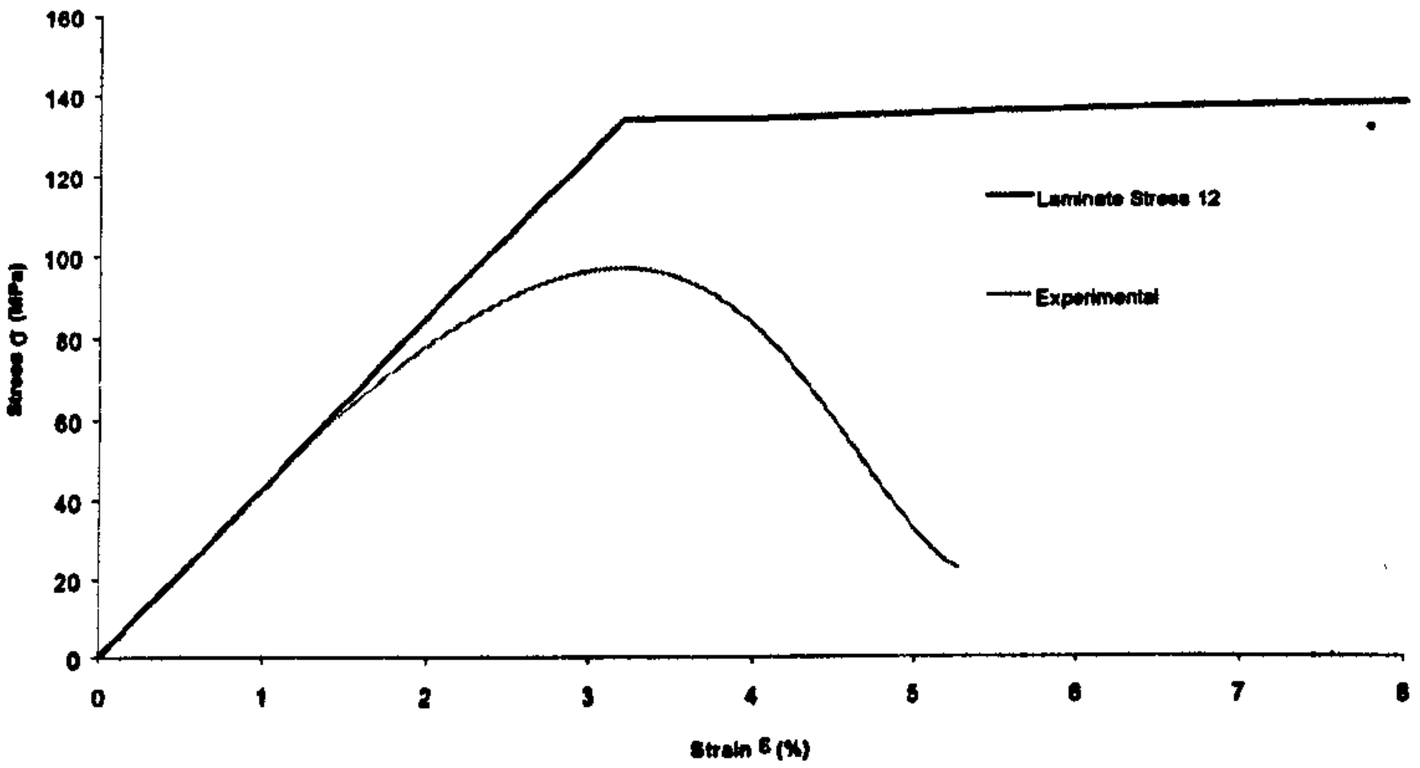
Stress-Strain Plot for CoFRM Material
Shear 12
Stress σ (MPa)
Strain ε (%)
Laminate Stress 12
Experimental
0
20
40
60
80
100
120
140
160
1
2
3
4
5
6
7
8

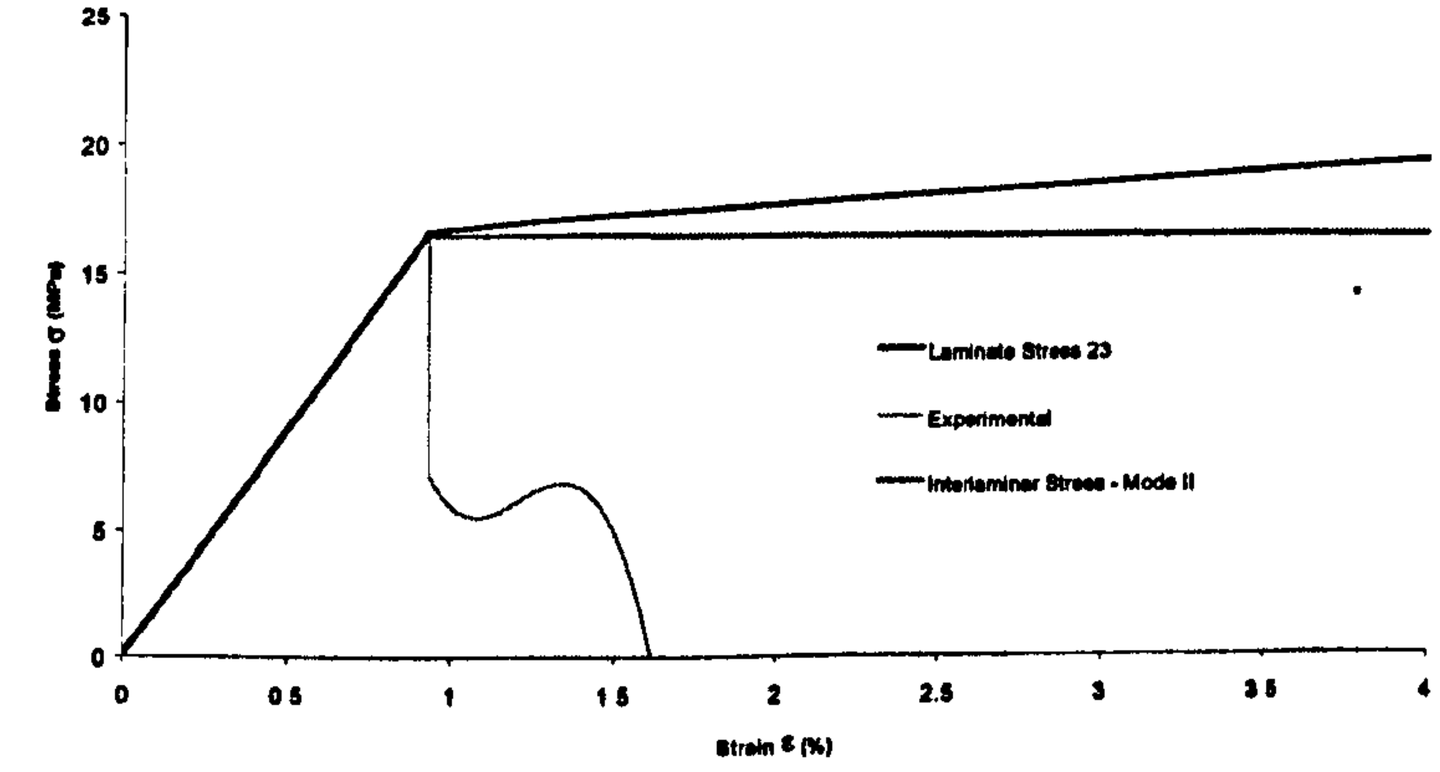
Stress-Strain Plot for CoFRM Material
Shear 23
Stress σ (MPa)
Strain ε (%)
Laminate Stress 23
Experimental
Interlaminar Stress - Mode II
0
5
10
15
20
25
0 5
1
1 5
2
2.5
3
3 5
4

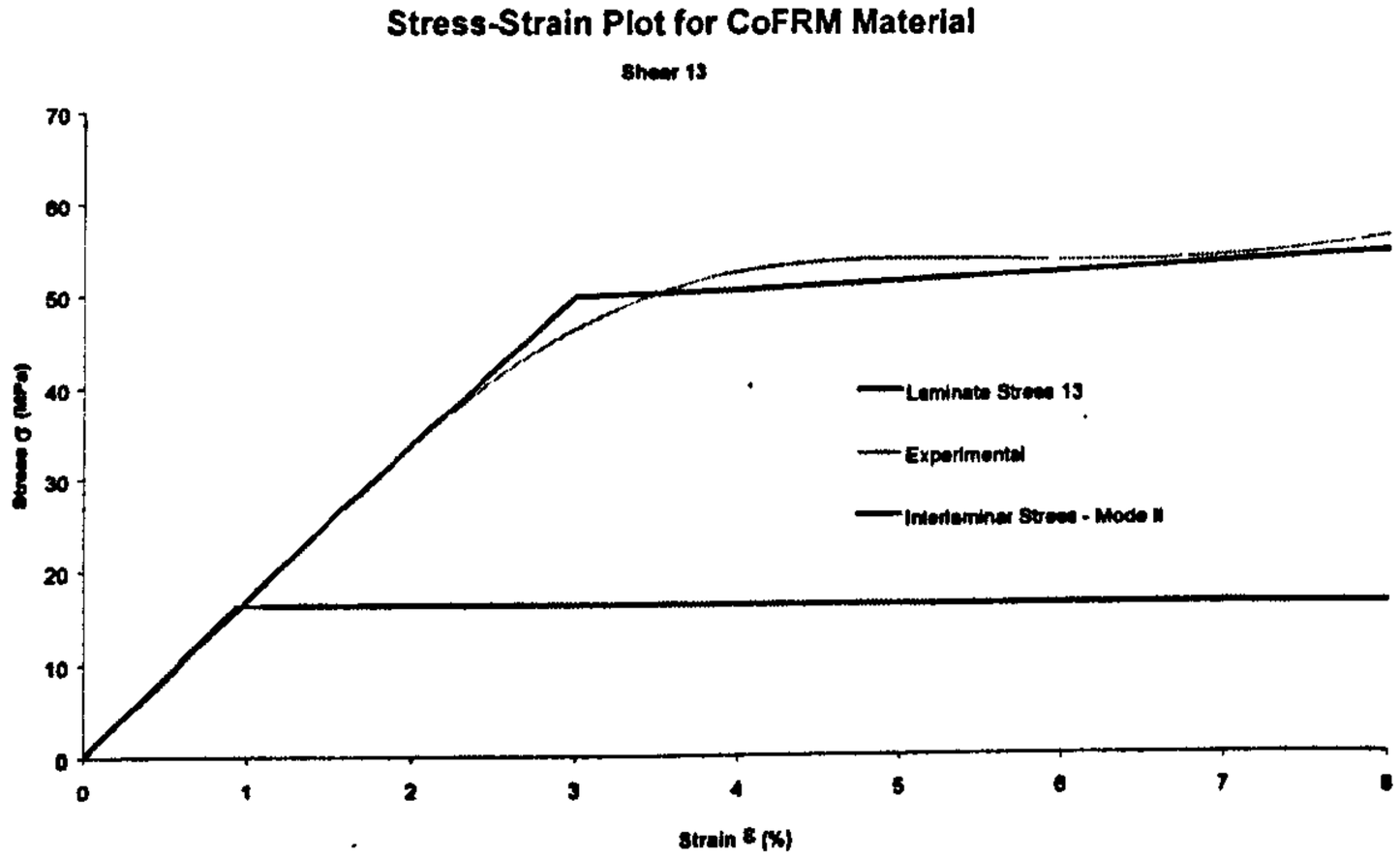
Stress-Strain Plot for CoFRM Material
Shear 13
Stress σ (MPa)
70
60
50
40
30
20
10
0
0
1
2
3
4
5
6
7
8
Strain ε (%)
Laminate Stress 13
Experimental
Interlaminar Stress - Mode II

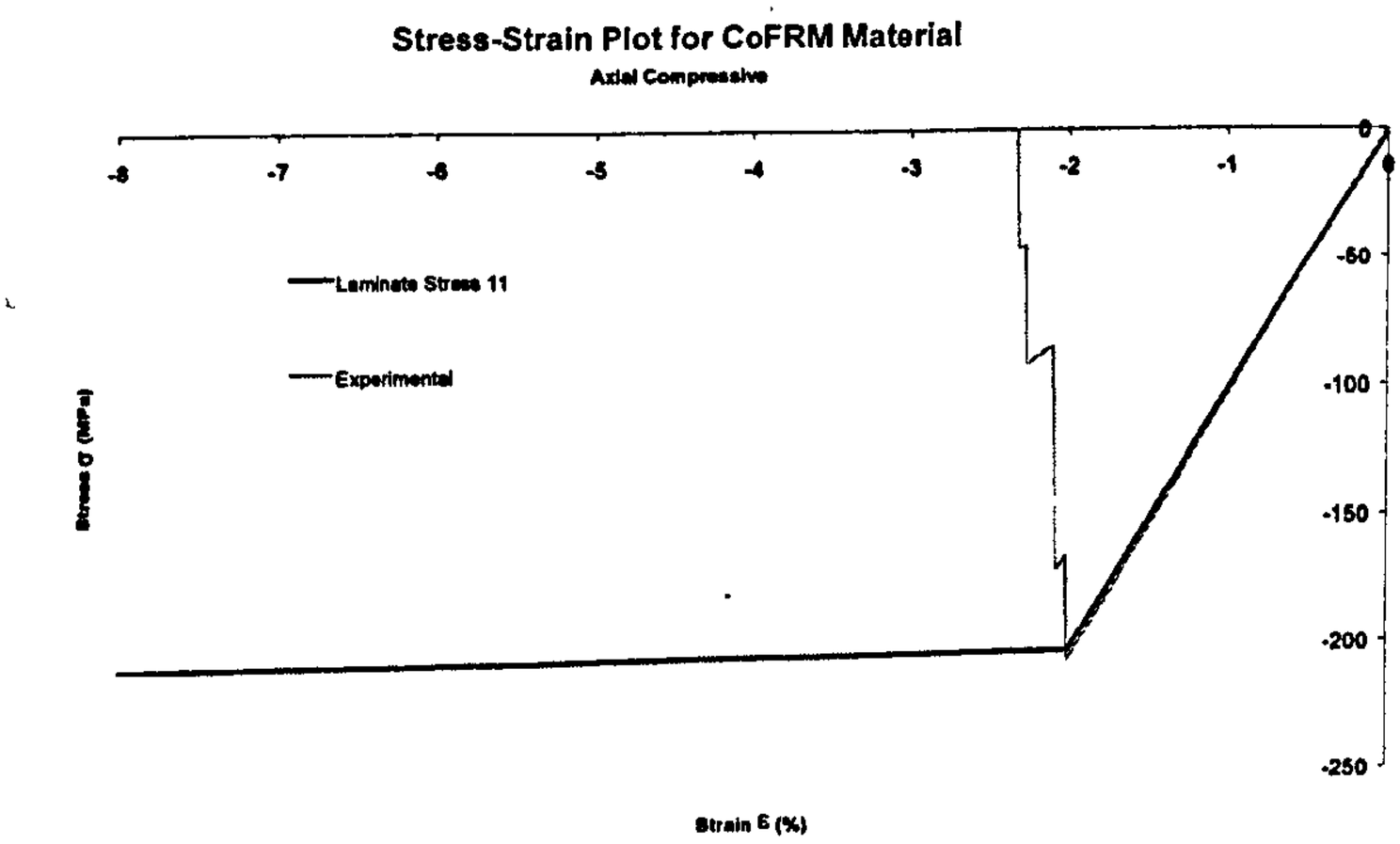
Stress-Strain Plot for CoFRM Material
Axial Compressive
Stress σ (MPa)
-8
-7
-6
-5
-4
-3
-2
-1
0
-50
-100
-150
-200
-250
Strain ε (%)
Laminate Stress 11
Experimental

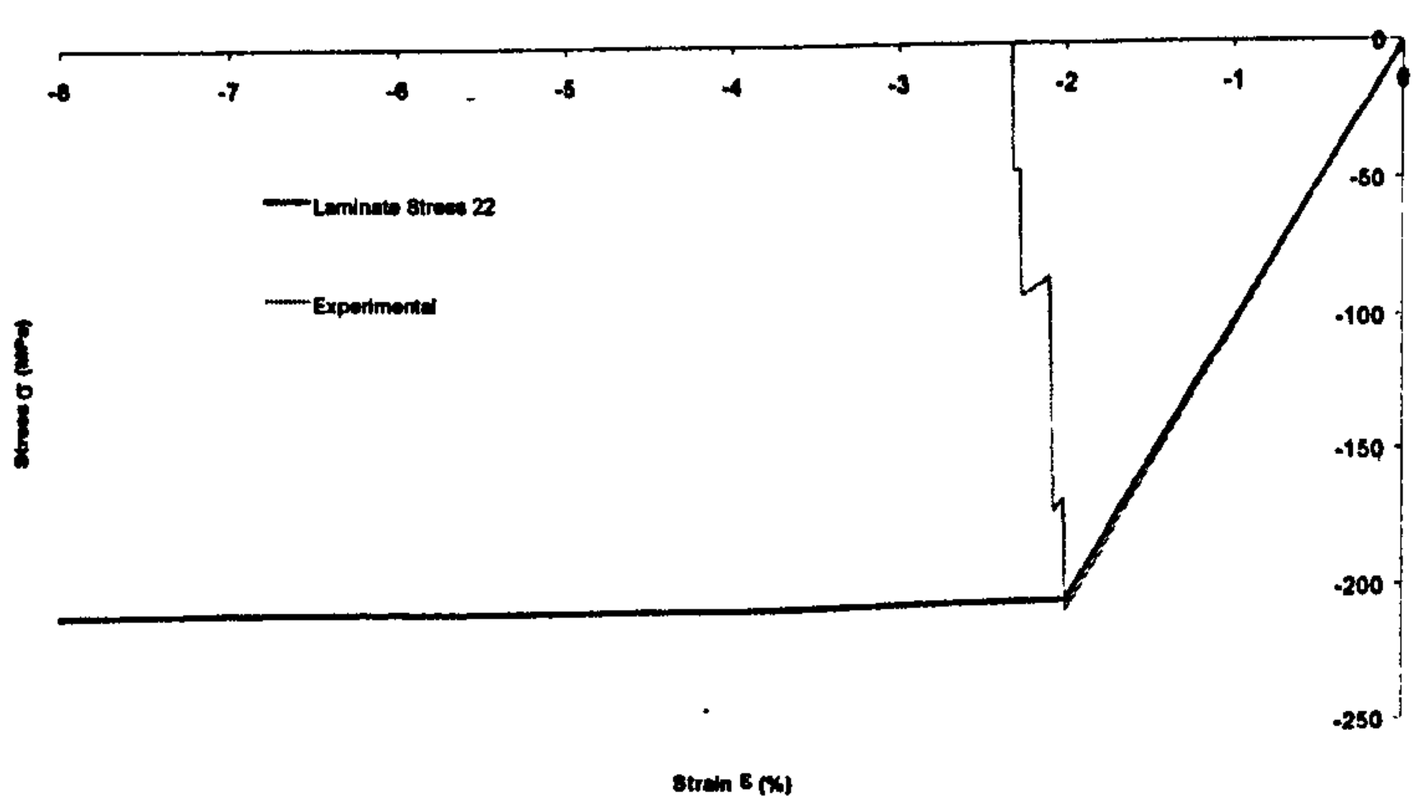
Stress-Strain Plot for CoFRM Material
Transverse Compressive
Stress σ (MPa)
-8
-7
-6
-5
-4
-3
-2
-1
0
-50
-100
-150
-200
-250
Strain ε (%)
Laminate Stress 22
Experimental

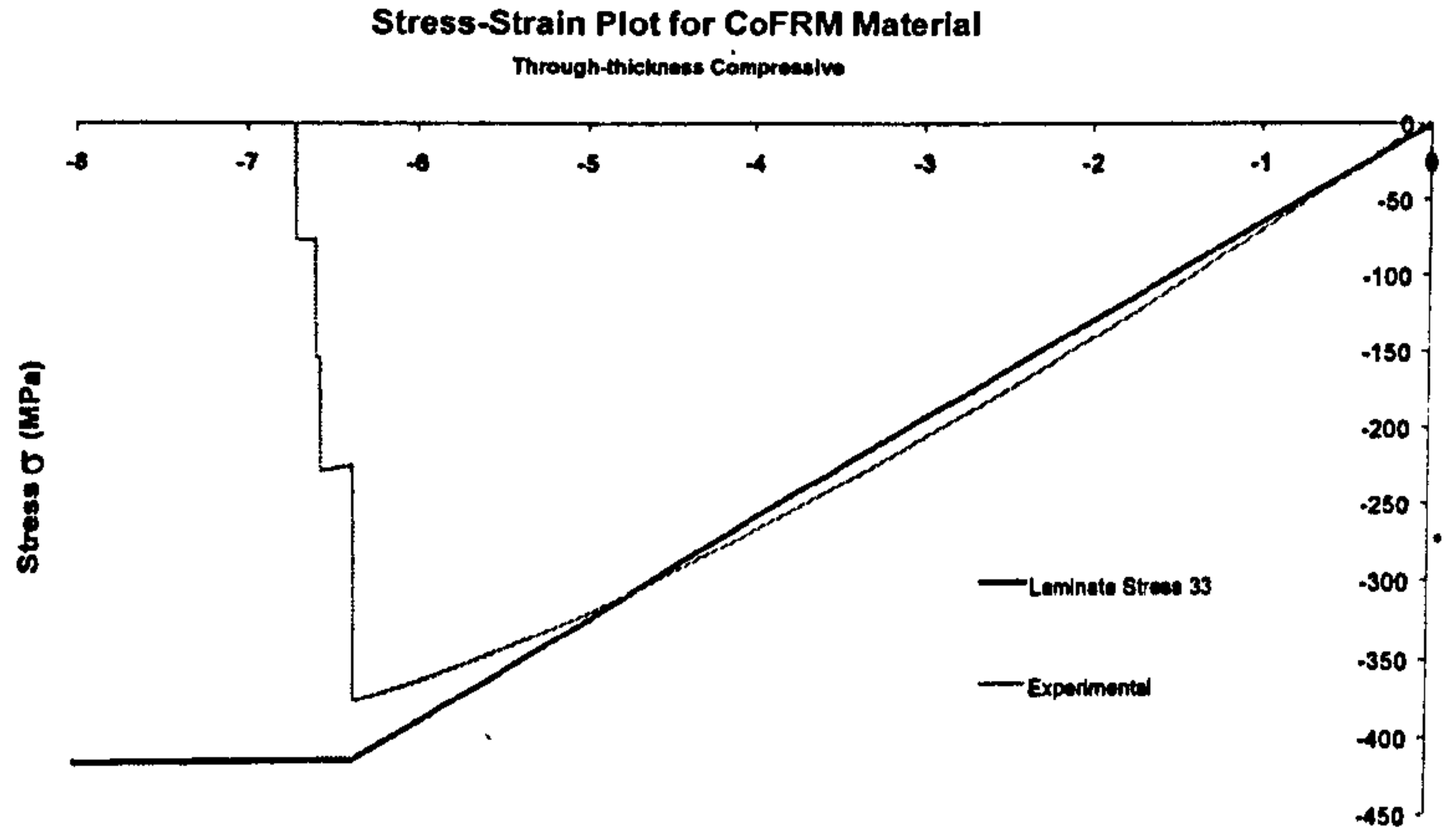
Stress-Strain Plot for CoFRM Material
Through-thickness Compressive
Stress σ (MPa)
Strain ε (%)
-8
-7
-6
-5
-4
-3
-2
-1
0
-50
-100
-150
-200
-250
-300
-350
-400
-450
Laminate Stress 33
Experimental

Tube Crush Results

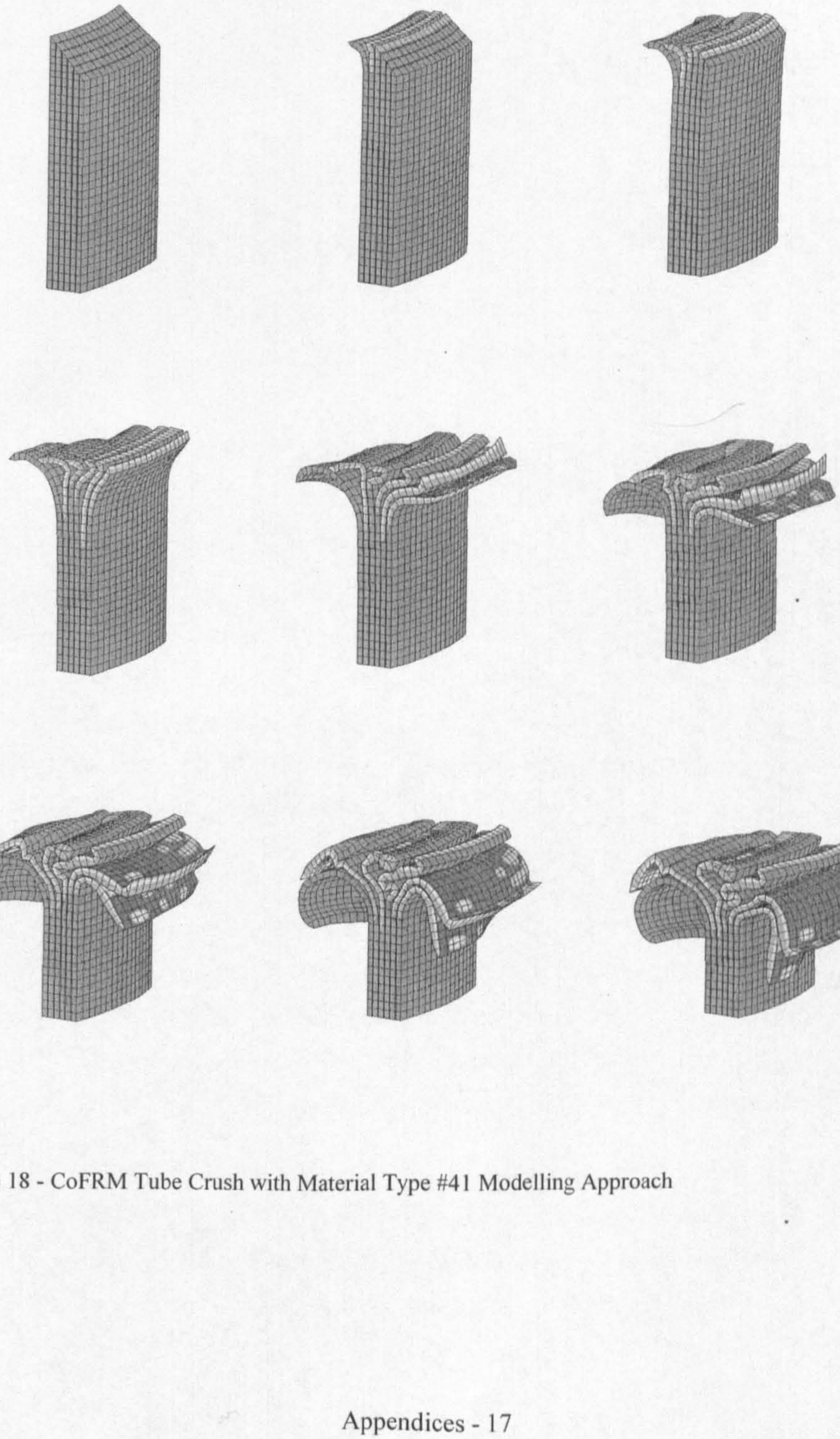

Figure 18 - CoFRM Tube Crush with Material Type #41 Modelling Approach

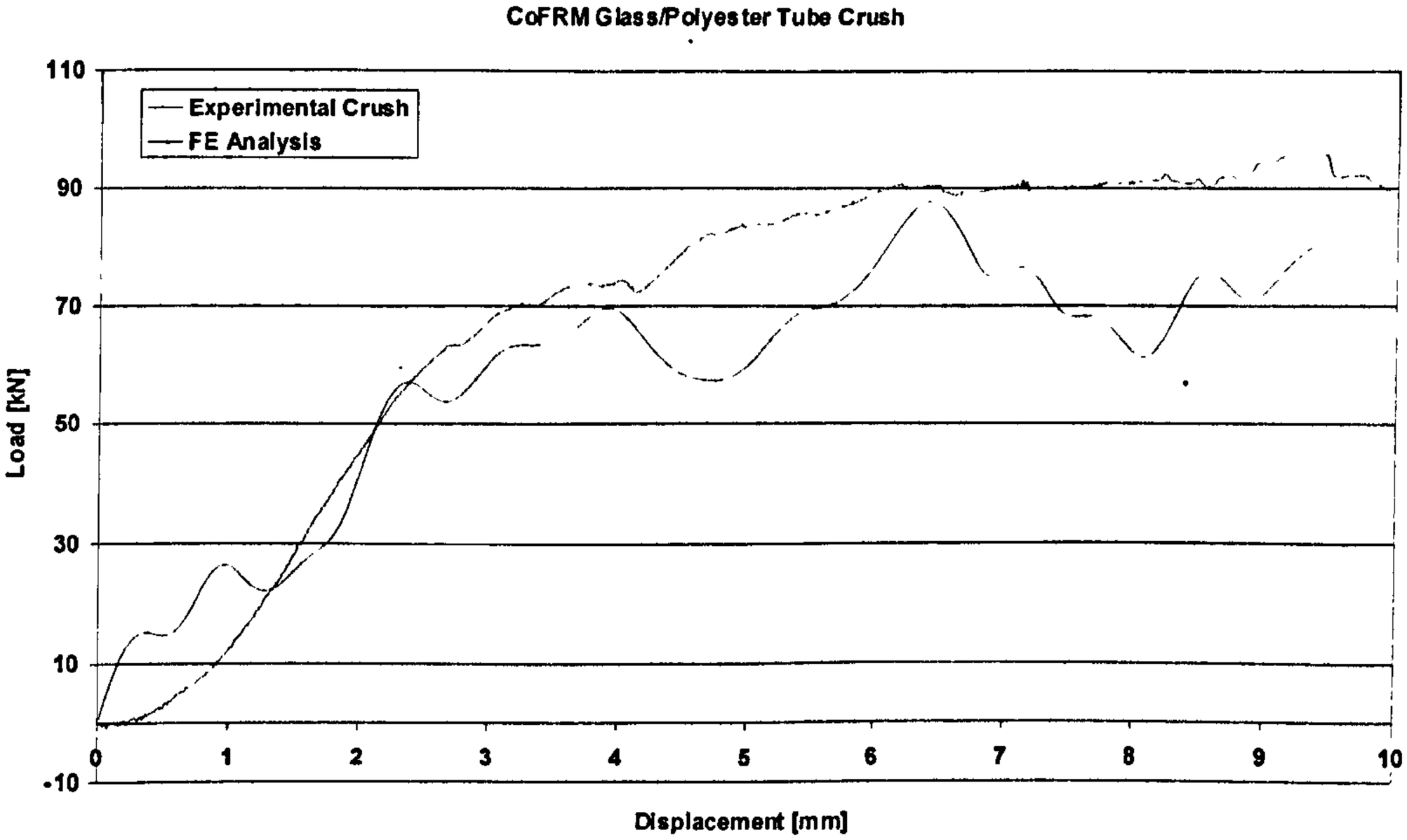

Figure 19 - Load-displacement of CoFRM Tube with Material Type #41 Modelling Approach

Assessment of PAM-CRASH Material Type #41

This material model was originally developed for impact barriers used in automotive crash simulation. However, it is appropriate for use with composite materials since each direction is modelled separately. As a result, the calibration procedure for highly anisotropic materials is simple when compared with the one used for the Degenerate Bi-phase model.. This material model also has only one set of damage parameters but the calibration approach proved much less time-consuming. This material model has rate effects included, by means of a Cowper-Symmonds rule, which scales the stress-strain curve depending on rate of loading [41].

The disadvantages in using this material model are that there is no coupling between the mechanical properties in the different directions, and the model is only available for solid elements. The uncoupled behaviour can lead to errors in predicting ply failure as, for example, a change in in-plane shear strength (due to an applied load) will lead to a lower in-plane compressive strength. This material model cannot capture that phenomenon.

The load-displacement curve of the FE model using Material Type #41 shows a better agreement with experimental when compared to the Degenerate-Bi-phase model. Formation and splaying of fronds was observed yet no formation of debris wedge took place. As with the degenerate Bi-phase model, no centre wall crack propagation was evident.

Observation of this tube model shows that not enough deformation of the solid elements is the most likely cause for no formation of a debris wedge. This in turn is responsible for an apparent separation of the plies at the interlaminar region leading to a "peeling-off" type of deformation which is not observed in experimental tube crush.

The use of Material Type 41 for modelling of braided carbon tubes showed stability problems, caused by the highly anisotropic behaviour of the material. Further investigation is required into the causes and solutions to overcome the instability observed.

Appendix 4. PAM-CRASH Input Parameters

In this section some of the PAM-CRASH input parameters for tube models are included, namely.

CoFRM Degenerate Bi-phase Material Cards

```
$
$   Bi-phase Solids
$
MATER /        1      30            1e-06      0       2
              12      13      14        1       2       90.000000
 bi-phase 1
    1
      0.03  100




                                                 0         0         0
$
$   PLY DATA CARDS
$
$---5---10----5---20----5---30----5---40----5---50----5---60----5---70----5---80
PLY   /     1    0          0    0
    Cont Glass Mat / Polyester for Square Solid E
     10.08     10.08      6.49
     4.246     1.759     1.684     0.296     0.353     0.353
   0.00725     0.016   0.02525     0.287     0.861
         0         0         0         0         0
         0         0         0         0         0         0         0
    2         0         1         0         1         0         0         0
     10.32     10.32     6.951
     4.246     1.759     1.684     0.302      0.35      0.35
   0.00725     0.016   0.02525     0.287     0.593
         0         0         0         0         0
         0         0         0         0         0         0         0
```

CoFRM Elastic-Plastic Material Cards

```
$
$   Elastic-Plastic Solids
$
MATER /       10       1            1e-06       1       0
               0       0       0        0       0       0   1.000
 plastic ply1
      4.46     0.082     0.001                                        0         0
     13.33
         0         0         0         0         0         0         0         0
         0         0         0         0         0         0         0         0

         0         0         0         0         0         0         0
```

CoFRM Delamination Cards

```
$
SLINT2/         1                32            0.0         0.10                  .10         2
 plies 1-2
          0.08      3.89     1.95     0.0      0.0           1
          .012    .030    .546e-03 .28e-02   .012       .030          1
                1
        MAT             12
        END
        MAT             21
        END
```

Braided Carbon 0/+30°/-30° Degenerate Bi-phase Material Cards

```
$
$    Bi-phase Solids
$
MATER /          1       30              1e-06        0         2
                12       13       14         1        2         90.000000
 bi-phase 1
     1
      0.032  100




                                                      0           0           0
$
$   PLY DATA CARDS
$
$---5---10----5---20----5---30----5---40----5---50----5---60----5---70----5---80
PLY    /      1    0          0     0
     Braided Carbon 0/+30/-30
      74.60       1.22       1.22
      3.500      3.500      3.500         0.5      0.308      0.263
     0.0050      0.009      0.016         0.2        0.7
          0          0          0           0          0
          0          0          0           0          0           0           0
     2          1          0           0          0          1           0           0
      57.70       3.00       3.00
      3.500      3.500      3.500       0.225      0.482      0.151
      0.001      0.010      0.012         0.6        0.7
          0          0          0           0          0
          0          0          0           0          0           0           0
$
```

Braided Carbon 0/+30°/-30° Elastic-Plastic Material Cards

```
$
$    Elastic-Plastic Solids
$
MATER /         10         1              1e-06         1         0
                 0         0         0          0         0         0    1.000
 plastic ply1
      3.500     0.0510      0.001                                                0           0
      7.580
          0          0          0           0          0          0           0           0
          0          0          0           0          0          0           0           0

          0          0          0           0          0          0           0
$
```

Braided Carbon 0/+30°/-30° Delamination Cards

```
$
SLINT2/         4                32             0.0        0.10                .10        2
 plies 1-2
          0.08      1.22     3.50     0.0       0.0          1
         .00771   .01635    1.0e-03 4.0e-03   .00771   .01635        1
                 1
         MAT              12
         END
         MAT              21
         END
```

Braided Carbon 0/+45°/-45° Degenerate Bi-phase Material Cards

```
$
$    Bi-phase Solids
$
MATER /          1       30              1e-06        0        2
                12       13       14         1        2        90.000000
 bi-phase 1
     1
      0.032  100




                                                    0          0          0
$
$   PLY DATA CARDS
$
$---5---10----5---20----5---30----5---40----5---50----5---60----5---70----5---80
PLY    /      1    0          0     0
     Braided Carbon 0/+45/-45
       62.6        5.74        5.74
        3.9         3.9         3.9       0.312       0.312       0.312
      0.005       0.010       0.021         0.2         0.7
          0           0           0           0           0
          0           0           0           0           0           0          0
     2          1          0          0          0          1          0          0
       70.6          10          10
        3.9         3.9         3.9       0.312       0.312       0.312
      0.001       0.006      0.0065         0.6         0.7
          0           0           0           0           0
          0           0           0           0           0           0          0
$
```

Braided Carbon 0/+45°/-45° Elastic-Plastic Material Cards

```
$
$    Elasto-Plastic Solids
$
MATER /         10         1              1e-06         1         0
                 0         0         0          0      0         0    1.000
 plastic ply1
      3.900     0.0675      0.001                                              0          0
      9.072
          0          0          0          0          0          0          0          0
          0          0          0          0          0          0          0          0

          0          0          0          0          0          0          0
$
```

Braided Carbon 0/+45°/-45° Delamination Cards

```
$
SLINT2/         4                32              0.0         0.10                .10         2
 plies 1-2
           0.08      1.22     3.50     0.0       0.0           1
         .00771   .01635    1.0e-03 4.0e-03   .00771   .01635        1
                1
         MAT              12
         END
         MAT              21
         END
```

Braided Carbon 0/+60°/-60° Degenerate Bi-phase Material Cards

```
$
$    Bi-phase Solids
$
MATER /          1       30              1e-06        0        2
                12       13       14         1        2        90.000000
 bi-phase 1
     1
      0.032  100




                                                    0          0          0
$
$   PLY DATA CARDS
$
$---5---10----5---20----5---30----5---40----5---50----5---60----5---70----5---80
PLY    /      1    0          0     0
     Braided Carbon 0/+60/-60
       58.9      16.74     16.74
        5.1        5.1       5.1       0.38      0.398     0.149
      0.005      0.010     0.021       0.15        0.7
          0          0         0          0          0
          0          0         0          0          0          0          0
     2          1          0          0          0          1          0          0
       53.5          18         18
        5.1        5.1       5.1       0.225     0.482     0.151
      0.001      0.006     0.0065        0.6        0.7
          0          0         0          0          0
          0          0         0          0          0          0          0
$
```

Braided Carbon 0/+60°/-60° Elastic-Plastic Material Cards

```
$
$    Elasto-Plastic Solids
$
MATER /         10         1              1e-06        1         0
                 0         0         0          0         0         0    1.000
 plastic ply1
      5.100     0.0929      0.001                                                0          0
      11.05
          0          0          0          0          0          0          0          0
          0          0          0          0          0          0          0          0

          0          0          0          0          0          0          0
$
```

Braided Carbon 0/+60°/-60° Delamination Cards

```
$
SLINT2/         4                32            0.0        0.10                .10        2
 plies 1-2
          0.08      1.22     3.50     0.0      0.0          1
         .00771   .01635    1.0e-03 4.0e-03  .00771   .01635        1
                 1
         MAT              12
         END
         MAT              21
         END
```

Appendix 5. Dimensions of Intralaminar Specimens

All the following dimensions are in mm.

CoFRM Tensile

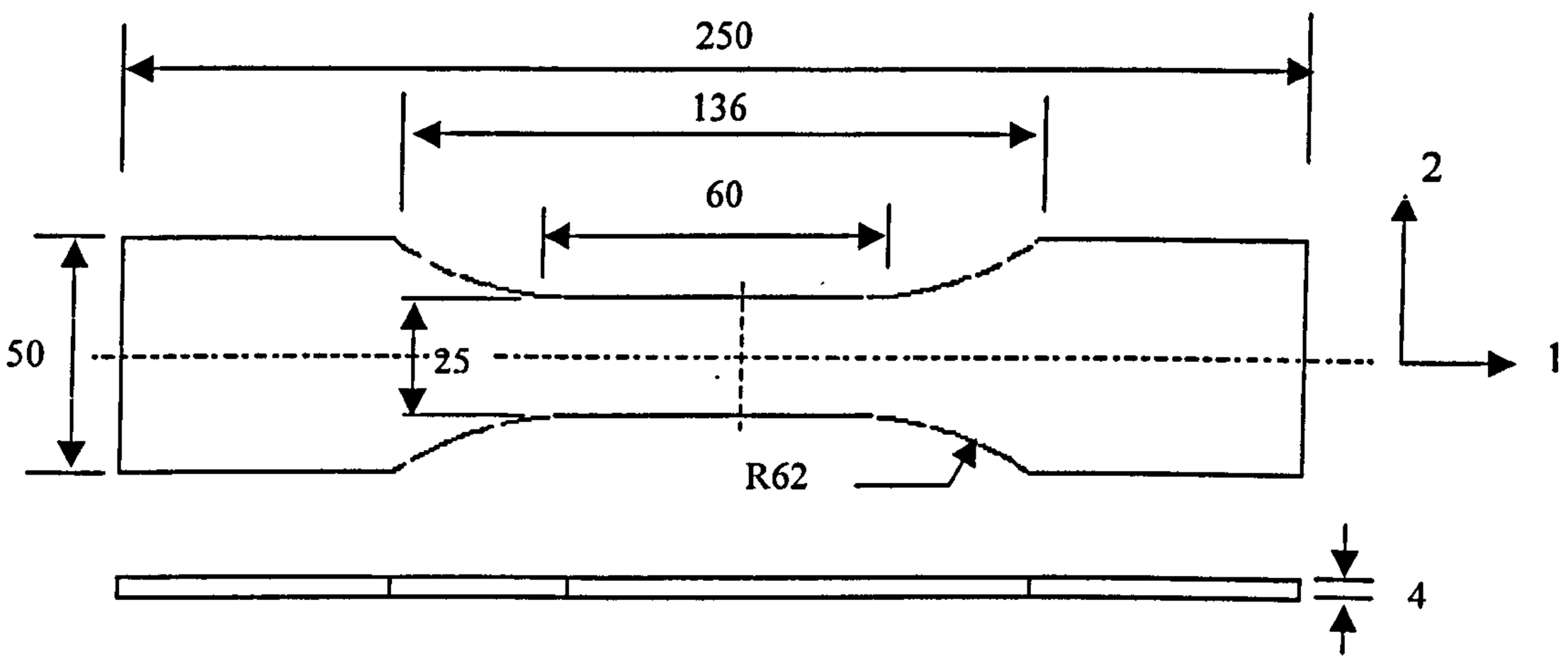

CoFRM Compressive

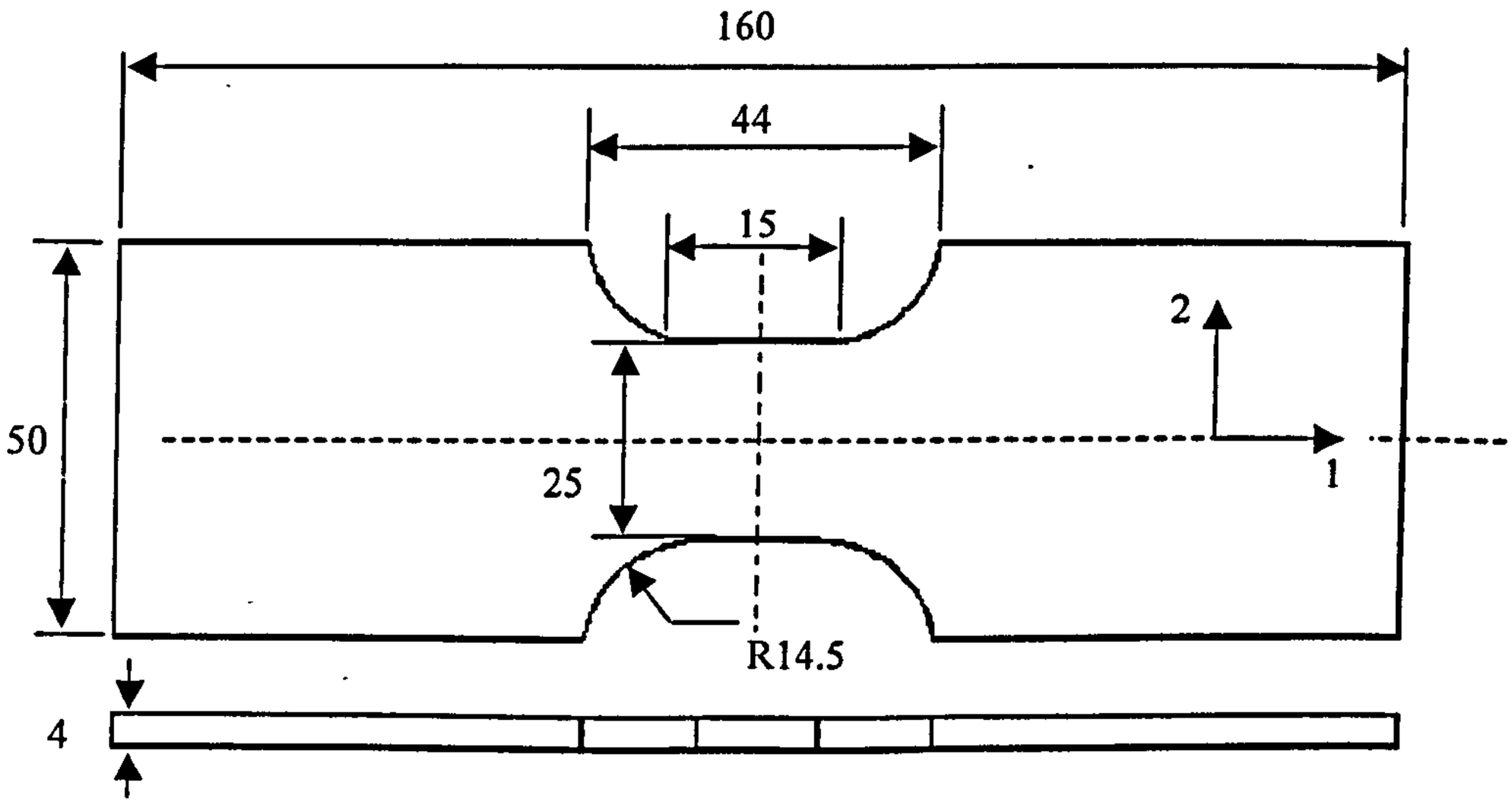

CoFRM Shear

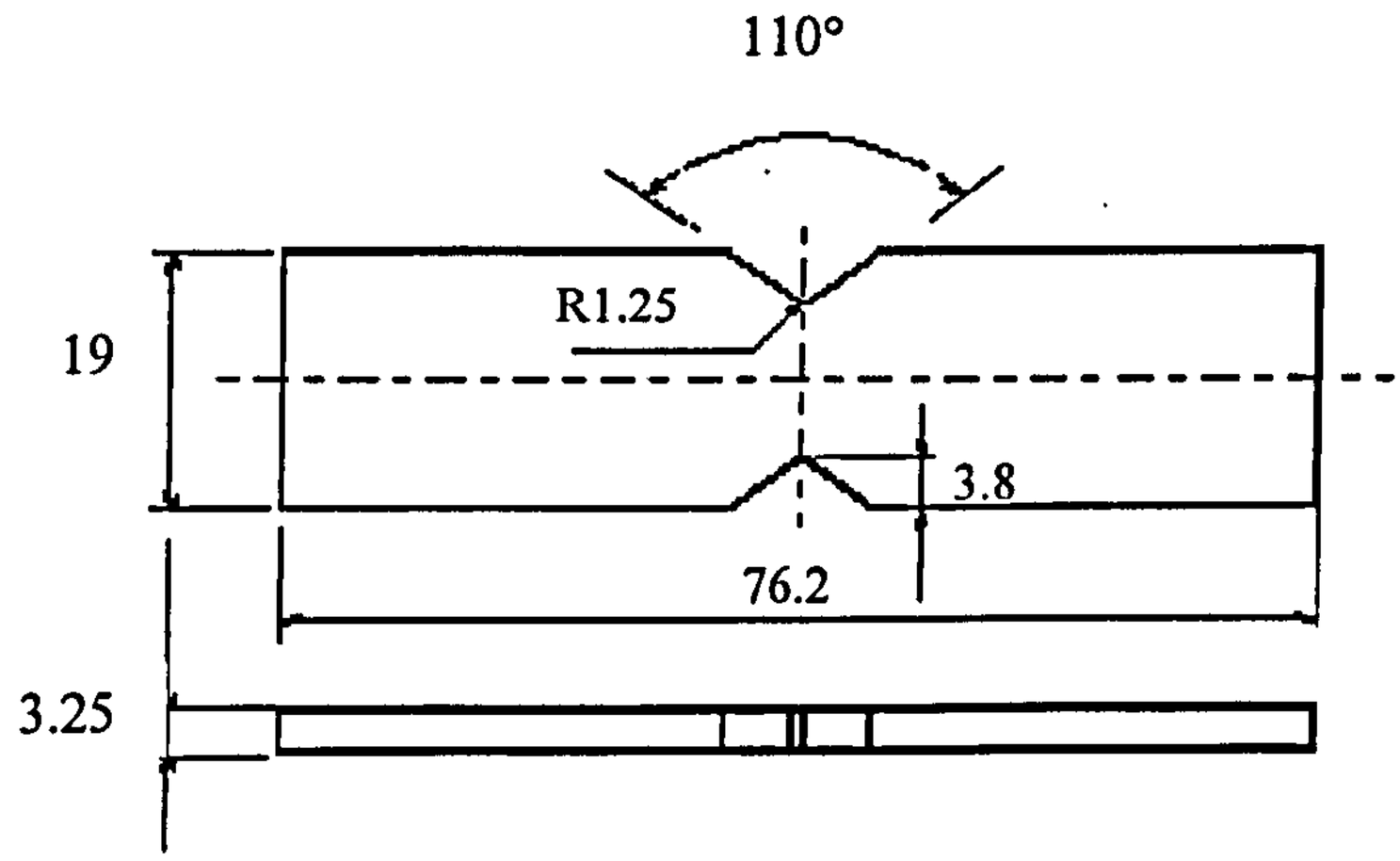

CoFRM Through-thickness Tension

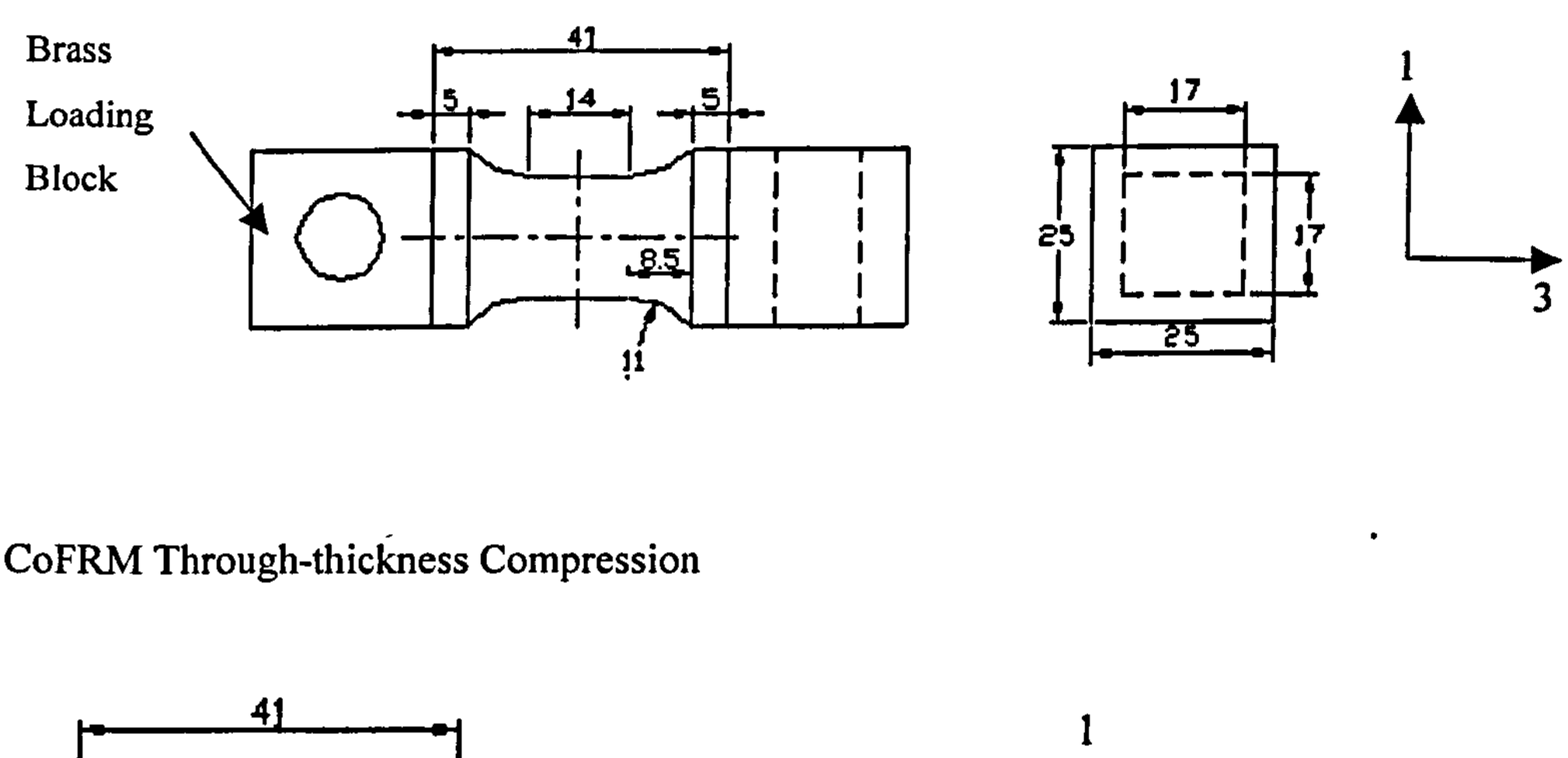

CoFRM Through-thickness Compression

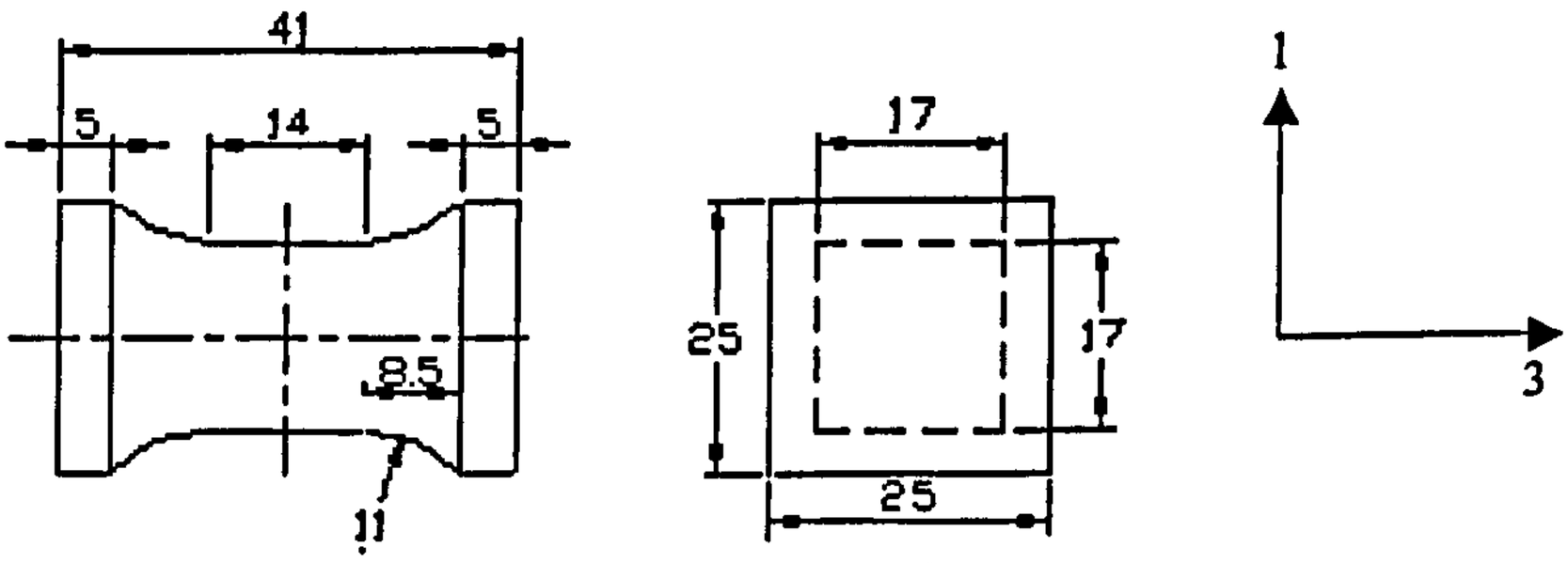

Braided Carbon Tensile

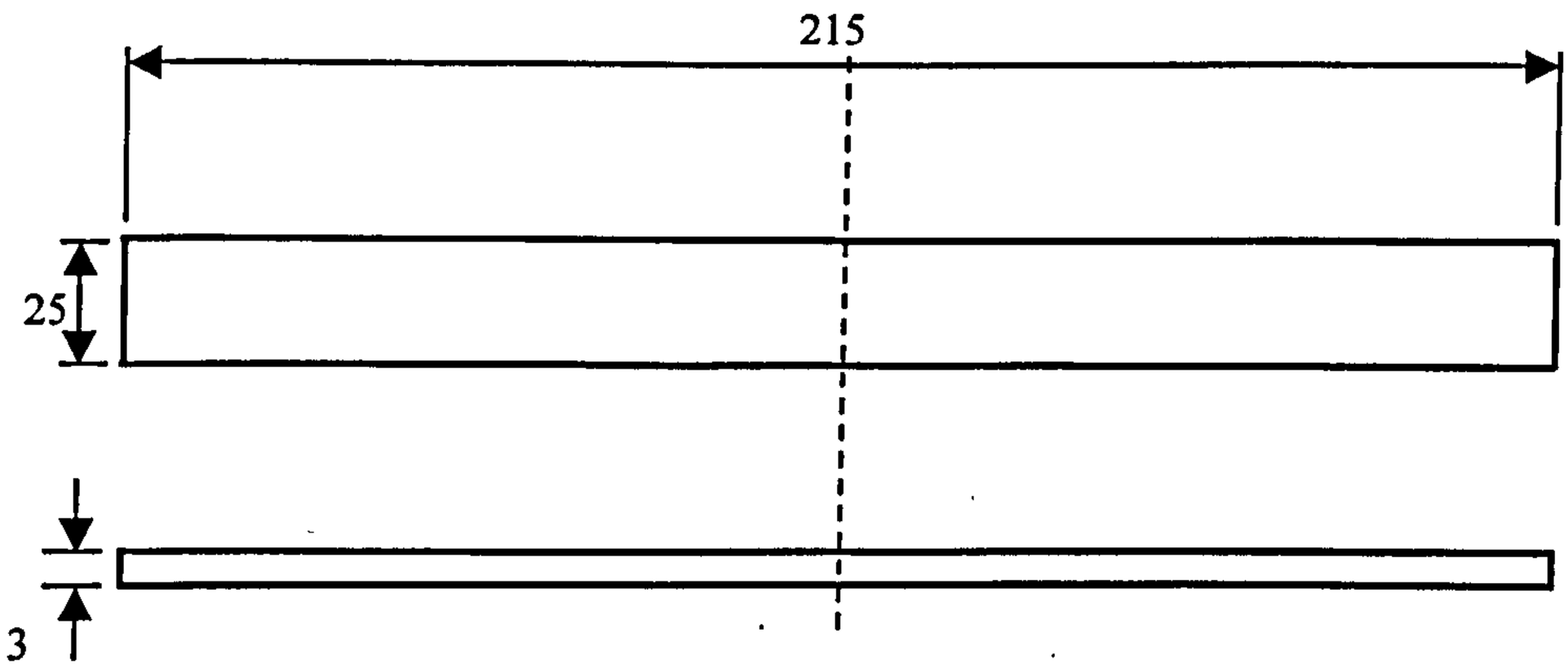

Braided Carbon Compressive

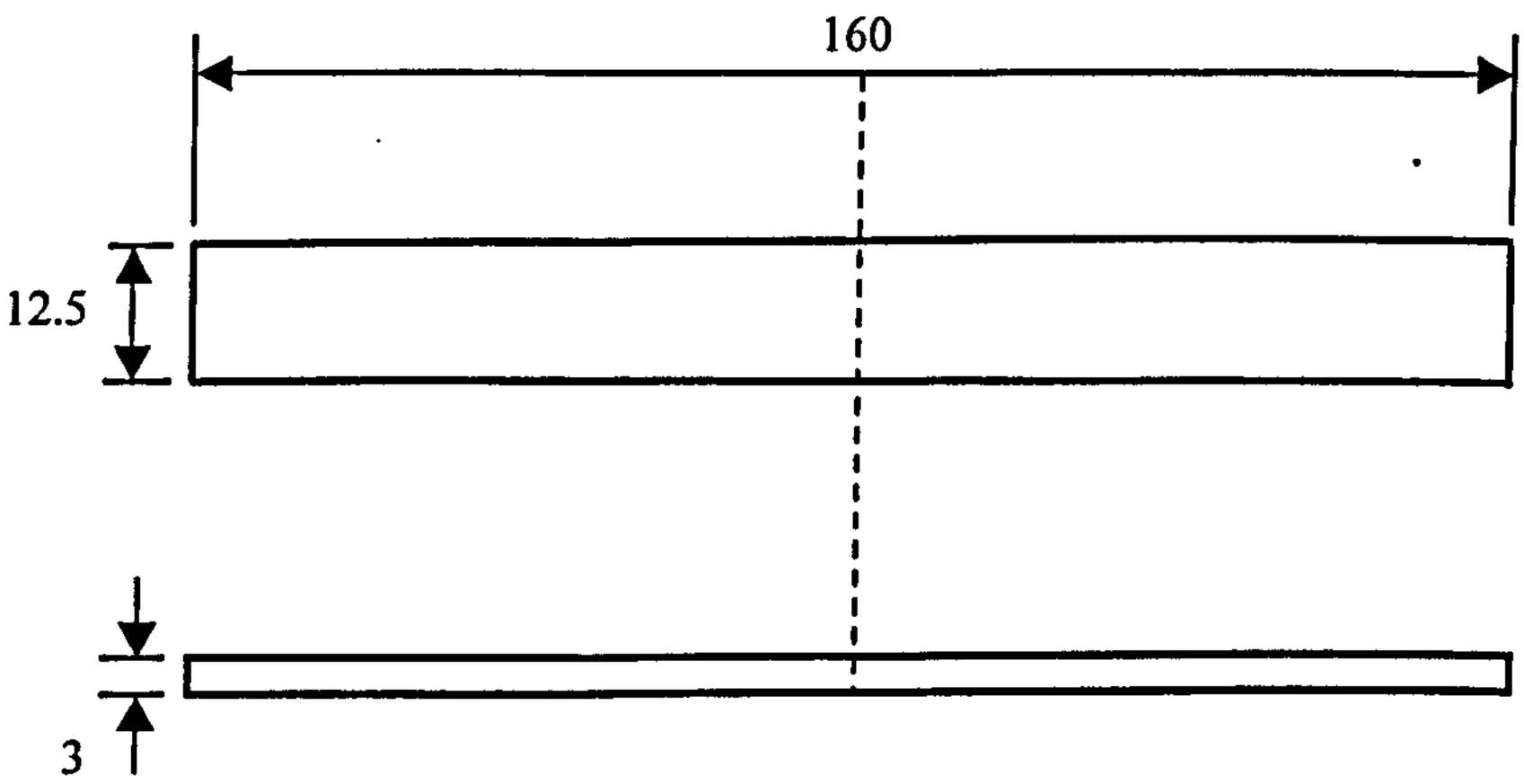

Braided Carbon In-Plane Shear

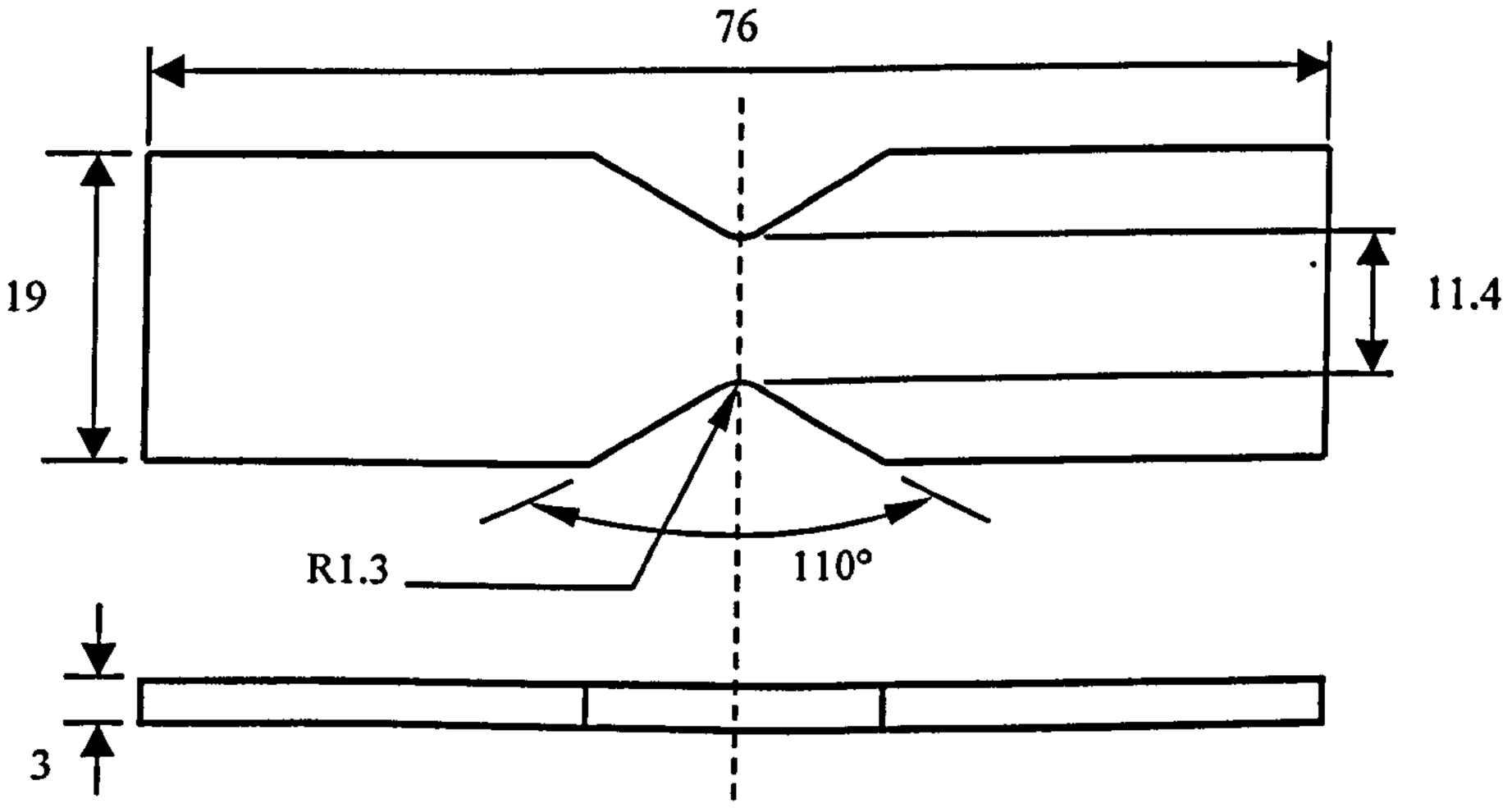

Braided Carbon Through-Thickness Shear